ABSTRACT

Title of Document: FLOW REGIME DRIVEN THERMAL ENHANCEMENT IN INTERNALLY-GROOVED TUBES

Darin Sharar, Doctor of Philosophy, 2016.

Directed by: Professor Avram Bar-Cohen
Department of Mechanical Engineering

Internally-grooved refrigeration tubes maximize tube-side evaporative heat transfer rates and have been identified as a most promising technology for integration into compact cold plates. Unfortunately, the absence of phenomenological insights and physical models hinders the extrapolation of grooved-tube performance to new applications. The success of regime-based heat transfer correlations for smooth tubes has motivated the current effort to explore the relationship between flow regimes and enhanced heat transfer in internally-grooved tubes. In this thesis, a detailed analysis of smooth and internally-grooved tube data reveals that performance improvement in internally-grooved tubes at low-to-intermediate mass flux is a result of early flow regime transition. Based on this analysis, a new flow regime map and corresponding heat transfer coefficient correlation, which account for the increased wetted angle, turbulence, and Gregorig effects unique to internally-grooved tubes, were developed.

A two-phase test facility was designed and fabricated to validate the newly-developed flow regime map and regime-based heat transfer coefficient correlation. As part of this setup, a non-intrusive optical technique was developed to study the dynamic nature of two-phase flows. It was found that different flow regimes result in unique temporally

varying film thickness profiles. Using these profiles, quantitative flow regime identification measures were developed, including the ability to explain and quantify the more subtle transitions that exist between dominant flow regimes.

Flow regime data, based on the newly-developed method, and heat transfer coefficient data, using infrared thermography, were collected for two-phase HFE-7100 flow in horizontal 2.62mm - 8.84mm diameter smooth and internally-grooved tubes with mass fluxes from 25-300 kg/m^2s, heat fluxes from 4-56 kW/m^2, and vapor qualities approaching 1. In total, over 6500 combined data points for the adiabatic and diabatic smooth and internally-grooved tubes were acquired.

Based on results from the experiments and a reinterpretation of data from independent researchers, it was established that heat transfer enhancement in internally-grooved tubes at low-to-intermediate mass flux is primarily due to early flow regime transition to Annular flow. The regime-based heat transfer coefficient outperformed empirical correlations from the literature, with mean and absolute deviations of 4.0% and 32% for the full range of data collected.

FLOW REGIME DRIVEN THERMAL ENHANCEMENT IN INTERNALLY-GROOVED TUBES

By:
Darin James Sharar

Dissertation Submitted to the Faculty of the Graduate School of the
University of Maryland, College Park in partial fulfillment
of the requirements for the degree
of Doctor of Philosophy
2016

Advisory Committee:
Dr. Avram Bar-Cohen, Chair
Dr. Bongtae Han
Dr. Michael Ohadi
Dr. Patrick McCluskey
Dr. Mario Dagenais, Dean's Representative

This work was supported by the U.S. Army Research Laboratory under Contract W911QX-15-D-0023, Task 0001. The views and conclusions contained in this document are those of the author, Darin J. Sharar, and should not be interpreted as presenting the official policies or position, either expressed or implied, of the U.S. Government.

Acknowledgements

I am most grateful to my advisor, Dr. Avram Bar-Cohen, for giving me the opportunity and motivation to undertake this work. Dr. Bar-Cohen, it's been an honor to complete my PhD under your direction.

I would like to thank my Dissertation defense committee; Professor Michael Ohadi, Professor Bongtae Han, Professor Patrick McCluskey, and Professor Mario Dagenais for their advice and guidance through all stages of this work. I would like to give special thanks to Dr. Arthur Bergles, whose guidance, insight, and support, as well as pioneering work on two-phase enhancement, has inspired and informed much of this ongoing research effort. He will be sorely missed, both professionally and personally.

Thanks to my colleagues at the Army Research Laboratory (ARL) and University of Maryland (UMD) for their cooperation and friendship. Among them, special thanks to Dr. Brian Morgan, Dr. Lauren Boteler, and Nicholas Jankowski for their constant support. I also acknowledge my former and current lab-mates, working in collaboration with the Maryland Embedded Cooling Center (MEmCo) and Thermal Management of Photonic and Electronic Systems (TherPES) laboratory: Dr. Emil Rahim, Dr. Peng Wang, Dr. Juan Cevallos, Dr. Mike Manno, Horacio Nochetto, Frank Robinson, Caleb Holloway, Alex Reeser, and Michael Fish.

Finally, many thanks to my parents Susan and Joseph Sharar, my wife Kristen Oursler Sharar, my sister Anne King, her husband Scott King, and their two beautiful children Ryleigh and Grayson, my friends, and my extended family for their enduring love and support. You mean the world to me.

Table of Contents

Acknowledgements ii

Table of Contents iii

List of Tables.. viii

List of Figures. xii

Chapter 1: Introduction 1

1.1 Power Conversion Electronics - Thermal Issue 2

1.2 Power Electronic Thermal Management 3

1.3 Two-Phase Surface Enhancements and Internally-Grooved Tubes 6

1.4 Goals and Outline 10

1.4.1 Goals 10

1.4.2 Outline 11

Chapter 2: Two-Phase Flow Boiling Fundamentals 14

2.1 Diabatic Two-Phase Flow Patterns and Dependence on Heat Transfer 14

2.2 Two-Phase Flow Pattern Maps 17

2.3 Smooth Tube Regime-Based Heat Transfer Models 21

Chapter 3: Fundamental Studies of Flow Patterns and Heat Transfer in Internally-Grooved Tubes 24

3.1 Flow Regime Quantification 25

3.2 Studies on Conventional Internally-Grooved Tubes 25

3.2.1 Flow Regime Transition Mechanisms 27

3.2.2 Halogenated Fluids at Standard Pressure and Temperature 30

3.2.3 Refrigerant/Oil Mixtures 40

3.2.4 Halogenated Fluids and CO_2 at Elevated Reduced Pressure 40

3.2.5 Geometric Considerations.....43

3.3 Studies on Small Internally-Grooved Tubes..... 44

3.3.1 Refrigerant/Oil Mixtures.....46

3.3.2 Geometric Considerations.....47

3.4 Flow Regime Maps and Regime-Inspired Heat Transfer Coefficient Correlations for Internally-Grooved Tubes 47

3.5 Summary 52

Chapter 4: New Flow Regime Map and Heat Transfer Coefficient Correlation for Internally-Grooved Tubes 57

4.1 Taitel-Dukler [46] Annular Transition Criteria 57

4.2 Traditional Wojtan et al. [30] Flow Regime Map for Smooth Tubes..... 60

4.3 Modified Sharar et al. [29] Flow Regime Map for Internally-Grooved Tubes 64

4.4 Traditional Wojtan et al. [31] Heat Transfer Coefficient Correlation 66

4.5 Modified Heat Transfer Coefficient Correlation 73

4.6 Model Simulation..... 75

4.7 Summary 82

Chapter 5: Experimental Setup and Procedures 84

5.1 Two-Phase Testing Setup 84

5.2 Tube Heating Method 88

5.3 Fluid Selection 89

5.4 Experimental Ranges 91

5.5 Data Acquisition 93

5.6 Deduction of Vapor Quality 94

5.7 Calculating Heat Transfer Coefficient 95

5.8 Uncertainty Analysis 98

Chapter 6: Total Internal Reflection Flow Regime Quantification 102

6.1 Flow Regime Quantification Methods Available in the Literature 103

6.2 Theory 104

6.3 TIR Setup and Procedures 107

6.3.1 Implementation of the TIR Technique 107

6.3.2 Experimental Ranges for Method Validation 108

6.3.3 Data Acquisition 108

6.3.4 Data Reduction 109

6.4 Experimental Results 112

6.4.1 Accuracy of the Total Internal Reflection Technique 112

6.4.2 Limitations of the Total Internal Reflection Technique during Two-Phase Testing 115

6.4.3 Characterization of Primary Flow Regimes 117

6.4.4 Characterization of Sub-Regimes and Subtle Differences of Primary Flow Regimes 121

6.4.5 TIR Validation with Existing Flow Regime Maps 125

6.5 Summary 131

Chapter 7: Single-Phase Data and Discussion 133

7.1 Single-Phase Energy Balance 133

7.2 Single-Phase Heat Transfer Measurements and Comparison to Smooth Tube Correlations 134

7.3 Single-Phase Heat Transfer Measurements and Comparison to Internally-Grooved Tube Correlations 137

Chapter 8: Two-Phase Data and Discussion 142

8.1 8.84mm Smooth and Internally-Grooved Tubes 143

8.1.1 Influence of Mass Flux and Flow Regime 143

8.1.2 Influence of Heat Flux 149

8.2 4.54mm Smooth and Internally-Grooved Tubes 153

8.2.1 Influence of Mass Flux and Flow Regime 153

8.2.2 Influence of Heat Flux 159

8.3 2.8mm Smooth and 2.62mm Internally-Grooved Tubes 162

8.3.1 Influence of Mass Flux and Flow Regime 162

8.3.2 Influence of Heat Flux 168

8.4 Tabulation of Flow Regime Modeling Results 171

8.5 Enhancement Ratio 173

8.6 Statistical Assessment of the Heat Transfer Coefficient Correlations 176

8.6.1 Smooth Tubes 177

8.6.2 Internally-Grooved Tubes 180

8.7 Comparison to Data from the Literature 186

8.7.1 Flow Regime Data 186

8.7.2 Heat Transfer Coefficient 192

8.8 Applicability of the Sharar et al. Model 196

8.9 Refitting the Sharar et al. Flow Regime Map 198

8.10 Summary 202

Chapter 9: Conclusions and Future Work 205

9.1 Conclusions 205

9.2 Future Work 209

Appendix A Atomic Layer Deposition Tube Coating Method 212

A.1 Candidate Heating Methods 212

A.2 Atomic Layer Deposition Heating 213

A .2.1 ALD Uniformity 214

A .2.2 Pinhole Defects in ALD 215

A .2.3 Ruthenium ALD.....218

Appendix B Matlab Code for Total Internal Reflection.....219

B.1 Preprocessing 221

B.2 Importing the Picture and Finding the Location of the First Fully Reflected Ray….. 221

B.3 Determining the Number of Pixels Between Lines 223

B.4 Defining Properties and Dimensions 227

B.5 TIR Film Thickness Calculation 227

Appendix C 8.84mm Smooth and Internally-Grooved Tube Data 229

Appendix D 4.54mm Smooth and Internally-Grooved Tube Data 239

Appendix E 2.8mm Smooth and 2.62mm Internally-Grooved Tube Data 248

Appendix F Statistical Analysis of Heat Transfer Results.....256

Chapter 10: Works Cited 267

List of Tables

Table 1: Classification of flow boiling enhancement techniques 7

Table 2: Geometric parameters and fin efficiencies for three Wieland copper internally-grooved tubes 8

Table 3: Performance comparison of internally-grooved tubes to smooth tubes 9

Table 4: Summary of relevant studies on flow patterns and heat transfer in macroscale internally-grooved tubes 26

Table 5: Summary of relevant studies on flow patterns and heat transfer in small and microscale internally-grooved tubes 45

Table 6: Summary of relevant studies on new flow pattern maps for internally-grooved tubes and regime-based heat transfer coefficient models 48

Table 7: Comparison of fluids (and properties) used for empirically fitted flow regime maps and candidate fluids 91

Table 8: Geometric parameters of internally-grooved and smooth tubes for the current study 92

Table 9: Heat transfer coefficients applied at different axially and circumferentially varying locations for the ANSYS numerical model 98

Table 10: Summary of uncertainties for sensors and parameters 101

Table 11: Comparison of thickness prediction using test setup and Matlab algorithm to actual thickness values 115

Table 12: Geometric properties and maximum measurable film thickness for different operating conditions 117

Table 13: Statistical analysis of the experimental single-phase smooth tube heat transfer measurements 137

Table 14: Statistical analysis of the experimental single-phase internally-grooved tube heat transfer measurements 139

Table 15: Predictive accuracy of Traditional Wojtan et al. [30] flow regime map for the smooth tube data 172

Table 16: Predictive accuracy of Traditional Wojtan et al. [30] and Modified Sharar et al. [29] flow regime maps for the internally-grooved tube data 173

Table 17: Predictive accuracy of two-phase smooth tube heat transfer coefficient correlations from Wojtan et al. [31], Chen [56], Shah [57], Kandlikar [93], and Gungor-Winterton [59] [60] 180

Table 18: Predictive accuracy of Modified Sharar and Bar-Cohen two-phase internally-grooved tube heat transfer coefficient correlation and correlations from Thome et al. [91], Cavallini et al. [117], Chamra and Mago [162], Wu et al. [103], and Yun et al. [90].... 182

Table 19: Predictive accuracy of Traditional Wojtan et al. [30] and Modified Sharar et al. [29] flow regime maps 192

Table 20: Saturated Properties of Various Fluids 198

Table 21: Material properties of interest for ALD coated copper tubes 214

Table 22: Predictive accuracy of two-phase smooth tube heat transfer coefficient correlations from Wojtan et al. [31], Chen [56], Shah [57], Kandlikar [93], and Gungor-Winterton [59] [60] 264

Table 23: Predictive accuracy of two-phase smooth tube heat transfer coefficient correlations from Wojtan et al. [31], Chen [56], Shah [57], Kandlikar [93], and Gungor-Winterton [59] [60] 264

Table 24: Predictive accuracy of two-phase smooth tube heat transfer coefficient correlations from Wojtan et al. [31], Chen [56], Shah [57], Kandlikar [93], and Gungor-Winterton [59] [60] 264

Table 25: Summary of the predictive accuracy of two-phase smooth tube heat transfer coefficient correlations from Wojtan et al. [31], Chen [56], Shah [57], Kandlikar [93], and Gungor-Winterton [59] [60] to the 2.8mm to 8.84mm experimental results..... 265

Table 26: Predictive accuracy of the Modified Sharar and Bar-Cohen internally-grooved tube correlation, and correlations from Thome et al. [91], Cavallini et al. [117], Chamra and Mago [162], Wu et al. [103], and Yun et al. [90] compared to the 8.84mm experimental results 265

Table 27: Predictive accuracy of the Modified Sharar and Bar-Cohen internally-grooved tube correlation, and correlations from Thome et al. [91], Cavallini et al. [117], Chamra and Mago [162], Wu et al. [103], and Yun et al. [90] compared to the 4.54mm experimental results 265

Table 28: Predictive accuracy of the Modified Sharar and Bar-Cohen internally-grooved tube correlation, and correlations from Thome et al. [91], Cavallini et al. [117], Chamra and Mago [162], Wu et al. [103], and Yun et al. [90] compared to the 2.62mm experimental results 266

Table 29: Summary of the predictive accuracy of the Modified Sharar and Bar-Cohen internally-grooved tube correlation, and correlations from Thome et al. [91], Cavallini et

al. [117], Chamra and Mago [162], Wu et al. [103], and Yun et al. [90] for the 2.62mm to 8.84mm experimental results 266

List of Figures

Figure 1: Midsize hybrid electric power requirements (adapted from [1]) 2

Figure 2: Dissipated heat vs flow rate for water using latent heat and sensible heat 6

Figure 3: a) Schematic of internally-grooved tube (adapted from [23]) and b) photograph of a 9.52 mm Wieland internally-grooved tube (adapted from [22]) 8

Figure 4: a) Schematic of flow patterns and b) the corresponding heat transfer mechanisms and qualitative variation of the heat transfer coefficients for flow boiling in a horizontal tube (adapted from [34]) 15

Figure 5: a) Taitel-Dukler [46] adiabatic flow regime map and b) Wojtan et al. [30] diabatic flow regime map for evaporation of R134a at -15ºC in a 9mm smooth tube with a heat flux of 4 kW/m² 19

Figure 6: Comparison of experimental heat transfer data (adapted from Filho and Jabardo [38]) (hollow data points) for R134a at 5ºC in an 8.92 mm smooth tube with a heat flux of 5 kW/m² to a) the Wojtan et al. heat transfer model [31] and b) Wojtan et al. flow regime map [30] 22

Figure 7: Film thickness profiles for smooth (dashed lines) and 18° internally-grooved (solid red lines) tubes with 15.1 mm ID and mass fluxes of a) G=44 kg/m²s and x=0.6 and b) G=120 kg/m²s and x=0.76 [27], plotted on the simplified Wojtan et al. [30] flow regime map 29

Figure 8: Experimental flow visualization results from Yu et al. [66] for R134a at 6ºC with a heat flux of 20 kW/m² plotted on a simplified Wojtan et al. [30] map for a) 10.7 mm ID smooth tube and b) 11.1 mm ID internally-grooved tube 31

Figure 9: a) Heat transfer coefficient vs vapor quality and b) accompanying enhancement factor from several researchers with low mass flux (100 – 163 kg/m²s) 32

Figure 10: a) Heat transfer coefficient vs vapor quality and b) accompanying enhancement factor from several researchers with high mass flux (300 - 326 kg/m²s) 33

Figure 11: Experimental flow visualization results of Filho and Barbieri [75] for R134a at 5ºC in an 8.92 mm smooth and internally-grooved tube with a heat flux of 5 kW/m² plotted on a simplified Wojtan et al. [30] flow regime map 35

Figure 12: Flow visualization results from Colombo et al. [79] for 8.92 mm ID a) smooth and b) internally-grooved tubes with R134a at 5ºC and a heat flux of 4.2 kW/m² plotted on the Wojtan et al. [30] flow regime map 37

Figure 13: Experimental flow visualization results from Spindler and Müller-Steinhagen [74] for a) R134a and b) R404A at -20ºC with a heat flux of 7.5 kW/m² in one 8.92 mm ID internally-grooved tube plotted on a corresponding Wojtan et al. [30] flow regime map 40

Figure 14: Experimental flow visualization results from Schael and Kind [70] for CO_2 flow boiling in an 8.92 mm ID internally-grooved tube with heat fluxes up to 120 kW/m² at reduced pressures of a) 0.54 (Tsat = 5°C) and b) 0.36 (Tsat = -10°C) plotted on the Mastrullo et al. [54] flow regime map 42

Figure 15: Generalized transition boundaries in Taitel-Dukler model (adapted from [46]) 58

Figure 16: Traditional smooth tube Wojtan et al. [30] diabatic flow regime map for evaporation of R134a at -15ºC in a 9mm smooth tube with a heat flux of 4 kW/m² 60

Figure 17: Two-phase Stratified flow cross-section (adapted from [30])..... 61

Figure 18: a) Traditional smooth tube Wojtan et al. [30] and b) modified Sharar et al. [29] internally-grooved tube diabatic flow regime map for evaporation of R134a at -15ºC in 9mm tubes with a heat flux of 4 kW/m² 66

Figure 19: Modeling simulation results for a) original Wojtan et al. [30] flow regime map and b) associated heat transfer coefficient [31] in an 8.84mm smooth tube with HFE-7100 at 61°C and a heat flux of 4 kW/m² 77

Figure 20: Modeling simulation results for a) Modified Sharar et al. [29] internally-grooved tube flow regime map and b) associated heat transfer coefficient in an 8.84mm internally-grooved tube with HFE-7100 at 61°C and a heat flux of 4 kW/m²..... 78

Figure 21: Simulated results comparing enhancement ratio vs mass flux for 8.84mm smooth and internally-grooved tubes with HFE-7100 at 61°C and a heat flux of 4 kW/m² as shown in Figure 19 and Figure 20 80

Figure 22: Simulated results comparing enhancement ratio, Emf, and Erb vs mass flux for 8.84mm smooth and internally-grooved tubes with HFE-7100 at 61°C and a heat flux of 4 kW/m² 82

Figure 23: Schematic of two-phase flow test setup: a) reservoir and degasser b) Fluid-o-Tech pump c) Atrato or Kobold flow meter d) control valves e) inline heater f) 0.2m developing flow section g) 0.2m test tube h) 8cm sight glass (location of high speed flow visualization and TIR method) i) condenser P) pressure transducers and T) thermocouple probes DP) differential pressure transducer..... 85

Figure 24: Schematic of custom IR mirror setup for measuring temperature on the top, middle, and side of the test section 87

Figure 25: Schematic of custom IR mirror setup for measuring temperature on the top, middle, and side of the test section, and an IR photograph of the 2.80mm smooth tube during testing 88

Figure 26: Photograph of a smooth tube coated with a thin-film heater 89

Figure 27: Schematic of 1-D radial heat conduction in the Parylene-C/Ti-Pt coated tubes 96

Figure 28: Numerical results for a circumferentially and axially varying heat transfer coefficient 97

Figure 29: Principle of Total Internal Reflection (TIR) film thickness measurement technique 104

Figure 30: Two-phase flow regimes (bottom) and associated film thickness profiles (top) 106

Figure 31: a) Raw image of reflected light ring on a glass tube with no film thickness, b) Image after converting to black and white and contrast enhancement, and c) Image after converting to binary 112

Figure 32: Binary images of validation samples a) 0 μm film, b) 183 μm film, c) 449 μm film, and d) 1005 μm film 114

Figure 33: Schematic of the maximum measurable film thickness (adapted from [154]) 116

Figure 34: Unique temporally varying two-phase film thickness profiles in an 8.84 mm ID smooth tube for a 'Flooded' condition (230 kg/m²s), 'Stratified' condition (15 kg/m²s, x=0.067), 'Intermittent' condition (230 kg/m²s, x=0.01), and 'Annular' condition (120 kg/m²s, x>0.15) 118

Figure 35: Photographs of high speed flow visualization..... 119

Figure 36: Intermittent flow film thickness profiles for a) 15 kg/m²s and x=0.004 and b) 230 kg/m²s and x=0.023..... 122

Figure 37: Film thickness profile for intermediate Slug-Annular flow with a) 60 kg/m²s and x=0.014 and b) 60 kg/m²s and x=0.066 124

Figure 38: Two-Phase flow regime data plotted on a) Taitel-Dukler [46] map, b) Ullmann-Brauner [141] map, and c) Wojtan et al. [30] map 127

Figure 39: Single-phase liquid energy balance ratio for HFE-7100 in different tube diameters 134

Figure 40: Experimental and predicted single-phase heat transfer coefficient vs mass flux for a) 8.84 mm smooth tube, b) 4.54 mm smooth tube, and c) 2.8 mm smooth tube..... 136

Figure 41: Experimental and predicted single-phase heat transfer coefficient vs mass flux for a) 8.84 mm internally-grooved tube, b) 4.54 mm internally-grooved tube, and c) 2.62 mm internally-grooved tube..... 140

Figure 42: 8.84mm smooth tube data plotted on a) the Wojtan et al. [30] map and 8.84mm internally-grooved tube data plotted on b) the Wojtan et al. [30] map and c) the Sharar et al. [29] map with HFE-7100 at 61°C, G=50 kg/m²s, and q”=9 kW/m²..... 144

Figure 43: Comparison of heat transfer coefficient vs vapor quality for a mass flux of a) 25 kg/m²s, b) 75 kg/m²s, and c) 200 kg/m²s with HFE-7100 at 61°C and q”=9 kW/m² in the 8.84mm tubes 148

Figure 44: Comparison of heat transfer coefficient vs vapor quality for the 8.84mm tubes with HFE-7100 at 61°C and a mass flux of 200 kg/m²s for heat fluxes of a) 4 kW/m², b) 9 kW/m², c) 18 kW/m², d) 28 kW/m², e) 40 kW/m², and f) 56 kW/m²..... 151

Figure 45: 4.54mm smooth tube data plotted on a) the Wojtan et al. [30] map and 4.54mm internally-grooved tube data plotted on b) the Wojtan et al. [30] map and c) the Sharar et al. [29] map with HFE-7100 at 61°C, G=50 kg/m²s, and q”=9 kW/m² 154

Figure 46: Comparison of heat transfer coefficient vs vapor quality for a mass flux of a) 50 kg/m²s, b) 75 kg/m²s, and c) 200 kg/m²s with HFE-7100 at 61°C and q”=9 kW/m² in the 4.54mm tubes 157

Figure 47: Comparison of heat transfer coefficient vs vapor quality for the 4.54mm tubes with HFE-7100 at 61°C and a mass flux of 200 kg/m²s for heat fluxes of a) 4 kW/m², b) 9 kW/m², c) 18 kW/m², d) 28 kW/m², e) 40 kW/m², and f) 56 kW/m² 160

Figure 48: 2.8mm smooth tube data plotted on a) the Wojtan et al. [30] map and 2.62mm internally-grooved tube data plotted on b) the Wojtan et al. [30] map and c) the Sharar et al. [29] map with HFE-7100 at 61°C, G=50 kg/m²s, and q”=9 kW/m² 164

Figure 49: Comparison of heat transfer coefficient vs vapor quality for a mass flux of a) 75 kg/m²s and b) 200 kg/m²s with HFE-7100 at 61°C and q”=9 kW/m² in 2.62-2.8mm tubes 166

Figure 50: Comparison of heat transfer coefficient vs vapor quality for the 2.62-2.8mm tubes with HFE-7100 at 61°C and a mass flux of 200 kg/m²s for heat fluxes of a) 4 kW/m², b) 9 kW/m², c) 18 kW/m², d) 28 kW/m², e) 40 kW/m², and f) 56 kW/m² 170

Figure 51: Enhancement ratio vs mass flux with current data for the 8.84mm, 4.54mm, and 2.62mm internally-grooved tubes 174

Figure 52: Comparison of the 8.84mm smooth tube experimental data for HFE-7100 at 61°C with correlations from a) Wojtan et al. [31], b) Chen [56], c) Shah [57], d) Kandlikar [93], e) Gungor-Winterton ‘original’ [59], and f) Gungor-Winterton ‘new’ [60] 178

Figure 53: Comparison of the 8.84mm internally-grooved tube experimental data for HFE-7100 at 61°C with a) the Modified Sharar and Bar-Cohen correlation and correlations from b) Thome et al. [91], c) Cavallini et al. [117], d) Chamra and Mago [162], e) Wu et al. [103], and f) Yun et al. [90] 181

Figure 54: Example of heat transfer coefficient uncertainty and deviation near the transition boundary between Stratified-Wavy and Annular flow for HFE-7100 at 61°C in the 8.84mm tubes; a) locus of different flowrates on the Modified flow regime map and b) resulting heat transfer coefficients 184

Figure 55: 11.1 mm ID internally-grooved tube experimental flow visualization results from Yu et al. [66] for R134a at 6ºC with a heat flux of 20 kW/m² plotted on the a) original Wojtan et al. [30] map and b) Modified Sharar et al. [29] map..... 187

Figure 56: 8.92 mm ID internally-grooved tube experimental flow visualization results from Colombo et al. [79] with R134a at 5ºC and a heat flux of 4.2 kW/m² plotted on the a) original Wojtan et al. [30] map and b) Modified Sharar et al. [29] map 189

Figure 57: 8.92 mm ID internally-grooved tube experimental flow visualization results from Spindler and Müller-Steinhagen [74] for R134a at -20ºC with a heat flux of 7.5 kW/m² plotted on the a) original Wojtan et al. [30] map and b) Modified Sharar et al. [29] map 190

Figure 58: 8.92 mm ID internally-grooved tube experimental flow visualization results from Spindler and Müller-Steinhagen [74] for R404a at -20ºC with a heat flux of 7.5 kW/m² plotted on the a) original Wojtan et al. [30] map and b) Modified Sharar et al. [29] map 191

Figure 59: Heat transfer coefficient vs vapor quality for the original Wojtan et al. [31] model, Modified heat transfer coefficient described in this Dissertation, and data from Yu et al. [66] for an 11.1 mm smooth and internally-grooved tube with R134a at 6ºC and a heat flux of 20 kW/m² 193

Figure 60: Normalized enhancement ratio vs mass flux with data from the current study and data from three independent researchers 195

Figure 61: 4.54mm internally-grooved tube data plotted on a) the Sharar et al. map [29] described in Chapter 4 and b) the adjusted map based on the current data set with HFE-7100 at 61°C, G=50 kg/m²s, and q”=9 kW/m² 199

Figure 62: Comparison of heat transfer coefficient vs vapor quality for a mass flux of 50 kg/m²s with HFE-7100 at 61°C and q”=9 kW/m² in the 4.54mm tubes superimposed with a) heat transfer coefficient based on Sharar et al. [29] map and b) adjusted Sharar et al. map 200

Figure 63: Schematic (side view) of the cantilever test setup made to test material thickness in the ALD tool 215

Figure 64: Schematic showing a copper metallic bump formed at a defect site when electroplating a conductive substrate in an electrolytic solution of H_2SO_4 and $CuSO_4$ (adapted from [165]) 216

Figure 65: Comparison between SEM images of 200nm thick Alumina deposited on Cu-coated Si substrates a) before and b) after electroplating process 217

Figure 66: SEM image of Ruthenium nucleation sites 218

Figure 67: a) Raw image of reflected light ring on a glass tube with no film thickness, b) Image after converting to black and white and contrast enhancement, and c) Image after converting to binary 220

Figure 68: Heat transfer coefficient vs vapor quality for 8.84 mm ID smooth and internally-grooved tubes at a mass flux of 300 kg/m²s and different heat fluxes..... 230

Figure 69: Heat transfer coefficient vs vapor quality for 8.84 mm ID smooth and internally-grooved tubes at a mass flux of 200 kg/m²s and different heat fluxes..... 231

Figure 70: Heat transfer coefficient vs vapor quality for 8.84 mm ID smooth and internally-grooved tubes at a mass flux of 175 kg/m²s and different heat fluxes..... 232

Figure 71: Heat transfer coefficient vs vapor quality for 8.84 mm ID smooth and internally-grooved tubes at a mass flux of 150 kg/m²s and different heat fluxes..... 233

Figure 72: Heat transfer coefficient vs vapor quality for 8.84 mm ID smooth and internally-grooved tubes at a mass flux of 125 kg/m²s and different heat fluxes..... 234

Figure 73: Heat transfer coefficient vs vapor quality for 8.84 mm ID smooth and internally-grooved tubes at a mass flux of 100 kg/m²s and different heat fluxes..... 235

Figure 74: Heat transfer coefficient vs vapor quality for 8.84 mm ID smooth and internally-grooved tubes at a mass flux of 75 kg/m²s and different heat fluxes..... 236

Figure 75: Heat transfer coefficient vs vapor quality for 8.84 mm ID smooth and internally-grooved tubes at a mass flux of 50 kg/m²s and different heat fluxes..... 237

Figure 76: Heat transfer coefficient vs vapor quality for 8.84 mm ID smooth and internally-grooved tubes at a mass flux of 25 kg/m²s and different heat fluxes..... 238

Figure 77: Heat transfer coefficient vs vapor quality for 4.54 mm ID smooth and internally-grooved tubes at a mass flux of 300 kg/m²s and different heat fluxes..... 240

Figure 78: Heat transfer coefficient vs vapor quality for 4.54 mm ID smooth and internally-grooved tubes at a mass flux of 200 kg/m²s and different heat fluxes..... 241
Figure 79: Heat transfer coefficient vs vapor quality for 4.54 mm ID smooth and internally-grooved tubes at a mass flux of 175 kg/m²s and different heat fluxes..... 242
Figure 80: Heat transfer coefficient vs vapor quality for 4.54 mm ID smooth and internally-grooved tubes at a mass flux of 150 kg/m²s and different heat fluxes..... 243
Figure 81: Heat transfer coefficient vs vapor quality for 4.54 mm ID smooth and internally-grooved tubes at a mass flux of 125 kg/m²s and different heat fluxes..... 244
Figure 82: Heat transfer coefficient vs vapor quality for 4.54 mm ID smooth and internally-grooved tubes at a mass flux of 100 kg/m²s and different heat fluxes..... 245
Figure 83: Heat transfer coefficient vs vapor quality for 4.54 mm ID smooth and internally-grooved tubes at a mass flux of 75 kg/m²s and different heat fluxes..... 246
Figure 84: Heat transfer coefficient vs vapor quality for 4.54 mm ID smooth and internally-grooved tubes at a mass flux of 50 kg/m²s and different heat fluxes..... 247
Figure 85: Heat transfer coefficient vs vapor quality for 2.8 mm ID smooth and 2.62 mm ID internally-grooved tubes at a mass flux of 300 kg/m²s and different heat fluxes..... 249
Figure 86: Heat transfer coefficient vs vapor quality for 2.8 mm ID smooth and 2.62 mm ID internally-grooved tubes at a mass flux of 200 kg/m²s and different heat fluxes..... 250
Figure 87: Heat transfer coefficient vs vapor quality for 2.8 mm ID smooth and 2.62 mm ID internally-grooved tubes at a mass flux of 175 kg/m²s and different heat fluxes..... 251
Figure 88: Heat transfer coefficient vs vapor quality for 2.8 mm ID smooth and 2.62 mm ID internally-grooved tubes at a mass flux of 150 kg/m²s and different heat fluxes..... 252

Figure 89: Heat transfer coefficient vs vapor quality for 2.8 mm ID smooth and 2.62 mm ID internally-grooved tubes at a mass flux of 125 kg/m²s and different heat fluxes..... 253

Figure 90: Heat transfer coefficient vs vapor quality for 2.8 mm ID smooth and 2.62 mm ID internally-grooved tubes at a mass flux of 100 kg/m²s and different heat fluxes..... 254

Figure 91: Heat transfer coefficient vs vapor quality for 2.8 mm ID smooth and 2.62 mm ID internally-grooved tubes at a mass flux of 75 kg/m²s and different heat fluxes..... 255

Figure 92: Comparison of the 8.84mm smooth tube experimental data for HFE-7100 at 61°C with a) Wojtan et al. [31], b) Chen [56], c) Shah [57], d) Kandlikar [93], e) Gungor-Winterton 'original' [59], and f) Gungor-Winterton 'new' [60] 258

Figure 93: Comparison of the 4.54mm smooth tube experimental data for HFE-7100 at 61°C with a) Wojtan et al. [31], b) Chen [56], c) Shah [57], d) Kandlikar [93], e) Gungor-Winterton 'original' [59], and f) Gungor-Winterton 'new' [60] 259

Figure 94: Comparison of the 2.8mm smooth tube experimental data for HFE-7100 at 61°C with a) Wojtan et al. [31], b) Chen [56], c) Shah [57], d) Kandlikar [93], e) Gungor-Winterton 'original' [59], and f) Gungor-Winterton 'new' [60] 260

Figure 95: Comparison of the 8.84mm internally-grooved tube experimental data for HFE-7100 at 61°C with a) the Modified Sharar and Bar-Cohen correlation, and correlations from b) Thome et al. [91], c) Cavallini et al. [117], d) Chamra and Mago [162], e) Wu et al. [103], and f) Yun et al. [90] 261

Figure 96: Comparison of the 4.54mm internally-grooved tube experimental data for HFE-7100 at 61°C with a) the Modified Sharar and Bar-Cohen correlation, and correlations from b) Thome et al. [91], c) Cavallini et al. [117], d) Chamra and Mago [162], e) Wu et al. [103], and f) Yun et al. [90] 262

Figure 97: Comparison of the 2.62mm internally-grooved tube experimental data for HFE-7100 at 61°C with a) the Modified Sharar and Bar-Cohen correlation, and correlations from b) Thome et al. [91], c) Cavallini et al. [117], d) Chamra and Mago [162], e) Wu et al. [103], and f) Yun et al. [90] 263

Chapter 1: Introduction

The last several decades have witnessed a dramatic increase in the use of electronics on a variety of transportation systems. This trend continues today in hybrid electric vehicle (HEV), electric vehicle (EV), and plug-in hybrid electric vehicle (PHEV) technologies for commercial and military applications. Military use can include both direct vehicle applications, such as propulsion, and indirect applications such as electrically operated arms or interfacing the vehicle electrical system to create a military base microgrid [1].

There are several motivations for replacing the traditional internal combustion (IC) motors and mechanical drives with HEV equivalents on military platforms. One of the most important reasons is the high cost of fuel. Transporting fuel to the theater through dangerous routes and over long distances to geographically dispersed troops can significantly increase the cost of fuel. The cost can rise from a commercial pump price of several dollars per gallon to about $400/gal in the battlefield. If an airlift is needed, the cost can reach $1000 per gallon [2]. As such, even a modest saving in fuel efficiency can lead to huge cost savings for the Department of Defense.

HEV platforms also promise reduced operation noise and, as a result, improve stealth capabilities and personnel safety in dangerous environments. Furthermore, HEVs can be designed with one motor per axle or even hub motors in each of the wheels for propulsion. This provides system redundancy, so that if one of the motors fails the vehicle can operate in a degraded mode to reach a safe or serviceable location. An indirect benefit of HEVs for military applications is the ability to interconnect multiple HEVs to provide utility-level power to bases and other infrastructures in combat zones. With appropriate

control electronics, several HEVs can form a 'micro-grid' with a robust source of utility power [1]. This use of HEVs can reduce the need for ancillary generators and power units, therefore leading to savings stemming from acquisition and transportation costs.

1.1 Power Conversion Electronics - Thermal Issue

Figure 1 illustrates the continuous power needs for current commercial midsize HEVs, full EVs, and PHEVs. As shown, continuous power demands increase through the transition from commercial HEVs to PHEVs and all-electric drive applications such as fuel cells or EVs. In the case of HEVs and PHEVs, electrical power requirements approach 30 to 60kW while the all-electric platforms reach 100kW for short durations.

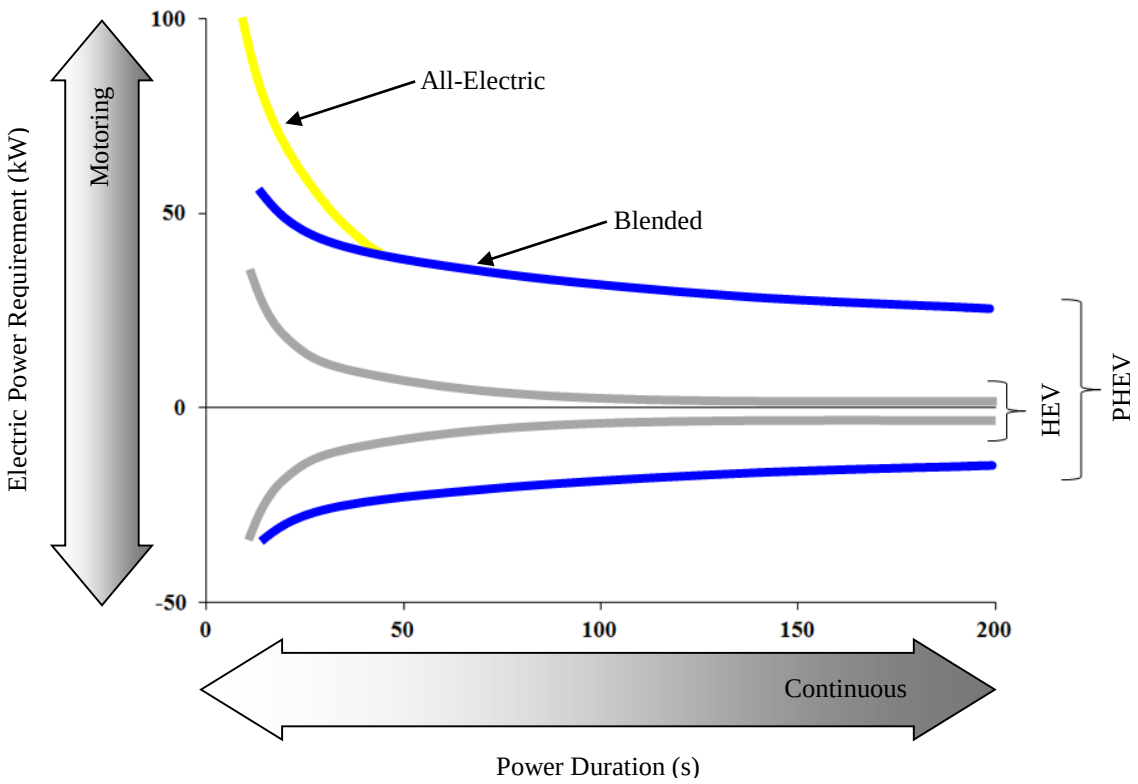

Figure 1: Midsize hybrid electric power requirements (adapted from [1])

Power conversion electronics are a ubiquitous and enabling technology for the success of current and future electric vehicle architectures; this is due to the disparate

electrical systems common to these programs and the need to draw from a platform's single-voltage electrical bus. This mainly involves the use of power semiconductor switches such as power diodes, metal oxide field effect transistors (MOSFETs), and insulated gate bipolar transistors (IGBTs). Unfortunately, such electronic energy conversion devices cannot be 100% efficient and vehicle systems requiring 100kW of electrical power would have thermal losses of 2 to 4 kW, even with power electronic conversion efficiencies of 96-98%. Larger systems or systems with multiple powertrain motors, high-power bidirectional DC-DC converters, and power electronics modules could have significantly higher waste heat challenges [1].

Aligned efforts aimed towards increasing total power while simultaneously decreasing the component size and weight [3] have led to improvements in cost and power density. However, increased power density has inevitably increased power electronic heat flux and is presenting thermal management challenges for current and future systems; fast, compact, IGBT devices can be expected to dissipate heat fluxes in upwards of 250 W/cm² [1]. The primary target for thermal management of Silicon power electronics is sustained operation below the maximum allowable temperature of 125˚C, since lower die temperatures result in lower losses and better electrical performance. As such, efficient thermal management of power electronics modules is critical to maintaining system-level operational specifications without undermining efforts to improve power electronic size, cost, weight, and power density.

1.2 Power Electronic Thermal Management

Traditionally, power electronics have relied on air-cooled heat sinks or liquid-cooled cold plates to manage electronic waste heat, however new power-dense electronic

systems are further increasing waste heat and presenting challenges to the capabilities of conventional cooling systems. The effect of higher heat flux electronics for air-cooled systems is larger, heavier, costlier heat sinks and fans to compensate for insufficient convective performance. The effect is equally dramatic with single-phase liquid cooling, with higher heat fluxes requiring larger coolant flow rates to sufficiently cool the system devices [4]. These large flow rates and subsequent pumping powers result in increasingly bulky, heavy systems that consume more fuel [5] and undermine the current and future efforts to reduce system cost and improve efficiency. Thus, there is a drive to develop improved cooling components that are smaller and lighter, and have increased performance relative to conventional liquid cold plates.

Cooling schemes using liquid-vapor phase change (two-phase cooling) have been examined as a practical and cost-conscious next step beyond single-phase cooling. A two-phase cooling system has several potential benefits over a standard single-phase liquid cooling approach. First, the latent heat of vaporization for a particular fluid, reflecting the heat absorbed to evaporate a unit mass, can be two orders of magnitude larger than the specific (sensible) heat used in single-phase liquid cooling [6]. Therefore, evaporative cooling provides the possibility of increased heat absorption per unit mass and volume of fluid and improved heat acquisition effectiveness. The single-phase heat dissipation relationship for water can be expressed as:

$$q = \dot{m}C_p dT = \dot{m} \times 4{,}186 \times 1 = 4{,}186\dot{m} \quad (1)$$

where q is the heat dissipation, $\dot{m}$ is the mass flow rate, C_p is the specific heat of the fluid (4186 kJ/kgK for water), and ΔT is the temperature rise of the fluid. Equation (1) assumes an allowable fluid temperature rise of 1ºC, such that the heat dissipation can be expressed

as the product of mass flow rate and a constant. Similarly, the two-phase latent heat dissipation relationship for water can be expressed as:

$$q = \dot{m}h_{lg}x = \dot{m} \times 2{,}257{,}000 \times 1 = 2{,}257{,}000\dot{m} \quad (2)$$

where q is the heat dissipation, x is the quality (fraction of the mass flow rate that has been vaporized), $\dot{m}$ is the mass flow rate, and h_{lg} is the latent heat of vaporization of the fluid (2,257 kJ/kg for water). Assuming full vaporization of the fluid (x=1.0), this heat dissipation can also be expressed as the product of the flow rate and a constant.

As shown symbolically in Equation (1) and Equation (2), and graphically in Figure 2, the increased heat acquisition effectiveness of two-phase flow translates into lower flow rates compared to single-phase flow for comparable heat dissipation. The potential benefit of lower flow rates includes: smaller fluid reservoirs; smaller onboard fluid volume; reduction in pumping power; smaller pumps; and a reduction in system weight and volume. Additionally, two-phase cooling has the potential benefit of a relatively isothermal cold plate surface, due to the use of latent heat absorption which occurs at nearly isothermal conditions [7], and order-of-magnitude larger heat transfer coefficients than equivalent single-phase forced convection methods [6]. Based on these benefits, cooling schemes utilizing liquid-vapor phase change are an attractive next-step beyond single-phase cooling to manage escalating power electronic thermal concerns.

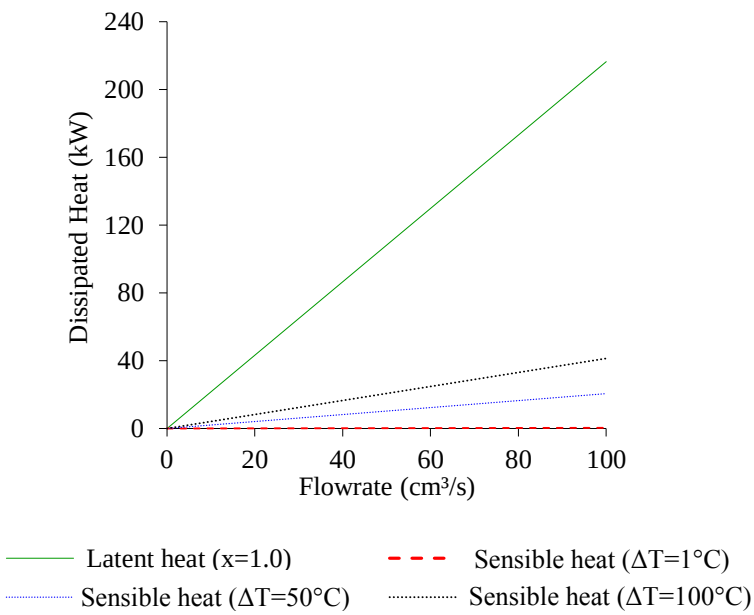

Figure 2: Dissipated heat vs flow rate for water using latent heat and sensible heat

1.3 Two-Phase Surface Enhancements and Internally-Grooved Tubes

As shown by Sharar et al. [8] and Saums [7], performance improvement can be accomplished by simply taking an existing single-phase system, for example, an IGBT cold plate for cooling power electronics, and operating it in two-phase. However, by understanding the mechanisms that make two-phase advantageous, surface enhancements have been developed to further improve two-phase cooling performance. Specific to flow boiling heat transfer, these enhancement techniques can be classified into two distinct categories: 1) nucleate boiling techniques and 2) convective vaporization techniques. A summary of these techniques can be found in Table 1 and are discussed more extensively by Bergles [9] [10], Thome [11], Webb [12], and Kandlikar [13]. Furthermore, a closer look at specific topics including, microporous coatings [14], reentrant cavities [15], nanoparticle fluid additives [16], twisted tape inserts [17] [18], corrugated tubes [17] [19], and internally-grooved tubes can be found in a presentation by Sharar et al. [20].

Table 1: Classification of flow boiling enhancement techniques

Nucleate Boiling	Convective Vaporization
Acoustic pulsation	
Mechanical and ultrasonic vibration	Fins
Porous surfaces	Twisted tape inserts
Structured surfaces (reentrant cavities)	Helical wire inserts
Screens	Corrugated or fluted tubes
Fins	Internally-grooved tubes
Electrohydrodynamic field effect	

Among the available enhancement techniques, internally-grooved tubes have been identified as a most promising technology for integration into vehicle power electronic cold plates. Helical internally-grooved tubes, also known as inner grooved tubes and micro-fin tubes, are perhaps the most prevalent passive two-phase enhancement technique in use today and are widely used for refrigerant tubes and for fin-tube heat exchangers, as well as shell and tube heat exchangers. Internally-grooved tubes were originally developed in Japan and gained widespread adoption in the 1980's [17]. Seamless internally-grooved tubes are typically manufactured by running a mandrel through a smooth bore copper tube but can also be made by embossing fin geometries on a metal strip, rolling, and seam welding. The latter manufacturing method provides a wider range of groove geometries, including 3-D geometries and herringbone tubes, however most commercial vendors continue to manufacture seamless tubes [21]. Figure 3a shows the characteristic internally-grooved tube geometry which is defined by the internal diameter, number of fins, helix angle β (or axial pitch), fin height, apex angle, γ, and the internal area ratio. Figure 3b shows a photograph of a commercial 9.52 mm diameter Wieland Cuprofin internally-grooved tube [22].

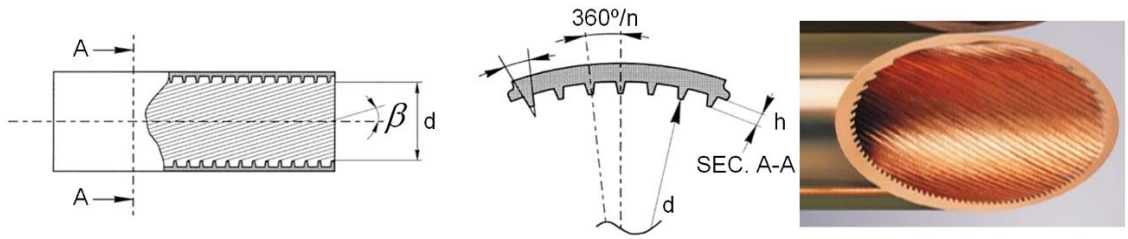

(a) (b)

Figure 3: a) Schematic of internally-grooved tube (adapted from [23]) and b) photograph of a 9.52 mm Wieland internally-grooved tube (adapted from [22])

Depending on the process, tube size, and manufacturer, the surface enhancement typically consists of 40-80 small, approximately 0.1 to 0.4 mm wide and 0.1 to 0.4 mm tall, fins with helix angles from 7˚ to 23˚, yielding typical area enhancement factors of 1.3 to 1.8. These tubes generally range in diameter from 5 to 15 mm, although recently internally-grooved tubes as small as 1.95 mm have been fabricated and tested [24]. The majority of internally-grooved tubes have fins with approximately trapezoidal cross-sectional shapes but triangular and rectangular fins have also been manufactured. Table 2 lists geometric parameters for three commercially available internally-grooved tubes from Wieland.

Table 2: Geometric parameters and fin efficiencies for three Wieland copper internally-grooved tubes

Name	Diameter (mm)	Wall thickness (mm)	# Fins	Fin height (mm)	Approximate fin base (mm)	ηf (%) h=1000 W/m²	ηf (%) h=20,000 W/m²	Surface enhancement (A/Ap)
S2AD-5	5	0.23	40	0.15	0.20	99	98	1.52
S2AD-952	9.52	0.34	60	0.2	0.25	99	97.5	1.52
S2AD-15	15	0.4	75	0.3	0.31	99	96.7	1.53

As tabulated in Table 2, the resulting fin efficiencies are greater than 95% for all three tubes with heat transfer coefficients ranging from 1,000 to 20,000 W/m²K. Furthermore, the curves for triangular, rectangular, and parabolic fins converge at $L_c^{3/2}\left(\mathrm{h}/kA_p\right)$ values less than 0.3 [25] which suggests that for a fixed fin profile area, the

fin geometry does not significantly affect fin efficiency in standard internally-grooved tubes.

In horizontal orientations, internally-grooved tubes typically show heat transfer enhancement ratios as high as 6-7 times that of smooth tubes at low mass velocities and improvement equal to or slightly greater than the internal area ratio at high mass velocities [26] [17]. The pressure drop of internally-grooved tubes is often equal to that of an equivalent smooth tube at low mass fluxes and rises to 1.5 times the smooth tube at high mass fluxes. The reported range of heat transfer improvement and pressure drop increase for internally-grooved tubes compared to smooth tubes are compiled in Table 3.

Table 3: Performance comparison of internally-grooved tubes to smooth tubes

Metric	Internally-Grooved Tube
Area ratio	**1.3-1.8x that of a plain tube**
Heat transfer augmentation at low mass flux	**3-7x that of a plain tube**
Heat transfer augmentation at high mass flux	**~ internal area ratio**
Pressure drop penalty	**1-1.5x that of a plain tube**

Researchers have speculated that the significant heat transfer improvement above the area enhancement at low mass flux is a result of several factors: thinning of the liquid film in Annular flow due to the larger surface area [26], redistribution of the liquid in Annular flow due to the helical grooves [27], and increased turbulence [28]. However, generalized models that attempt to capture these effects have proven unreliable. It has recently been suggested that flow regime transition from an undesirable flow regime, such as Stratified flow (where only the bottom portion of the tube is wetted), to a desirable flow regime, such as Annular flow (where thin film evaporation around the periphery leads to

high heat transfer rates), may well explain the observed enhancement in internally-grooved tubes at low mass flux [29].

1.4 Goals and Outline

1.4.1 Goals

Despite the documented performance improvement in internally-grooved tubes, the flow mechanisms that deliver performance enhancement are not fully understood. The absence of phenomenological insights and physical models makes it difficult to transition internally-grooved tube technology from conventional refrigeration equipment to compact cold plates for vehicle power electronics. Therefore, a stronger experimental and theoretical knowledge base needs to be established for this enhancement mode, focusing on a more comprehensive understanding of the physical mechanisms responsible for improved performance in internally-grooved tubes. To this end, this Dissertation focuses on the analytical development and experimental validation of a physics-based flow regime map and heat transfer coefficient model that recognizes the role played by surface structures in enhancing two-phase thermal transport within internally-grooved tubes. These new models mark a significant contribution to the scientific community, allowing better thermofluid prediction and enabling more reliable design and optimization of two-phase cooling systems. In addition to the intellectual merits, the research is directly impactful to ongoing efforts in the Army and is more broadly applicable to ubiquitous refrigeration equipment.

Since the flow regime is a key parameter in analytically defining thermal performance, an additional target is to develop a new non-intrusive optical film thickness measurement technique to provide a quantitative characterization of the flow regime.

Using temporally-varying film thickness profiles produced by this technique, quantitative identification measures were developed for the primary flow regimes, including the ability to explain and quantify the more subtle transitions that exist between dominant regimes. This quantitative methodology assists in establishing the effect of flow regime on thermal and momentum transport in internally-grooved tubes.

1.4.2 Outline

In Chapter 2, a description of two-phase flow boiling fundamentals is provided. Heat transfer mechanisms and the interrelationship between two-phase flow regime and local heat and mass transfer are discussed. A brief review of smooth tube flow regime maps and heat transfer coefficient correlations, with a focus on flow regime based heat transfer models, is provided. The Wojtan et al. flow regime map [30] and associated heat transfer coefficient correlation [31] are compared to data in the literature to demonstrate the validity of this regime-based approach to defining thermal transport.

Fundamental studies of thermofluid performance in internally-grooved tubes are reviewed and analyzed to demonstrate the relationship between flow regime and evaporative heat transfer rates, in Chapter 3. Through reinterpretation of data in the literature, it is shown that performance improvement in internally-grooved tubes at low mass flux is a result of early transition to Annular flow. Finally, the current state of two-phase flow regime maps and heat transfer correlations for internally-grooved tubes is summarized and motivation for the current research effort is established.

Chapter 4 outlines the original Wojtan et al. [31] formulation and describes the current modification to the existing flow regime map and heat transfer coefficient correlation to better reflect the trends discussed in Chapter 3. The original and newly

proposed model are simulated through a range of operating conditions to demonstrate how the model works and to verify that the model can successfully predict 6 to 7 times higher heat transfer coefficients at low mass flux and enhancement approaching the area enhancement at high mass flux (refer to Table 3).

Chapter 5 describes the design and fabrication of the single- and two-phase test facility used to experimentally validate the model developed in Chapter 4. The tube heating method, fluid selection, parametric space tested, tube parameters, data acquisition and reduction, and experimental uncertainty are described. Appendix A describes lessons learned from an attempt to heat the tubes with Atomic Layer Deposition (ALD) thin film heaters.

Common experimental flow regime definitions are based on visual and verbal descriptions, which can be subjective and unreliable. Chapter 6 describes the theory, development, and validation of an objective non-intrusive optical flow regime characterization methodology based on Total Internal Reflection (TIR). Results are compared to several flow regime maps available in the literature for validation. Appendix B provides additional details on the Matlab code developed to process the TIR data.

Chapter 7 shows single-phase heat transfer coefficient and energy balance results. Theoretical predictions were compared to the experimental results to demonstrate the accuracy of the experimental apparatus and test methods. Good agreement with several turbulent flow models was shown.

Flow regime data, obtained with dynamic total-internal-reflection measurements, and heat transfer coefficient data, obtained with infrared thermography, are presented and analyzed in Chapter 8 for two-phase HFE-7100 flow in horizontal 2.62mm - 8.84mm

diameter smooth and internally-grooved tubes with mass fluxes from 25-300 kg/m²s, heat fluxes from 4-56 kW/m², and vapor qualities approaching 1. This data, along with data from the literature, is then compared to the new flow regime map and associated heat transfer coefficient correlation and additional models from the literature. Furthermore, suggestions for future experimental and modeling research are given, based on insights from the current study. Appendix C - Appendix F provide additional experimental results, as well as a more detailed statistical analysis of the data.

Finally, conclusions and recommendation for future research are provided in Chapter 9.

The reader is reminded that this Dissertation has a focus on exploring an internally-grooved tube cold plate 'unit cell' (single tubes) as a lower complexity 'building block' for future applications. Lessons learned from a 'unit cell' study will aid in the development of future internally-grooved tube power electronic cold plates. Additionally, it's important to note that while the primary application for this work is vehicle power electronics, the concepts and ideas presented herein for internally-grooved tubes are broadly applicable to refrigeration, air-conditioning, and other power electronic platforms such as solar, wind turbines, and 'smart grids'.

Chapter 2: Two-Phase Flow Boiling Fundamentals

During two-phase flow, the vapor and liquid phases are in simultaneous motion inside the channel or pipe. The physics involved are typically more complicated than single-phase flow. In addition to the viscous, pressure, and inertial effects existing in single-phase flow, two-phase flows are also affected by the wetting characteristics of the liquid on the channel wall, momentum exchange between the liquid and vapor phases, interfacial tension forces, and by gravity (due to the large density differences between the phases). The particular flow regime resulting from these interactions plays a critical role in the local heat and mass transfer. Understanding these distinct effects in plain tubes provides a baseline for understanding the behavior and performance of enhanced channels.

The remainder of this chapter provides a brief overview of the dominant flow regimes, flow regime maps for smooth tubes under adiabatic and diabatic conditions, and the regime-based heat transfer models. Please refer to the reviews by Cheng et al. [32] and Thome, Bar-Cohen, Revellin, and Zun [33] for a more comprehensive discussion of two-phase flow pattern and flow pattern maps in smooth macro- and microscale channels.

2.1 Diabatic Two-Phase Flow Patterns and Dependence on Heat Transfer

During diabatic two-phase flow, as the quality and void fraction change in the flow direction, the flow pattern may undergo a sequence of transitions altering both the magnitude and character of the local heat transfer. Figure 4 is a schematic representation of a typical diabatic flow boiling process in a horizontal smooth channel, with saturated inlet liquid and a uniform heat flux, and the associated heat transfer regimes. As the process proceeds down the length of the tube, the percentage of the flow that has been vaporized

increases. Conservation of mass dictates that as the mean density of the flow decreases, due to the formation of vapor, the mean flow velocity must increase. The accompanied acceleration of the flow results in varying liquid and vapor velocities, which together with the increasing mass fraction of the flowing vapor, causes a progressive series of changes in the flow regime.

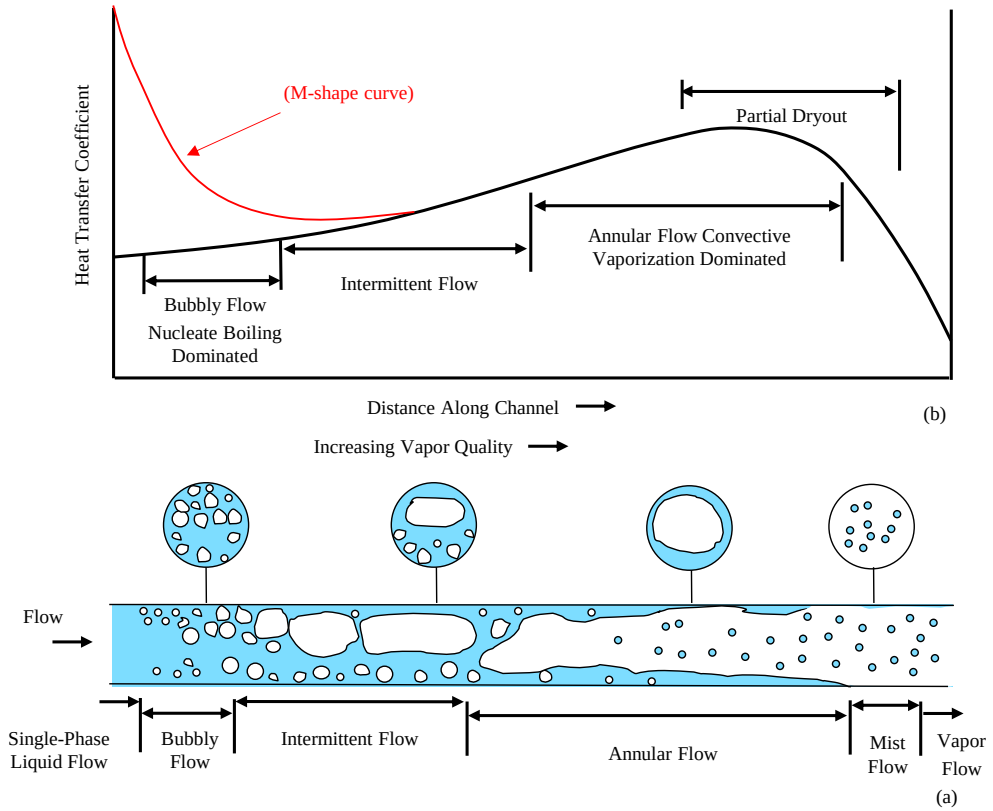

Figure 4: a) Schematic of flow patterns and b) the corresponding heat transfer mechanisms and qualitative variation of the heat transfer coefficients for flow boiling in a horizontal tube (adapted from [34])

During Bubble flow, nucleate boiling is the dominant vaporization mechanism. The added turbulence and mixing resulting from the bubble formation results in a 'nucleate boiling dominated' region and an increase in the heat transfer coefficient, as indicated by the red line on Figure 4. As the quality downstream increases, bubbles begin to coalesce

and Intermittent flow develops. In the Intermittent regime, the tube wall is intermittently cooled by liquid plugs and vapor slugs, often (but not always) resulting in a decrease in the heat transfer coefficient prior to transition to Annular flow. This leads to the characteristic M-shaped curve, as identified by Bar-Cohen and Rahim [35] and shown by the 'red' line in Figure 4. This effect was also shown by Cortina-Diaz and Schmidt [36] and Yang and Fujita [37] for flow boiling in minichannels and microgap channels, respectively. As shown by the black profile in Figure 4, the effect of nucleate boiling can also be less dramatic; this effect was shown by Filho and Jabardo [38] and will be shown later in this chapter. It's important to note that for both Intermittent and Bubby flow, the heat transfer coefficient is expected to be higher than for a comparable single-phase flow. At very low flow rates, Stratified flow may occur where the upper portion of the tube is completely occupied by vapor and the bottom by liquid. Stratified flow is marked by drastically reduced heat transfer coefficients due to the dry upper surface.

In the Annular flow regime, evaporation from the liquid-vapor interface is the dominant heat transfer mechanism. Annular flow is considered a desirable flow regime because it can provide relatively high heat transfer coefficients, as shown schematically in Figure 4. As with adiabatic flow, gravity effects may result in a thicker film at the bottom, however, at appropriately high vapor velocities strong shear forces serve to redistribute the fluid more evenly around the perimeter of the tube. Entrained droplets, as a result of strong shear forces, along with continual downstream vaporization tend to further thin the liquid film and increase the heat transfer coefficient. Eventually, however, the film may completely disappear from portions of the tube wall. Such local dryout causes a drastic decrease in the average heat transfer coefficient and expands to cover wider and wider

areas for longer and longer periods, as the flow quality increases towards complete vaporization. It is important to note that Figure 4 represents general trends for fluids at standard temperature and pressure. As described by Thome and Ribatski [39] and Cheng et al. [40] [41] flow boiling of high reduced pressure fluids, such as CO_2, can significantly affect the progression of these flow regimes, the dominant heat transfer mechanisms, and the resulting heat transfer coefficients.

2.2 Two-Phase Flow Pattern Maps

The observed dependence of heat transfer performance on flow regime led researchers to analytically describe and map the dominant flow regimes in channels. Baker [42] provided the earliest empirical flow regime map and other generalized flow regime maps followed: Mandhane et al. [43], Taitel and Dukler [44], and Weisman et al. [45]. Most notable among these was the phenomenological map by Taitel and Dukler which used underlying physical mechanisms to define and map the four primary adiabatic flow regimes using superficial velocity coordinates: Stratified, Intermittent, Bubbly, and Annular. In 1990 the Unified Model was developed to predict the adiabatic flow regime in a variety of channel sizes and orientations based on two-phase non-dimensional groupings [46]. The Taitel-Dukler physics-based models contain little empirical fitting and have been successfully applied to many fluids and channel sizes, including evaporating refrigerant flows in microchannels [35]. A Taitel-Dukler flow regime map [46], converted to coordinates of mass flux and vapor quality for ease of interpretation, for R134a flowing in a 9 mm smooth channel at a saturation temperature of -15ºC is shown in Figure 5a. The extent of the flow regimes were calculated through an iterative process and the solid lines represent the general loci of predicted regime transition.

Adiabatic models do not account for axial variation in quality nor thermal interactions inside the channel and their use in diabatic channels is based on an assumed dominance of local conditions. Consequently, these models are not strictly valid for diabatic heating and cooling applications in which heat is added to or removed from the two-phase mixture and, in which, acceleration terms and entry length effects may dominate. As a result, diabatic flow regime maps have been developed to account for these interactions. Beginning in 1998 Kattan, Thome, and Favrat [47] empirically-modified the Steiner map, a modification of the Taitel-Dukler map [46], and introduced a method for determining the onset of dryout during Annular flow. Since then, other empirically-modified diabatic flow regime maps have followed: Zurcher, Thome, and Favrat [48], Zurcher, Favrat, and Thome [49], Thome and El Hajal [50], and Wojtan, Ursenbacher, and Thome [30]. These modifications provide a more-accurate prediction of flow regimes and dryout in real-world diabatic systems with halogenated refrigerants at standard temperature and pressure (reduced pressure typically less than 0.1), but have not yet gained the generality of the Taitel-Dukler adiabatic map. A Wojtan et al. [30] flow regime map for R134a in a smooth 9 mm diameter tube is shown in Figure 5b. The Wojtan et al. [30] map defines 8 distinct flow regimes: Stratified, Stratified-Wavy, Slug and Stratified-Wavy, Slug, Intermittent, Annular, Dryout, and Mist in coordinates of mass flux (G) and vapor quality (x).

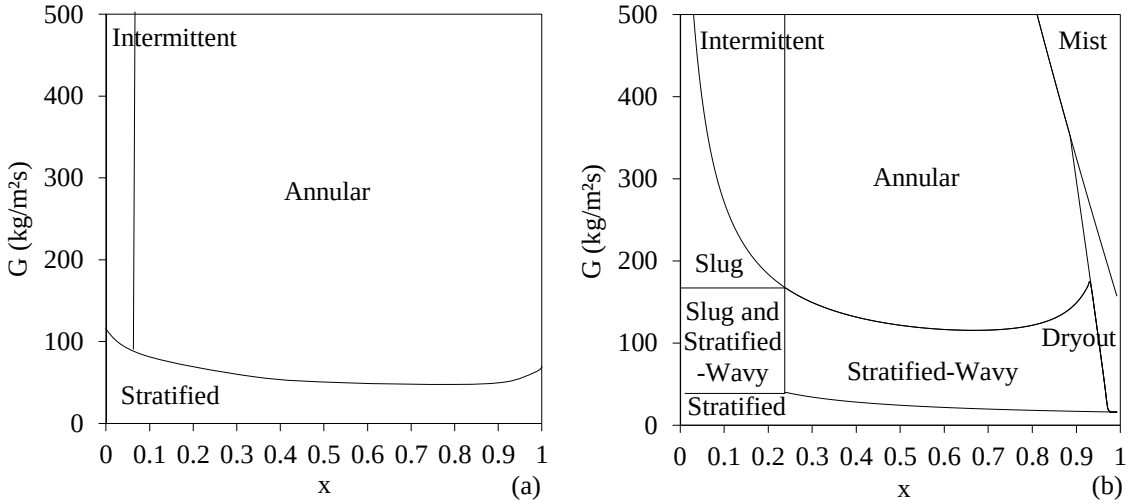

Figure 5: a) Taitel-Dukler [46] adiabatic flow regime map and b) Wojtan et al. [30] diabatic flow regime map for evaporation of R134a at -15ºC in a 9mm smooth tube with a heat flux of 4 kW/m²

Recently, there has been a renewed interest in the use of CO_2, as an environmentally friendly alternative refrigerant, and halogenated refrigerants at high reduced pressure for clothes dryers [51], solar assisted heat pumps [52], and electronic cooling applications [53]. Thome and Ribatski [39] published a comprehensive review of smooth tube flow boiling of CO_2 and found that the high reduced pressure and associated high vapor density, low surface tension, high vapor viscosity, and low liquid viscosity resulted in significant flow regime and heat transfer variations compared to traditional refrigerants. Consequently, the available diabatic flow regime maps described above did not adequately predict flow regimes for CO_2. In response, Mastrullo et al. [54] collected heat transfer and flow regime measurements for CO_2 and R410A at reduced pressures from 0.19 to 0.64 and developed new 'easy to use' semi-empirical models to improve predictive accuracy at high reduced pressure.

It's interesting to note that the Taitel-Dukler [46] and Wojtan et al. [30] flow regime maps in Figure 5 share distinct similarities, such as the general locations of the dominant

flow regimes, but the transitions from one flow regime to the next occur at significantly different mass fluxes and vapor qualities. In addition, creating the Taitel-Dukler map [46] requires complex calculations and an iterative process to determine the extent of each regime, while rather simple calculations are required to implement the Wojtan et al. [30] and Mastrullo et al. [54] maps, to describe the loci of flow regime transitions. Therefore, the Wojtan et al. [30] and Mastrullo et al. [54] maps will be used herein as diagnostic tools and to provide a baseline for the evaluation of flow regime transition in internally-grooved tubes with refrigerants at standard and reduced pressure, respectively.

Regarding applicability to a range of working fluids and channel sizes, the database used to create the most-recent Wojtan et al. [30] flow regime map covers data from three common refrigerants, namely R134a, R22, and R410A, but only a limited range of internal diameters, from 12 to 14 mm. The Mastrullo et al. [54] flow regime map was validated using one 6 mm diameter smooth tube, reduced pressure from 0.57 to 0.64 for CO_2 and 0.19 to 0.52 for R410A, mass fluxes from 150 to 500 kg/m²s, and heat fluxes between 5 and 20 kW/m². Since these models originated with the physics-based transition criteria of Taitel-Dukler [46], it is expected that they will apply to a wider range of tube diameters and fluids than that presented in the validating data set.

It is to be noted that unlike the eight unique flow regimes defined by the Wojtan et al. [30] map, most two-phase researchers [55] have limited their classification to the previously described primary flow regimes. In the interest of uniformity and consistency, and to avoid confusion that may derive from the diversity of names used by authors for some of the observed sub-regimes, the present effort will follow the classification proposed by Rahim et al. [55], combining Slug, Plug, and Intermittent data points into Intermittent

flow, combining Slugging-Annular flow, Wavy-Annular flow, and Semi-Annular data into Annular flow, and defining Stratified-Wavy flow as a sub-regime of Stratified flow, leading to the presence of just 4 primary regimes: Stratified, Bubbly, Intermittent, and Annular.

2.3 Smooth Tube Regime-Based Heat Transfer Models

As shown schematically in Figure 4, the heat transfer coefficient during two-phase flow is generally dependent on the predominant flow regime and, in diabatic flow, varies axially as the quality changes from the inlet to the outlet of the channel. Therefore, accurate prediction of two-phase heat transfer coefficients requires prediction and knowledge of the prevailing flow regime and its axial progression. Despite this fact, the most widely used heat transfer coefficient correlations are empirical, failing to incorporate flow structure in the prediction method, or based on a physical representation of a specific flow regime but used indiscriminately across all the prevailing regimes, as for example with the smooth tube correlations of Chen [56], Shah [57], Kandlikar and Balasubramanian [58], and Gungor and Winterton [59] [60]. Studies such as the one by Bar-Cohen and Rahim [35] suggest that substantially improved predictive agreement can be achieved when the selection of a correlation includes consideration of its phenomenological underpinnings.

To more accurately capture the regime-dependent performance during diabatic flow in tubes, Kattan et al. [61] [62] developed the first comprehensive flow pattern based heat transfer model. Based on the predicted flow regime, the Annular film thickness, turbulence, and dry perimeter during Stratified flows were determined and used to calculate the local heat transfer coefficient. The Kattan, Thome, and Favrat flow regime and heat transfer models [61] [62] have since been modified by other researchers. Each successive

flow regime map, as described above, had an accompanying regime-based heat transfer coefficient correlation. The most recent version, as developed by Wojtan et al. [31], includes the onset of nucleate boiling as defined by Zurcher at al. [49], a Dryout and Mist flow regime at high vapor quality, and a more detailed description of the Stratified-Wavy sub-regime of Stratified flow.

As an example of the power of this regime-based approach, Figure 6 shows a comparison of two-phase data from Filho and Jabardo [38] with the predicted heat transfer coefficient and the flow regime map from Wojtan et al. [30] for flow boiling in an 8.92 mm ID tube with R134a at a saturation temperature of 5ºC and mass fluxes of 100 and 300 kg/m²s.

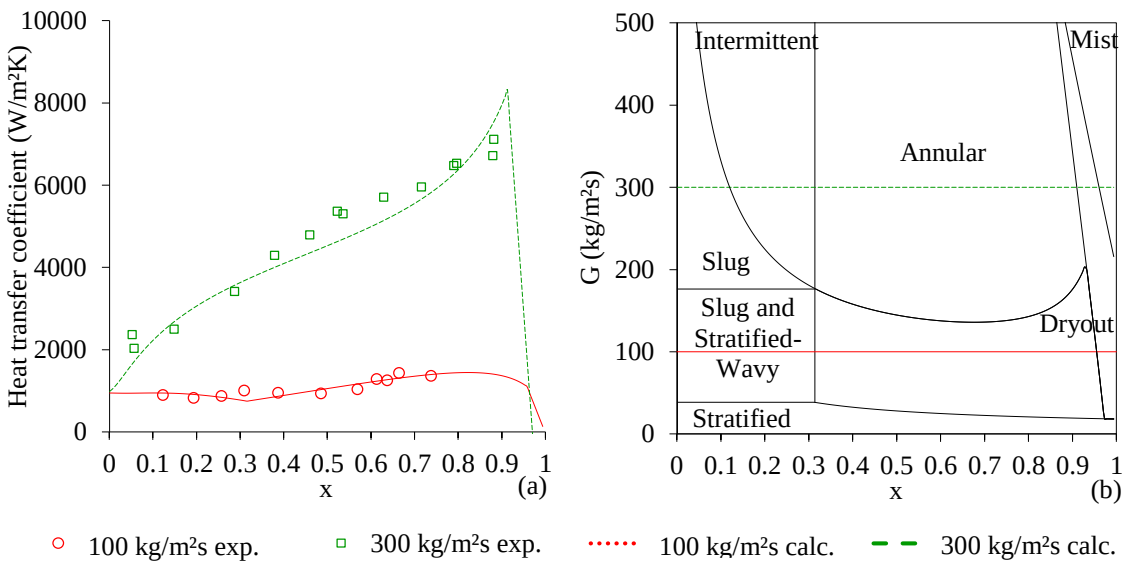

Figure 6: Comparison of experimental heat transfer data (adapted from Filho and Jabardo [38]) (hollow data points) for R134a at 5ºC in an 8.92 mm smooth tube with a heat flux of 5 kW/m² to a) the Wojtan et al. heat transfer model [31] and b) Wojtan et al. flow regime map [30]

At a mass flux of 100 kg/m²s, the locus of which is shown in Figure 6b, the model correctly predicts a low heat transfer coefficient characteristic of Stratified flow and a large dry perimeter. When the flow regime transitions from Intermittent to Annular flow at a

mass flux of 300 kg/m²s, as may be seen from the locus shown in Figure 6b, the model predicts an increase in heat transfer coefficient due to enhanced convective cooling and a thinning Annular film. Additionally, the heat transfer coefficient correlation correctly predicts the smooth transition between the respective flow regimes and the sharp reduction at high vapor qualities due to dryout.

Chapter 3: Fundamental Studies of Flow Patterns and Heat Transfer in Internally-Grooved Tubes

Two-phase flow boiling in internally-grooved tubes has been a subject of interest since they were invented in 1977, with notable reviews by Thome of internally-grooved tube studies prior to 1990 [11], a quality general review by Bergles and Manglik [63], and an update on boiling heat transfer inside enhanced tubes published by Thome in 2004 [17]. Since early 2000, there have been a large number of studies in the literature exploring evaporative heat transfer in internally-grooved tubes but few, if any, researchers have made an effort to compile this data and analyze the relationship between flow regime and evaporative heat transfer rates.

Based on this apparent void in the literature and the demonstrated success of regime-based analyses and correlations in providing improved predictive accuracy for heat transfer coefficients in smooth tubes, as described in Chapter 2, this chapter aims to explore the relationship between two-phase flow regimes and heat transfer rates in internally-grooved tubes. First, fundamental studies of thermofluid performance in internally-grooved tubes are reviewed and compared to the Wojtan et al. [30] and Mastrullo et al. [54] flow regime maps. Then, the current state of two-phase flow regime maps and heat transfer coefficient correlations for internally-grooved tubes is described. Finally, results and general comments are summarized and research directions for the current effort are developed. The majority of studies, reviewed herein, deal with halogenated fluids in conventional-sized tubes at standard temperature and pressure. However, studies of small diameter tubes, as well as alternative refrigerants and operation at reduced pressure, are

also considered. The majority of this chapter was published as a paper in the Journal of Enhanced Heat Transfer by Sharar and Bar-Cohen [64].

3.1 Flow Regime Quantification

Although the common flow regime definitions are typically based on visual and verbal descriptions, the complex nature of two-phase flow limits the accuracy and utility of such subjective determinations of flow models [65]. Regrettably, the majority of the studies to be discussed in the following chapter relied solely on subjective flow regime determination methods. These studies provide an adequate starting point for developing a physical relationship between flow regime and heat transfer in internally-grooved tubes, however, more subjective techniques will be needed to firmly establish the nature and repeatability of the dependence of thermal and momentum transport on the prevailing flow regime in such tubes. The reader is referred to Chapter 6 for a more detailed description of subjective determination techniques in the literature and the Total Internal Reflection technique used in the current study.

3.2 Studies on Conventional Internally-Grooved Tubes

The majority of the experiments focusing on flow regime and heat transfer in internally-grooved tubes have been conducted in conventional tubes ranging in size from 5 to 15 mm. Such tubes are more widely available and have been extensively tested, whereas tubes smaller than 5 mm have only recently gained attention. Table 4 is a summary of relevant studies of flow pattern and heat transfer in ‘meso’-sized internally-grooved tubes, focusing on studies that demonstrate heat transfer improvement through early flow regime transition. Most of the studies examined used refrigerant - refrigerant vapor (of a single fluid) under diabatic conditions and standard temperature and pressure.

Some studies explored halogenated fluids and CO_2 at high reduced pressure while others explored refrigerant/oil mixtures. Several studies used adiabatic water - air as the working fluids.

Table 4: Summary of relevant studies on flow patterns and heat transfer in macroscale internally-grooved tubes

Authors/References	Fluid and test section description	Main research content
Yu, Lin, and Tseng [66]	R134a evaporation, 1.5 m horizontal smooth and internally-grooved tube, 10.7 mm ID	Flow regime was mapped for both tubes, heat transfer coefficient was measured, new heat transfer coefficient correlation was developed
Oh and Bergles [67]	R134a evaporation, one smooth and 3 internally-grooved tubes with helix angles of 6º, 18º, and 44º, horizontal 9.52 mm ID tubes	Used a boroscope visualization technique to relate fluid redistribution to helix angle
Shedd and Newell [27]	Adiabatic water-air, 0.8 m horizontal smooth and internally-grooved PVC tubing, 15.1 mm ID	Flow regime, pressure drop, and circumferential Annular film thickness were measured
Shedd, Newell, and Lee [68]	Adiabatic water-air, 0.8 m horizontal smooth and internally-grooved PVC tubing, 15.1 mm ID	Flow regime, pressure drop, and circumferential Annular film thickness were measured, influence of number and angle of microgrooves was reported
Shen and Groll [69]	A critical review of lubricant influence on pool and flow boiling in smooth and enhanced tubes	Comprehensive summary of recent work and technical recommendations
Kim Shin [26]	R22 and R410A evaporation, 0.92 m horizontal smooth, 5 internally-grooved, and 1 herringbone tube, 8.14-8.7 mm ID	Heat transfer coefficient was measured for all tubes, heat transfer data compared to heat transfer coefficient correlations available in the literature
Schael and Kind [70]	Reduced pressure CO_2 evaporation, 0.2 m horizontal internally-grooved tube, 8.62 mm ID	Flow regime was mapped, heat transfer coefficient was measured and compared to previous smooth tube data
Filho and Jabardo [38]	R134a evaporation, 1.5 m horizontal smooth, herringbone, and internally-grooved tube, 8.76-8.92 mm ID	Flow visualization for smooth and internally-grooved tubes, heat transfer coefficient and pressure drop were measured
Cho and Kim [71]	Reduced pressure CO_2 evaporation, 0.2 m horizontal internally-grooved tube, 8.62 mm ID	Heat transfer coefficient and pressure drop was measured and compared to heat transfer coefficient and pressure drop correlations available in the literature
Targanski and Cieslinski [72]	R407C and R407C/oil mixture evaporation in two smooth tubes, one corrugated tube, and one internally-grooved tube, 2 m long, 8-8.92 mm ID	Heat transfer coefficient and pressure drop was measured for all tubes

Hu, Ding, and Wang [73]	R410A and R410A-oil mixture evaporation in a 7 mm OD internally-grooved tube	Heat transfer coefficient was measured for nominal oil concentrations from 0-5%, new heat transfer coefficient correlation was developed
Spindler and Müller-Steinhagen [74]	R134a and R404A evaporation, two 0.5 m horizontal internally-grooved tubes, 8.95 mm ID	Flow regime was mapped for both fluids, heat transfer coefficient was measured and compared to correlations in the literature, modified constants on existing heat transfer coefficient correlation
Filho and Barbieri [75]	R134a evaporation, 1.5 m horizontal smooth and two internally-grooved tubes, 8.92 mm ID	Flow visualization for both tubes, heat transfer coefficient and pressure drop were measured
Padovan et al. [76]	Reduced pressure (0.19-0.49) R134a and R410A evaporation, 0.3 m horizontal internally-grooved tube, 8.15 mm ID	heat transfer coefficient and dryout vapor quality were measured and compared to correlations available in the literature, new dryout inception model was developed
Hatamipour and Akhavan-Behabadi [77]	R134a evaporation, 1.1 m horizontal smooth and internally-grooved tube, 8.92 mm ID	Flow regime was mapped for both tubes, heat transfer coefficient was measured
Zhao and Bansal [78]	Reduced pressure CO_2 evaporation, 1 m horizontal internally-grooved tube, 7.3 mm ID	Heat transfer coefficient was measured and compared to heat transfer coefficient correlations available in the literature
Colombo et al. [79]	R134a evaporation, 1.3 m horizontal smooth and two internally-grooved tubes, 8.62-8.92 mm ID	Flow regime was mapped on existing maps, pressure drop and heat transfer coefficient were measured and compared to correlations available in the literature
Sharar and Bar-Cohen [80]	HFE-7100 evaporation, 0.2 m horizontal smooth and internally-grooved tubes, 8.84 mm ID	Flow regime was mapped and heat transfer coefficient was measured for both tubes. New heat transfer coefficient was introduced based on previous flow regime map [29]. Model matched well with results and data from 3 independent researchers.

3.2.1 Flow Regime Transition Mechanisms

The smooth tube regime transition from Stratified to Annular flow is modeled in the Taitel-Dukler flow regime map [46] by the waves produced due to the Kelvin-Helmholtz instability or the impingement of liquid drops on the upper surfaces, while the Intermittent to Annular transition is modeled by the rupture of the liquid plug by the vapor flow. Annular flow in internally-grooved tubes appears to exist at lower mass flux and

vapor quality than in smooth tubes [29], suggesting that the physics of flow regime transition in internally-grooved tubes is more complex. In addition to the inertial and surface tension effects mentioned above, it is believed that fluid flow redirection from axial to helical flow in the grooves (momentum change), as well as capillary force in the groove structures, and centrifugal force due to flow circulation, play a role in early transition to Annular flow in these tubes.

Shedd and Newell [27] [81] [82] [68] used a non-intrusive optical film thickness measurement technique to observe the liquid distribution in horizontal adiabatic water-air flow through 15.1 mm ID smooth and internally-grooved tubes with helix angles of 9° and 18°. These studies demonstrated the impact of grooves on liquid redistribution and early transition to Annular flow in internally-grooved tubes. Liquid film thickness profiles for Stratified/Annular flow through 15.1 mm smooth and internally-grooved tubes at mass fluxes of 44 and 120 kg/m²s are shown schematically in Figure 7. Additionally, these data points are plotted on the Wojtan et al. [30] flow regime map. The smooth tube films are represented by dotted lines and the grooved tube film thicknesses are shown with solid lines.

At low mass flux, 44 kg/m²s, the smooth tube profiles were symmetric from left to right with thicker liquid films on the bottom and dry patches at the top surface; this can be identified as Stratified flow and corresponds to a Stratified-Wavy regime on the Wojtan et al. map [30]. The grooved tube profiles appeared to be rotated counterclockwise (the same direction as the groove), achieving wetting of nearly 94% of the periphery vs only 62% for the smooth tube, and displaying behavior that can be identified as Annular flow. Shedd and Newell [27] also reported that the liquid film profiles for the smooth and internally-

grooved tubes tended to converge at higher mass flux, as seen in the film profiles for 120 kg/m²s, corresponding to Annular flow on the Wojtan et al. [30] map in Figure 7. The preferential redistribution of liquid in the direction of the helical grooves, achieving greater wetting at low mass fluxes, supports the existence of a secondary Stratified-to-Annular flow regime transition mechanism in internally-grooved tubes and could be expected to lead to higher heat transfer coefficients. Moreover, the similarity in film profiles at the higher mass fluxes would appear to be consistent with the decrease in enhancement at higher mass flux, as reported in the literature and outlined in Table 3.

Based on heat transfer experiments with liquid capillary rise on grooved flat plates, Kimura and Ito [83] and Ito and Kimura [84] hypothesized that capillary force in the grooves is a dominant factor for enhanced heat transfer in internally-grooved tubes. Essentially, the capillary force works to redistribute fluid from the bottom or sides of the tube to the top. This mode of enhancement in internally-grooved tubes has also been suggested by Yoshida et al. [85] [86] and Cui et al. [87] .

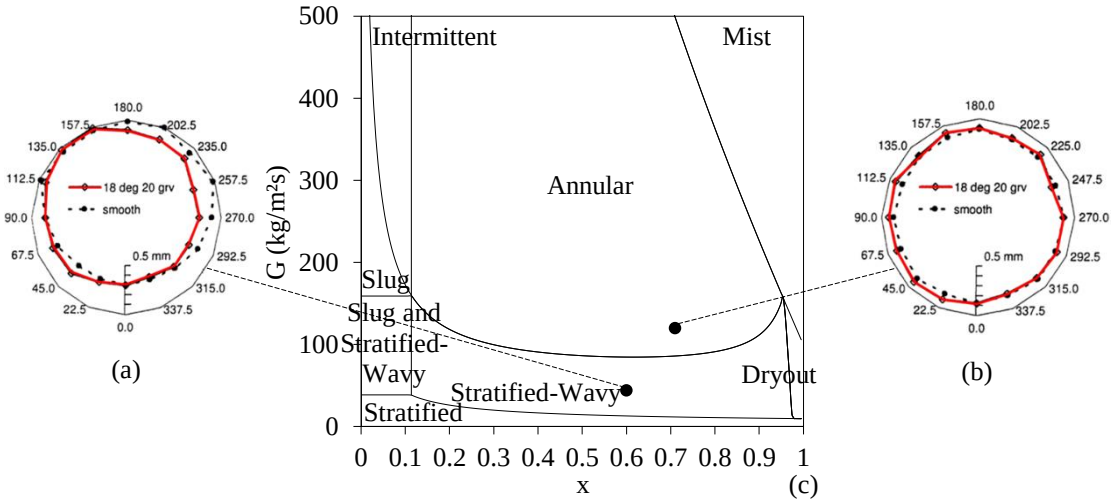

Figure 7: Film thickness profiles for smooth (dashed lines) and 18° internally-grooved (solid red lines) tubes with 15.1 mm ID and mass fluxes of a) G=44 kg/m²s and x=0.6 and b) G=120 kg/m²s and x=0.76 [27], plotted on the simplified Wojtan et al. [30] flow regime map

3.2.2 Halogenated Fluids at Standard Pressure and Temperature

Yu, Lin, and Tseng [66] performed a flow visualization and heat transfer study with R134a at 6ºC in a 10.7 mm ID smooth and an 11.1 mm ID internally-grooved tube with an 18° helix angle. Mass fluxes from 163 to 408 kg/m²s, heat flux between 2.2 and 56 kW/m², and a fixed heated length of 1.5 m were tested. Figure 8 shows the results of the flow visualization, plotted in the coordinates of mass flux and vapor quality and superimposed on the Wojtan et al. [30] flow regime map; Figure 8a is the smooth tube experimental results and Figure 8b is the internally-grooved tube results. The transitions of flow pattern visually observed were Stratified, Intermittent, and Annular in the direction of increasing mass flux and vapor quality.

It was reported in the study, and also apparent from Figure 8, that the transitions in the internally-grooved tube occurred at lower mass flux and vapor quality compared with the smooth tube. Thus, at a mass flux of 163 kg/m²s and a quality greater than 0.3, Annular flow was encountered in the internally-grooved tube while the smooth tube was operating in the Stratified regime. Additionally, at a mass flux of 245 kg/m²s and a quality greater than 0.15, Annular flow was encountered in the internally-grooved tube while the smooth tube was operating in the Intermittent regime. The Wojtan et al. [30] flow regime map was shown to satisfactorily predict flow regime in the smooth tube, but due to the observed early flow regime transition in the internally-grooved tube at lower mass flux and vapor quality, the Wojtan et al. [30] map did a poor job predicting flow regimes in the internally-grooved tube [29].

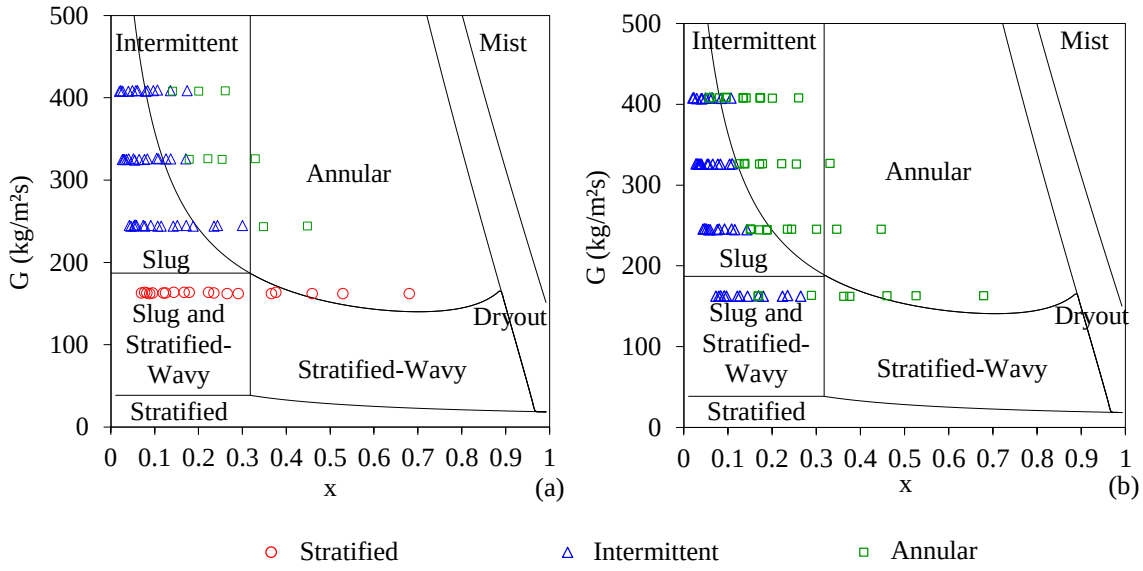

Figure 8: Experimental flow visualization results from Yu et al. [66] for R134a at 6ºC with a heat flux of 20 kW/m² plotted on a simplified Wojtan et al. [30] map for a) 10.7 mm ID smooth tube and b) 11.1 mm ID internally-grooved tube

The aforementioned early flow regime transitions at low mass flux improved heat transfer in the internally-grooved tube relative to the smooth tube. Figure 9a shows the average heat transfer coefficient vs. vapor quality for a mass flux of 163 kg/m²s and Figure 9b shows the internally-grooved enhancement factor. The enhancement factor is defined as the ratio of the internally-grooved tube heat transfer coefficient to the smooth tube heat transfer coefficient. The additional area provided by the internally-grooved tube of Yu, Lin, and Tseng [66] was accounted for in Figure 9, resulting in a smooth tube equivalent heat transfer coefficient.

As can be seen in Figure 9a, the increase in the smooth tube heat transfer coefficient was minimal due to the dominance of Stratified flow. Alternatively, when the flow pattern was changing, the rise in the heat transfer coefficient was dramatic. At a mass flux of 163 kg/m²s and quality of 0.3 there was a sharp increase in the heat transfer coefficient, from

approximately 4 to 5.5 kW/m²K (40% improvement), accompanying the flow regime transition from Intermittent to Annular flow in the internally-grooved tube. Consequently, the maximum heat transfer enhancement of 2.25, as shown in Figure 9b, occurred at a flow rate of 163 kg/m²s and qualities 0.3<x<0.7 where Stratified flow dominated in the smooth tube and flow transition to Annular was achieved in the internally-grooved tube.

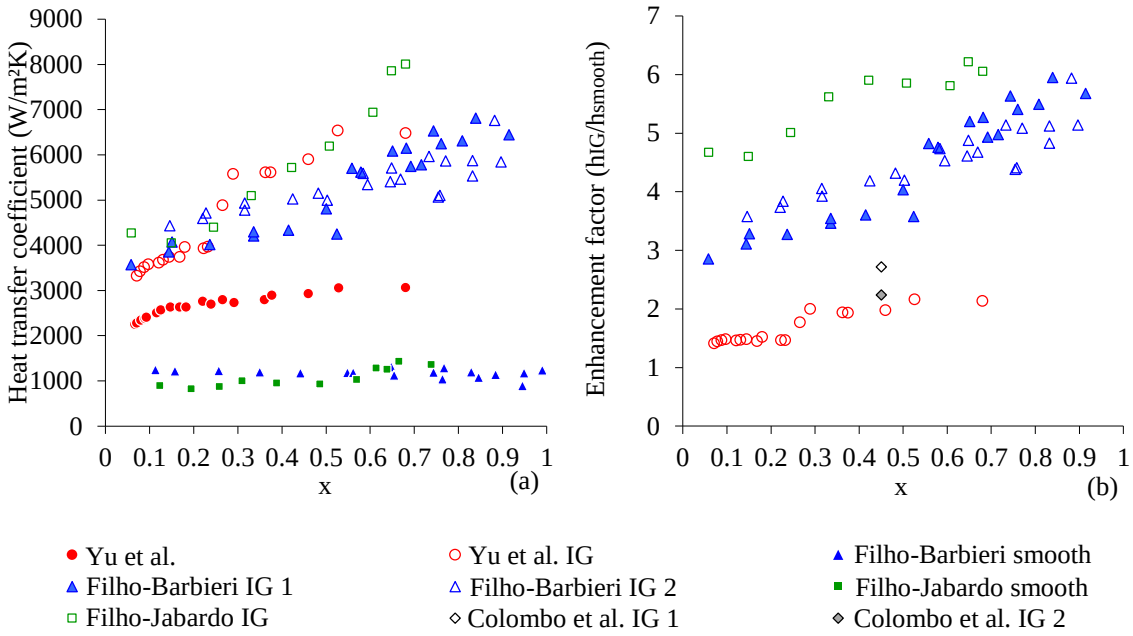

Figure 9: a) Heat transfer coefficient vs vapor quality and b) accompanying enhancement factor from several researchers with low mass flux (100 – 163 kg/m²s)

As may be seen in Figure 8a, at a mass fluxes of 326 kg/m²s or above, the observed flow regimes for the smooth and internally-grooved tubes tended to converge to Annular flow. Figure 10a and Figure 10b show the average heat transfer coefficient vs. vapor quality for the smooth tube and internally-grooved tube and the enhancement factor at the higher mass flux of 326 kg/m²s. As can be seen in Figure 10a, a significant increase in heat transfer coefficient is observed in the smooth tube at a mass flux of 326 kg/m²s and a vapor quality of 0.2, coinciding with transition to Annular flow and yielding a smooth tube

heat transfer coefficient profile that more closely resembles that of the internally-grooved tube. Calculation of the internally-grooved tube enhancement factor reveals that the heat transfer improvement approaches 1.3 at high mass flux and high vapor quality. The marginal improvement beyond area enhancement at higher mass fluxes may be a result of extra turbulence, mixing, or nucleate boiling due to the grooved structures. These trends are consistent with trends discussed in Table 3, and as described, are directly related to the observed flow regime. The experimental data were compared with existing smooth tube correlations from Kattan et al. [62], Chen [56], Shah [57], Gungor and Winterton [60], Liu and Winterton [88] and a newly-proposed heat transfer coefficient correlation by Yu, Lin, and Tseng [66]. Their experimental data was found to correlate well with the most recent heat transfer coefficient correlation.

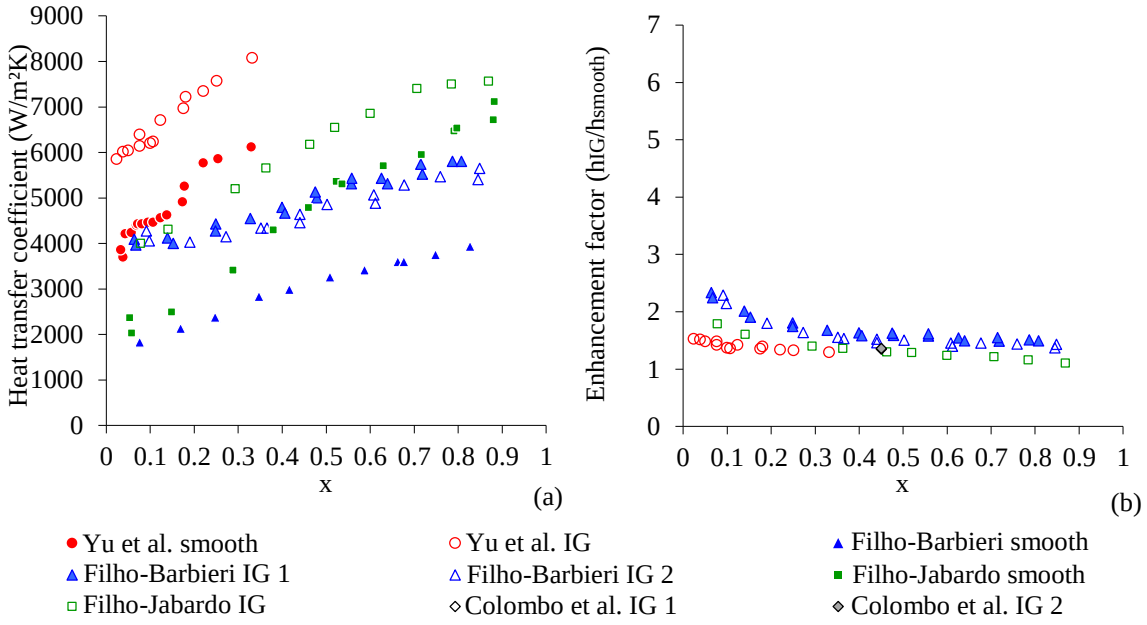

Figure 10: a) Heat transfer coefficient vs vapor quality and b) accompanying enhancement factor from several researchers with high mass flux (300 - 326 kg/m²s)

Bandarra Filho and co-workers [75] [38] reported experimental investigations of flow boiling of R134a in a smooth tube and two internally-grooved tubes with inside diameters of 8.76 to 8.92 mm, helix angles of 18°, fin heights of 0.2 mm, and between 60 and 80 grooves. Tests were performed in 1.5 m long tubes with a saturation temperature of 5°C, a heat flux of 5 kW/m², vapor qualities up to 90%, and mass fluxes from 100 to 500 kg/m²s. The area enhancement of the internally-grooved tube was 1.91 times the smooth tube in the Filho and Jabardo [38] study but was not reported in the Filho and Barbieri [75] study. Filho and Barbieri [75] provided representative flow regime photographs for several operating conditions and described the flow regime trends but did not plot their flow visualization data.

Figure 11 shows the Filho and Barbieri [75] flow regime data plotted on a Wojtan et al. [30] flow regime map. For the smooth tubes they visually observed that Annular flow was the dominant regime at high vapor quality and mass flux greater than 150 kg/m²s. For mass fluxes higher than 150 kg/m²s and low vapor quality, Intermittent flow was the dominant regime. At mass velocities lower than 150 kg/m²s, Stratified flow was observed for the entire range of vapor qualities tested. These trends are captured well by the Wojtan et al. [30] flow regime map.

The trends were different in the internally-grooved tubes. Stratified flow was never observed in the internally-grooved tubes, even at mass fluxes as low as 100 kg/m²s. Instead, earlier transition to Intermittent and Annular flow was reported at lower mass flux and vapor quality than observed in the smooth tube. One specific example on Figure 11 is at a mass flux of 300 kg/m²s and a vapor quality of 0.1 where the smooth tube was operating in Stratified flow while the internally-grooved tube was operating in Annular flow. It's

also interesting to point out that at a mass flux of 500 kg/m²s and a vapor quality around 0.65, the smooth tube was operating in Annular flow and the internally-grooved tube prematurely transitioned to Mist flow. Similar flow regime trends were reported by Filho and Jabardo [38] for similar test conditions.

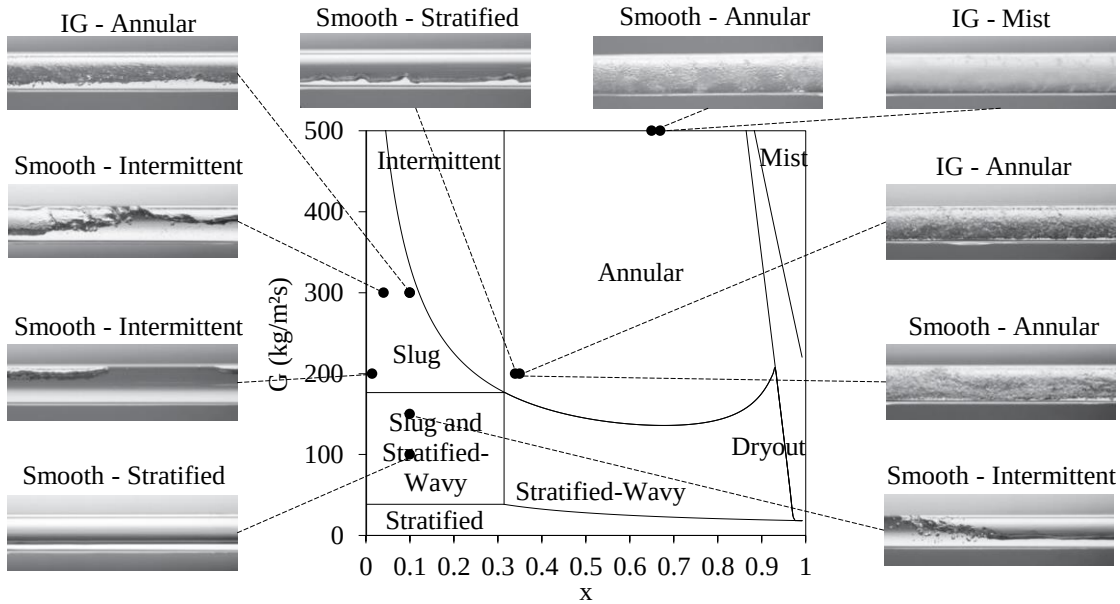

Figure 11: Experimental flow visualization results of Filho and Barbieri [75] for R134a at 5ºC in an 8.92 mm smooth and internally-grooved tube with a heat flux of 5 kW/m² plotted on a simplified Wojtan et al. [30] flow regime map

Figure 9a shows the average heat transfer coefficient vs. vapor quality for the smooth tube and three internally-grooved tubes at a mass flux of 100 kg/m²s for Filho and Barbieri [75] and Filho and Jabardo [38]. It's important to note that - in these studies - the increased internally-grooved tube surface area was not accounted for when calculating the heat transfer coefficient, so it's expected that the heat transfer coefficient should be close to 1.3 to 1.91 times larger than the smooth tube values for all test conditions. At a mass flux of 100 kg/m²s the heat transfer coefficient in the smooth tube is low and appears to slightly deteriorate over the whole range of vapor qualities; this is indicative of the

observed Stratified flow regime at mass fluxes below 150 kg/m²s. Under the same conditions, the heat transfer coefficient increases in all of the internally-grooved tubes. As described above, this is a result of the dominance of Intermittent and Annular flow in the internally-grooved tube. As shown in Figure 9b, the effect is heat transfer enhancement close to 6 times that of the plain tube. However, at a higher mass flux of 300 kg/m²s, where Intermittent and Annular flow were the dominant regimes in both the smooth and internally-grooved tubes, the heat transfer trends begin to converge to the internal area enhancement. This effect is clearly shown in Figure 10a and b.

Additionally, at a mass flux of 500 kg/m²s and vapor quality above 0.5, Filho and Barbieri [75] and Filho and Jabardo [38] reported worse performance in the internally-grooved tubes compared to the smooth tube as a result of the premature transition to Mist flow. The results were not compared to existing internally-grooved tube heat transfer coefficient correlations. It's interesting to note that Filho and Jabardo [38] and Filho and Barbieri [75] reported similar trends with respect to flow regime and thermal performance, however, subtle differences in performance between the two studies can be seen in Figure 9 and Figure 10, presumably as a result of varying geometric parameters.

Colombo et al. [79] performed a flow visualization and evaporative/condensing heat transfer study with R134a at a saturation temperature of 5°C in a horizontal 8.92 mm ID smooth tube and two internally-grooved tubes with inside diameters of 8.62 and 8.92 mm. Both internally-grooved tubes had helix angles of 18° and apex angles of 40º, but had alternating fin heights ranging from 0.16 to 0.23 mm and the number of grooves ranging from 54 to 82. The resulting internally-grooved tube area enhancement ranged from 1.55 to 1.82. Mass fluxes from 100 to 340 kg/m²s, heat flux between 2.2 and 56 kW/m², vapor

qualities from 0.1 to 0.9, and a fixed heated length of 1.3 m were tested. Figure 12 shows the results of the flow visualization, plotted in the coordinates of mass flux and vapor quality and superimposed on the Wojtan et al. [30] flow regime map; Figure 12a is the smooth tube experimental results and Figure 12b is the results for one of the internally-grooved tubes. The transitions of flow pattern visually observed were Stratified, Intermittent, and Annular in the direction of increasing mass flux and vapor quality.

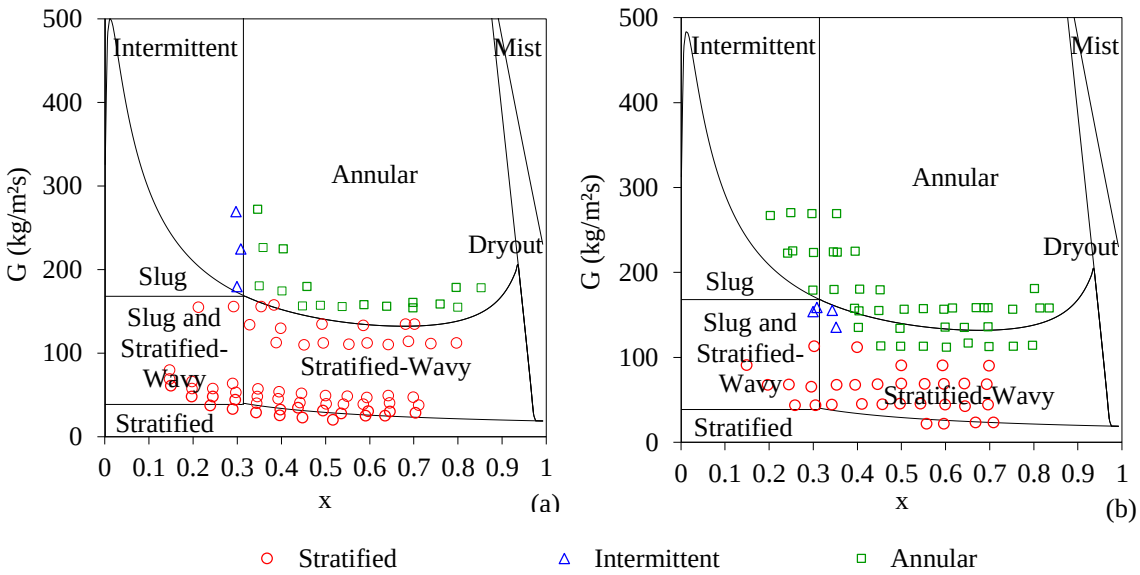

Figure 12: Flow visualization results from Colombo et al. [79] for 8.92 mm ID a) smooth and b) internally-grooved tubes with R134a at 5ºC and a heat flux of 4.2 kW/m² plotted on the Wojtan et al. [30] flow regime map

Figure 12 makes it very clear that there are distinct differences in flow regimes between the smooth and internally-grooved tubes, with the latter shifting the onset of Annular flow to lower mass flux and vapor quality. One example is at a mass flux of 100 kg/m²s and a quality greater than 0.4 where Annular flow was encountered in the internally-grooved tube, while the smooth tube was operating in the Stratified regime. Additionally, at vapor qualities close to 0.3 and mass fluxes greater than 180 kg/m²s, the smooth tube was operating in Intermittent flow and the internally-grooved tube was operating in

Annular flow. Annular flow was observed in both the smooth and internally-grooved tubes at high mass flux and vapor quality. The Wojtan et al. [30] flow regime map accurately predicted flow regime and flow regime transitions in the smooth tube, but due to the observed early flow regime transition in the internally-grooved tube at lower mass flux and vapor quality, the Wojtan et al. [30] map was unable to properly predict flow regimes in the internally-grooved tube.

Due to limitations in the data of Colombo et al. [79], it could not be included in the overall plot of the heat transfer coefficient vs vapor quality, Figure 9a and Figure 10a. However, they reported enhancement factors at an average vapor quality of 0.45 for mass fluxes ranging from 90 to 320 kg/m²s and these values were added to the enhancement factor plots, Figure 9b and Figure 10b. As shown in Figure 9b, the heat transfer enhancement at a mass flux of 90 kg/m²s and mean vapor quality of 0.45 was 2.4 to 2.7 times higher than the smooth tube. This corresponds to Annular flow in the internally-grooved tube and Stratified flow in the smooth tube. As shown in Figure 10b, at a higher mass flux of 320 kg/m²s and the same vapor quality where Annular flow is the dominant regime in both the smooth and internally-grooved tubes, the enhancement ratio reduces to 1.35 for both internally-grooved tubes. It is to be noted that Colombo et al. [79] did not account for the increased internally-grooved tube surface area when calculating the heat transfer coefficient. So, it's to be expected that the heat transfer enhancement should be at least 1.55 to 1.82 times larger than the smooth tube values for all test conditions. The researchers did not comment on this discrepancy. Though not explicitly described here, it's important to note that the Colombo et al. [79] results showed performance differences

between the two internally-grooved tubes, which reinforces that the specific geometric parameters may affect thermal performance.

The internally-grooved tube experimental data was compared with existing internally-grooved correlations from Murata et al. [89], Yun et al. [90], and Thome et al. [91]. The measured heat transfer coefficients were not well correlated by any of the existing correlations, with average percent errors ranging from -39% to +156%.

Spindler and Müller-Steinhagen [74] performed an experimental investigation of heat transfer and flow regime during evaporative cooling in an 8.92 mm ID internally-grooved tube with a 15° helix angle using two different refrigerants, R134a and R404A. Experiments were conducted in a 1 m long heated test section with mass fluxes ranging from 25 to 150 kg/m², heat flux from 1 to 15 kW/m², inlet vapor qualities ranging from 0.1 to 0.7, and a saturation temperature of -20ºC. Stratified, Intermittent, and Annular flow were observed. Annular flow was the dominant regime for mass fluxes at or above 65 kg/m²s. Shown in Figure 13 is the experimental visual flow regime data of Spindler and Müller-Steinhagen [74] for R134a and R404A plotted on the Wojtan et al. [30] flow regime map.

The Wojtan et al. [30] map over-predicts the mass flux at which transition from Stratified to Annular flow occurs for both fluids. They hypothesized that the spiral grooves worked to redistribute the liquid, resulting in early transition to Annular flow. Unfortunately they did not perform flow regime and heat transfer experiments for a comparable smooth tube as a benchmark for comparison. The experimental heat transfer coefficients were compared to the correlations from Koyama et al. [92] and Kandlikar [93] and average deviations of ±15% and ±30%, respectively, were observed.

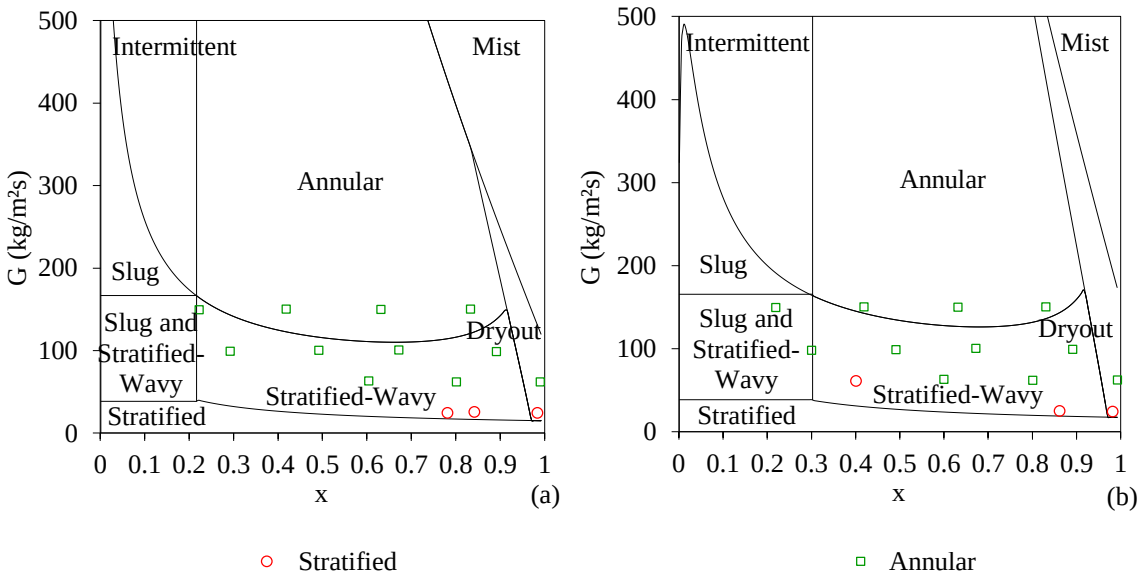

Figure 13: Experimental flow visualization results from Spindler and Müller-Steinhagen [74] for a) R134a and b) R404A at -20ºC with a heat flux of 7.5 kW/m² in one 8.92 mm ID internally-grooved tube plotted on a corresponding Wojtan et al. [30] flow regime map

3.2.3 Refrigerant/Oil Mixtures

In operating refrigeration systems, it is not uncommon to encounter boiling of refrigerant/oil mixtures. The amount of oil in the mixture, which is dependent on system wear and worker expertise, will increase pressure drop and may help or hinder cooling performance. Therefore, it is essential to test flow boiling of refrigerant/oil mixtures for a wide range of test conditions and a wide range of refrigerants and oils. While not the main intent of the current research effort, several representative reviews and studies [72] [73] [69] on the performance of refrigerant/oil mixtures in internally-grooved tubes have been included in Table 4 for the sake of completeness.

3.2.4 Halogenated Fluids and CO_2 at Elevated Reduced Pressure

Most macro-channel internally-grooved tube flow boiling studies in the open literature are concerned with halogenated fluids at standard pressures and temperatures ranging from -15 to 20°C for refrigeration systems. However, some researchers have

looked at CO_2 and halogenated fluids at higher saturation temperatures (and higher reduced pressures) for clothes dryers [51], solar assisted heat pumps [52], and electronic cooling applications [53]. As mentioned earlier in Chapter 2, reduced pressure has been shown to play a significant role in predicting the flow regime and heat transfer coefficient. Thus, there is a need to explore heat transfer coefficients and flow regimes in internally-grooved tubes with CO_2 and halogenated refrigerants at high reduced pressure to establish performance trends. A brief description of CO_2 and refrigerant flow boiling at high reduced pressure are given below; please refer to Table 4 for a more comprehensive list of high reduced pressure studies in internally-grooved tubes.

Schael and Kind [70] visually observed flow patterns and measured heat transfer coefficients in an 8.92 mm ID internally-grooved tube and a comparable smooth tube with CO_2 at reduced pressures of 0.54 (T_{sat} = 5°C) and 0.36 (T_{sat} = -10°C). Shown in Figure 14 is the experimental flow regime data of Schael and Kind [70] plotted on the Mastrullo et al. [54] map for CO_2 and halogenated fluids at elevated reduced pressures. It is clear from the figure that for both reduced pressures, the experimental transition from Stratified to Annular flow and Intermittent to Annular flow occurs at lower mass flux and vapor quality than predicted by the map. They showed a marked improvement in heat transfer coefficient when increasing the mass flux from 75 to 250 kg/m²s in the internally-grooved tube and related this enhancement to early regime transition to Intermittent and Annular flow, as shown in Figure 14.

Similarly, Zhao and Bansal [78] compared their experimental data for CO_2 flow boiling in a 7.3 mm ID internally-grooved tube, at a reduced pressure of 0.19 (T_{sat} = -30°C), with comparable smooth tube data from Park and Hrnjak [94], and deduced that early flow

regime transition to Annular flow at low mass flux was an enhancement mechanism for CO_2 flow boiling in internally-grooved tubes.

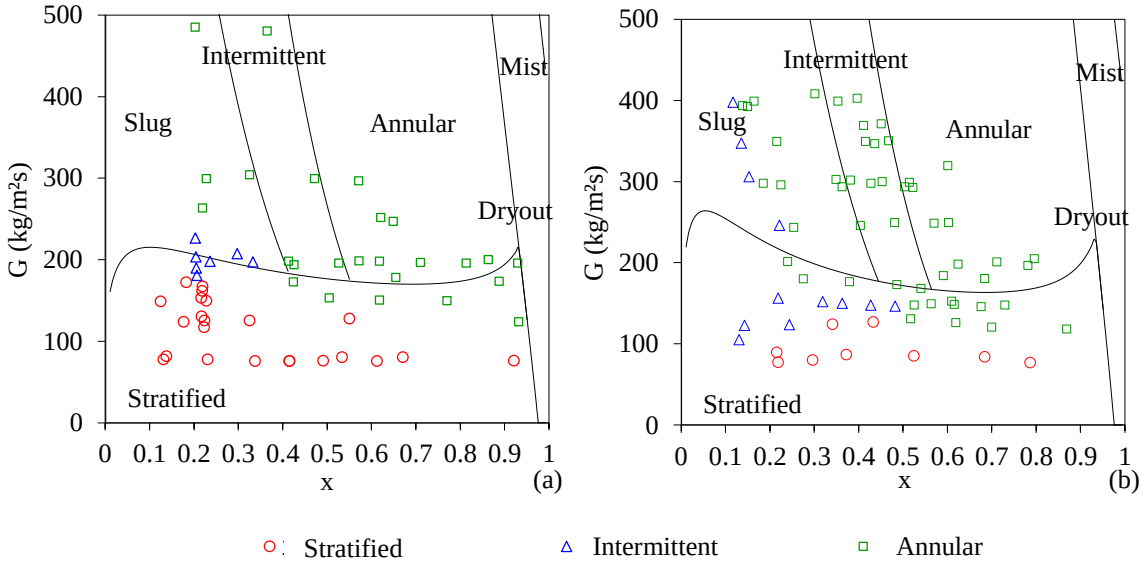

Figure 14: Experimental flow visualization results from Schael and Kind [70] for CO_2 flow boiling in an 8.92 mm ID internally-grooved tube with heat fluxes up to 120 kW/m² at reduced pressures of a) 0.54 (Tsat = 5°C) and b) 0.36 (Tsat = -10°C) plotted on the Mastrullo et al. [54] flow regime map

Schael and Kind [70] and Padovan, Del Col, and Rossetto [76] showed performance degradation at high mass flux during flow boiling at high reduced pressure. Unlike Filho and Barbieri [75] and Filho and Jabardo [38], who associated this reduction with premature Mist flow, Schael and Kind [70], and Padovan, Del Col, and Rossetto [76] hypothesized that the heat transfer reduction was likely a result of nucleate boiling suppression. Along the same lines, Zhoa and Bansal [78] correlated an observed heat flux dependence according to the power law (i.e. $h \alpha \dot{q}^n$), which identifies nucleate boiling as a key mechanism in high reduced pressure internally-grooved tubes. The exponent 'n' varied between 0.67 and 0.73 for the internally-grooved tube. This exponent is the same value as the exponent used in the correlation by Cho and Kim [71], 0.67, for flow boiling of CO_2 in internally-grooved tubes but higher than the exponent used in the model of Cheng et al.

[40] for flow boiling of CO_2 in smooth tubes. However, this is the opposite trend of Schael and Kind [70], who showed a smaller exponent for the internally-grooved tube, 0.4 to 0.5, than the smooth tube, 0.5 to 0.55.

3.2.5 Geometric Considerations

Geometric parameters have been shown to play a critical role in flow redistribution and the thermal performance of internally-grooved tubes. Oh and Bergles [67] used a boroscope visualization technique to study the effect of helical groove angle on enhancement during flow boiling of R134a in internally-grooved tubes. The behavior of the liquid was observed for four tubes including a smooth tube and three internally-grooved tubes with helix angles of 6°, 18°, and 44°, operating with mass fluxes of 50, 100, and 200 kg/m²s and heat fluxes ranging from 5 to 20 kW/m². They found that the 18° helix angle caused earlier transition to Annular flow and provided the most enhancement at a mass flux of 50 kg/m²s, while the 6° helix angle was optimal for a mass flux of 200 kg/m²s. These results are consistent with conclusions drawn earlier by Yoshida et al. [85]. They investigated heat transfer and flow pattern in an internally-grooved tube with R22 at a pressure of 5.9 bar (p_r=0.12) and found that the grooves worked to redistribute fluid to the top of the channel, even at mass fluxes as low as 50 kg/m²s.

Kim and Shin [26] performed an extensive experimental flow boiling study with R22 and R410A in one 8.70 mm ID smooth tube, five 8.46-8.68 mm ID internally-grooved tubes, and two 8.14-8.51 mm ID cross grooved tubes with mass fluxes of 136, 205, and 273 kg/m²s. Helix angles for the internally-grooved tubes varied from 15.5° to 30°, apex angles varied from 25° to 53°, fin heights varied from 0.12 to 0.25 mm, the number of fins ranged from 54 to 65, and the resulting area enhancement ranged from 1.28 to 1.85. The

heat transfer enhancement was 1.86 to 3.27 depending on the particular tube. The best performing tube had the largest fin height to diameter ratio, largest area enhancement, most fins, and the smallest apex and helix angles. In addition, Filho and Barbieri [75], Filho and Jabardo [38], and Colombo et al. [79], independently identified relationships between heat transfer and various geometric parameters such as fin profile, number of fins, apex angle, helix angle, and fin height to diameter ratio, and ratio of the fin height to the liquid film thickness.

3.3 Studies on Small Internally-Grooved Tubes

Flow patterns and heat transfer mechanisms can be different in small smooth channels from those in conventional channels. For example, the effect of channel orientation tends to disappear, flow regimes tend to converge to Annular flow, and new flow patterns such as wedge flow [95] and lump flow [96] have been observed. Reducing the size of refrigeration tubes offers the potential for more compact and efficient heat exchangers [71], but before small diameter internally-grooved tubes can be considered as a viable replacement for conventional channels the impact of channel size on thermofluid performance needs to be revealed. Unfortunately, as shown in Table 5, the study of small diameter internally-grooved tubes has only been a topic of research since 2006 and, as such, the literature contains only a few studies for this form factor. All of the reported studies used refrigerant – refrigerant vapor (of a single fluid) under diabatic conditions and elevated reduced pressure. In fact, none of the studies in Table 5 are at an elevated reduced pressure less than 0.12. Fortunately, many of the studies considered the effect of refrigerant/oil mixtures to simulate more realistic operating conditions.

Table 5: Summary of relevant studies on flow patterns and heat transfer in small and microscale internally-grooved tubes

Authors/References	Fluid and test section description	Main research content
Gao et al. [97] [98] [99]	Reduced pressure CO_2 and CO_2-oil evaporation, 1 m long horizontal and smooth internally-grooved tubes, 3.04 mm ID	Measured heat transfer coefficient and pressure drop
Cho and Kim [71]	Reduced pressure CO_2 evaporation, 0.2 m horizontal smooth and internally-grooved tube, 4.4 mm ID	Measured heat transfer coefficient and pressure drop, compared experimental database to existing pressure drop and heat transfer coefficient correlations
Kim, Cho, and Kim [100]	Reduced pressure CO_2 evaporation, one vertical smooth tube and one vertical internally-grooved tube, 4-4.4 mm ID	Measured heat transfer coefficient and pressure drop, compared experimental database to existing pressure drop and heat transfer coefficient correlations
Ono, Gao, Honda [101]	Reduced pressure CO_2 and CO_2-oil evaporation, 1 m long horizontal and smooth internally-grooved tubes, 3.75 mm ID	Observed flow regime, measured heat transfer coefficient and pressure drop, reported higher dryout quality in the internally-grooved tube, compared results to Cheng et al. flow regime map [102]
Gao et al. [24]	Reduced pressure CO_2 and CO_2-oil evaporation, 1 m long horizontal and smooth internally-grooved tubes, 1.95 mm ID	Observed flow regime, measured heat transfer coefficient, reported delayed dryout and sustained performance in the internally-grooved tubes, compared results with Cheng et al. [102] flow regime map and heat transfer coefficient correlation
Dang, Haraguchi, and Hihara [23]	Reduced pressure CO_2 evaporation, 1.43-5.72 m horizontal smooth and internally-grooved tubes, 2 mm ID	Observed flow regime, measured heat transfer coefficient and pressure drop, reported delayed dryout and sustained performance in the internally-grooved tubes
Wu, Wu, Sunden, and Li [103]	Reduced pressure R22 and R410A evaporation, one horizontal smooth tube and five internally-grooved tubes, 4.4-4.6 mm ID	Measured heat transfer coefficient and pressure drop, developed a new semi-empirical heat transfer model based on past and present data
Mancin, Diani, and Rossetto [104]	Reduced pressure R134a evaporation, 0.3 m horizontal internally-grooved tube, 3.4 mm ID	Measured heat transfer coefficient, pressure drop, and vapor quality at onset of dryout
Diani et al. [53]	Reduced pressure R1234ze(E) evaporation, 0.3 m horizontal internally-grooved tube, 3.4 mm ID	Measured heat transfer coefficient, pressure drop, and dryout, compared data to that of Mancin et al. [104]

Considering flow boiling of CO_2 and refrigerants at elevated reduced pressure, few studies have been conducted at mass fluxes low enough to demonstrate early flow regime transition in internally-grooved tubes. For example, Gao et al. [24], Dang et al. [23], Cho and Kim [71], Diani et al. [53], and Mancin et al. [104] all tested mass fluxes above 190 kg/m²s, where one would expect Intermittent and Annular flow to be the dominant flow regimes for both smooth and internally-grooved tubes. For these high mass fluxes, the researchers generally reported enhancement factors close to the area enhancement, which is consistent with trends in Table 3. Regrettably, flow regime visualization (let alone quantification) was not typically performed in these studies. To reiterate a sentiment expressed by Wu et al. [103], future research should pay closer attention to flow boiling in internally-grooved tubes at low mass flux.

One interesting trend reported by Gao et al. [24] and Dang et al. [23], for CO_2 flow boiling in 1.95-2.65 mm ID tubes at a saturation temperature of 10ºC, was dryout in the smooth tubes at vapor qualities ranging from 0.4 to 0.8 and sustained performance in the internally-grooved tubes up to vapor qualities approaching 1. These results are similar to those reported by Padovan et al. [76] for flow boiling of R134a and R404A in conventional 8.15 mm ID tubes at reduced pressures ranging from 0.19 to 0.49.

3.3.1 Refrigerant/Oil Mixtures

For the sake of brevity, studies of flow boiling with refrigerant/oil mixtures in small diameter internally-grooved tubes will not be described in great detail. Please refer to studies by Gao et al. [97] [98] [99] [24] and Ono et al. [101]. They report varying, and sometimes contradictory, pressure drop, heat transfer, and flow regime trends for smooth and internally-grooved tubes with a strong dependence on heat and mass flux. All of these

studies used CO_2 at 10ºC and polyalkylene glycol (PAG). Thus, there is a need to extend the experimental database to other refrigerant and oil combinations.

3.3.2 Geometric Considerations

Geometric parameters play a critical role in flow redistribution and the thermal performance of conventional sized internally-grooved tubes. As shown by Wu et al. [103], who described a strong relationship between performance and the ratio of the fin height to the liquid film thickness, this appears to be the case for small diameter internally-grooved tubes, as well. Additionally, Diani et al. [53] and Mancin et al. [104] speculated that the observed maximum heat transfer coefficient at moderate mass fluxes may be a result of tube geometric parameters. Despite this dependence, a systematic study of fin shape, fin height, number of fins, helix and apex angle, and ratio of relevant parameters has not been performed to determine the relationship between geometric parameters and thermofluid performance in small diameter internally-grooved tubes.

3.4 Flow Regime Maps and Regime-Inspired Heat Transfer Coefficient Correlations for Internally-Grooved Tubes

As the previous discussion has made abundantly clear, thermal performance during two-phase flow boiling in internally-grooved tubes is dependent on the predominant flow regime. Despite this fact, the most widely used heat transfer coefficient correlations for internally-grooved tubes are empirical and do not account for the prevailing flow regime. Others assume a fixed flow regime, such as Annular flow, and are unable to universally predict heat transfer. Furthermore, geometric parameters that have been proven to affect performance are often not considered. Although the eventual goal is to develop a physics-based heat transfer model that represents the impact of two-phase flow structures and is

coupled to a reliable flow regime map [105], the literature suggests that we are still far from having a universally accurate model to predict flow boiling heat transfer in internally-grooved tubes.

A number of researchers have recognized the dependence of heat transfer on the particular flow regime in internally-grooved tubes. As such, flow regime maps for internally-grooved tubes and regime-inspired heat transfer coefficient correlations have been developed. A summary of these studies can be found in Table 6 and are discussed in more detail below.

Table 6: Summary of relevant studies on new flow pattern maps for internally-grooved tubes and regime-based heat transfer coefficient models

Authors/References	Main research content
Nozu and Honda [106]	Developed a model to predict condensation heat transfer for Annular flow in internally-grooved tubes. Compared model to data for four refrigerants and three tubes and found good agreement.
Honda, Wang, and Nozu [107]	Developed a model to predict condensation heat transfer for Stratified flow in internally-grooved tubes. Model was compared to heat transfer coefficient correlations available in the literature and data for five tubes and five refrigerants. New model outperformed empirical models.
Wang, Honda, Nozu [108]	Modified previous condensation models to account for effects of surface tension in Stratified flow and shear stress in Annular flow. Compared modified model to experimental data for six tubes and five refrigerants and showed good agreement.
Mori et al. [109]	Proposed a new Stratified flow internally-grooved tube model that expressed the circumferential average heat transfer coefficient as the sum of thin film evaporation between the grooves on the top surface and convective boiling of the stratified liquid at the bottom surface.
Honda and Wang [110]	Modified Stratified flow condensation models to predict evaporation heat transfer in internally-grooved tubes. Good agreement was found with data available in the literature.
Makishi, Honda, and Wang [111]	Proposed a new Stratified and Annular flow model of evaporation heat transfer in horizontal internally-grooved tubes. Used the Stratified-Wavy to Annular flow transition of Kattan et al. [47] to predict heat transfer in the intermediate region. Compared new model to experimental data for ten tubes and four refrigerants.
Wang, Wang, Wang, Honda [112]	Modified previous Annular and Stratified evaporation model to account for local heat transfer enhancement due to disturbance waves in internally-grooved tubes. Comparison of the model to data in the literature revealed good agreement.

Momoki et al. [113]	Proposed a prediction method for evaporating heat transfer coefficient of refrigerants in a horizontal internally-grooved tube with consideration of flow regime. Classified four flow regimes: Annular flow, Annular flow with liquid meniscus, separated flow with liquid meniscus, and separated flow with dry surface. Experimental data matched the calculated values well.
Liebenberg and Meyer [114]	Observed flow regime, measured heat transfer coefficient and pressure drop, developed semi-empirical equations for heat transfer and pressure drop, modified I/A transition for condensation on past flow regime maps.
Doretti, Zilio, Mancin, Cavallini [115]	Detailed literature review of two-phase flow regime, heat transfer, and pressure drop during condensation in internally-grooved tubes. Observed flow regime, measured heat transfer coefficient and pressure drop. Developed new Annular flow transition model.
Sharar et al. [29]	Re-interpreted data in the literature to show that flow regime transition from Stratified flow to Annular flow in internally-grooved tubes is a key enhancement mechanism. Modified the Wojtan et al. flow regime map by shifting the Intermittent to Annular transition to lower vapor quality and the Stratified-Wavy transition to lower mass flux. New model matched well with data from the literature.
Rollman and Spindler [116]	Flow regime was mapped and heat transfer coefficient was measured for R134a in one 8.8mm ID internally-grooved tube. A new flow regime map was developed.
Sharar and Bar-Cohen [64]	Performed an extensive literature review of internally-grooved tube studies since 2004 with a focus on identifying the relationship between flow regime transition and thermal enhancement.
Sharar and Bar-Cohen [80]	Flow regime was mapped and heat transfer coefficient was measured for a smooth and grooved tube. New heat transfer coefficient correlation was introduced based on previous flow regime map [29]. Model matched well with current results and data from 3 independent researchers.

Nozu and Honda [106] and Honda, Wang, and Nozu [107] recognized the dependence of heat transfer on the particular flow regime and, as such, developed Annular and Stratified flow models for condensing heat transfer in internally-grooved tubes. Wang, Honda, and Nozu [108] later modified the previous condensation models to account for interfacial shear stresses during Annular flow and curvature of the condensate film during Stratified flow due to surface tension forces. Around the same time, Mori et al. [109] proposed a Stratified flow model for evaporation in internally-grooved tubes. The model assumed a thin film on the upper portion of the tube and a thick Stratified liquid layer on the bottom portion due to gravity. Mori et al. [109] compared their heat transfer model to

10 correlations available in the literature and experimental data for nine refrigerants and 26 tubes and found that their correlation had the best agreement with a mean absolute error of 19% for the entire dataset. Momoki et al. [113] later extended the Mori et al. [109] model and classified four heat transfer regimes: Annular flow, Annular flow with a liquid meniscus, separated flow with a liquid meniscus, and separated flow with a dry surface, and proposed empirical correlations for flow regime transitions. They compared their correlation to experimental data and showed that their regime-informed correlation outperformed correlations available in the literature.

Honda and Wang [110] modified the condensation Stratified model of Honda, Wang, and Nozu [107] using the newly-developed Stratified evaporation flow model of Mori et al. [109] and found reasonable agreement with data in the literature. The agreement was good for low mass flux and vapor where Stratified flow would be expected but poorly predicted heat transfer coefficients at high mass flux and vapor quality where Annular flow would be expected. Additionally, the model did not account for the contribution of nucleate boiling. In response, Makishi et al. [111] developed a new theoretical model for Stratified and Annular flow in internally-grooved tubes that considered the effect of nucleate boiling and forced convection. A modified version of the Kattan et al. [47] Stratified to Annular transition was used to predict the weighted average heat transfer coefficient in the intermediate region. The predictions of the new theoretical models and previously proposed empirical models by Koyama et al. [92], Murata [89], Thome et al. [91], Cavallini et al. [117], Yun et al. [90], and Mori et al. [109] were compared to available experimental data for ten internally-grooved tubes and four refrigerants. The model developed to account for the dependence of flow regime had smaller RMS errors than the

empirical models. However, the RMS error of the theoretical model was still fairly high, at 22.4% to 25.7%.

Finally, Wang et al. [112] modified the previous Makishi et al. [111] model to account for local heat transfer enhancement due to disturbance waves in internally-grooved tubes and compared the model to data from the literature. Reasonably good agreement was found but improvement is needed if they are to be used as a general prediction and design tool. Specifically, the Wang et al. [112] model uses the dimensionless liquid Froude number to distinguish between Stratified and Annular flow. Unfortunately, the liquid Froude number is not sufficient for determining the transition from Stratified to non-stratified flow [105]. Additionally, the model does not account for Dryout or the effect of Intermittent flow. Thus, a comprehensive tool similar to the coupled flow regime map and heat transfer coefficient correlation of Wojtan et al. [30] [31] needs to be developed for internally-grooved tubes.

In an attempt to answer this call, Liebenberg, Thome, and Meyer [118] observed and described flow regimes and heat transfer during condensation in horizontal internally-grooved tubes. They modified the Intermittent to Annular transition on the Thome map [119] and developed new semi-empirical flow regime based heat transfer and pressure drop correlations. The modification shifted the Intermittent to Annular transition to lower vapor quality, a trend apparent from the previous discussion, and greatly improved the predictive accuracy of condensing flow in internally-grooved tubes. Unfortunately, flow boiling is not fully analogous to condensation [120] and the flow regime maps and associated heat transfer models developed for condensation cannot be strictly used for flow boiling. For example, Liebenberg et al. [114] did not report early transition from Stratified to Annular

flow during condensation in internally-grooved tubes. As shown in the preceding discussion, this is a dominant trend during flow boiling. In addition, nucleate boiling, Stratified flow with a completely dry upper surface, and dryout do not occur for condensation.

Thus, research is progressing in the proper direction but, as of yet, a coupled flow regime map and heat transfer coefficient correlation for flow boiling in internally-grooved tubes have not been developed. A stronger experimental and theoretical knowledge base needs to be established, focusing on a more comprehensive understanding of the physical mechanisms responsible for improved performance in internally-grooved tubes.

3.5 Summary

The preceding has presented a survey of two-phase flow boiling studies in internally-grooved tubes. The vast majority of the discussion dealt with halogenated fluids in conventional sized tubes at standard temperature and pressure. Studies of small diameter tubes, alternative refrigerants, refrigerant/oil mixtures, and elevated reduced pressure were also considered. Additionally, existing flow regime maps and regime-informed heat transfer coefficient correlations for internally-grooved tubes were discussed. Through this process, parametric trends have been identified and goals for the current research effort have been developed.

In meso-scaled (i.e. “conventional”) internally-grooved tubes, heat transfer enhancement generally exceeded the area enhancement at low mass flux by factors of 3-7 times a plain tube, but decreased to the area enhancement at high mass flux, yielding improvement of just 1.3-1.8 times a plain tube. This trend is summarized in Table 3 and displayed in Figure 9 and Figure 10. It was shown that this performance enhancement at

low mass flux can be correlated to early transition to Annular flow in internally-grooved tubes, for conditions in which smooth tubes were operating in Stratified flow. However, at high mass flux where the smooth and internally-grooved tubes are both operating in Annular flow, the enhancement decreased towards the area enhancement. It is argued that this early transition in internally-grooved tubes is primarily a result of fluid flow redirection from axial to helical flow (momentum change), augmented by favorable capillary force in the groove structures. Minor deviations from these parametric trends were observed, such as enhancement factors larger or smaller than the area ratio at high mass flux, and may be a result of the particular geometric parameters for the various internally-grooved tubes tested, turbulence, or nucleate boiling. The trends are less clear for refrigerants and CO_2 at high reduced pressure.

The study of small internally-grooved tubes is still in its infancy and the experimental studies available are not sufficient to draw clear trends or conclusions regarding the impact of flow regime on heat transfer performance. Specifically, the available studies generally tested mass fluxes above 190 kg/m²s where the hypothesized benefit of early transition from Stratified to Annular flow, with significant enhancement in the heat transfer coefficient, at low mass flux is not achievable. However, in a fashion similar to larger diameter tubes, small diameter internally-grooved tubes demonstrated enhancement close to the internal area ratio at high mass fluxes due to the prevalence of Intermittent and Annular flow.

The Wojtan et al. [30] flow regime map proved useful for predicting flow regimes in the smooth channel studies reported above. However, due to observed early transition to Annular flow at lower mass flux and vapor quality, the Wojtan et al. [30] map, and

Mastrullo et al. [54] map, had diminished predictive accuracy for the internally-grooved tube experimental data. Furthermore, many researchers reported poor agreement with the most widely used heat transfer coefficient correlations for internally-grooved tubes because they are either: a) empirical and do not account for flow regime or b) assume a fixed flow regime, such as Annular flow, and are unable to universally predict heat transfer.

Based on these findings, research objectives and guidelines have been identified that will provide a more comprehensive understanding of the physical mechanisms responsible for improved performance in internally-grooved tubes:

a. Concurrent heat transfer and quantitative flow regime data will be collected over a wide range of operating conditions, particularly low mass flux, to establish the intrinsic relationship between the dominant flow structure and thermofluid performance in internally-grooved tubes. Additionally, comparison to existing correlations, flow regime maps, and smooth tube data as a means to normalize the results will accompany all experiments to determine the current state of internally-grooved tube predictive methods.
b. The majority of the studies in the literature relied solely on subjective flow regime data collection, which calls into question the accuracy of the results. The current study will focus on an objective Total Internal Reflection (TIR) flow regime determination method to obtain more accurate data.
c. The study of small diameter internally-grooved tubes has only been a topic of research since 2006 and, as such, the available experimental data set is incomplete. Therefore, the current effort aims to test both conventional

tubes and extend the small diameter data to a wider range of refrigerants and operating conditions.

d. The eventual goal of the current research effort is to develop a physics-based heat transfer model that represents the impact of two-phase flow structures and is coupled to a reliable flow regime map [105]. Based on the above research initiatives, a stronger experimental and theoretical knowledge base will be established, focusing on a more comprehensive understanding of the physical mechanisms responsible to improved performance in internally-grooved tubes.

Though outside the scope of the current effort, several additional conclusions and recommendations for future internally-grooved tube research have been identified based on the preceding literature review and analysis:

a. It is not entirely clear what impact operation of refrigerants and CO_2 at high reduced pressure has on flow regimes and heat transfer in internally-grooved tubes. Future studies should be conducted with a focus on items 'a' and 'b' above.

b. Researchers have observed performance discrepancies for identical test conditions but variable tube groove parameters. Therefore, a more systematic study of the effect of tube diameter, fin shape, fin height, number of fins, helix and apex angle, and ratio of relevant parameters needs to be undertaken to determine the relationship between these parameters, flow regime, and thermofluid performance, and what constitutes a geometrically-optimum tube for given operating conditions.

Greater detail on the analytical and experimental research plan, including specifics on the breadth of work necessary to achieve items ‘a’ through ‘d’ above, are described in the following chapters.

Chapter 4: New Flow Regime Map and Heat Transfer Coefficient Correlation for Internally-Grooved Tubes

Heat transfer enhancement in internally-grooved tubes is related to early transition to Annular flow at relatively low mass flux and vapor quality, where a comparable smooth tube is expected to operate in Stratified or Intermittent flow. As such, the capability to accurately predict this early transition to Annular flow for a range of tube diameters is critical to predicting the improved performance in internally-grooved tubes. As shown in the previous chapter, the original formulations by Wojtan et al. [30] for transition from Intermittent to Annular and Stratified to Annular flow are adequate for predicting flow regime in smooth channels for a range of fluids and operating conditions, however, they are not sufficient for predicting flow regimes in internally-grooved tubes. Therefore, this chapter gives a description of the original Wojtan et al. [30] [31] formulation and outlines current modifications to the existing flow regime map and regime-based heat transfer coefficient correlation to better reflect the trends described in Chapter 3. Lastly, the new model is simulated through a range of operating conditions to verify that it accurately captures the trends previously described, namely 3-7x improvement at low-to-moderate mass flux.

4.1 Taitel-Dukler [46] Annular Transition Criteria

The Wojtan et al. flow regime map [30] is a modification of the Taitel-Dukler [46] flow regime map. Thus, understanding the Annular flow transition mechanisms outlined by Taitel-Dukler [46] is a logical starting point for understanding the Wojtan et al. [30] flow regime map. Taitel-Dukler [46] expressed the Stratified to Annular transition in terms

of inertial effects using two-phase non-dimensional groupings. As shown in Figure 15, the transition to Annular flow can be described using the modified Froude number (F), non-dimensional Z parameter (Z), and non-dimensional liquid height (h_L/D), where h_L is the Stratified liquid height and D is the channel diameter. The Froude number and Z parameter represent transition 'F' and transition 'Z' on Figure 15, respectively.

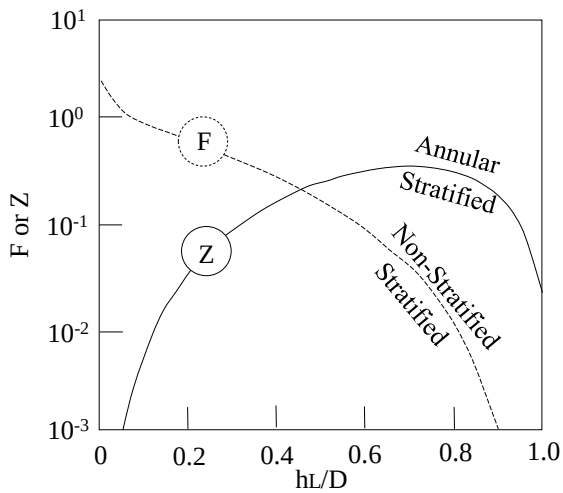

Figure 15: Generalized transition boundaries in Taitel-Dukler model (adapted from [46])

The first inertial effect to consider, as described by the Froude number, is the stability of the Stratified flow due to the Kelvin-Helmholtz instability. Assuming a stationary wave on the Stratified liquid interface, two forces can be identified: gravity force tends to flatten the wave and stabilize the Stratified configuration while the Bernoulli force, due to the increased gas velocity and associated pressure decrease above the interface, tends to increase the wave amplitude. If the Bernoulli force is large enough to overcome the gravity force, the wave will wet the dry upper surface of the channel. A force balance results in a dimensionless Froude number modified by the density ratio as shown in Equation (3):

$$F = \left(\frac{\rho_g}{\rho_L - \rho_g}\right)^{1/2} \frac{u_{gs}}{\sqrt{Dg\cos\beta}} \tag{3}$$

where ρ_g is the vapor density, ρ_L is the liquid density, u_{gs} is the superficial gas velocity, D is the channel diameter, g is the acceleration of gravity, and β is the tube inclination.

The second transition criterion is attributed to the impingement of liquid droplets on the top surface, which are torn away from the Stratified liquid-vapor interface. In this case, transition to Annular flow will occur when liquid droplets have enough kinetic energy to reach the top of the channel. Calculation of the liquid droplet trajectory is related to the maximum turbulent velocity fluctuations as estimated by Barnea et al. [121]. The criterion for Annular flow becomes:

$$u_L^2 = \frac{gD\left(1 - \frac{h_L}{D}\right)\cos\beta}{f_L} \tag{4}$$

where u_L^2 is the liquid velocity and f_L is the liquid friction factor. This transition criterion can be represented in dimensionless form as the Z parameter:

$$Z = \frac{(dp/dx)_{Ls}}{\rho_L g\cos\beta} \tag{5}$$

where $(dp/dx)_{Ls}$ is the pressure drop when the tube is completely filled with liquid. The non-dimensional transition criteria can also be expressed in terms of superficial liquid and vapor velocities.

The full description of the sequence of tests for iteratively calculating flow regime for the Taitel-Dukler maps is not included here, for the sake of brevity, but please refer to [46] for a more comprehensive explanation.

4.2 Traditional Wojtan et al. [30] Flow Regime Map for Smooth Tubes

The Taitel-Dukler [46] map requires complex calculations (and an iterative process) and is not coupled to a reliable flow regime based heat transfer model. This limits its practical applicability. The Wojtan et al. [30] flow regime map, on the other hand, can be implemented with simple calculations and has an accompanying comprehensive flow pattern based heat transfer model; more detail on the Wojtan et al. [31] regime based heat transfer model will be described in Section 4.4. For these perceived benefits, the Wojtan et al. [30] map for smooth tubes (and heat transfer coefficient correlation [31]) will be used as a starting point for analytically describing and mapping early flow regime transition to Annular flow in internally-grooved tubes. For the sake of completeness, the entire Wojtan et al. [30] flow regime transition criteria will be described below. Refer to Figure 16 for a graphical representation of the original smooth tube Wojtan et al. [30] flow regime map.

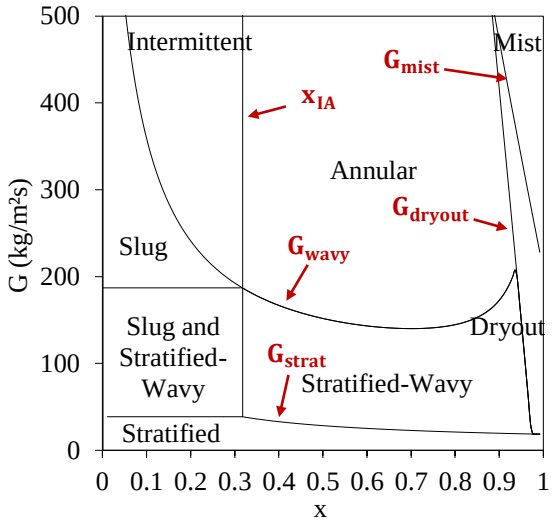

Figure 16: Traditional smooth tube Wojtan et al. [30] diabatic flow regime map for evaporation of R134a at -15ºC in a 9mm smooth tube with a heat flux of 4 kW/m²

As shown on Figure 16, the Wojtan et al. [30] map consists of five governing equations to represent the loci of flow regime transition; G_{strat}, G_{wavy}, x_{IA}, G_{dryout}, and

G_{mist}. In order to calculate these transition curves the following three dimensionless geometric variables must first be defined:

$$h_{LD} = 0.5\left(1 - \cos\left(\frac{2\pi - \theta_{dry}}{2}\right)\right) \tag{6}$$

$$A_{VD} = \frac{A\varepsilon}{D^2} \tag{7}$$

$$A_{LD} = \frac{A(1-\varepsilon)}{D^2} \tag{8}$$

As shown in Figure 17, h_{LD} is the dimensionless vertical height of the liquid, A is the total cross-sectional area of the tube, A_{VD} is the dimensionless cross-sectional area occupied by the vapor phase, A_{LD} is the dimensionless cross-sectional area occupied by the liquid, and D is the internal tube diameter.

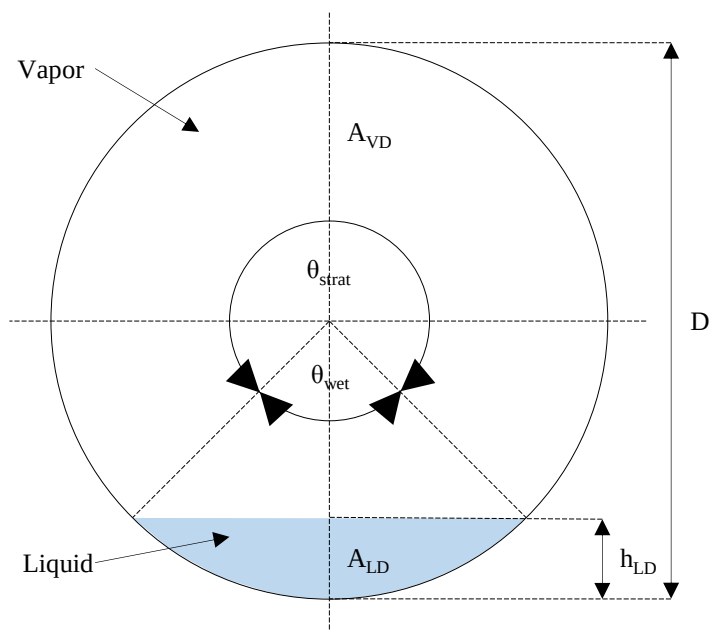

Figure 17: Two-phase Stratified flow cross-section (adapted from [30])

ε is the void fraction calculated using the Steiner version of the Rouhani-Axelsson drift flux model for horizontal tubes [122]. This drift flux model, as opposed to the method employed by Taitel-Dukler [46], is easy to implement and provides void fraction as a

function of mass flux and vapor quality. The applicability of this model was proven by Wojtan et al. [123] by optically measuring dynamic void fractions in Stratified types of flow with R-22 and R-410A as the working fluids. θ_{strat} is an approximation of the Stratified angle as described by Biberg [124] and θ_{wet} is simply θ_{strat}-2π. These terms can be directly evaluated as:

$$\varepsilon = \frac{x}{\rho_V}\left[\left(1 + 0.12(1-x)\right)\left(\frac{x}{\rho_V} + \frac{1-x}{\rho_L}\right) + \frac{1.18(1-x)[g\sigma(\rho_L - \rho_V)]^{0.25}}{G\rho_L^{0.5}}\right]^{-1} \tag{9}$$

$$\theta_{strat} = 2\pi - 2\left\{\pi(1-\varepsilon) + \left(\frac{3\pi}{2}\right)^{\frac{1}{3}}\left[1 - 2(1-\varepsilon) + (1-\varepsilon)^{\frac{1}{3}} - \varepsilon^{\frac{1}{3}} - \frac{1}{200}(1-\varepsilon)\varepsilon[1-2(1-\varepsilon)][1+4((1-\varepsilon)^2+\varepsilon^2]\right]\right\} \tag{10}$$

where x is the vapor quality, G is the mass flux, σ is the fluid surface tension, g is gravitational acceleration, ρ_V is the vapor density, and ρ_L is the liquid density.

After the geometric parameters have been calculated, the Stratified-Wavy to Intermittent/Annular transition curve (labeled as G_{wavy} on Figure 16) can be calculated from the following equation:

$$G_{wavy} = \left\{\frac{16A_{VD}^3 gD\rho_L\rho_V}{x^2\pi^2(1-(2h_{LD}-1)^2)^{0.5}} \times \left[\frac{\pi^2}{25h_{LD}^2} \times \left(\frac{We}{Fr}\right)_L^{-1} + 1\right]\right\}^{0.5} + 50 \tag{11}$$

where G_{wavy} is the mass flux at which transition occurs, We is the liquid Weber number, and Fr is the liquid Froude number. It's interesting to note that the Weber number is a measure of the relative importance of a fluid's inertia to its surface tension and is useful for analyzing the formation of droplets in multiphase flows. Additionally, the Froude

number is defined as the ratio of a body's inertia to gravity forces and, in two-phase flows, is useful for describing wave formation. Thus, the physical mechanisms described by the Wojtan et al. [30] G_{wavy} transition from Stratified to Annular flow are consistent with those described by Taitel-Dukler and outlined in Section 4.1 above.

The Stratified to Stratified-Wavy transition (labeled as G_{strat} on Figure 16) is calculated from:

$$G_{strat} = \left[\frac{226.3^2 A_{LD} A_{VD}^2 \rho_V (\rho_L - \rho_V) \mu_L g}{x^2 (1-x) \pi^3}\right]^{\frac{1}{3}} \tag{12}$$

The Intermittent to Annular transition (labeled as x_{IA} on Figure 16) is calculated from:

$$x_{IA} = \left\{\left[0.34^{\frac{1}{0.875}} \left(\frac{\rho_V}{\rho_L}\right)^{\frac{-1}{1.75}} \left(\frac{\mu_L}{\mu_V}\right)^{\frac{-1}{7}}\right] + 1\right\}^{-1} \tag{13}$$

The Annular to Dryout and Dryout to Mist (labeled as G_{dryout} and G_{mist} on Figure 16, respectively) are empirically-modified from the dryout inception-completion model of Mori et al. [125]:

$$G_{dryout} = \left[\frac{1}{0.235}\left(\ln\left(\frac{0.58}{x}\right) + 0.52\right)\left(\frac{D}{\rho_v \sigma}\right)^{-0.17} \times \left(\frac{1}{gD\rho_v(\rho_L - \rho_v)}\right)^{-0.37} \left(\frac{\rho_v}{\rho_L}\right)^{-0.25} \left(\frac{q}{q_{crit}}\right)^{-0.70}\right]^{0.926} \tag{14}$$

$$G_{mist} = \left[\frac{1}{0.0058}\left(\ln\left(\frac{0.61}{x}\right) + 0.57\right)\left(\frac{D}{\rho_v \sigma}\right)^{-0.38} \times \left(\frac{1}{gD\rho_v(\rho_L - \rho_v)}\right)^{-0.15} \left(\frac{\rho_v}{\rho_L}\right)^{0.09} \left(\frac{q}{q_{crit}}\right)^{-0.27}\right]^{0.943} \tag{15}$$

where q is the applied heat flux (at the inside surface of the tube) and q_{crit} is the critical heat flux as described by Kutateladze [126]:

$$q_{crit} = 0.131\rho_v^{0.5} h_{LV}[g(\rho_L - \rho_v)\sigma]^{0.25} \quad (16)$$

where h_{LV} is the latent heat of vaporization.

Once the main transition lines are calculated, further subdivisions at low vapor quality and high vapor quality, respectively, are made to better predict trends described by Wojtan et al. [30]. The subdivisions at low vapor quality are described below and shown on Figure 16:

a. If $G > G_{wavy}(x_{IA})$ and $< G_{wavy}(x)$, the flow regime becomes Slug.

b. If $G_{strat} < G < G_{wavy}(x_{IA})$ and $x < x_{IA}$, the flow regime becomes Slug and Stratified-Wavy.

c. If $G_{strat} < G < G_{wavy}(x_{IA})$ and $x \geq x_{IA}$, the flow regime is the Stratified-Wavy zone.

d. If $x < x_{IA}$, $G_{strat} = G_{strat}(x_{IA})$.

The subdivisions to describe dryout and mist conditions at high vapor quality are as follows:

a. If $G_{strat}(x) \geq G_{dryout}(x)$, then $G_{dryout}(x) = G_{strat}(x)$.

b. If $G_{wavy}(x) \geq G_{dryout}(x)$, then $G_{dryout}(x) = G_{wavy}(x)$.

c. If $G_{dryout}(x) = G_{mist}(x)$ (which is possible at low heat flux and high mass velocity) then $G_{dryout}(x) = G_{mist}(x)$.

4.3 Modified Sharar et al. [29] Flow Regime Map for Internally-Grooved Tubes

As described in great detail in Chapter 2 and Chapter 3, the Wojtan et al. [30] flow regime methodology works particularly well for predicting refrigerant evaporation in conventionally-size smooth tubes. However, as evident by the early flow regime

transitions in internally-grooved tubes and the efforts to modify existing flow regime maps to account for these variations [111] [118], smooth tube flow regime maps do not accurately predict flow regimes in internally-grooved tubes. In addition to the inertial and surface tension effects discussed above, it is suggested in the literature that the capillary force in the groove structures [111] [110] [84], as well as fluid flow redirection from an axial direction to a direction following the helix angle of the groove (momentum change) [27], play a favorable role in transitioning from Stratified and Intermittent flow to Annular flow.

In order to better capture these trends for evaporative two-phase flow, Sharar et al. [29] recently modified the existing Wojtan et al. [30] flow regime map by adopting the Liebenberg et al. [118] and Liebenberg and Meyer [114] Intermittent to Annular transition criteria and modifying the existing Stratified to Annular transition. The modified Intermittent to Annular transition is defined by:

$$x_{IA} = \left\{\left[C\left(\frac{\rho_L}{\rho_V}\right)^{0.5}\left(\frac{\mu_V}{\mu_L}\right)^{0.1}\right]^{1/0.9} + 1\right\}^{-1} \tag{17}$$

where μ_L is the liquid viscosity, μ_V is the vapor viscosity, ρ_L is the liquid density, ρ_V is the vapor density, and C is the transition coefficient. For smooth tubes, C=0.3218 and for internally-grooved tubes C=0.6678 [114]. The modified Stratified-Wavy to Annular transition was defined by Sharar, Jankowski, and Bar-Cohen [29]:

$$G_{wavy\ IG} = \left\{\frac{16A_{VD}^3 g D \rho_L \rho_V}{x^2\pi^2(1-(2h_{LD}-1)^2)^{0.5}} \times \left[\frac{\pi^2}{25h_{LD}^2} \times \left(\frac{We}{Fr}\right)_L^{-1} + 1\right]\right\}^{0.5} - 15 \tag{18}$$

where $G_{wavy\ IG}$ is the mass flux at which transition occurs, A_{VD} is the dimensionless cross-sectional area occupied by the vapor phase, g is gravitational acceleration, D is the internal tube diameter, x is the vapor quality, h_{LD} is the dimensionless vertical height of the liquid,

We is the liquid Weber number, and Fr is the liquid Froude number. In practice, Equations (17) and (18) replace Equations (11) and (13) in the original formulation; all other equations remain the same.

Figure 18 shows the original and modified Sharar et al. [29] flow regime maps for R134a at -15ºC in a 9 mm diameter tube; Figure 18a is the original smooth tube map proposed by Wojtan et al. [30] and Figure 18b is the modified Sharar et al. [29] flow regime map for a comparable internally-grooved tube. Both maps define 8 distinct flow regimes: Stratified, Stratified-Wavy, Slug and Stratified-Wavy, Slug, Intermittent, Annular, Dryout, and Mist in coordinates of mass flux (G) and quality (x). The modified map reflects early transition to Annular flow at lower vapor quality and lower mass flux compared to a smooth tube.

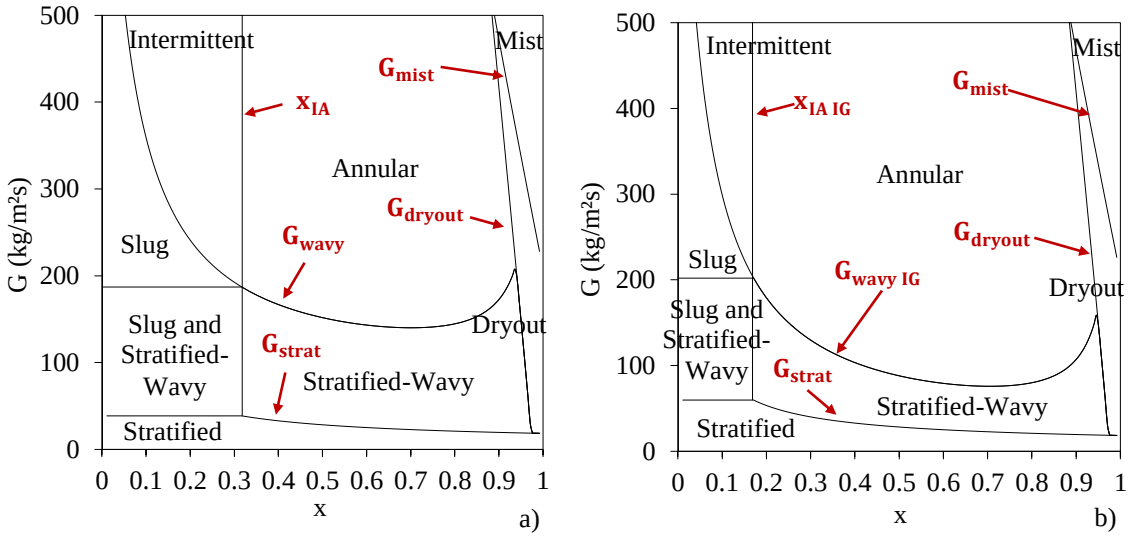

Figure 18: a) Traditional smooth tube Wojtan et al. [30] and b) modified Sharar et al. [29] internally-grooved tube diabatic flow regime map for evaporation of R134a at -15ºC in 9mm tubes with a heat flux of 4 kW/m²

4.4 Traditional Wojtan et al. [31] Heat Transfer Coefficient Correlation

The Wojtan et al. [31] heat transfer coefficient correlation will be used as a starting point for analytically describing enhanced heat transfer in internally-grooved tubes

associated with early transition to Annular flow. Wojtan et al. [31] modified the regime-based heat transfer model of Kattan, Thome, and Favrat [62] using the flow regime map described in Section 4.2 and shown in Figure 16 and Figure 18a. This model improved heat transfer prediction during Stratified-Wavy flow, and extended the applicability to high vapor quality and heat flux where Dryout and Mist flow can occur. The model also considers the effects of flow regime on the Annular film thickness, turbulence, nucleate boiling, and the dry perimeter during Stratified flows in smooth tubes to calculate the local heat transfer coefficient.

During Stratified, Stratified-Wavy, and Annular flow with partial dryout, at least a portion of the tube is cooled by vapor at the top surface. Therefore, they proposed the following equation to calculate the heat transfer coefficient as the average of the dry and wet surfaces:

$$h_{tp} = \frac{\theta_{dry} h_v + (2\pi - \theta_{dry}) h_{wet}}{2\pi} \tag{19}$$

where h_{tp} is the two-phase heat transfer coefficient, θ_{dry} is the dry angle (from 0 to 2π), and h_v is the heat transfer coefficient associated with vapor flow on the dry perimeter. The dry perimeter heat transfer coefficient is expressed in terms of the vapor thermal conductivity, k_v, vapor Reynolds number, Re_v, and vapor Prandtl number, Pr_v:

$$h_v = 0.023 Re_v^{0.8} Pr_v^{0.4} \frac{k_v}{D} \tag{20}$$

h_{wet} is the heat transfer coefficient for the wet perimeter. Wojtan et al. [31] use an asymptotic model accounting for the effect of convective vaporization and nucleate boiling:

$$h_{wet} = [(h_{cb})^3 + (h_{nb})^3]^{\frac{1}{3}} \tag{21}$$

The convective vaporization heat transfer coefficient, h_{cb}, is calculated based on the predicted film thickness, δ, fluid thermal conductivity, k_L, liquid film Reynolds number, Re_δ, and liquid Prandtl number, Pr_L:

$$h_{cb} = 0.0133 Re_\delta^{0.69} Pr_L^{0.4} \frac{k_L}{\delta} \tag{22}$$

The nucleate boiling heat transfer coefficient, h_{nb}, is calculated from a slightly modified version of the Cooper correlation [127] :

$$h_{nb} = S \times 55 (Pr)^{0.12} (-\log Pr)^{-0.55} M^{-0.5} q^{0.67} \tag{23}$$

where M is the fluid molar mass, q is the heat flux, and S is a suppression factor of 0.8 proposed by Wojtan et al. [31] to better match their experimental data; the degree of improvement obtained by applying the suppression factor was not quantified by Wojtan et al. [31].

The parameter which takes into account the flow regime in Equation (19) is the dry angle, θ_{dry}, as shown schematically in Figure 17; The original formulation by Kattan, Thome, and Favrat [62] assumed a linear variation in the wetted perimeter between Stratified and Annular flow. However, Wojtan et al. [31] found that the complexity resulting from subdivisions of Stratified-Wavy flow regimes requires a different approach to calculating dry angle.

For Slug, Intermittent, and Annular flow where the entire perimeter of the channel is covered with a continuous thick or thin layer of liquid, the dry angle is 0:

$$\theta_{dry} = 0 \tag{24}$$

For Stratified-Wavy flow, Wojtan et al. [31] proposed a modified version of the El Hajal et al. [128] model which used a quadratic interpolation to calculate θ_{dry}. An exponent of 0.61 showed best agreement with the data from Wojtan et al. [31]:

$$\theta_{dry} = \left[\frac{(G_{wavy}-G)}{(G_{wavy}-G_{strat})}\right]^{0.61} \theta_{strat} \tag{25}$$

where θ_{strat} is an approximation of the stratified angle as described by Biberg [124], shown in Figure 17, and expressed in Equation (10). Quantitative measures of 'improvement' obtained by adopting the new exponent of 0.61 were not provided by Wojtan et al. [31].

In the Slug and Stratified-Wavy region, it is possible to have both low amplitude waves with a dry upper surface and liquid Slugs that completely wet all surfaces of the tube. As vapor quality increases for a fixed mass flux, the frequency of Slugs decreases and Stratified-Wavy flow becomes the dominant regime. As the vapor quality approaches x_{IA}, slugs disappear completely [30]. To capture this trend Wojtan et al. [31] proposed the following dry angle correlation when $x < x_{IA}$:

$$\theta_{dry} = \frac{x}{x_{IA}}\left[\frac{(G_{wavy}-G)}{(G_{wavy}-G_{strat})}\right]^{0.61} \theta_{strat} \tag{26}$$

Based on the dry angle, the liquid film thickness is calculated using the equation by El Hajal et al. [128]:

$$\delta = \frac{D}{2} - \sqrt{\left(\frac{D}{2}\right)^2 - \frac{2A_L}{(2\pi-\theta_{dry})}} \tag{27}$$

When/if Equation (27) gives a value larger than $D/2$, δ is set to $D/2$ because a symmetric film thickness larger than the tube radius is geometrically impossible.

The model of Kattan et al. [62] did not cover Mist flow or Dryout due to a lack of experimental data at the time. Wojtan et al. [31] collected heat transfer data and modified the Groeneveld Mist flow correlation [129] which is a modification of the Dougall-

Rohsenow Mist flow correlation [130]. The Dougall-Rohsenow Mist flow correlation [130] takes the form:

$$h_{mist} = 0.023 Re_H^{0.8} Pr_v^{0.4} \frac{k_v}{D} \tag{28}$$

where Re_H is the homogeneous Reynolds number:

$$Re_H = \frac{GD}{\mu_v}\left(x + \frac{\rho_L}{\rho_v}(1 - x)\right) \tag{29}$$

Groeneveld [129] determined that the homogeneous Reynolds number described by Dougall-Rohsenow [130] was not consistent with homogenous theory because vapor and liquid properties were used rather than homogeneous properties. Therefore, Groeneveld [129] proposed a correction factor, Y, to be used in calculating $h_{mist}$and defined it as:

$$Y = 1 - 0.1\left[\left(\frac{\rho_L}{\rho_v} - 1\right)(1 - x)\right]^{0.4} \tag{30}$$

Groeneveld [129] used data obtained from experiments with water as the working fluid at high mass fluxes, >700 kg/m²s, high saturation pressures, >34 bar, and high heat fluxes, >120 kW/m², to modify Equation (28), using the proposed correction factor, Y, with an exponent of -1.5, altering the exponents on the Reynolds and Pradtl numbers, and introducing a vastly lower value of the empirical coefficient to yield:

$$h_{mist} = 0.00327 Re_H^{0.901} Pr_v^{1.32} Y^{-1.5} \frac{k_v}{D} \tag{31}$$

Wojtan et al. [31] further modified the empirical coefficients in the Groeneveld [129] correlation based on their experimental results to yield Equation (32) below.

$$h_{mist} = 0.0117 Re_H^{0.79} Pr_v^{1.06} Y^{-1.83} \frac{k_v}{D} \tag{32}$$

Wojtan et al. [31] compared Mist flow heat transfer results for R-22 and R-410A in a 13.84mm test section with the correlations from Dougall-Rohsenow [130], Groeneveld

[129], and the new Mist flow correlation in Equation (32). They reported that the values predicted by the Dougall-Rohsenow [130] correlation were considerably higher than their experimental results. The Groeneveld [129] correlation, which was empirically optimized based on experimental results for high mass fluxes, saturation pressures, and heat fluxes with water as the working fluid, had an average deviation, $\bar{\varepsilon}$, mean absolute deviation, $|\bar{\varepsilon}|$, and standard deviation, σ, of 13.6%, 9.0%, and 10.7%, respectively. Much better agreement was shown for the re-optimized Groeneveld [129] correlation described by Wojtan et al. [31]; the average deviation, $\bar{\varepsilon}$, mean absolute deviation, $|\bar{\varepsilon}|$, and standard deviation, σ, for all experimental data points was only -0.04%, 6.31%, and 8.32%, using the new re-optimized model, respectively. Additionally, the new Mist flow model predicted 93% of the experimental R-22 and R-410A results to within ±15% error.

Wojtan et al. [31], based on the original formulation by Mori et al. [125], showed that the heat transfer coefficient falls sharply from the two-phase heat transfer coefficient at the dryout inception vapor quality, x_{di}, to the Mist flow heat transfer coefficient at the dryout completion vapor quality, x_{de}. Therefore, they proposed a Dryout flow correlation based on linear interpolation between dryout inception and dryout completion as expressed by:

$$h_{dryout} = h_{tp}(x_{di}) - \frac{x - x_{di}}{x_{de} - x_{di}}\left[h_{tp}(x_{di}) - h_{mist}(x_{de})\right] \tag{33}$$

where $h_{tp}(x_{di})$ is the two-phase heat transfer coefficient at x_{di}, as calculated from Equation (19), and $h_{mist}(x_{de})$ is the Mist flow heat transfer coefficient at x_{de}, as calculated from Equation (32). x_{di} and x_{de} can be calculated directly from the following equations:

$$x_{di} = 0.58e^{\left[0.52 - 0.235 We_V^{0.17} Fr_V^{0.37} \left(\frac{\rho_V}{\rho_L}\right)^{0.25} \left(\frac{q}{q_{crit}}\right)^{0.70}\right]} \tag{34}$$

$$x_{di} = 0.61e^{\left[0.57-5.8\cdot10^{-3}We_V^{0.38}Fr_V^{0.15}\left(\frac{\rho_V}{\rho_L}\right)^{-0.09}\left(\frac{q}{q_{crit}}\right)^{0.27}\right]} \quad (35)$$

where q_{crit} is the critical heat flux calculated by Kutateladze [126] in Equation (16).

The regime-informed heat transfer coefficient model described above was statistically compared to 413 experimental data points for R-22 flow boiling in the 13.84mm smooth tube at mass fluxes from 70 to 700 kg/m²s, heat fluxes from 2 to 57.5 kW/m², and vapor qualities from 0 to x_{di}. Additionally, 121 data points for Dryout and Mist flow, $x>x_{di}$, were collected to extend the experimental database and heat transfer methodology to higher vapor qualities and to serve as a basis for model comparison. The average deviation, $\bar{\varepsilon}$, mean deviation, $\bar{\varepsilon}$, and standard deviation, σ, of the data were calculated based on the original regime-based approach of Kattan, Thome, and Favrat [62] and the 'new' Wojtan et al. [31] model.

For vapor qualities from 0 to x_{di}, the original Kattan et al. [62] heat transfer coefficient had an average deviation, $\bar{\varepsilon}$, mean deviation, $|\bar{\varepsilon}|$, and standard deviation, σ, of 15.43%, 9.56%, and 14.26%, respectively. For the same conditions, the Wojtan et al. [31] improved the average deviation, $\bar{\varepsilon}$, mean deviation, $|\bar{\varepsilon}|$, and standard deviation, σ, to 2.48%, 6.83%, and 10.39%, respectively. For vapor qualities after dryout, $x>x_{di}$, the original Kattan et al. [62] heat transfer coefficient had an average deviation, $\bar{\varepsilon}$, mean deviation, $|\bar{\varepsilon}|$, and standard deviation, σ, of 913.24%, 725.30%, and 886.80%, respectively. After dryout ($x>x_{di}$), the Wojtan et al. [31] improved the average deviation, $\bar{\varepsilon}$, mean deviation, $|\bar{\varepsilon}|$, and standard deviation, σ, to 91.05%, 116.44%, and 155.59%, respectively. Wojtan et al. [31] correlated the relatively large, but still markedly improved, predictive error at high vapor quality in the dryout region to error in experimentally predicting vapor quality. For

example, a small error in predicting vapor quality can result in relative errors of 2000% due to the sharp slope of the heat transfer coefficient in this region [31]. Additional statistical analysis was provided in the PhD Thesis by Wojtan [131].

To enhance the credibility of the new model, Wojtan et al. [31] compared independent data from Lallemand et al. [132] for flow boiling of R-22 and R-407C in a smooth tube at mass fluxes from 100 to 300 kg/m²s and showed equally-good agreement. Statistical measures were not provided to quantify the agreement between the Lallemand et al. [132] data and the Wojtan et al. [31] model. Additionally, Chapter 2 (Figure 6) provides an additional qualitative example of the validity of the Wojtan et al. [30] flow regime map and associate heat transfer coefficient correlation [31] with more recent data from Filho and Jabardo [38].

4.5 Modified Heat Transfer Coefficient Correlation

In the current study, the Wojtan et al. [31] heat transfer coefficient described in Section 4.4 is modified to represent improved performance in internally-grooved tubes, particularly at low mass flux. A portion of this enhancement will originate from Equation (25) and Equation (26) whereby a modified (reduced) Stratified-Wavy to Annular transition, $G_{wavy\ IG}$, and Intermittent to Annular transition, $x_{IA\ IG}$, will result in a smaller dry angle, θ_{dry}, and a larger two-phase heat transfer coefficient, h_{tp}, in Equation (19). The remaining enhancement derives from an internally-grooved tube enhancement factor for single-phase turbulent flow, E_{rb}, (developed by Ravigururajan and Bergles [28]) and an empirically derived enhancement factor introduced by Thome et al. [91], E_{mf}, that accounts for the effects of film flow and the Gregorig effect. The turbulent enhancement factor, E_{rb}, can be expressed as:

$$E_{rb} = \left\{1 + \left[2.64 Re_{\delta}^{0.036} Pr_{L}^{-0.024} \left(\frac{e_f}{d_f}\right)^{0.212} \left(\frac{p_f}{d_f}\right)^{-0.21} \left(\frac{\alpha_f}{90°}\right)^{0.29}\right]^7\right\}^{1/7} \tag{36}$$

where e_f is the groove height, d_f is the nominal inside diameter at the fin base, p_f is the axial pitch from groove to groove, and α_f is the helix angle of the grooves. With this modification, h_{wet} from Equation (21) and Equation (19) becomes:

$$h_{wet} = E_{mf}[(E_{rb} h_{cb})^3 + (h_{nb})^3]^{\frac{1}{3}} \tag{37}$$

where E_{mf} is an additional enhancement factor proposed by Thome et al. [91] that accounts for the effects of film flow and the Gregorig effect. The Gregorig effect enhances evaporation by drawing liquid from the microfin tips towards the base as described by Carey [34]. The enhancement factor, E_{mf}, takes the form:

$$E_{mf} = 1.89 \left(\frac{\dot{m}}{\dot{m}_{ref}}\right)^2 - 3.7 \left(\frac{\dot{m}}{\dot{m}_{ref}}\right) + 3.02 \tag{38}$$

where $\dot{m}_{ref}$ is the maximum mass flux tested (500 kg/m²s). This was introduced to non-dimensionalize the expression.

Ravigururajan and Bergles [28] developed their model based on a broad collection of data from the literature. The data covered a wide range of Reynolds numbers (from 6000 to 440000), Prandtl numbers (from 0.66 to 37.6), and tube variables. Specifically, $\frac{e_f}{d_f}$ values from 0.01 to 0.218, $\frac{p_f}{d_f}$ values from 0.1 to 17.81, and $\frac{\alpha_f}{90°}$ values from 0.27 to 1 were used. Semi-circular, wire coils, rectangular, and triangular 'fin' shapes were compared to the model. The Ravigururajan and Bergles [28] correlation was found to accurately predict 99% of the data from the literature to within ±50% accuracy.

Ravigururajan and Bergles [28] performed independent experiments to further determine the applicability of the correlation. Water or air were used as the heat transfer

fluids for four commercially available tubes from General Atomic, Wolverine, and Turbo Refrigerating as well as four wire-coil tubes fabricated by the researchers. The normalized roughness heights, $\frac{e_f}{d_f}$, varied from 0.038 to 0.127, the normalized pitch, $\frac{p_f}{d_f}$, ranged from 0.169 to 1.05, and the normalized helix angle, $\frac{\alpha_f}{90°}$, ranged from 0.33 to 0.91. Reynolds numbers from 150 to 20000 were tested. The new correlation was 'in excellent agreement' with the heat transfer data for both air and water, although quantitative measures of statistical fit were not provided.

As shown in Equation (36) and also reported by Ravigururajan and Bergles [28], the increase in the augmentation was predominantly controlled by the tube design rather than the cooling liquid and flow parameters. This is evidenced by the very low powers of Re and Pr. This suggests that this correlation should generally work well for fluids and flowrates outside the range experimentally validated by Ravigururajan and Bergles [28].

Thome et al. [91] validated the use of the E_{mf} correlation with a statistical comparison of 362 local heat transfer coefficients for R-134a and R-123 with vapor qualities from 0.15 to 0.85. The standard deviation, mean deviation, and average deviation for the R-134a data was 18.5%, 12.8%, and 2.0%, respectively. The standard deviation, mean deviation, and average deviation for the R-123 data was 12.9%, 11.8%, and 6.4%. The authors indicated that future work should involve validation for a wider range of tube geometries and fluids.

4.6 Model Simulation

As previously described, internally-grooved tubes have shown heat transfer enhancement ratios as high as 6 to 7 times that of smooth tubes at low mass velocities and

improvement equal to, or slightly greater than, the internal area ratio, 1.3-1.8x that of a smooth tube, at high mass velocities [26] [17]. The goal of this section is to perform simulations of the above flow regime based heat transfer coefficient model with a range of operating conditions to determine if the updated model is capable of capturing these trends. This also provides examples to demonstrate how the physical model works.

Figure 19 and Figure 20 show flow regime maps and heat transfer coefficient modeling results for 8.84mm inside diameter smooth and internally-grooved tubes for HFE-7100 at 61°C with mass fluxes of 25, 50, 100, 150, 200, 250, and 300 kg/m²s and a heat flux of 4kW/m². Figure 19a and Figure 19b show the traditional Wojtan et al. [30] flow regime map and corresponding heat transfer coefficient [31], respectively, superimposed on the locus of mass fluxes described above. Figure 20a and Figure 20b show the modified Sharar et al. [29] flow regime map and corresponding heat transfer coefficient described in Section 4.3 and Section 4.5, respectively, superimposed with the same mass fluxes. The internally-grooved tube parameters used for this simulation are for the Wieland Cuprofin copper tube S2AD-952 described in Table 2; the simulated tube has 60-0.2mm tall fins with a helix angle of 18° and an area enhancement of 1.52.

As shown in Figure 19a and Figure 20a, the smooth and internally-grooved tube are predicted to operate in Slug, Intermittent, and Annular flow (before dryout occurs) for mass fluxes of 200, 250, and 300 kg/m²s. In these cases, the dry angle (θ_{dry}) is zero and the film thickness in Equation (22) is decreasing as the vapor quality increases. The result, as shown in Figure 19b and Figure 20b, is a monotonically increasing heat transfer coefficient with increasing vapor quality and internally-grooved tube enhancement ratios, (i.e. the internally-grooved tube heat transfer coefficient divided by the smooth tube heat

transfer coefficient) that approaches the area enhancement provided by the grooves. This is clear at the highest mass flux 300 kg/m²s and a moderate vapor quality of 0.5 where the internally-grooved tube has a heat transfer coefficient of 7428W/m²K and the smooth tube has a heat transfer coefficient of 3,599W/m²K; 7,428/3,599=2.06. It's important to note that as the mass flux decreases from 300 to 200 kg/m²s and below, the convective vaporization component of the two-phase heat transfer coefficient decreases because the Reynolds number value in Equation (22) is decreasing.

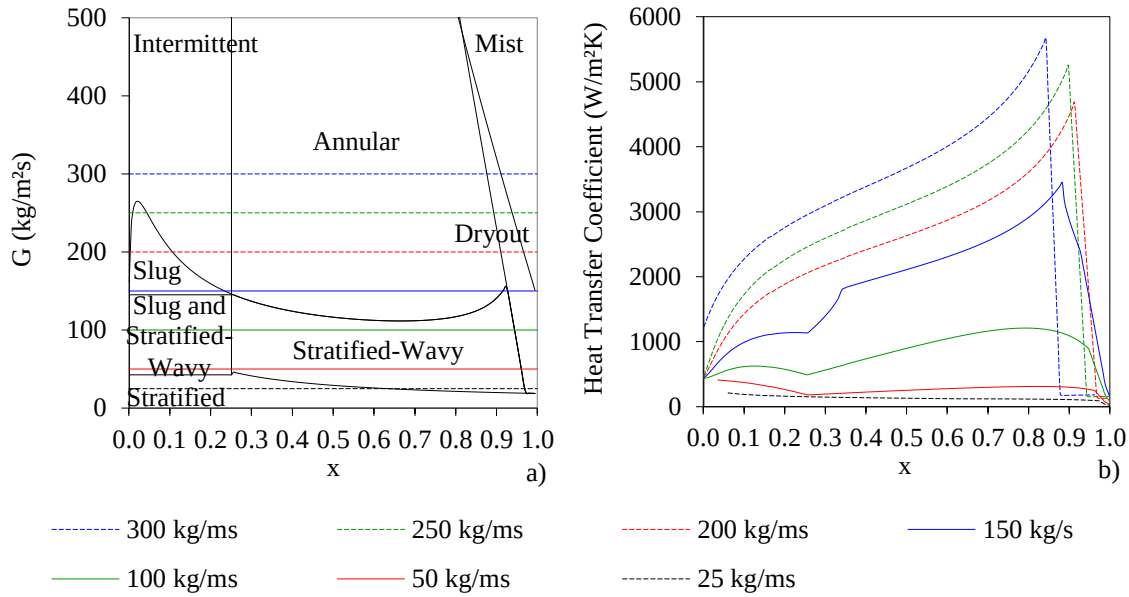

Figure 19: Modeling simulation results for a) original Wojtan et al. [30] flow regime map and b) associated heat transfer coefficient [31] in an 8.84mm smooth tube with HFE-7100 at 61°C and a heat flux of 4 kW/m²

At a mass flux of 150 kg/m²s and below, the results for smooth tube and internally-grooved tube begin to diverge. At a mass flux of 150 kg/m²s on Figure 19a, the smooth tube is operating in the Slug and Stratified-Wavy regime for vapor qualities from 0 to 0.23. For this case, the dry angle ranges from 0 to θ_{strat}, as dictated by Equation (26), and the two-phase heat transfer coefficient, given by Equation (19), decreases. Annular flow is

reached after a vapor quality of 0.23 and the dry angle is then zero. At this point, the smooth tube is operating in Annular flow and the heat transfer coefficient profile begins increasing monotonically. The internally-grooved tube shows a similar, yet slightly altered profile. Similar to the smooth tube, the internally-grooved tube begins operating in the Slug and Stratified-Wavy flow regime, the dry angle is non-zero, and the heat transfer coefficient remains low. However, because the Intermittent to Annular transition line is shifted to a lower vapor quality (Equation (17)), the internally-grooved tube reaches Annular flow at a lower vapor quality of 0.12 in Figure 20a. After this point, it follows a similar monotonically increasing Annular flow profile to that exhibited by the smooth tube.

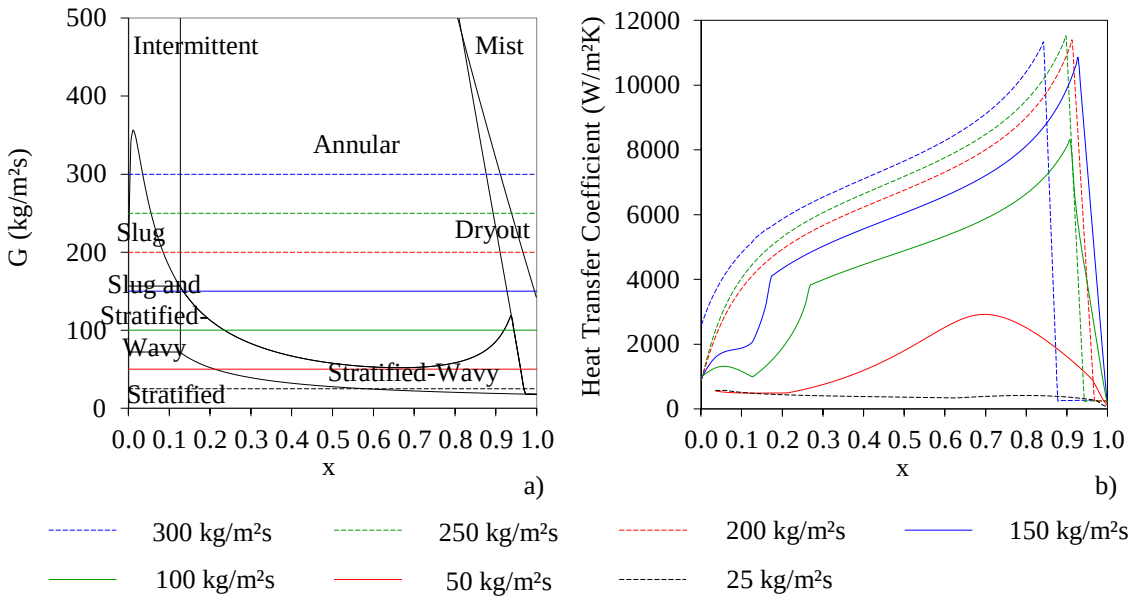

Figure 20: Modeling simulation results for a) Modified Sharar et al. [29] internally-grooved tube flow regime map and b) associated heat transfer coefficient in an 8.84mm internally-grooved tube with HFE-7100 at 61°C and a heat flux of 4 kW/m²

At a mass flux of 100 kg/m²s, the smooth tube is operating in the Slug and Stratified-Wavy or Stratified flow regime for all vapor qualities and the internally-grooved tube begins operating in the Slug and Stratified-Wavy flow regime and transitions to Annular flow at a vapor quality of 0.25. For the smooth tube, the dry angle ranges from 0

to θ_{strat} as dictated by Equation (25) and (26) for all vapor qualities. The result is a relatively poor, yet slightly increasing, heat transfer coefficient as the vapor quality increases. Under the same conditions, the internally-grooved tube transitions to Annular flow and the heat transfer coefficient increases sharply with increasing vapor quality. At a moderate vapor quality of 0.5 where the internally-grooved tube is operating in Annular flow (h=4,968W/m²K) and the smooth tube is operating in Stratified-Wavy flow (h=954W/m²K) the enhancement ratio is 5.2.

The simulation showed similar performance enhancement in the internally-grooved tube at a mass flux of 50 kg/m²s. As shown in Figure 19a, the smooth tube is operating in the Slug and Stratified-Wavy or Stratified flow regime. The internally-grooved tube, shown in Figure 20a, begins operating in the Slug and Stratified-Wavy flow regime at low vapor quality and approaches Annular flow at higher vapor qualities. The resulting smooth tube heat transfer coefficient remains low due to Stratified flow, and a large dry angle in Equation (19), and reaches a value of 320W/m²K at a vapor quality of 0.5. However, because the internally-grooved tube flow regime is approaching Annular flow, the dry angle decreases with increasing vapor quality and the heat transfer coefficient increases to a value of 1,737W/m²K at the same vapor quality. This represents an enhancement ratio of 5.4.

At the lowest vapor quality modeled, 25 kg/m²s, both the smooth tube and internally-grooved tube are operating exclusively in the Stratified and Stratified-Wavy flow regimes. In this case, the dry angle is always between the stratified angle, Equation (10), and θ_{dry} as described by Equation (25). The combined effect of a poor convective vaporization term (Equation (22)) and a large dry angle is a poor heat transfer coefficient,

as calculated by Equation (19). For a mass flux of 25 kg/m²s, the smooth tube had a heat transfer coefficient of 207W/m²K and the internally-grooved tube simulation showed a heat transfer coefficient of 553W/m²K. The enhancement ratio in this case reduced to 2.6, again approaching the area enhancement provided by the grooves.

Figure 21 shows a graphical summary of the enhancement ratio vs mass flux based on Figure 19, Figure 20, and the analysis above. The green dashed line represents the predicted enhancement ratios for a vapor quality of 0.5 and plotted as a function of mass flux; again, the enhancement ratio is defined as the internally-grooved tube heat transfer coefficient divided by the smooth tube heat transfer coefficient. The solid red line is the area enhancement of the internally-grooved tube.

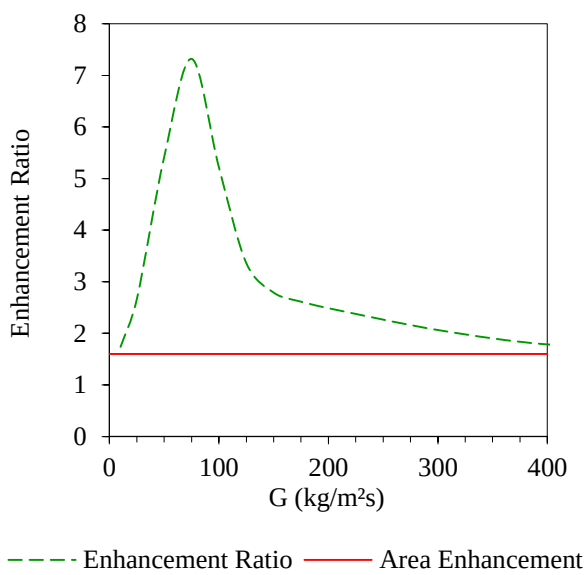

Figure 21: Simulated results comparing enhancement ratio vs mass flux for 8.84mm smooth and internally-grooved tubes with HFE-7100 at 61°C and a heat flux of 4 kW/m² as shown in Figure 19 and Figure 20

The figure shows heat transfer improvement approaching the area enhancement of 1.52 at sufficiently low mass flux, where both tubes were operating in Stratified or

Stratified-Wavy flow, and at high mass flux, where both tubes are predicted to operate in the Slug, Intermittent, or Annular flow regimes. Large enhancement (6 to 7x) was predicted at low-to-intermediate mass fluxes where the smooth tube was operating in Stratified flow and the internally-grooved tube is operating in Annular flow. The practical benefit of operating at low mass flux, where the enhancement is predicted to be 6-7x, is the reduction in pumping power associated with this operating condition. These trends are consistent with those described earlier, in Chapter 1 and Chapter 3, and indicate that the new flow regime map and associated heat transfer coefficient correlation likely capture the physical mechanisms responsible for enhancement in internally-grooved tubes.

Figure 22 shows a more detailed summary of the enhancement mechanisms responsible for improved performance in internally-grooved tubes. As shown, the Ravigururajan and Bergles [28] turbulent enhancement does not vary significantly over the range of mass fluxes considered; the enhancement factor is 1.426 at a mass flux of 400 kg/m^2s and 1.271 at a mass flux of 10 kg/m^2s. The Thome et al. [91] enhancement factor, on the other hand, increases from 1.269 at a mass flux of 400 kg/m^2s to 2.947 at a mass flux of 10 kg/m^2s. As shown in Figure 22, the enhancement ratio has the same slope as the Thome et al. [91] enhancement factor for mass fluxes ranging from 400 kg/m^2s to approximately 150 kg/m^2s where Slug, Intermittent, and Annular flow are the dominant flow regimes for both the smooth and internally-grooved tubes; please refer to Figure 19 and Figure 20. For this range of mass fluxes, enhancement is dominated by area enhancement, turbulence (as described by Ravigururajan and Bergles [28]), and the Gregorig effect/film flow (as described by Thome et al. [91]).

At mass fluxes below 150 kg/m²s, the slope and value of the enhancement ratio significantly increases due to sustained Annular flow in the internally-grooved tube and transition to Stratified-Wavy flow in the smooth tube. In this case, enhancement is dominated by the observed/predicted dominance of Annular flow in the grooved tube. Annular flow results in a dry angle of zero for the internally-grooved tube and Stratified flow results in a dry angle between 0 and 2π for the smooth tube; again, please refer to Figure 19 and Figure 20. At low mass flux, the total enhancement is less than the component of the Thome et al. [91] enhancement because a large dry angle is predicted in the internally-grooved tube during Stratified flow. Recall that the Ravigururajan and Bergles [28] and Thome et al. [91] enhancement factors only contribute to the wet angle heat transfer coefficient, as shown in Equation (37).

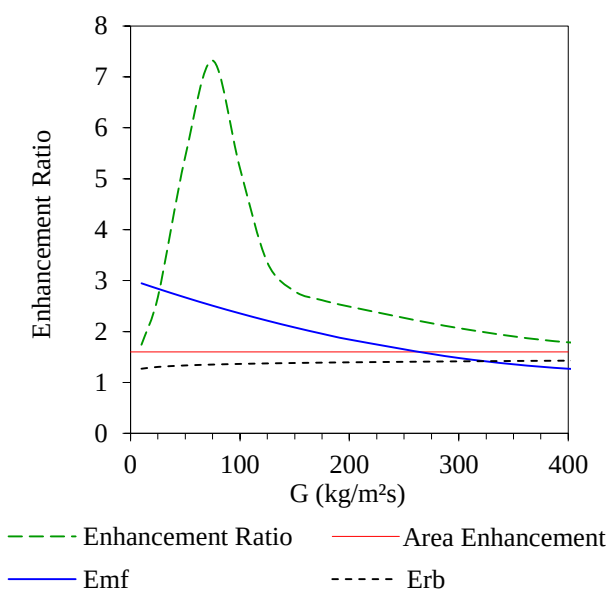

Figure 22: Simulated results comparing enhancement ratio, Emf, and Erb vs mass flux for 8.84mm smooth and internally-grooved tubes with HFE-7100 at 61°C and a heat flux of 4 kW/m²

4.7 Summary

In this chapter, a new flow regime map and heat transfer coefficient correlation were developed that consider the impact of the internal grooves on the flow regime and

heat transfer enhancement. The existing Wojtan et al. [30] flow regime map was modified using the Liebenberg et al. [118] and Liebenberg and Meyer [114] Intermittent to Annular transition and the Sharar, Jankowski, and Bar-Cohen [29] Stratified-Wavy to Annular transition. Additionally, the Ravigururajan and Bergles [28] turbulence factor and an empirically derived enhancement factor, introduced by Thome et al. [91], were adopted to modify the associated heat transfer coefficient correlation. These modifications resulted in varying the calculated dry perimeter angle, θ_{dry}, and represent the physical mechanisms responsible for enhancement in internally-grooved tubes.

Through analytical modeling simulations, it was shown that heat transfer enhancement at high mass flux (>150 kg/m²s) is dominated by area enhancement, turbulence (as described by Ravigururajan and Bergles [28]), and the Gregorig effect/film flow (as described by Thome et al. [91]). Enhancement of 6-7x at low-to-intermediate mass flux is dominated by transition to Annular flow in the internally-grooved tube. Additionally, predicted heat transfer enhancements approach the area enhancement when the smooth and internally-grooved tubes are operating in the same flow regime; this was shown at sufficiently low mass flux, where Stratified flow is expected, as well as high mass flux, where Annular flow is expected.

One motivation for the current research effort is to experimentally validate the peak enhancement demonstrated in Figure 21 and Figure 22. Clearly, understanding performance at and near this high enhancement operating space is critical to proper design and optimization of two-phase systems.

Chapter 5: Experimental Setup and Procedures

In the course of this study, the thermofluid characteristics of a series of experimental tests for single, uniformly heated horizontal internally-grooved tubes and smooth tubes with various IDs were experimentally studied. Focus was given to collecting and processing flow regime and heat transfer coefficient data to validate flow regime transition as a key enhancement mechanism in internally-grooved tubes and validate the new flow regime map and heat transfer model described in Chapter 4. This chapter describes the test facility designed and fabricated to collect flow regime data, using a new Total Internal Reflection method, and heat transfer coefficient data, using infrared thermography, for two-phase HFE-7100 flow in horizontal 2.62mm - 8.84mm diameter smooth and internally-grooved tubes with mass fluxes from 25-300 kg/m²s, heat fluxes from 4-56 kW/m², and exit vapor qualities approaching 1.

The following sections outline the experimental flow loop, tube heating method, fluid selection, experimental ranges, tube parameters, data acquisition scheme, vapor quality and heat transfer coefficient calculation, and uncertainty analysis. This approach is inspired by the tasks and goals set forth in previous chapters.

5.1 Two-Phase Testing Setup

As shown schematically in Figure 23, a test setup was developed to test single- and two-phase performance in smooth and internally-grooved horizontal tubes with water (for calibration and system validation purposes) and HFE-7100 as the working fluids. A custom reservoir and degasser (a) and a Fluid-o-Tech TMFR motor/pump system (b) are used to store, degas, heat, and pump the fluid during testing. The degasser is necessary to

remove dissolved air in the fluid, before two-phase experiments commence, because dissolved gasses have been shown to affect performance in smooth channels [133]. To the author's knowledge, the effect of degassed and gassy fluid on heat transfer in internally-grooved tubes has not been experimentally explored. The current setup is a closed loop system to allow degassing of dielectric fluid and prolonged testing, without the possibility of non-condensible gas entering the system.

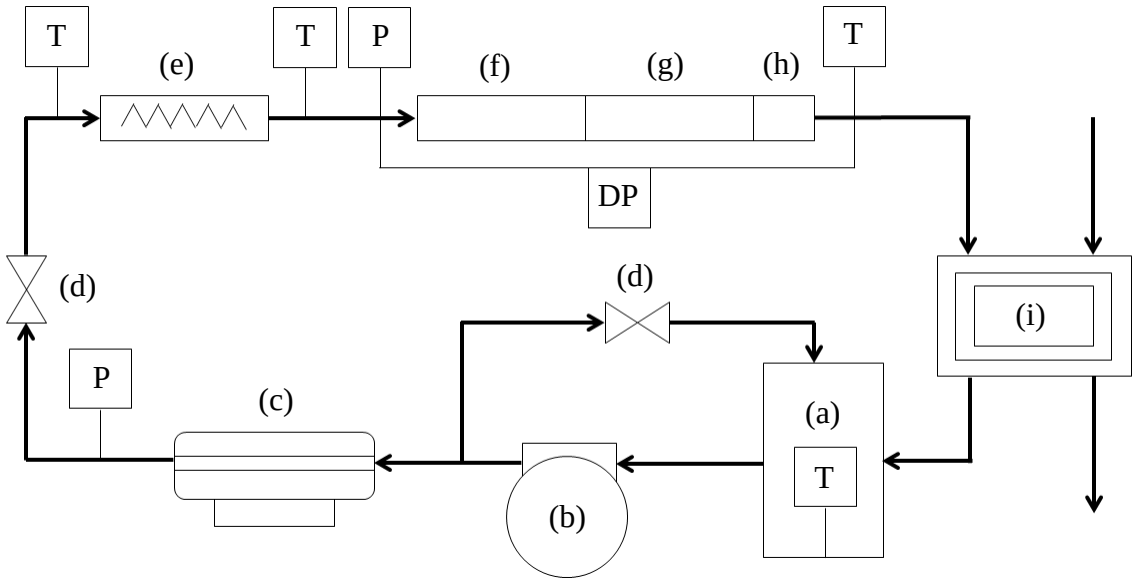

Figure 23: Schematic of two-phase flow test setup: a) reservoir and degasser b) Fluid-o-Tech pump c) Atrato or Kobold flow meter d) control valves e) inline heater f) 0.2m developing flow section g) 0.2m test tube h) 8cm sight glass (location of high speed flow visualization and TIR method) i) condenser P) pressure transducers and T) thermocouple probes DP) differential pressure transducer

An Atrato ultrasonic flow meter with ±1.5% absolute reading accuracy and 250:1 turndown ratio (20 mL/min to 5 L/min) was used to measure flow rate for water calibration tests. Kobold DPM 1153 and 1170 pelton wheel flow sensors with ±1.5% full scale accuracy and flowrate ranges of 0.24-4.8 GPH and 0.8-30 GPH, respectively, were used to measure flowrate for HFE-7100 tests (c). It's interesting to note that the Atrato ultrasonic flow meter did not work with HFE-7100 due to fluid compressibility and ultrasonic

modulation. Swagelok fluid control valves (d) were used to better control system flowrate and pressure. An Omegalux inline heater (e) was installed to further preheat and vaporize the fluid when necessary. A 0.2m-long smooth or – alternatively – an internally-grooved tube developing flow section (f) was placed directly before a corresponding 0.2m-long test section (g) and was connected with custom tube fittings made using a FDM Titan rapid prototyping machine. A custom 0.08m-long Pyrex sight glass (h), with the same ID as the internally-grooved and smooth tubes, was placed at the exit of the test section (g) to observe the local flow regime. A parallel plate heat exchanger (i) was used to re-condense the vapor produced during two-phase operation.

Fluid pressure was measured by two Omega MMG050 pressure transducers (P), with ±0.05% full scale reading accuracy and 0-50psi pressure limits, after the flowmeter and before the test section. Pressure drop across the developing flow section, test section, and 0.08m-long sight glass was measured with a Setra Model 230 wet-to-wet differential pressure transducer with ±0.25% full scale reading accuracy and 0-25psi differential pressure limits. The fluid temperature at the inlet and outlet of the test section was measured by two Special Limits of Error (SLE) Omega Type T thermocouples with ±0.5ºC accuracy. Similarly, two SLE Type T thermocouples were used to measure the fluid temperature before the inline heater and after the condenser. An AeroVironment MT30 power supply, capable operating up to 120 V and 330 A, was used to supply electrical power to the inline heater. Delivered power was measured by a Tektronix TC312 current probe and Yokogawa 7000924 differential voltage probe. A Tenma 72-6851 power supply capable of 35V (±0.1% absolute reading) and 10A (±0.2% absolute reading) was used to heat the test tube and was interfaced with a GPIB for ease of experimentation.

The tube outside wall temperature was measured using a FLIR ThermoVisionA40 long wave IR thermal camera (7.5 to 13 μm, ±0.3ºC accuracy [134]) at 14 discrete locations along the tube and three axial locations (top, side, and bottom), providing 42 discrete temperature data points. This was accomplished with the use of a custom fabricated 5-inch long IR mirror, as shown schematically in Figure 24. An IR photograph, taken during testing of the 2.80mm smooth tube, is shown in Figure 25. The ABS mirror mount was created using a FDM Titan rapid prototyping machine. Using a CHA E-Beam evaporator, the mirror surfaces were created by depositing an adhesion layer of 50nm of titanium (Ti), at a rate of 5Å/s for 100s, followed by 150nm of gold (Au), at a rate of 5Å/s for 300s, on Pyrex strips that measured 0.1”x1.15”x5”. The IR mirrors were attached to the mirror mount, metallization side facing towards the camera, using Loctite E-20HP structural adhesive. Gold is an excellent IR reflector beyond 1.5 μm with reflectance greater than 99% and, unlike aluminum or silver, is resistant to oxidation and degradation over time [135] [136]. Therefore, gold was an ideal candidate for the current experiments.

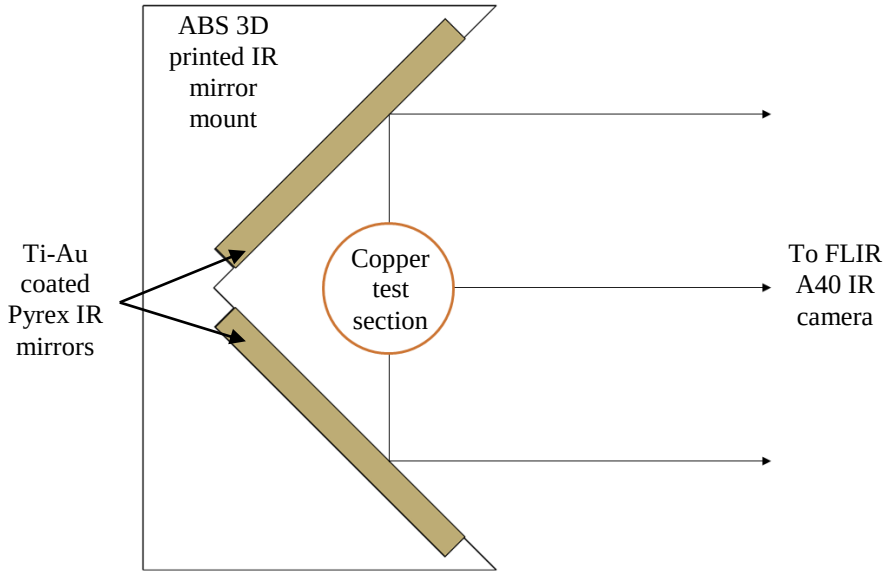

Figure 24: Schematic of custom IR mirror setup for measuring temperature on the top, middle, and side of the test section

A Keyence VW6000 high speed camera capable of up to 25,000 fps was used to observe the flow regimes in the sight glass. At the same location, an optical total internal reflection (TIR) method using a red fiber optic light source [137] was used to observe and quantify flow regime; more detail will be given in Chapter 6. It is noteworthy to point out that flow patterns were observed through sight glasses that are smooth rather than internally-grooved. Nevertheless, they are assumed to be representative of the flow regimes actually occurring at the internally-grooved tube exit. It is conjectured that the internally-grooved tube flow structure persists into the sight glass section and experiences only minor disruptions do to its short length and low L_h/D; the distance from the end of the test section and the location of the total internal reflection measurement, and high speed flow visualization, is 0.015m and 0.03m, respectively.

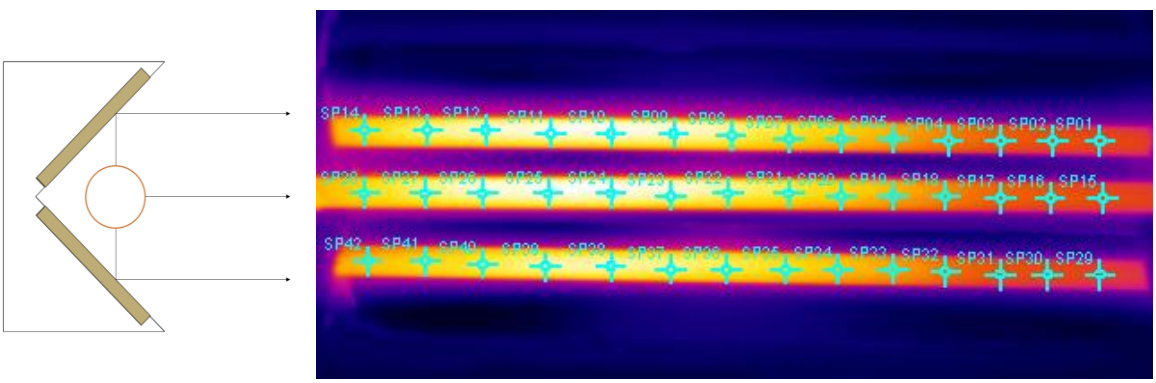

Figure 25: Schematic of custom IR mirror setup for measuring temperature on the top, middle, and side of the test section, and an IR photograph of the 2.80mm smooth tube during testing

5.2 Tube Heating Method

The smooth and internally-grooved tube diabatic test sections ('g' on Figure 23) were experimentally heated using custom-fabricated thin-film heaters deposited on the outside of the tubes. To create the heaters, the tubes were coated with 8 μm Parylene-C in a Specialty Coating Systems PDS2010 coating tool. This provided a dielectric layer to prevent electrical energy from shorting through the highly conductive copper tube. Next,

the resistor material, consisting of 12,000 Å of Titanium at a rate of 4 Å/s and 2,000 Å of Platinum at a rate of 2 Å/s, was deposited in a CHA E-beam evaporator using a rotating stepper motor assembly. These thicknesses were chosen to provide an appropriate resistance, ~5-20Ω, for electrically heating the tube; details on these values are provided in Appendix A. Then, copper electrical leads were attached to the metalized tube with EPO-TEK H20E silver-filled epoxy. Finally, the entire assembly was sprayed with Boron Nitride to provide a uniform emissivity. During testing, the thin film resistor was heated with a TENMA 72-6851 DC power supply. Figure 26 shows a photograph of the smooth tube before attaching the electrical leads and spraying with Boron Nitride. Boron Nitride emissivity was assumed to be 0.96 for all test conditions [138]. Please refer to Appendix A for a discussion of alternative tube heating methods considers as well as an attempt to make thin film resistors using atomic layer deposition (ALD).

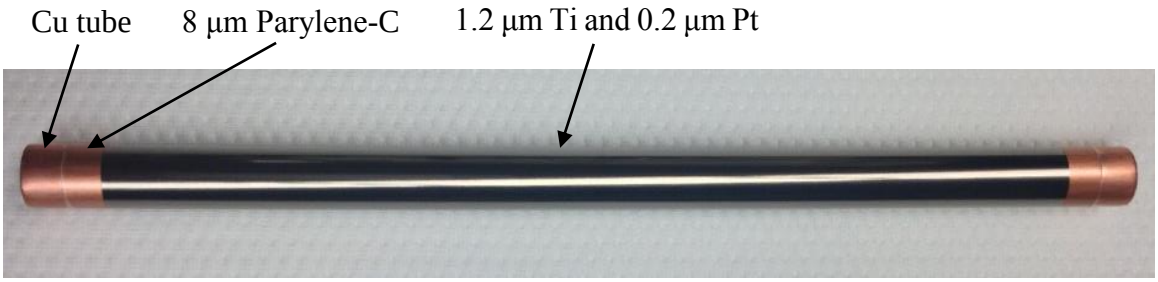

Figure 26: Photograph of a smooth tube coated with a thin-film heater

5.3 Fluid Selection

As discussed in Chapter 2 and Chapter 4, the Taitel-Dukler [46], original Wojtan et al. [30], and modified Sharar et al. [29] maps were developed using phenomenological models and, as such, are amenable to general use and applicable to a variety of fluids and flow conditions. From this perspective, any fluid could theoretically be used in the following tests and extrapolated to other conditions. However, the fluid selected should

have properties close to the fluid used in other internally-grooved tube studies [110] [111] [66] [77] so that direct comparison can be made. Furthermore, selecting a fluid with properties similar to the fluids used to develop semi-empirical flow regime [47] [48] [49] [50] [30] maps provides the added benefit of a large database of smooth tube data for comparison. Additional considerations when choosing a fluid are saturation temperature, saturation pressure, and latent heat of vaporization. If the fluid boils at a relatively high saturation temperature in atmospheric pressure, the vapor can be condensed by an air- or water-cooled condenser, as in the schematic shown in Figure 23, and a refrigeration compression loop is not necessary. Furthermore, if the fluid has a low to moderate latent heat of vaporization, less heat will be required to reach the desired vapor quality; this should be considered beneficial from an experimental standpoint.

Table 7 summarizes the fluids and properties used in the empirical flow regime maps discussed in Chapter 2 and Chapter 4, [47] [48] [49] [50] [30], along with several candidate fluids, FC-72, HFE-7100, and water. Water, which is renowned as a thermal management fluid, has dramatically different properties than the refrigerants and dielectric liquids and is not suitable as a heat transfer fluid for the current study. As shown in Table 7, HFE-7100 has fluid properties similar to the fluids used to define the empirical flow regime maps and similar to the studies outlined in the literature review (most of which used R-134a). Additionally, HFE-7100 has a moderate boiling point (61˚C) at ambient pressure and a relatively low latent heat of vaporization (112 kJ/kg). Therefore, the current research used degassed HFE-7100 as the working fluid. Fluid properties for FC-72 and HFE-7100 were not included in the table for pressure of 900 kPa (0.9 MPa) because properties were not available. Additionally, it should be noted that there appears to be some inconsistencies

in reported properties for HFE-7100, FC-72 and other 3M Novec fluids [139]; this will inevitably lead to uncertainty in measurement and modeling results. Unfortunately, this uncertainty cannot be quantified at this time. Efforts should be made to better characterize these fluids.

Table 7: Comparison of fluids (and properties) used for empirically fitted flow regime maps and candidate fluids

	Boiling Point (˚C)		ρl (kg/m³)		ρg (kg/m³)		σ (mN/m)		μl (μPa-s)		μg (μPa-s)		hlg (kJ/kg)	
Fluid	**0.1 MPa**	**0.9 MPa**	**0.1 MPa**	**0.9 MPa**	**0.1 MPa**	**0.9 MPa**	**0.1 MPa**	**0.9 MPa**	**0.1 MPa**	**0.9 MPa**	**0.1 MPa**	**0.9 MPa**	**0.1 MPa**	**0.9 MPa**
R-22	-41	20	1410	1211	4.64	38.05	18.1	8.8	347	174	9.68	12.2	234	188
R-134a	-26	36	1377	1165	5.19	44.08	15.5	6.7	380	171	9.76	12.2	217	168
R-410a	-52	4	1361	1154	4.12	33.82	17.8	8.5	387	162	9.89	12.8	272	216
FC-72	56	N/A	1680	N/A	13.4	N/A	10	N/A	262	N/A	12.1	N/A	88	N/A
HFE-7100	61	N/A	1370	N/A	9.87	N/A	14	N/A	275	N/A	11.3	N/A	112	N/A
Water	100	175	958	891	0.59	4.653	58.9	43.2	283	154	12.3	14.9	2257	2030

5.4 Experimental Ranges

Wieland, a leading manufacturer of smooth and internally-grooved refrigeration tubes, was contacted, informed of the current research initiative, and agreed to provide smooth and internally-grooved copper tubes. They provided six, 1 meter long lengths of various internally-grooved and smooth tubes. Additional smooth tubes with comparable inside diameters and wall thicknesses were purchased from McMaster-Carr. Table 8 outlines the parameters of interest for the smooth and internally-grooved tubes used for the current study. As shown, tube inside diameters ranged from 2.62mm to 8.84mm, tube wall thicknesses range from 0.19 to 0.9mm, number of fins ranges from 36 to 60, fin height ranges from 0.12 to 0.2mm, fin base ranges from approximately 0.12 to 0.25mm, and helix angles range from 10˚ to 18˚. All the internally-grooved tubes have trapezoidal fin profiles and surface enhancements between 152-160% compared to smooth tube equivalents.

18cm-long heated tube lengths of the 2.62mm, 4.54mm, and 8.84mm ID tubes were used to simulate channel lengths typical in an IGBT cold plate, thus creating the cold plate 'unit cell'. These tube diameters cover the range of past research, for comparison purposes,

and also smaller sized channels that approach mini- and microchannels to explore the size effects in internally-grooved tubes. It is unclear what effect heated length has on internally-grooved tube performance, however, this aspect is outside the scope of the current effort.

Table 8: Geometric parameters of internally-grooved and smooth tubes for the current study

Manufacturer	Type	Inside Diameter (mm)	Wall thickness (mm)	# fins	Fin height (mm)	Fin base (mm)	Helix angle α (°)	Surface enhancement (%)
Wieland	IG	2.62	0.19	36	0.12	0.12	10	160
McMaster	Smooth	2.8	.9	N/A	N/A	N/A	N/A	N/A
Wieland	IG	4.54	0.23	40	0.15	0.20	18	152
McMaster	smooth	4.54	0.23	N/A	N/A	N/A	N/A	N/A
Wieland	IG	8.84	0.34	60	0.2	0.25	18	152
Wieland	smooth	8.84	0.34	N/A	N/A	N/A	N/A	N/A

Nine different flowrates were tested (25, 50, 75, 100, 125, 150, 175, 200, and 300 kg/m²s) for the 8.84mm ID tubes, eight flowrates were tested for the 4.54mm tubes (50-300 kg/m²s), and seven flowrates were tested for the 2.62 – 2.8mm tubes (75-300 kg/m²s). This represents Reynolds numbers ranging from 640 to 12000; this is based on average liquid/vapor properties, superficial velocities, and vapor qualities from 0 to 1. The Kobold flow meters used in the current study could not accurately measure flowrates below these lower bounds. Six different tube heat fluxes were tested; 4, 9, 18, 28, 40, and 56 kW/m². Vapor qualities ranging from 0 to 1 were tested. These mass fluxes centered around regions near the Stratified/Annular, Stratified/Intermittent, and Intermittent/Annular transitions because these are the regions where internally-grooved tubes have demonstrated heat transfer improvement that can be explained by flow regime transition. However, data well within a specified flow regime (away from the transitions, as is the case with mass fluxes

of 25, 200, and 300 kg/m²s) were also explored to assess the flow regime map's ability to predict general trends.

5.5 Data Acquisition

All measurements, with exception of the TIR flow quantification and high speed camera data, were collected by National Instruments DAQ accessories and transmitted to an adjacent desktop computer running a LabView interface. During testing, the flowrate was fixed and the inline heater power was incrementally increased, such that the inlet vapor quality was increased by steps of approximately 0.1, until either the maximum inline heater load of 1.2 kW was reached or the vapor quality exceeded 1. It's worth noting that the inlet temperature at the inline heater changed over the course of testing and the incremental increase in quality did not match 0.1 for every data point.

At each inlet vapor quality, the six different heat fluxes were sequentially applied to the heater until dryout or excessive overheating occurred. For the current test setup, the maximum allowable temperature of the tubes before damage to the thin film heaters was 120ºC. Data was acquired when the system had reached steady state, which, depending on the mass flux and heat load, usually took no more than 10-15 minutes after changing a system parameter. After achieving steady state, high speed image data was recorded at a frame rate of 250-500 fps for 5 seconds. Then, the TIR data images were collected at 30 fps for 10 seconds (300 data points per test condition). The high speed and TIR imaging could not be performed simultaneously because the high intensity light required for the high speed camera saturated the CMOS camera used for the TIR method. This data was later post-processed using a custom MATLAB code. Please refer to Chapter 6, Appendix

B, and the journal paper by Sharar et al. [137] for a detailed description of the TIR methodology.

It is to be noted that unlike the eight unique flow regimes defined by the Wojtan et al. map [30] and the Sharar et al. map [29], most two-phase researchers [55] have limited their classification to the primary flow regimes: Stratified, Intermittent, Annular, and Bubbly. In the interest of uniformity and consistency, and to avoid confusion that may derive from the diversity of names used by authors for some of the observed sub-regimes, the present effort will follow the classification proposed by Rahim et al. [55], combining Slug, Plug, and Intermittent data points into Intermittent flow, combining Slugging-Annular flow, Wavy-Annular flow, and Semi-Annular flow into Annular flow, and defining Stratified-Wavy flow as a sub-regime of Stratified flow. This classification (simplification) will be applied to the current study when experimentally defining flow regime. One exception is Chapter 6, where sub-regimes are defined to demonstrate the more-subtle capabilities of the optical technique.

5.6 Deduction of Vapor Quality

The vapor quality at the inlet of the diabatic test section was calculated using Equation (39) below:

$$x_{inlet} = \frac{Kq_{inline} - \dot{m}C_p(T_{sat-inlet} - T_i)}{\dot{m}h_{lv}} \tag{39}$$

where q_{inline} is the applied heat load from the inline heater and the diabatic test section, $\dot{m}$ is the mass flowrate, C_p is the specific heat of HFE-7100 at the specified temperature, x is the vapor quality, $T_{sat-inlet}$ is the saturation temperature of HFE-7100 at the inlet of the test section, T_i was the temperature at the inline heater inlet ($T_i < T_{sat}$), h_{lv} is the latent

heat of the fluid, and K is the percentage of the applied heat from the inline heater that entered the fluid. For the current study, K was determined to always be greater than 95% (0.95) with HFE-7100 as the working fluid. More details on calculating K, based on a single-phase energy balance, are described in Chapter 7.

The vapor quality at the outlet of the diabatic test section was calculated using Equation (40) below:

$$x_{outlet} = \frac{Kq_{total} - \dot{m}C_p(T_{sat-outlet} - T_i)}{\dot{m}h_{lv}} \tag{40}$$

where q_{total} is the total heat applied to the inline heater and the diabatic test section and $T_{sat-outlet}$ is the saturation temperature of HFE-7100 at the outlet of the test section. Again, K was assumed to be 0.95 based on single-phase results. Vapor qualities shown in the Results and Discussion sections are average values between the inlet and outlet of the diabatic section.

5.7 Calculating Heat Transfer Coefficient

The average heat transfer coefficient was calculated experimentally with knowledge of the fluid saturation temperature, tube inside wall temperature, and tube heat flux:

$$h = \frac{q''}{T_{wall} - T_{sat}} \tag{41}$$

where q'' is the heat flux, T_{wall} is the average of the 42 discrete temperatures of the liquid/wall interface, and T_{sat} is the saturation temperature of the fluid at the specified pressure. Each measured heat transfer coefficient is the mean value of ten sequential acquisitions; as discussed later in the uncertainty analysis, averaging reduces the experimental uncertainty in the calculated heat transfer coefficient. A linear pressure drop

was assumed between the inlet and outlet of the tube to determine the saturation temperature. Based on a simple conduction model, the inner wall temperature was calculated as:

$$T_{wall} = T_0 - \frac{q\ln\left({}^{r_3}/_{r_2}\right)}{2\pi k_p L} + \frac{q\ln\left({}^{r_2}/_{r_1}\right)}{2\pi k_{cu} L} \tag{42}$$

where T_0 is the outside temperature of the tube as measured by the IR camera, q is the total heat dissipation of the tube, r_3 is the outside radius of the tube and the 8 μm Parylene-C layer, r_2 is the tube outside radius, r_1 is the tube inside radius at the base of the fins, k_p is the Parylene thermal conductivity, k_{cu} is the copper tube thermal conductivity, and L is the length of the tube. A physical representation of this is shown schematically in Figure 27.

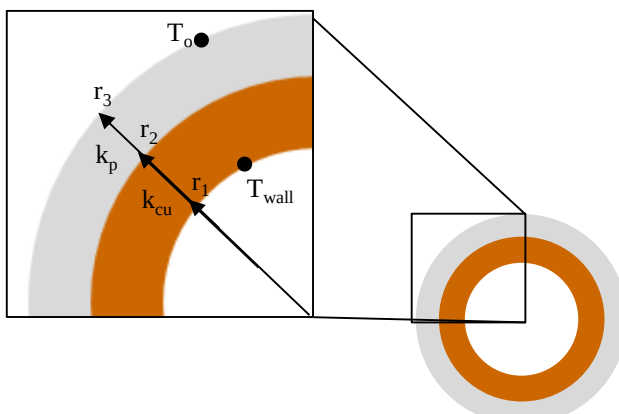

Figure 27: Schematic of 1-D radial heat conduction in the Parylene-C/Ti-Pt coated tubes

ANSYS simulations were performed to determine if the conduction model accurately captured the inside wall temperature. The concern was that significant spreading in the tube wall would lead to significant '3-D effects' and predicted wall temperature values would not be a good representation of the actual values. This would lead to uncertainty in the experimental heat transfer coefficient; this is less of a concern for the current study because average heat transfer coefficient values were reported, however,

for future studies where local variations in the heat transfer coefficient may be of interest, this analysis is of obvious practical importance.

Figure 28a shows a screenshot of the ANSYS model and Figure 28b shows the difference between the numerical and predicted (based on Equation (42)) values. These results are for a circumferentially and axially varying heat transfer coefficient profile that would induce spreading and non-linearities in the heat flow and resulting temperature profile. The values applied to the model are listed in Table 9 and are meant to represent low-to-moderate inlet heat transfer coefficient values (perhaps single-phase saturated liquid), followed by progressively higher heat transfer coefficients (Intermittent and Annular flow), followed by an abrupt drop in heat transfer coefficient from 7000 W/m²K to only 300 W/m²K (which represents Dryout). It is expected that the sharp contrast in heat transfer coefficient between Annular flow and Dryout would lead to the most heat spreading and the largest errors in the predicted value. This is considered a 'worst case' scenario and is a good indicator of the accuracy of the conduction model.

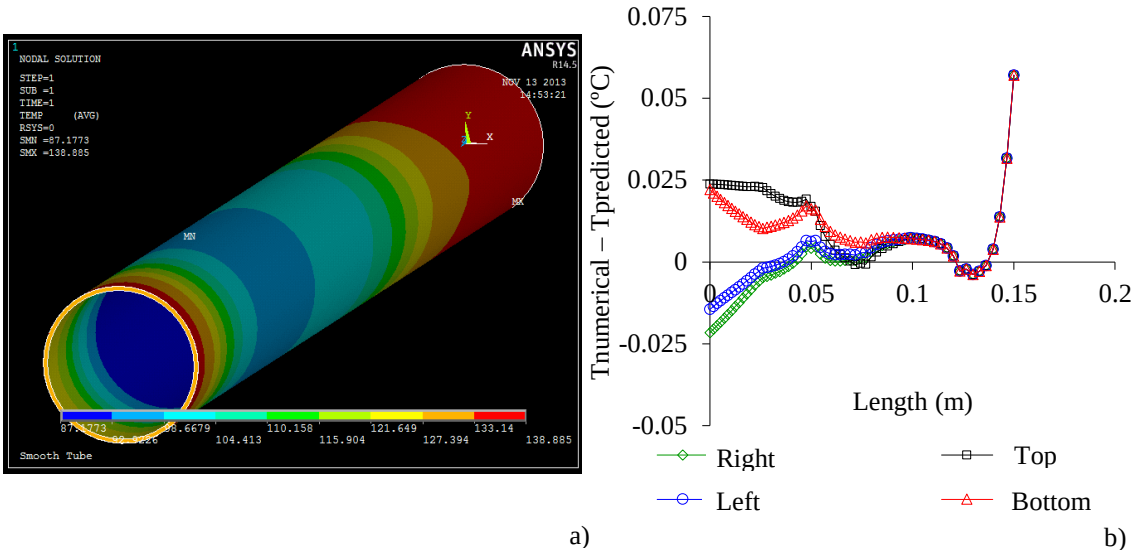

a) b)

Figure 28: Numerical results for a circumferentially and axially varying heat transfer coefficient

As shown in Figure 28b, the largest difference between the predicted and numerical results was, as expected, at the boundary between Annular flow and Dryout. However, the difference between the expected values, based on the above conduction model, and the numerical simulation was always less than ±0.06ºC. Since the measurement error in the IR camera is an order of magnitude larger than the spreading error, ±0.3ºC accuracy vs ±0.06ºC, heat spreading in the Parylene and copper layers is negligibly small and the conduction model above is appropriate for calculating local and average heat transfer coefficients for the current test setup.

Table 9: Heat transfer coefficients applied at different axially and circumferentially varying locations for the ANSYS numerical model

	Heat Transfer Coefficient at Different Axial Locations (W/m²K)						
Circumferential Location	**0cm**	**2.5cm**	**5cm**	**7.5cm**	**10cm**	**12.5cm**	**15cm**
0º (Right)	1000	3000	3000	5500	6000	7000	300
90º (Top)	1000	2000	2500	6000	6000	7000	300
180º (Left)	1000	3000	3000	5500	6000	7000	300
270º (Bottom)	1000	2500	2500	6000	6000	7000	300

5.8 Uncertainty Analysis

Measurement uncertainty was estimated using the root-sum-square method [140] and is based on the accuracies outlined in the above sections. The error in the measured heat transfer coefficient is a function of the tube heat flux and the difference between the saturation temperature and tube wall, ΔT:

$$\frac{\delta h}{h} = \sqrt{\left(\frac{\delta q''}{q''}\right)^2 + \left(\frac{\delta \Delta T}{\Delta T}\right)^2} \Big/ \sqrt{n} \tag{43}$$

For the current data set, the reported heat transfer coefficient was the average of 10 successive measurements at steady state conditions. In accordance with the method outlined by Bevington and Robinson [140], averaging reduces the uncertainty by a factor

of $\sqrt{n}$, where 'n' is the number of samples. In practice, the averaging of 10 samples reduces the uncertainty in the experimental heat transfer coefficient by a factor of 3.16.

The error in the experimental heat flux is a function of the error in the applied heat, q, the internal diameter of the tube, D, and the tube length, L. Both the heated length and internal diameter were measured using calipers with accuracy of ±0.01mm. Variations in the tube diameter for a given test section were considered nonexistent. The error in the heat flux is calculated by:

$$\frac{\delta q''}{q''} = \sqrt{\left(\frac{\delta q}{q}\right)^2 + \left(\frac{\delta D}{D}\right)^2 + \left(\frac{\delta L}{L}\right)^2} \tag{44}$$

The error in the applied heat load is dependent on the accuracy of the power supply voltage, V, and current, I:

$$\frac{\delta q}{q} = \sqrt{\left(\frac{\delta V}{V}\right)^2 + \left(\frac{\delta I}{I}\right)^2} \tag{45}$$

The error in the heat transfer coefficient varied depending on the applied heat flux and measured temperature rise of the tube wall. Generally, error bars were smallest for low mass flux and high heat flux where heat transfer coefficients are low and ΔT values are large. Conversely, error bars were typically larger at high mass flux and low heat flux where heat transfer coefficients were higher and ΔT values were small.

It's important to note that the heat transfer coefficients reported in Chapter 8 and Appendix C-Appendix E for the internally-grooved tubes are average augmented values accounting for the increased area enhancement of the groove structures. Therefore, uncertainty stemming from ambiguity in the reported area enhancement is not propagated in the heat transfer error measurement. However, when normalizing the results to account

for area enhancement in summary charts, it should be expected that small ~1-5% error (based on a conversation with Wieland and the understanding that this is a carefully controlled industrial process) is introduced due to slight manufacturing deviations.

Vapor quality uncertainty is a function of the applied heat, latent heat (which is assumed to be a constant and whose uncertainty is ignored), and the mass flowrate:

$$\frac{\delta x}{x} = \sqrt{\left(\frac{\delta q}{q}\right)^2 + \left(\frac{\delta G}{G}\right)^2} \tag{46}$$

The error in vapor quality was generally small for high mass flux cases, ±0.005, but was as high as ±0.1 for low mass fluxes.

Experimental uncertainty for mass flux was a fixed value of ±10.5 kg/m²s for the 8.84mm tubes, 12.49 kg/m²s for the 4.54mm tubes, and ±14 kg/m²s for the smallest diameter tubes. Vertical error bars shown in the Results and Discussion section are based on the above analysis while horizontal error bars (for vapor quality) are omitted for figure clarity. A summary of typical measurement and uncertainties for the sensors and thermofluid parameters, based on the above analysis, are listed in Table 10. Please note that these are 'typical' values and, as described above, the actual experimental uncertainty values can vary depending on the specific operating conditions.

Table 10: Summary of uncertainties for sensors and parameters

Sensors	Uncertainty (typical)
Diameter/Length	±0.01 mm
Temperature (TC)	±0.5ºC
Temperature (IR)	±0.3ºC
Pressure (absolute)	±0.05% F.S.
Pressure (differential)	±0.25% F.S.
Voltage	±0.1% reading
Current	±0.2% reading
Flowrate	±1.5% F.S.
TIR film thickness	±17μm
Parameters	**Uncertainty (typical)**
Heat transfer coefficient	±1-5%
Heat flux	±1-2%
Vapor quality	±1-2%
Mass flux	±10.5 to 14 kg/m²s

Chapter 6: Total Internal Reflection Flow Regime Quantification

As described in Chapter 2 and Chapter 3, and analytically defined in Chapter 4, local heat transfer rates in smooth and internally-grooved tubes are inherently tied to the local flow regime. Therefore, any efforts aimed towards experimentally determining and correlating heat transfer rates in internally-grooved tubes should focus heavily on collecting reliable flow regime data. For this purpose, the intent of this chapter is to; (a) demonstrate the ability to accurately determine flow regime and intermediate sub-regimes based on a non-intrusive flow visualization method; (b) use the non-intrusive flow visualization method with the two-phase experimental setup, described in Chapter 5, to collect adiabatic data for water in an 8.84 mm smooth tube; and (c) compare the results of the new flow visualization method to the phenomenological flow regime maps of Taitel-Dukler [46], Ullmann-Brauner [141], and Wojtan et al. [30] for validation purposes.

This chapter will begin with a discussion of the non-intrusive optical flow identification technique and experimental setup. Next, experimental TIR flow regime data and high speed photographs are presented. From this data, unique temporally varying film thickness profiles for different flow regimes and sub-regimes are identified. Then, the experimental flow regime data is compared to the Taitel-Dukler [46], Ullman-Brauner [141], and Wojtan et al. [30] flow regime maps to determine accuracy of the experimental method and analytical flow regime maps alike. Finally, conclusions on the relative applicability of the existing flow regime maps with water as the working fluid are presented. This chapter is based on a journal paper published in the Journal of Heat

Transfer Engineering titled 'Non-Intrusive Optical Validation of Two-Phase Flow Regimes in a Small Diameter Tube' [142].

6.1 Flow Regime Quantification Methods Available in the Literature

Drahos and Cermak [143] performed a review of available quantitative techniques and divided them into two categories. The first category is measurement of some parameter that is influenced differently by the presence of liquid or vapor. Examples of such a method are X-ray photography [144], photon attenuation [145], hot film anemometry, ultrasonic transmission [146], electrical impedance [147] [148], and a variety of optical methods based on light modulation [142] [149] [150] [151] [81]. The second category is measurement of an energetic parameter such as pressure fluctuation or wall shear stress fluctuation [118], which varies in a known way with the vapor or liquid content of the flow. For additional useful information and a description of these techniques, with a focus on electrical impedance and capacitance methods, the reader is directed to the Ph.D. Thesis by Canièri [152].

Of these methods, the optical techniques appear to be the most promising for the present study because they have been shown to be simple to implement, non-intrusive, inexpensive, and can provide film thickness measurement in addition to broad flow regime determination. Specific to the current study, reapplication of a total internal reflection (TIR) optical method, originally developed by Shedd and Newell [81], can provide a temporally-varying film thickness profile. Based on the observed film profile, both flow regime and local film thicknesses can be obtained. Use of a complimentary flow visualization technique, in this case a high speed camera, will provide validation of the TIR film thickness measurements.

6.2 Theory

A schematic representation of the TIR method is provided in Figure 29. As shown, diffuse light emitted from a point light source on the outside of an optically transparent wall, tube, or channel will be reflected via total internal reflection at the liquid-vapor interface. The reflected light will travel back to the outside surface of the wall, tube, or channel and an image will be formed. The image can be recorded with a camera, captured with a frame grabber, and processed using custom software or the Matlab Image Processing Toolbox [153].

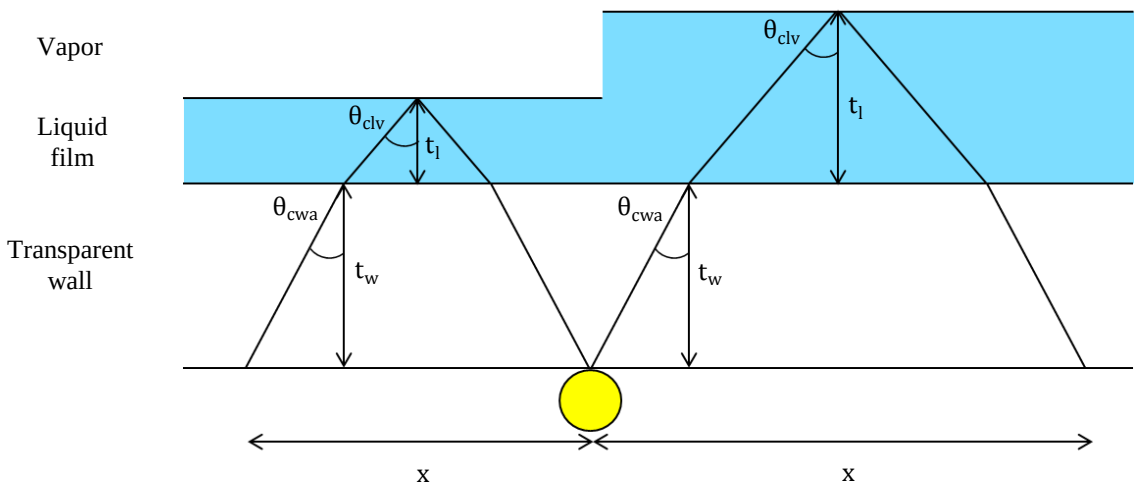

Figure 29: Principle of Total Internal Reflection (TIR) film thickness measurement technique

The TIR thickness measurement relates the distance between a light source and the reflected rays to the liquid film thickness. Figure 29 shows the geometric relationships defined by the liquid and wall thicknesses, t_l and t_w, and critical angles, θ_{clv} and θ_{cwa}. The distance from the source to the location where the reflected light passes back through the incident surface is:

$$x = 2t_l \tan\theta_{clv} + 2t_w \tan\theta_{cwa} \tag{47}$$

where θ_{clv} and θ_{cwa} are the critical angles at liquid-vapor and wall-air interfaces:

$$\theta_c = \sin^{-1}\frac{n_2}{n_1} \tag{48}$$

Rearranging Equation (47) for t_l yields:

$$t_l = \frac{x - 2t_w \tan\theta_{cwa}}{2\tan\theta_{clv}} \tag{49}$$

With knowledge of the optical properties of the materials and the tube wall thickness, the liquid film thickness can be determined by measuring the distance between the light source and first fully reflected ray. However, there is also total internal reflection at the wall-liquid interface at sufficiently large angles. If the film thickness is sufficiently large, then the first fully reflected ray from the liquid-vapor interface will fall beyond the reflected ray from the wall-liquid interface. This makes image processing difficult [154] [27] [153] and, therefore, poses an upper limit on the film thickness that can be measured for a particular setup. This effect is discussed later in this chapter. A complete discussion and derivation of the TIR liquid thickness measurement technique, including this upper limit, is described in a Master's Thesis by Shedd [81].

Different flow regimes will result in unique temporally varying film thickness measurements when taken at the top of a transparent tube, as shown in Figure 30. Therefore, two-phase flow regimes can be identified by measuring film thickness at a fixed point on the top (with respect to gravity) of a horizontal transparent channel and comparing the results to a catalog of known profiles. Single-phase flow, not shown, would result in a first fully reflected ray at the wall-liquid interface and a constant film thickness measurement at the upper limit of the measurement technique. Ideally, Bubbly flow would result in a relatively large average thickness with quick oscillations. Intermittent flow would have slower temporal response and a larger variation as liquid plugs and vapor slugs

intermittently pass the stationary sensor. Annular flow, which is traditionally characterized by a thin Annular film around the perimeter of the tube and a fast moving vapor core, would result in a relatively uniform film thickness with an occasional excursion due to dryout or rivulets, and the possibility of wave-induced relatively high-frequency ripples. Stratified flow, where vapor occupies the top of the channel and liquid settles to the bottom due to buoyancy forces, would show no film thickness at the top of the channel. In this way, flow regime can be objectively quantified by fixing a stationary TIR film thickness sensor at the top of a horizontal transparent channel.

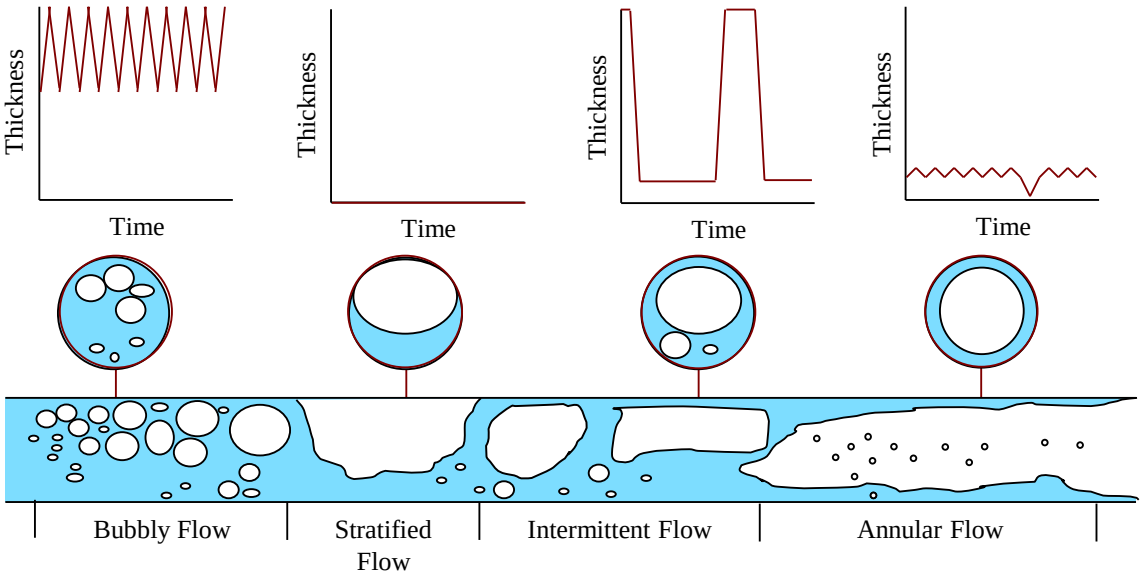

Figure 30: Two-phase flow regimes (bottom) and associated film thickness profiles (top)

This methodology would work for inclined, declined, and vertical flow as well, because the orientation of the sensor with respect to gravity does not affect the path of the reflected light in the present parametric range. Light can be affected by intense gravitational fields and/or long paths, neither of which pertain to the present study. However, one would expect different flow regimes for different channel orientations due

to gravity effects on phase distribution. For example, asymmetrical phase distributions such as Stratified flow, which are common in meso-and macro-scale tube horizontal flow, are not encountered in vertical flow, but may well dominate a wide range of qualities for a declined flow. Also, Annular films tend to be thinner at the top of horizontal tubes compared to the bottom, whereas vertical flows maintain more uniform Annular films. In general, flow patterns in inclined and declined tubes tend to share attributes of both horizontal and vertical two-phase flow. For more information on the effect of channel orientation on flow regimes, please refer to reviews by Cheng et al. [32] and Rouhani and Sohal [155].

6.3 TIR Setup and Procedures

6.3.1 Implementation of the TIR Technique

The TIR optical flow regime technique consists of a diffuse light source on the top (with respect to gravity) of an optically transparent horizontal tube, a charge coupled device (CCD) camera to capture the resulting light ring, and image processing software to extract a film thickness value. For the current study, this was accomplished by using a clear borosilicate glass tube from Precision Glass Blowing, IF-E96 red LED light source with internal microlens and a precision-molded PBT housing to maximize optical coupling into standard 1000 μm core plastic fiber cable, and an EO-1312C CMOS color USB camera with focusing optics. The cladding was stripped off of the fiber cable to reduce the diameter so that the light ring could be viewed with greater ease; subsequently, the stripped fiber core had to be painted black to prevent saturation of the image. A 27426 diffuse film from Edmund Optics was attached to the outside of the tube using UV-curing Norland Optical Adhesive 65. This coating homogenized the light leaving the LEDs and distributed

the light diffusely. Additionally, the diffuse film serves to couple the light out of the tube and scatter it so that an image of the light ring may be detected. Image processing and measurement automation were accomplished using a custom Matlab code, and are discussed further in Section 6.3.4 and Appendix B.

6.3.2 Experimental Ranges for Method Validation

Water at atmospheric pressure was used as the working fluid to validate the TIR method. Five different flowrates were tested; 60, 125, 250, 500, and 1000 mL/min equating to mass fluxes in the range of approximately 15 to 230 kg/m²s. Flowrates fluctuated by 3-5% during testing due to oscillations in the pump. The fluid reservoir was kept at 95˚C resulting in temperatures between 80˚C and 90˚C at the heater inlet. Higher reservoir temperatures were not possible due to cavitation in the pump. Nominal heat addition from the inline heater ranged from 150 to 1.2 kW, resulting in experimental vapor qualities ranging from 0.00012 to 0.32. All of the tests were performed with the test setup shown in Chapter 5.

6.3.3 Data Acquisition

All measurements, with exception of the TIR flow identification and high speed camera data, were collected by National Instruments DAQ accessories and controlled by an adjacent desktop computer running a LabView interface to allow real-time system monitoring. During testing, the flowrate was fixed and the power was incrementally increased until the maximum power level of 1.2 kW was reached. After achieving steady state, high speed image data was recorded at a framerate of 250-500 fps for 5 seconds. Then, the TIR data images were collected at 30 fps for 10 seconds (300 data points per test condition). The high speed and TIR imaging could not be performed simultaneously

because the high intensity light required for the high speed camera saturated the CMOS camera. This data was later post-processed using the custom Matlab code; the code is fully documented in Appendix B.

6.3.4 Data Reduction

6.3.4.1 Deduction of Vapor Quality and Superficial Velocities

The Taitel-Dukler [46] and Ullman-Brauner [141] maps have coordinates of superficial liquid velocity and superficial gas velocity while the Wojtan et al. [30] flow regime map has coordinates of mass flux and vapor quality. Therefore, plotting experimental data on the respective maps required the calculation of vapor quality, superficial liquid velocity, and superficial gas velocities from the available data.

First, a single-phase energy balance on the system was used to determine the percentage of the applied heat (from the inline heater) that remained in the fluid when it reached the outlet of the sight glass. This was possible by measuring the temperature change of the fluid between the heater inlet and the outlet of the sight glass and comparing this value to the total heat input. Single-phase tests were conducted for all flowrates with reduced inlet temperature and various heat loads, such that the water was within a few degrees of saturation at the heater outlet but did not vaporize. All of the heat was assumed to sensibly heat the fluid or be lost to the ambient. It was found that at least 80% of the applied heat remained in the fluid at the exit of the sight glass using Equation (50) below:

$$q = \dot{m} C_p \Delta T \tag{50}$$

where q is the applied heat load, $\dot{m}$ is the mass flowrate (kg/s), C_p is the specific heat of water at the specified temperature, and ΔT is the temperature rise in the fluid. As system heat losses should be primarily driven by the fluid temperature, the same losses were

assumed when testing under two-phase operation with water as the working fluid. Improved insulation and lower operating temperatures for HFE-7100 testing explains the discrepancy in system losses between this data set and those described in Chapter 5 and later in Chapter 7.

Considering that approximately 80% of the applied heat remained in the fluid at the exit of the sight glass, and that any heat in excess of what is required to bring the fluid up from the subcooled single-phase condition at the heater inlet to the saturation temperature goes toward vaporizing the fluid, vapor quality was estimated using Equation (39) below:

$$x = \frac{0.8q - \dot{m}C_p(T_{sat} - T_i)}{\dot{m}h_{lv}} \tag{51}$$

where x is the vapor quality, T_{sat} is the saturation temperature of water at the outlet of the sight glass, T_i was the temperature at the heater inlet ($T_i < T_{sat}$), and h_{lv} is the latent heat of water (2.26 kJ/kg). It's important to note that the flow was always single-phase liquid at the inlet of the heater and T_{sat}, typically 100˚C, was calculated based on the pressure measurement at the exit of the sight glass. Then, superficial liquid and vapor velocities could be directly calculated from:

$$J_L = \frac{G(1 - x)}{\rho_l} \tag{52}$$

$$J_G = \frac{Gx}{\rho_g} \tag{53}$$

where G is the mass flux, ρ_l is the liquid density (958.4 kg/m³), and ρ_g is the vapor density (0.59 kg/m³). All values used in these calculations were averages of 120 data points taken over the course of 60s of steady state operation. The 3-5% flowrate (mass flux) variation indicated in the Experimental Ranges section would, in turn, translate to a 3-5% fluctuation in superficial velocity.

6.3.4.2 Algorithm for Film Thickness Determination

A custom Matlab image processing algorithm was developed to post process the TIR image data. This algorithm determined the distance between the light source and the reflected rays, and calculated the liquid film thickness using the relationship shown in Equation (49). The Matlab code and a brief description can be found in Appendix B.

Several image processing steps were required to extract a film thickness value from an unrefined image. First, the image was captured with an appropriate camera. A captured image for a dry channel, i.e. with no liquid film, is shown in Figure 31. The black shaft on the bottom-center of the figure is the painted fiber optic LED connecting to the diffuse coating. The reflected light ring is visible, but not distinct enough to extract accurate film thickness values. Next, the image was converted to red-only to eliminate background light noise. Then, adaptive contrast enhancement was performed to normalize the image and remove complications stemming from intensity variations in the reflected light ring as a result of LED mounting imperfections. Figure 31b shows the image after eliminating green and blue light, and applying adaptive contrast enhancement. Next, a 2-D median filter was applied to eliminate salt and pepper noise and a simple contrast enhancement code was applied resulting in a binary image, shown in Figure 31c. The reflected light ring is now clearly visible.

The center of the LED was manually identified. In Figure 31c, the center of the LED is indicated with a red point. Next, a Sobel filter was used to locate the edges where the binary image changes from black to white and vice versa; the Sobel filter function outputs a matrix of these locations. As shown on Figure 31c, the third ‘edge’ identified by the Sobel filter will represent the first fully reflected ray. Then, a custom Matlab code was

used to count left and right (pixel-by-pixel) out from the LED center point while searching for the third location where the contrast changes. The diameter of the light ring, in pixels, is the sum of the distance measured to the left and right. Next, the pixel distance was translated to a physical distance using the width of the LED (1.27 mm) as a reference scale. Finally, Equations (47)-(49) were used to relate the light ring to a liquid film thickness.

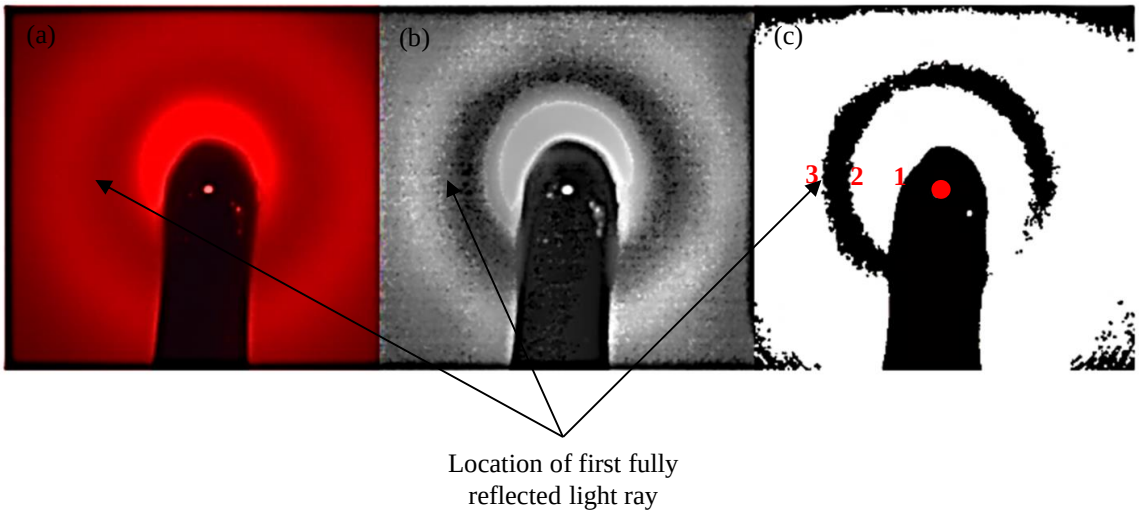

Figure 31: a) Raw image of reflected light ring on a glass tube with no film thickness, b) Image after converting to black and white and contrast enhancement, and c) Image after converting to binary

6.4 Experimental Results

6.4.1 Accuracy of the Total Internal Reflection Technique

The experimental system and the proposed image processing Matlab code were validated for static films before exploring temporally varying films. This was achieved by confirming that the proposed method generates results that are consistent with known film thickness and index of refraction data. Four different samples were prepared with film thicknesses of 0 μm, 183 μm, 449 μm, and 1005 μm. For each sample, a 27426 diffuse film from Edmund Optics was attached to the bottom of a 1 mm thick microscope slide using UV-curing Norland Optical Adhesive 65. Varying thicknesses of UV-curing Norland

Optical Adhesive 65 were then applied to the top of the slide to achieve the desired sample thickness. The fiber optic LED was spring clipped against the diffuse coating.

The different thicknesses of UV-curing adhesive were obtained by liberally applying the adhesive, placing precision ball bearings or microscope slides to act as spacers, clamping a microscope slide on top to ensure a flat surface, and then curing the assembly. The top microscope slide was coated with a thin layer of Duraseal stress-free silicon so it could be removed after the curing process to provide a simulated liquid-vapor interface. Adhesive thicknesses of 0 μm, 183μm, 449 μm, and 1005 μm were measured using a LEXT OLS4000 3D Laser Measuring Microscope designed for nanometer level imaging. These values represent an average of 10 data points taken from various locations for each of the samples. The error of the LEXT measurement can be determined by the following equation [156]:

$$\varepsilon = 0.2 + \frac{L}{100} \tag{54}$$

where L is the observed height of the film in μm. The resulting accuracy for the 0 μm, 183 μm, 449 μm, and 1005 μm films, as measured by the LEXT, are ±0.2 μm, ±2 μm, ±4.7 μm, and ±10.3 μm, respectively.

The TIR optical method has a theoretical accuracy resulting from the resolution of the CMOS camera. The spatial resolution of the camera, ± 1 pixel, can be related to a physical dimension, x, which can be translated to a film thickness resolution based on Equation (49). From an image captured of the setup, a total of 176 pixels were counted for the 1.27 mm fiber optic cable, resulting in a pixel distance of 7.2 μm/pixel. This suggests an inherent accuracy of the light ring radius measurement of ±7.2μm. Based on Equations

(47)-(49), this propagates to a best-case film thickness accuracy of ±2.8μm in the ideal case of a perfectly resolved light ring.

The cured Norland Optical Adhesive 65 and microscope slides both have an index of refraction of 1.52 [157]. There was no upper limit on the measurable film thickness for the test cases because the refractive index of the slide and film are identical, therefore, there was no total internal reflection at the slide-film interface. The predicted light ring radius was calculated using Equations (47)-(49) with known optical properties and thickness of the microscope slides and adhesive films. Figure 32 shows binary images of the four different test cases. The distance of the first fully reflected light ray increased as the film thickness increased. This trend is consistent with theory.

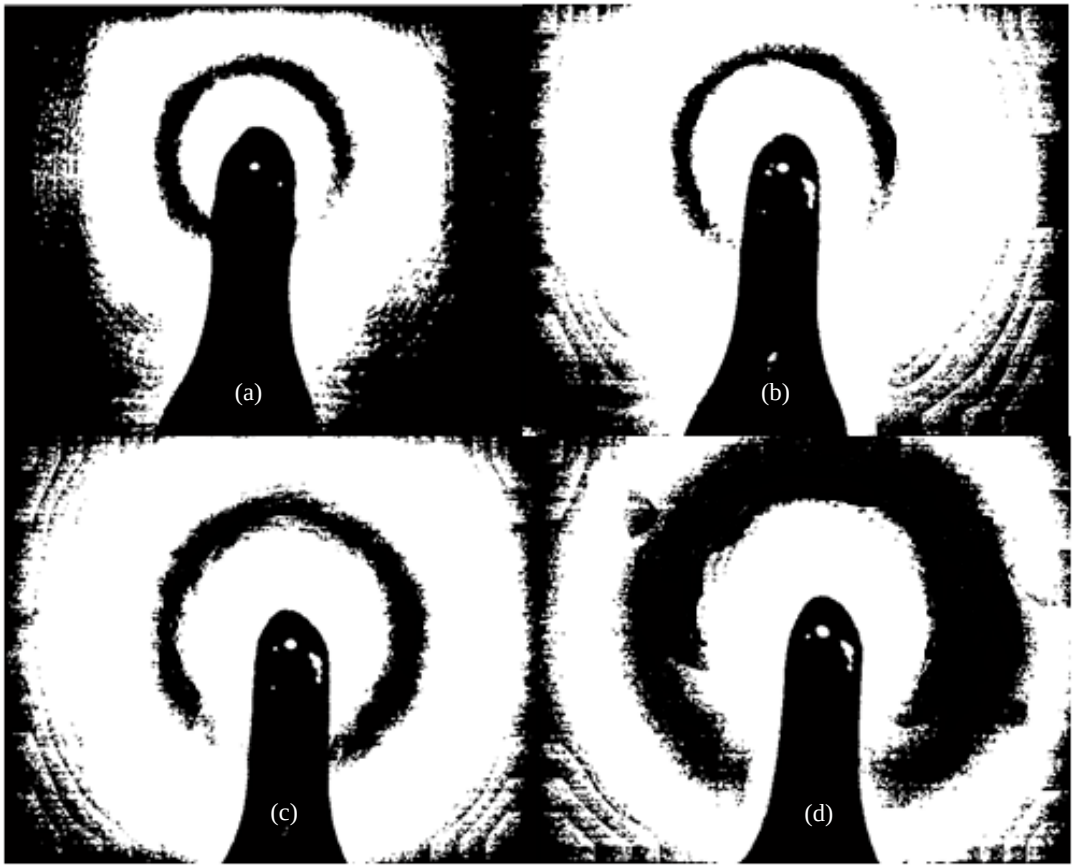

Figure 32: Binary images of validation samples a) 0 μm film, b) 183 μm film, c) 449 μm film, and d) 1005 μm film

Table 11 is a tabulation of the actual thickness as measured by the LEXT OLS4000 3D Laser Measuring Microscope, the accuracy of the LEXT, experimentally determined film thickness using the test setup and Matlab code, accuracy of the optical method, and a comparison of the actual and predicted values. The maximum difference between the actual and experimental result occurred with the maximum thickness tested, 1005 μm, with a difference of 17 μm. The sample with no film thickness demonstrated a difference of 8 μm while the 183 μm and 449 μm samples demonstrated 3 μm and 1 μm differences, respectively. For the range of film thicknesses tested, the experimental values were always within 20 μm of the actual value, and in most cases within 10 μm of the actual value. Therefore, the TIR optical method and accompanying Matlab code were validated with an accuracy of 20 μm for static films.

Table 11: Comparison of thickness prediction using test setup and Matlab algorithm to actual thickness values

LEXT thickness	TIR determined thickness	Difference in LEXT and TIR values	% error
0 μm ± 0.2 μm	8 μm ± 2.8 μm	8 μm	N/A
183 μm ± 2 μm	180 μm ± 2.8 μm	3 μm	1.6%
449 μm ± 4.7 μm	450 μm ± 2.8 μm	1 μm	0.2%
1005 μm ± 10.3 μm	1022 μm ± 2.8 μm	17 μm	1.7%

6.4.2 Limitations of the Total Internal Reflection Technique during Two-Phase Testing

There was total internal reflection at the wall-liquid interface at sufficiently large angles due to the difference in index of refraction between the borosilicate glass tube (n=1.52) and fluid (water n=1.33 and HFE-7100 n=1.27). This makes image processing difficult [154] [27] [153] and, therefore, poses an upper limit on the film thickness that can be measured for the current two-phase setup. The maximum measurable film thickness can be calculated with the following equation, and is shown schematically in Figure 33:

$$t_{lMAX} = \frac{t_w(\tan\theta_{wl} - \tan\theta_{cwa})}{\tan\theta_{clv}} \tag{55}$$

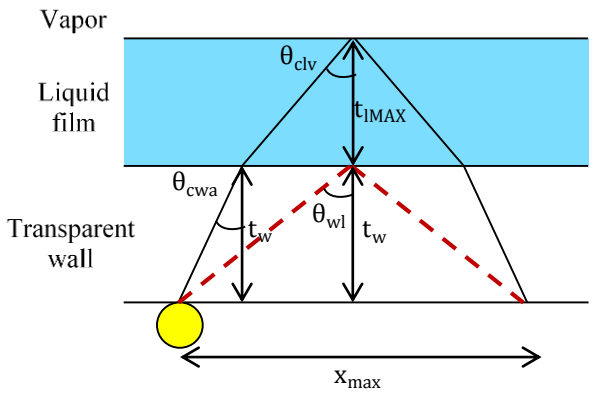

Figure 33: Schematic of the maximum measurable film thickness (adapted from [154])

The maximum measurable thickness for the current setup with a tube wall thickness of 1.12 mm and the above glass and water properties was 940 µm. It should be anticipated that the measurement technique will calculate a maximum value of 940 µm for instances where the liquid is thicker than 940 µm such as single-phase flow and during Intermittent flow where liquid plugs are passing the sensor. Film thickness during Intermittent bubble passage and Annular thin film flow should fall well below the 940µm upper limit. Additionally, the camera sampled at a discrete rate of 30 fps so the maximum resolvable film thickness frequency was 15 hz (0.066 seconds) based on the Nyquist sampling criterion. The maximum measurable film thickness varied for different tubes with HFE-7100 as the working fluid because the tubes had different wall thicknesses and HFE-7100 has a lower index of refraction (n=1.27) than water. Table 12 shows a summary of the borosilicate glass tubes geometric parameters and the resulting maximum measurable film thicknesses with water and HFE-7100 as the working fluids.

Table 12: Geometric properties and maximum measurable film thickness for different operating conditions

Fluid	Nominal Tube ID	Tube Wall Thickness	Maximum Measurable Film Thickness
Water	8.84 mm	1.12 mm	940 μm
HFE-7100	8.84 mm	1.12 mm	494 μm
HFE-7100	4.54 mm	1.21 mm	534 μm
HFE-7100	2.64-2.8 mm	0.94 mm	419 μm

Film thickness measurement error may come from electronic noise, vibrational noise, large disturbances in the film, poor image contrast, and camera movement with respect to the light source. Shedd and Newell discuss the relative effect of these noise sources on the measurement, and validate the technique for thin films ($\leq$1 mm) [154]. It's important to note that the resulting light ring during two-phase flow is slightly distorted in the circumferential direction due to the curvature of the tube. Measurements were taken in the axial direction to eliminate this source of error.

6.4.3 Characterization of Primary Flow Regimes

The previous section validated the ability to accurately measure static films in the range of 0-1005 μm and established the upper limits of the measurement technique for the existing test setup, 419 μm - 940 μm depending on the specific tube and fluid. The next step was to operate the system under various two-phase conditions to observe temporally varying film thickness profiles. Evaluating film thickness profiles 'deep' in the dominant flow regimes is desirable to observe ideal scenarios. This was possible for single-phase flow, Stratified flow, and Intermittent flow by flowing subcooled water or evaporating water in the existing two-phase setup. It was not possible to obtain high quality Annular flow (which occurs at higher vapor quality) with the 1.2 kW inline heater due to the high

latent heat of water. Instead, water and nitrogen were flowed to simulate water liquid/vapor Annular flow. The following sections outline the experimental results for water flow but are representative of the HFE-7100 results, as well.

Figure 34 shows representative data for single-phase flow, Stratified flow, Intermittent flow, and Annular flow. Please note that only one second of the ten second recording is shown in Figure 34 to maintain profile clarity. Figure 35 shows accompanying high speed flow visualization data taken immediately preceding the TIR data. The results, as shown on Figure 34, match well with the ideal cases identified in Figure 30 with a stationary TIR sensor at the top of a transparent tube. Single-phase flow was examined at a flowrate of 1000 mL/min (230 kg/m²s) with water at 90˚C. Single-phase flow shows a constant thick film equivalent to the maximum thickness the method can measure, 940 µm.

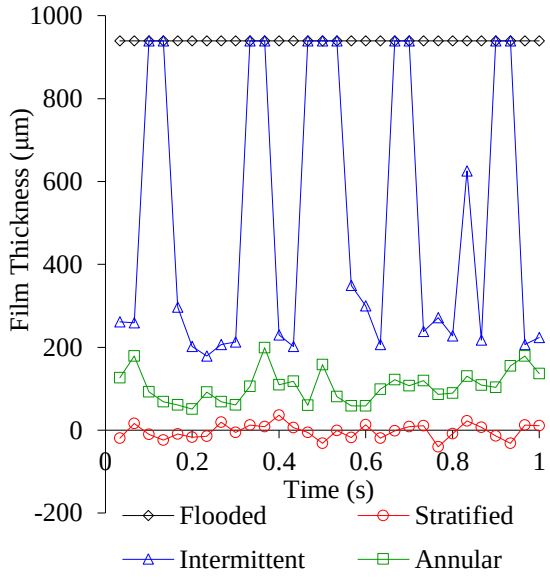

Figure 34: Unique temporally varying two-phase film thickness profiles in an 8.84 mm ID smooth tube for a 'Flooded' condition (230 kg/m²s), 'Stratified' condition (15 kg/m²s, x=0.067), 'Intermittent' condition (230 kg/m²s, x=0.01), and 'Annular' condition (120 kg/m²s, x>0.15)

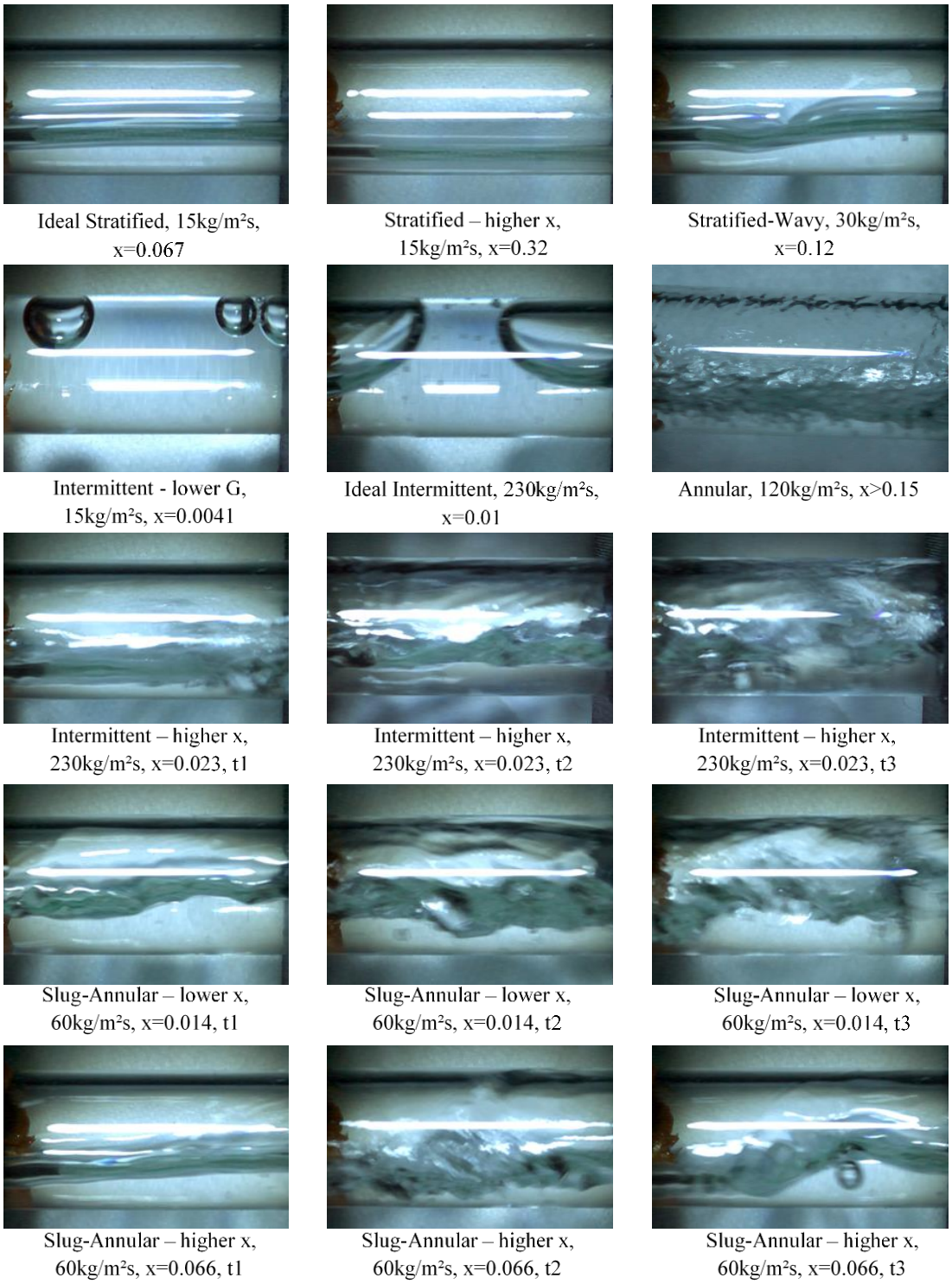

Figure 35: Photographs of high speed flow visualization

Stratified flow was studied at a flowrate of 60 mL/min (15 kg/m²s), heat input of 350 W, and vapor quality of 0.067. This regime showed an average film thickness of 0 µm due to the resulting dry upper surface. This data point is identified on Figure 35 as 'Ideal Stratified'. It is important to note that the film thickness profile shown in Figure 34 for no-film Stratified flow fluctuates by as much as 50 µm, indicating as-yet-unidentified noise in the measurement technique.

The film thickness for Intermittent flow was examined at a flowrate of 1000 mL/min (230 kg/m²s), heat input of 750 W, and vapor quality of 0.01. The Intermittent profile demonstrates a film thickness that fluctuates between the saturation point of the technique, 940 µm, and 200µm, indicating the periodic passage of a liquid plugs and vapor slugs. This data point is identified on Figure 35 as 'Ideal Intermittent'. During Annular flow, the water flowrate was kept at 500 mL/min (120 kg/m²s) and the nitrogen flowrate was increased until steady Annular flow was reached. It was estimated that this Annular data point represents a vapor quality exceeding 0.15, superficial liquid velocity of 0.12 m/s, and superficial vapor velocity exceeding 30 m/s. During Annular flow, a finite film thickness centered around 100 µm and fluctuations between 30 and 330 µm were observed. This data point is identified on Figure 35 as 'Annular'. It is interesting to note that the fluctuations for Annular flow were six times larger than the noise-related fluctuations for Stratified flow. This suggests that the fluctuations measured during Annular flow could be a real phenomenon and not a result of noise in the measurement technique. This assertion is supported by the photograph of Annular flow in Figure 35 that clearly shows a wavy Annular interface at the upper portion of the tube.

6.4.4 Characterization of Sub-Regimes and Subtle Differences of Primary Flow Regimes

The two-phase film thickness profiles shown in Figure 34 are ideal cases, demonstrating the ability to determine the primary flow regimes with the TIR method. Flow regimes such as Stratified flow and single-phase liquid flow did not deviate from the ideal cases because, generally speaking, a continuously flooded tube or continuously dry upper surface are not dynamically changing conditions. As expected, the three photographs of Stratified flow on Figure 35 did not result in unique film thickness profiles despite varying vapor quality, mass flux, and Stratified liquid-vapor interfacial structure. Intermittent/Slug flow, on the other hand, varied significantly depending on the specific operating conditions, namely mass flux and vapor quality. Additionally, Slug-Annular flow was observed as a sub-regime between Intermittent/Slug and Annular flow. This demonstrates the utility of the TIR method for explaining and quantifying the more subtle transitions that exist between dominant flow regimes.

Unique to Intermittent flow, regardless of operating parameters, was saturation of the film thickness measurement (indicating liquid plug passage) and abrupt decrease in the film thickness (indicating vapor slug passage). Despite the similarities, deviations from the ideal periodic Intermittent case in Figure 34 arose from the relative velocity of the liquid and vapor phases, bubble size, and bubble frequency for different operating conditions. The varying film thicknesses that Intermittent flow can exhibit are shown in Figure 36.

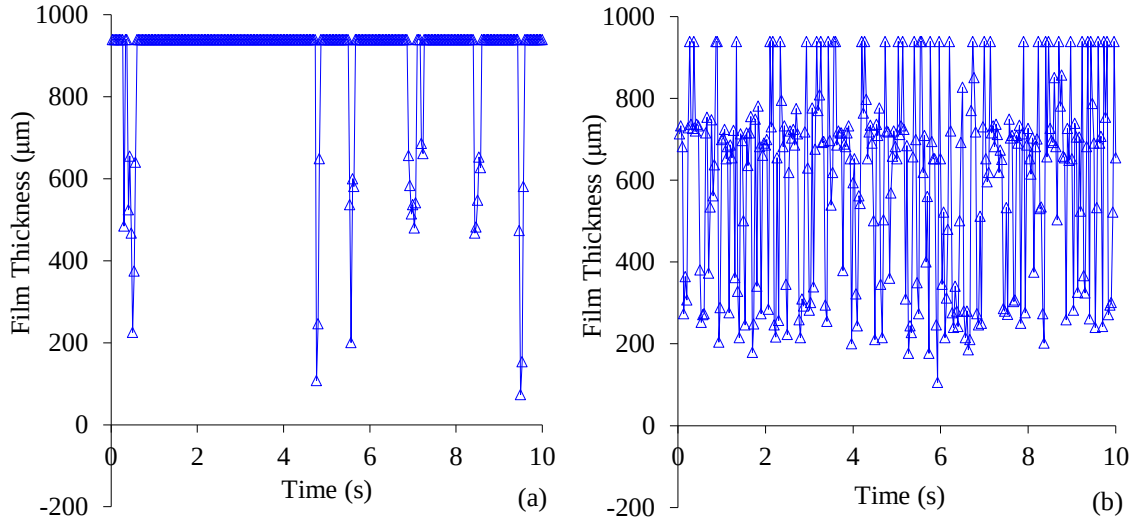

Figure 36: Intermittent flow film thickness profiles for a) 15 kg/m²s and x=0.004 and b) 230 kg/m²s and x=0.023

Figure 36a shows data for a flowrate of 60 mL/min (15 kg/m²s), heat input of 150 W, and vapor quality of 0.0041. Due to the low flowrate and low heat input, the channel was primarily occupied by slow moving liquid with a few small Intermittent bubbles. The result was a film thickness profile pinned at the saturation point of the measurement technique (indicating all liquid) with an intermittent drop in film thickness (indicating bubble passage). This data point is identified on Figure 35 as 'Intermittent – lower G'. Figure 36b shows data for a flowrate of 1000 mL/min (230 kg/m²s), heat input of 1200 W, and vapor quality of 0.023. The channel was occupied by fast moving liquid plugs and vapor slugs due to the high liquid flowrate and the vaporization of a large quantity of liquid. The result was a highly oscillatory film thickness profile with several high magnitude fluctuations per second. This effect is represented on Figure 35 as 'Intermittent – higher x' at three different discrete times, labeled 't1', 't2', and 't3'. 't1' shows a relatively thin film at the top of the channel, which would represent a valley in the film thickness profile shown in Figure 36b. 't2' represents a slightly thicker film and may describe the locus of

data points that fall close to 700 μm on Figure 36b. Finally, the TIR sensor reached the saturation point of the measurement technique at 't3'. Both of the scenarios shown in Figure 36 are experimentally defined as Intermittent flow (both here and for the duration of the Dissertation), but were differentiated here for academic purposes.

Another subtle difference between the ideal cases and actual experimental cases is the presence of unstable Slug-Annular flow as an intermediate sub-regime between the Slug flow and Annular flow regimes for moderate flowrates, 250 and 500 mL/min (60-125 kg/m²s), and vapor qualities exceeding 0.01. Other researchers have observed this phenomenon and referred to this regime as Aerated Slug [141] [158], Slug/Semi-Annular [159], and churn flow.

Two examples of the unstable film thickness profile characteristic of Slug-Annular flow are shown in Figure 37. Slug-Annular flow had characteristics of both Annular and Intermittent flow. For both cases, Slug-Annular flow was marked by an unstable film, similar to the ideal Annular flow case in Figure 34, with the passage of an occasional liquid plug, similar to the Intermittent flow cases in Figure 34 and Figure 36. For a flowrate of 250 mL/min (60 kg/m²s) and vapor quality of 0.014, the passing liquid plugs were thick enough to saturate the film thickness measurement technique. Figure 35 shows Slug-Annular high speed photographs for this operating condition, labeled as 'Slug-Annular – lower x' at three different time steps. As the time progresses from 't1' to 't3', it can be seen that the film thickness progresses from relatively thin to thick, resulting in occasional saturation of the measurement technique and the film thickness profile shown in Figure 37a. However, as the vapor quality increased from 0.014 to 0.066 in Figure 37b, the liquid plugs reduced in thickness and did not saturate the technique. In other words, as vapor

quality increased the film thickness profile appeared to approach a more-Annular (and less Intermittent) operating condition. This is shown in Figure 35, labeled as 'Slug-Annular – higher x' at three different time steps, where the film fluctuates from relatively thin to relatively thick without completely saturating the technique.

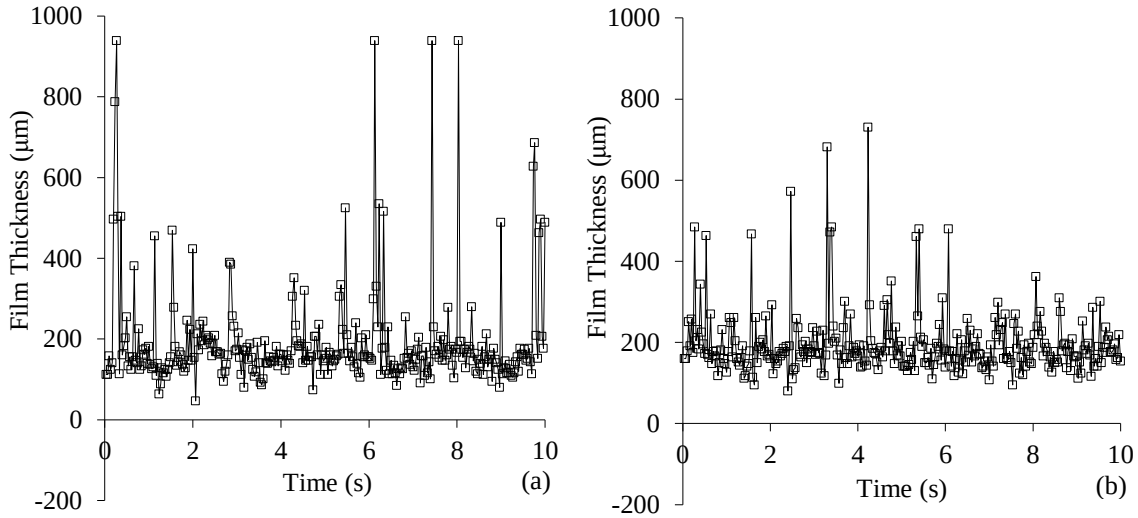

Figure 37: Film thickness profile for intermediate Slug-Annular flow with a) 60 kg/m²s and x=0.014 and b) 60 kg/m²s and x=0.066

For the HFE-7100 results in Chapter 8, the flow regime is defined as Annular flow if a thin film is present but the technique is not saturated (Figure 37b) and Intermittent flow if the passing liquid plug saturates the technique (Figure 37a). However, one could be inclined to believe that the profile shown in Figure 37b is representative of Intermittent flow, as well. Therefore, it's necessary to acknowledge that this method is not fully-objective. In order to classify the film thickness profiles into useful flow regime categories, objective qualifiers must be chosen or set. Such is the case with differentiating between Intermittent and Annular flow in Figure 37a and Figure 37b, above. However, when these classifications are well argued and consistently applied, this method provides a much less subjective, and much more repeatable method for determining flow regime.

6.4.5 TIR Validation with Existing Flow Regime Maps

Horizontal two-phase flow regime data was collected, using the TIR method at the top of an 8.84mm ID transparent tube, across the parametric space described in Section 6.3.2. Then, the data was converted to a usable form and plotted on the Taitel-Dukler [46], Ullmann-Brauner [141], and Wojtan et al. [30] flow regime maps using Equations (50)-(53).

Three dominant experimental flow regimes were observed; Stratified; Intermittent/Slug; and Slug-Annular as an intermediate flow regime between Slug and Annular flow. It is to be noted that unlike the eight unique flow regimes defined by the Wojtan et al. [30] map, most two-phase researchers [55] have limited their classification to the Bubbly, Intermittent, Stratified, and Annular flow. In the interest of uniformity and consistency, and to avoid confusion that may derive from the diversity of names used by authors for some of the observed sub-regimes, the classifications of flow regime beyond this chapter will follow the classification proposed by Rahim et al. [55], combining Slug, Plug, and Intermittent data points into Intermittent flow, combining Slugging-Annular flow, Wavy-Annular flow, and Semi-Annular data into Annular flow, and defining Stratified-Wavy flow as a sub-regime of Stratified flow, leading to the presence of just 4 primary regimes: Stratified, Bubbly, Intermittent, and Annular. For the remainder of this chapter, however, the sub-regime of Slug-Annular flow is differentiated to further demonstrate the capabilities and subtleties of the optical technique.

Figure 38 shows the experimental data plotted on the three respective flow regime maps. The circle data points are Stratified observations, the triangular data points are the Intermittent/Slug observations, and the square data points are the Slug-Annular

observations. It should be noted that the transition boundaries on these flow regime maps are typically ±25%, so data points on or near the border may fall within this error band.

The Taitel-Dukler [46] flow regimes are marked in coordinates of superficial liquid velocity and superficial gas velocity with the transition locus for Stratified, Intermittent, Annular, and Bubbly flow marked by solid black lines. The Ullmann-Brauner [141] map, displayed in the same coordinates as Taitel-Dukler [46], plotted Stratified flow, Slug flow, Aerated Slug flow, Annular flow, Bubbly flow, and Dispersed Bubbly flow with solid lines separating the flow regimes. The Wojtan et al. [30] flow regime map plotted Stratified flow, Stratified-Wavy flow, Slug and Stratified-Wavy flow, Slug flow, Intermittent flow, and Annular flow in coordinates mass flux and vapor quality with solid lines separating the flow regimes.

Data points at higher superficial liquid velocity or mass flux correspond to higher flowrate (1000, 500, 250, 125, or 62 mL/min). Superficial liquid velocity decreased slightly for a fixed flowrate and increasing vapor quality according to Equation (52). However, superficial vapor velocity increased significantly as vapor quality increased, as shown by Equation (53). Therefore, tracking horizontally from left to right on these flow regime maps provides flow regime data for a fixed flowrate with increasing vapor quality.

For a flowrate of 1000 mL/min (225 kg/m²s), the vapor quality ranged from 0.0001 to 0.0232 and the observed fluctuations in film thickness always corresponded to Intermittent/Slug flow. The data point labeled 'Ideal Intermittent' on Figure 38 represents the ideal Intermittent film thickness profile shown in Figure 34 and visually in Figure 35. The data point labeled 'Intermittent – higher x' represents the highly oscillatory Intermittent film thickness profile shown in Figure 36b and visually in Figure 35.

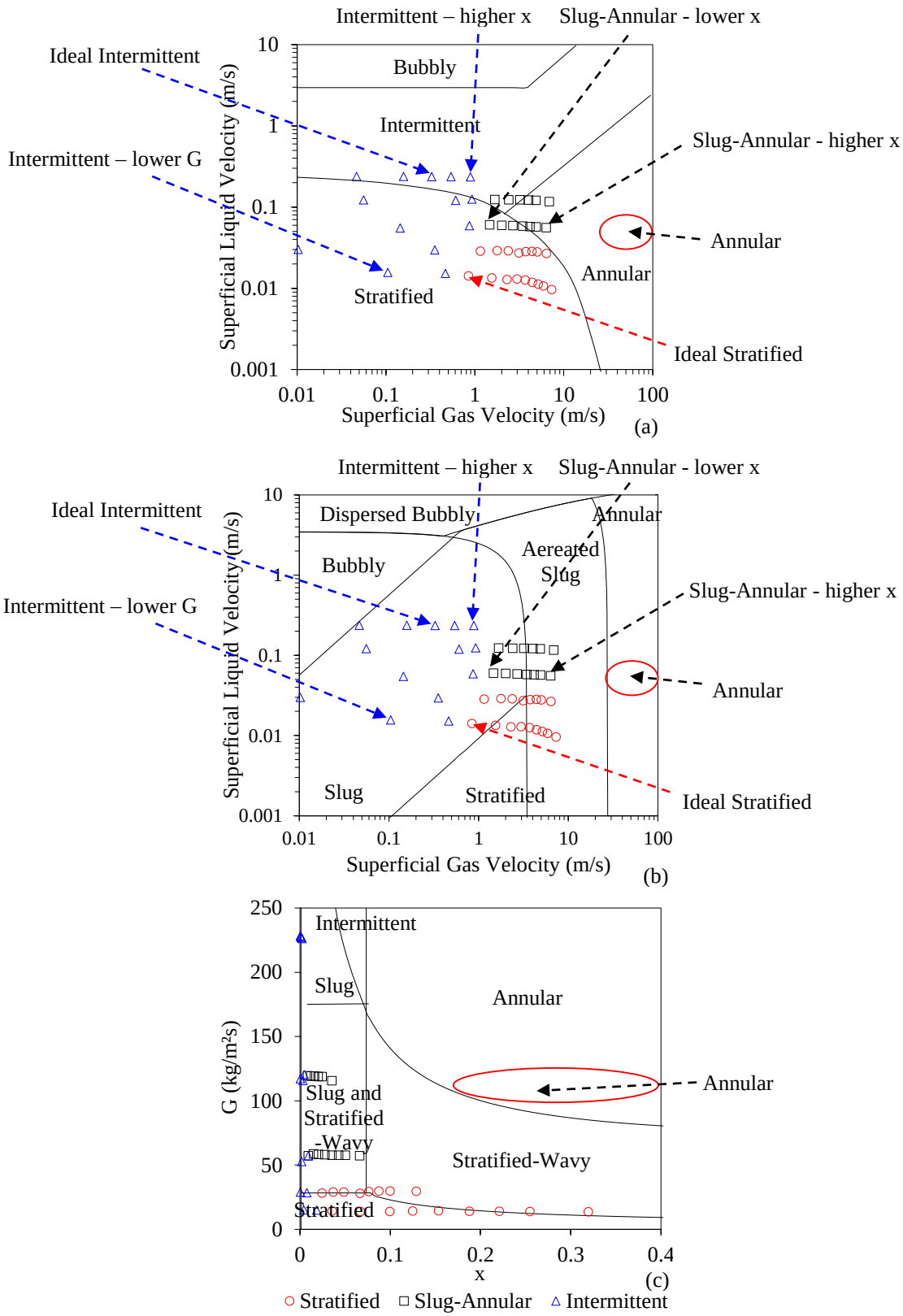

Figure 38: Two-Phase flow regime data plotted on a) Taitel-Dukler [46] map, b) Ullmann-Brauner [141] map, and c) Wojtan et al. [30] map

For a flowrate of 500 mL/min (120 kg/m²s) the vapor quality ranged from 0.0003 to 0.0353. The flow regime started as Intermittent/Slug flow at low vapor quality but transitioned to Slug-Annular flow at higher vapor quality and superficial gas velocity. The data point labeled 'Slug-Annular - lower x' represents Slug-Annular flow that has characteristics closely related to Intermittent flow, as shown in Figure 37a and Figure 35. The data point labeled 'Slug-Annular – higher x' represents Slug-Annular flow at higher vapor quality that more closely resembles Annular flow, as shown in Figure 37b and Figure 35. The flow regime would presumably transition to the data point labeled 'Annular', the Annular flow film thickness profile shown in Figure 34 and Figure 35, if more heat was added to the system.

With a flowrate of 250 mL/min (60 kg/m²s), the vapor quality ranged from 0.0016 to 0.066 and, similar to the 500 mL/min (120 kg/m²s) case, the flow regime started as Intermittent/Slug flow at low vapor quality but transitioned to Slug-Annular flow at higher vapor quality. At a flowrate of 125 mL/min (30 kg/m²s), the vapor quality ranged from 0.0002 to 0.129 and the flow regime transitioned from Intermittent/Slug flow to Stratified flow at vapor qualities greater than 0.02.

For a flowrate of 60 mL/min (15kg/m²s), the vapor quality ranged from 0.004 to 0.319 and, similar to 125 mL/min, the flow regime was Intermittent/Slug at low vapor quality and appeared to transition to Stratified flow at qualities greater than 0.3. The data point labeled 'Intermittent – lower G' represents Intermittent/Slug flow at low flowrate and low vapor quality resulting in a channel primarily occupied by slow moving liquid with a few Intermittent bubbles as shown in Figure 36a and Figure 35. The data point labeled

‘Ideal Stratified’ represents the ideal Stratified film thickness profile shown in Figure 34 and Figure 35.

All three flow regime maps accurately predicted the primary flow regimes shown in Figure 34 and identified by the labeled data points on Figure 35 and Figure 38. The flow regime maps also accurately predicted the natural transition from Intermittent/Slug flow to Annular flow with increasing vapor quality and superficial vapor velocity, as well as other trends as discussed above. Deviation in predictive accuracy arose when observing the full parametric space tested for a variety of flow rates and vapor qualities. The predominance of Slug-Annular flow suggests that the transition from one flow regime to another cannot necessarily be identified by a discrete point or curve, but rather a range of operating conditions. Along these same lines, it is to be noted that the observed discrepancy between predicted and measured flow regimes for data in the literature is commonly within a ±25% band.

In addition to general trends and ideal cases consistent from one map to the next, the results agreed reasonably well with the Taitel-Dukler [46] flow regime map. Every Stratified data point is correctly predicted, every Intermittent/Slug flow data point at 1000 mL/min, over the full range of vapor qualities tested is predicted, and the model appears to predict the transition towards more-Annular flow for 250 and 500 mL/min. The Taitel-Dukler [46] flow regime map does not correctly predict the parametric space occupied by Intermittent flow at relatively low superficial gas velocity (less than 1 m/s). From Figure 38, it incorrectly predicts these Intermittent data points as Stratified flow. However, these data points exist at low heat dissipation and low vapor quality which are of little importance in most practical applications.

The Ullmann-Brauner [141] model reflects trends indicative of the experimental data and matches closely with many data points. It predicts the correct vicinity of the Stratified flow regime and identifies that this flow regime may occupy a smaller parametric space than previously hypothesized by Taitel-Dukler [46]. Additionally, the Ullmann-Brauner [141] map identifies the possibility to transition from Intermittent/Slug flow to Stratified flow at low flowrate and increasing vapor quality. Three additional trends the Ullmann-Brauner [141] map accurately captures are; presence of Annular flow at higher superficial gas velocity; dominance of the Aerated Slug regime as an intermediate regime between Slug and Annular flow; and extension of Intermittent/Slug flow regime to lower superficial liquid and vapor velocities.

The Wojtan et al. [30] flow regime map accurately predicts all of the Stratified data points. This map also accurately predicts the dominance of Intermittent/Slug flow at low vapor quality across a wide range of flowrates. One exception is at very low mass flux and vapor quality where Intermittent/Slug data points are incorrectly predicted as Stratified flow. However, these data points exist at low heat dissipation and low vapor quality which are of little importance in most applications and occupy a very small region of the operating space. The Wojtan et al. [30] map also predicts the natural progression from Slug-Annular flow at 500 mL/min (120 kg/m²s) to Annular flow, the data point labeled 'Slug-Annular – higher x', with increasing vapor quality. One discrepancy is the location of the Annular flow regime with relation to the observed Slug-Annular data points for 250 mL/min (50 kg/m²s). From Figure 37, it was shown that as vapor quality increases from 0.014 to 0.066 the liquid slugs reduce in thickness and do not saturate the measurement technique. In other words, as vapor quality increases the film thickness profile appears to approach a

more-Annular (and less Intermittent) operating condition. However, with a fixed flowrate of 250 mL/min (50 kg/m²s) the Wojtan et al. [30] map predicts transition to Stratified-Wavy flow, not Annular flow. A likely explanation for this deviation is that the Wojtan et al. [30] flow regime map was empirically fit to match common refrigerants, which have fluid properties vastly different than water (see Table 7). In effect, the empirical constants allow for better predictive accuracy for operating conditions close to the data set used to develop the correlations, but do not extrapolate well to different conditions. Conversely, due to the generality of the Taitel-Dukler [46] and Ullmann-Brauner [141] flow regime maps, they can often be 'less accurate' at times but applicable to a wider range of fluids and operating conditions. Consequently, the Taitel-Dukler [46] and Ullman-Brauner [141] maps both predict transition to Annular flow at a fixed flowrate of 250 mL/min and increasing vapor quality with water as the working fluid.

The three maps above all correctly predicted the primary flow regimes, the natural transition from Intermittent/Slug flow to Annular flow with increasing vapor quality and superficial vapor velocity, as well as other trends. No single flow regime map accurately predicted every data point, however, each individual map did provide specific advantages and the ability to predict certain flow regimes better than others (with water as the working fluid). As suggested by Rahim et al. [55], and consistent with trends in the current study, a combination of these maps might better predict the prevailing flow regimes.

6.5 Summary

An optical, non-intrusive, flow pattern identification method was developed to validate flow regime maps for two-phase adiabatic water/vapor/nitrogen flow in an 8.84 mm diameter tube. The method consisted of shining a red fiber-optic light source through

the top of an optically transparent glass tube, using a CMOS camera to capture light rings resulting from total internal reflection at the liquid-vapor interface, and extracting a film thickness profile from the resulting images. It was found that different flow regimes resulted in unique temporally varying film thickness profiles, which were confirmed using high speed visualization. Using these profiles, quantitative flow regime identification measures were developed, including the ability to explain and quantify the more subtle transitions that exist between dominant flow regimes. This method is applicable to two-phase flow in transparent tubes and substrates alike, with a variety a working fluids.

The principal flow regimes, Stratified, Intermittent/Slug, and Annular flow were experimentally observed. Additionally, Slug-Annular flow as an intermediate flow regime between Intermittent/Slug and Annular flow was observed and quantified. The phenomenological flow regime maps of Taitel-Dukler [46], Ullmann-Brauner [141], and Wojtan et al. [30] were found to capture the smooth tube experimental data, with varying accuracy, validating the use of the TIR technique in predicting flow regime. Please note, sub-regimes were described here to demonstrate the capabilities of the technique, however, in Chapter 8 flow regime definitions will be simplified to avoid overcomplicating the data and analysis.

Chapter 7: Single-Phase Data and Discussion

This chapter considers heat transfer rates for horizontal in-tube single-phase flows. Single-phase tests were performed with the three-different smooth and internally-grooved tubes described in Table 8, coated with the thin-film heaters described in Section 5.2, and operating with HFE-7100 as the working fluid. Theoretical predictions were compared to the experimental results to determine the accuracy and reliability of the test setup and to assess the accuracy of single-phase, smooth and internally-grooved tube, heat transfer models in the literature.

7.1 Single-Phase Energy Balance

As described in Chapter 5, a single-phase energy balance was first performed to ensure that the majority of the heat electrically applied to the system was entering the fluid and to make sure the thermofluid delivery and measurement system was calibrated and working properly. This step was an essential first-step for validating the test setup; without this analysis, the local and exit vapor qualities as well as the experimental heat transfer coefficients during two-phase testing cannot be trusted. For these tests, the fluid inlet temperature was held around 15ºC and the tube outside wall temperature was not allowed to exceed 61ºC, the boiling temperature of HFE-7100 at atmospheric pressure. This reduced the likelihood of pseudo-boiling (air coming out of the solution) and the occurrence of sub-cooled flow boiling, which could affect the heat transfer coefficient. The input energy was the electrical power applied to the system. The output energy was calculated based on the fluid temperature rise, ΔT, mass flowrate, $\dot{m}$, and specific heat, C_p, based on the equation below:

$$Q_{out} = \dot{m}C_p\Delta T \tag{56}$$

Figure 39 shows the single-phase energy balance ratio for the 2.8mm, 4.54mm, and 8.84mm smooth tubes with a heat flux of 18 kW/m², mass fluxes ranging from 150 to 1100 kg/m²s, and HFE-7100 as the working fluid. The ratio of heat out to heat in, as measured through the temperature rise in the fluid, was generally less than 1 but always greater than 0.95. This reveals that there is a minor source of heat loss and measurement uncertainty in the system. However, the results are always within ±5% of the expected value, which is considered acceptable for the current study.

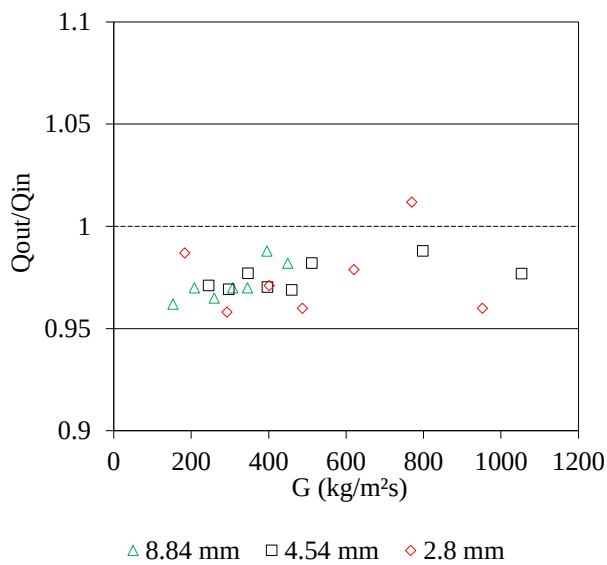

Figure 39: Single-phase liquid energy balance ratio for HFE-7100 in different tube diameters

7.2 Single-Phase Heat Transfer Measurements and Comparison to Smooth Tube Correlations

Measured heat transfer coefficients for the 2.8mm, 4.54mm, and 8.84mm smooth tubes with a heat flux of 18 kW/m², mass fluxes ranging from 150 to 1100 kg/m²s, and HFE-7100 as the working fluid were compared to the two correlations of Dittus-Boelter ('common' and 'original' form), Colburn, and Gnielinski; all four correlations were taken from the Incropera et al. Fundamentals of Heat and Mass Transfer Handbook [25]. Since

turbulent flow is convoluted, emphasis has been placed on empirical correlations. The 'common' Dittus-Boelter correlation for heating takes the form:

$$\mathrm{Nu_D} = 0.023\mathrm{Re}^{0.8}\mathrm{Pr}^{0.4} \tag{57}$$

where Re is the Reynolds number and Pr is the Prandtl number. The 'original' Dittus-Boelter equation for heating is of the form:

$$\mathrm{Nu_D} = 0.0243\mathrm{Re}^{0.8}\mathrm{Pr}^{0.4} \tag{58}$$

The Colburn equation is:

$$\mathrm{Nu_D} = 0.023\mathrm{Re}^{0.8}\mathrm{Pr}^{0.333} \tag{59}$$

Finally, the Gnielinski correlation, which is valid over a large Reynolds number range ($3000<\mathrm{Re}<5\mathrm{x}10^6$), takes the form:

$$\mathrm{Nu_D} = \frac{\left(\frac{\mathrm{f}}{8}\right)(\mathrm{Re} - 1000)\mathrm{Pr}}{1 + 12.7\left(\frac{\mathrm{f}}{8}\right)^{0.5}(\mathrm{Pr}^{0.667} - 1)} \tag{60}$$

where f is friction factor, which can be obtained from a Moody diagram or calculated directly for smooth tubes as:

$$\mathrm{f} = (0.790\ln\mathrm{Re} - 1.64)^{-2} \tag{61}$$

Figure 40 shows the experimental single-phase heat transfer coefficient vs mass flux results, compared to the predictions. The properties used while evaluating these correlations were the average values between the inlet and outlet of the test section. The results show that the heat transfer coefficient increases with increasing flowrate, for all three tube diameters, to the power of approximately 0.8; the reader is directed to the correlations shown in Equation (57)-(59) where the Reynolds number is raised to the power of 0.8. For a fixed flowrate, heat transfer coefficients slightly increased as the tube diameter decreased. These trends are predicted well by the correlations.

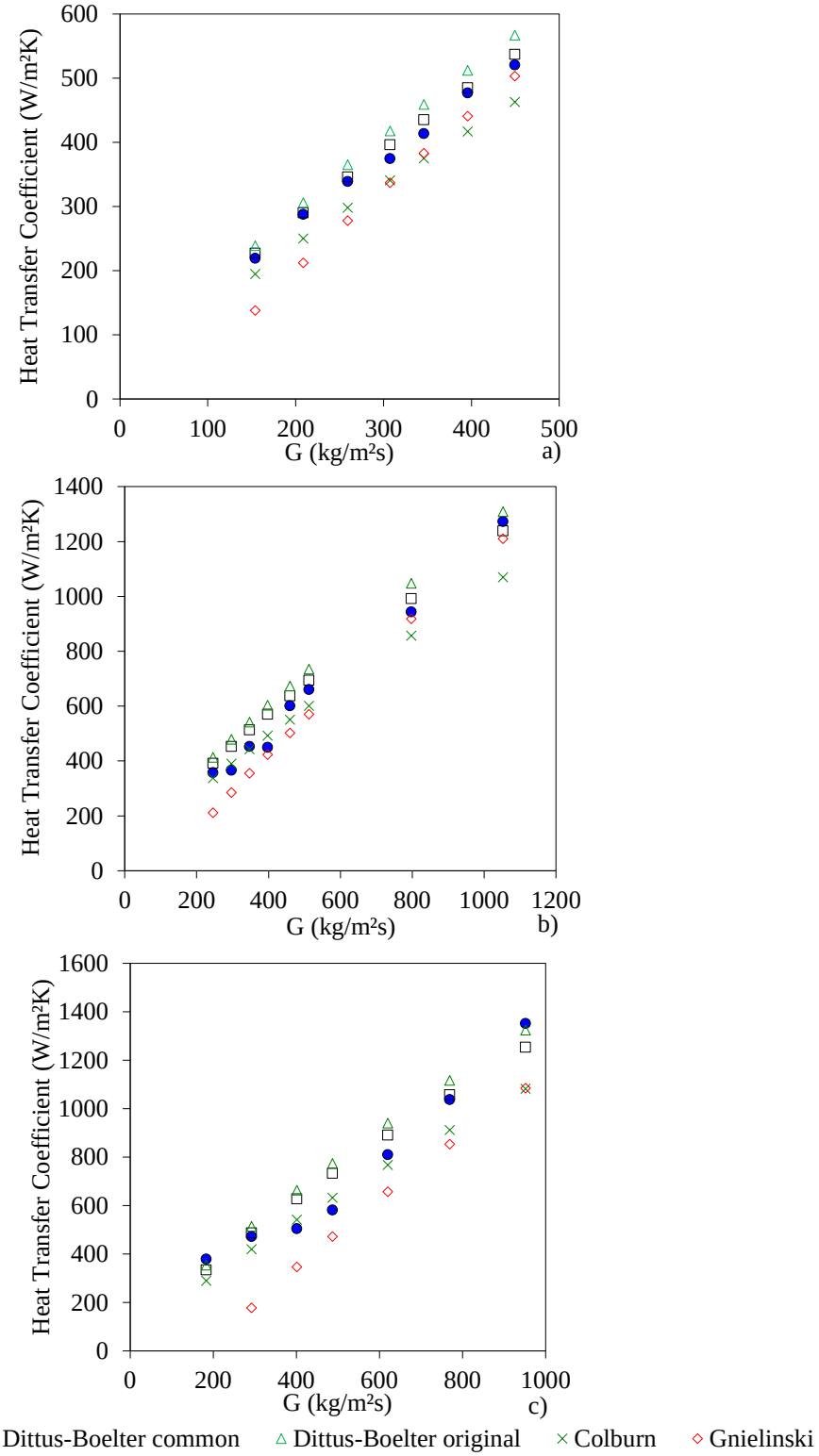

Figure 40: Experimental and predicted single-phase heat transfer coefficient vs mass flux for a) 8.84 mm smooth tube, b) 4.54 mm smooth tube, and c) 2.8 mm smooth tube

The statistical parameters of mean deviation, $\bar{\varepsilon}$, and mean of absolute value of deviations, $|\bar{\varepsilon}|$, were calculated based on the equations below:

$$\bar{\varepsilon} = \sum\left[\left(h_{predicted} - h_{experimental}\right)100/h_{experimental}\right] \tag{62}$$

$$|\bar{\varepsilon}| = \sum \mathrm{ABS}\left[\left(h_{predicted} - h_{experimental}\right)100/h_{experimental}\right] \tag{63}$$

where $h_{predicted}$ is the heat transfer coefficient predicted by the respective heat transfer coefficient correlation and $h_{experimental}$ is the measured heat transfer coefficient.

Table 13 lists a summary of the statistical parameters for the four correlations used. As shown, and also apparent from Figure 40, the 'common' form of the Dittus-Boelter correlation was generally the most accurate, with deviations of just 7% and 9% in the mean deviation and absolute deviation, for single-phase flow of HFE-7100 in the 2.8 mm to 8.84 mm smooth tubes. The Colburn correlation was second best with deviations between -7.62% and 10.55%, followed by the 'original' Dittus-Boelter correlation with 13.08% and 13.86%, and the Gnielinski correlation with -18.49% and 18.49%.

Table 13: Statistical analysis of the experimental single-phase smooth tube heat transfer measurements

	Dittus-Boelter 'common'	Dittus-Boelter 'original'	Colburn	Gnielinski
$\bar{\varepsilon}$	7.07%	13.08%	-7.62%	-18.49%
$\lvert\bar{\varepsilon}\rvert$	9.02%	13.86%	10.55%	18.49%

7.3 Single-Phase Heat Transfer Measurements and Comparison to Internally-Grooved Tube Correlations

Originally developed for single-phase flow in ribbed tubes and tubes with helical wire inserts, the Ravigururajan and Bergles [28] correlation has been widely adopted for internally-grooved tubes [11]. In fact, the Ravigururajan and Bergles [28] correlation is incorporated in the current two-phase flow boiling model for internally-grooved tubes, as

described in Chapter 4, Equation (36). The final, normalized, heat transfer coefficient for internally-grooved tubes is given by:

$$\mathrm{Nu_{rb}/Nu_s} = \mathrm{E_{rb}} = \left\{1 + \left[2.64\mathrm{Re}^{0.36}\mathrm{Pr_L}^{-0.024}\left(\frac{\mathrm{e_f}}{\mathrm{d_f}}\right)^{0.212}\left(\frac{\mathrm{p_f}}{\mathrm{d_f}}\right)^{-0.21}\left(\frac{\alpha_\mathrm{f}}{90^\circ}\right)^{0.29}\right]^7\right\}^{1/7} \tag{64}$$

where $\mathrm{e_f}$ is the groove height, $\mathrm{d_f}$ is the nominal inside diameter at the fin base, $\mathrm{p_f}$ is the axial pitch from groove to groove, and α_f is the helix angle of the grooves. As shown in Equation (64) and discussed in Chapter 4, the single-phase turbulent correlation developed by Ravigururajan and Bergles [28] was described as an 'enhancement' over a comparable smooth tube. For the current analysis, the reference smooth-tube heat transfer correlations will be the two correlations of Dittus-Boelter ('common' and 'original' form), Colburn, and Gnielinski; all four correlations were taken from the Incropera et al. Fundamentals of Heat and Mass Transfer Handbook [25] and are described formulaically above. The 'common' Dittus-Boelter correlation adjusted for predicting heat transfer coefficient in internally-grooved tubes becomes:

$$\mathrm{Nu_D} = \mathrm{E_{rb}}0.023\mathrm{Re}^{0.8}\mathrm{Pr}^{0.4} \tag{65}$$

The 'original' Dittus-Boelter equation for heating takes the form:

$$\mathrm{Nu_D} = \mathrm{E_{rb}}0.0243\mathrm{Re}^{0.8}\mathrm{Pr}^{0.4} \tag{66}$$

The Colburn equation is now:

$$\mathrm{Nu_D} = \mathrm{E_{rb}}0.023\mathrm{Re}^{0.8}\mathrm{Pr}^{0.333} \tag{67}$$

Finally, the Gnielinski correlation becomes:

$$\mathrm{Nu_D} = \frac{\mathrm{E_{rb}}\left(\frac{\mathrm{f}}{8}\right)(\mathrm{Re} - 1000)\mathrm{Pr}}{1 + 12.7\left(\frac{\mathrm{f}}{8}\right)^{0.5}(\mathrm{Pr}^{0.667} - 1)} \tag{68}$$

where f is the smooth-tube friction factor, which can be calculated directly:

$$f = (0.790 \ln \mathrm{Re} - 1.64)^{-2} \quad (69)$$

Figure 41 shows the measured and predicted (based on Equations (65)-(68) above) heat transfer coefficients for the 2.62mm, 4.54mm, and 8.84mm internally-grooved tubes with a heat flux of 18 kW/m², mass fluxes ranging from 150 to 1100 kg/m²s, and HFE-7100 as the working fluid. The properties used while evaluating these correlations were the average values between the inlet and outlet of the test section. The results show that the heat transfer coefficient increases with increasing flowrate, for all three tube diameters. For a fixed flowrate, heat transfer coefficients slightly increased as the tube diameter decreased.

Table 13 lists a summary of the statistical parameters for the four correlations used. As shown, the 'common' form of the Dittus-Boelter correlation (adjusted with the Ravigururajan and Bergles [28] enhancement factor) was generally the most accurate for the range of internally-grooved tube diameters and mass fluxes tested, with mean and absolute deviations of only 4.46% and 11.08%. The Colburn correlation was second best with deviations between -9.87% and 10.56%, followed by the 'original' Dittus-Boelter correlation with 10.33% and 13.91%, and the Gnielinski correlation with -23.38% and 26.26%. These predictive trends are consistent with those reported for the smooth tubes.

Table 14: Statistical analysis of the experimental single-phase internally-grooved tube heat transfer measurements

	Dittus-Boelter 'common'	Dittus-Boelter 'original'	Colburn	Gnielinski
$\bar{\varepsilon}$	4.46%	10.33%	-9.87%	-23.38%
$\lvert\bar{\varepsilon}\rvert$	11.08%	13.91%	10.56%	26.26%

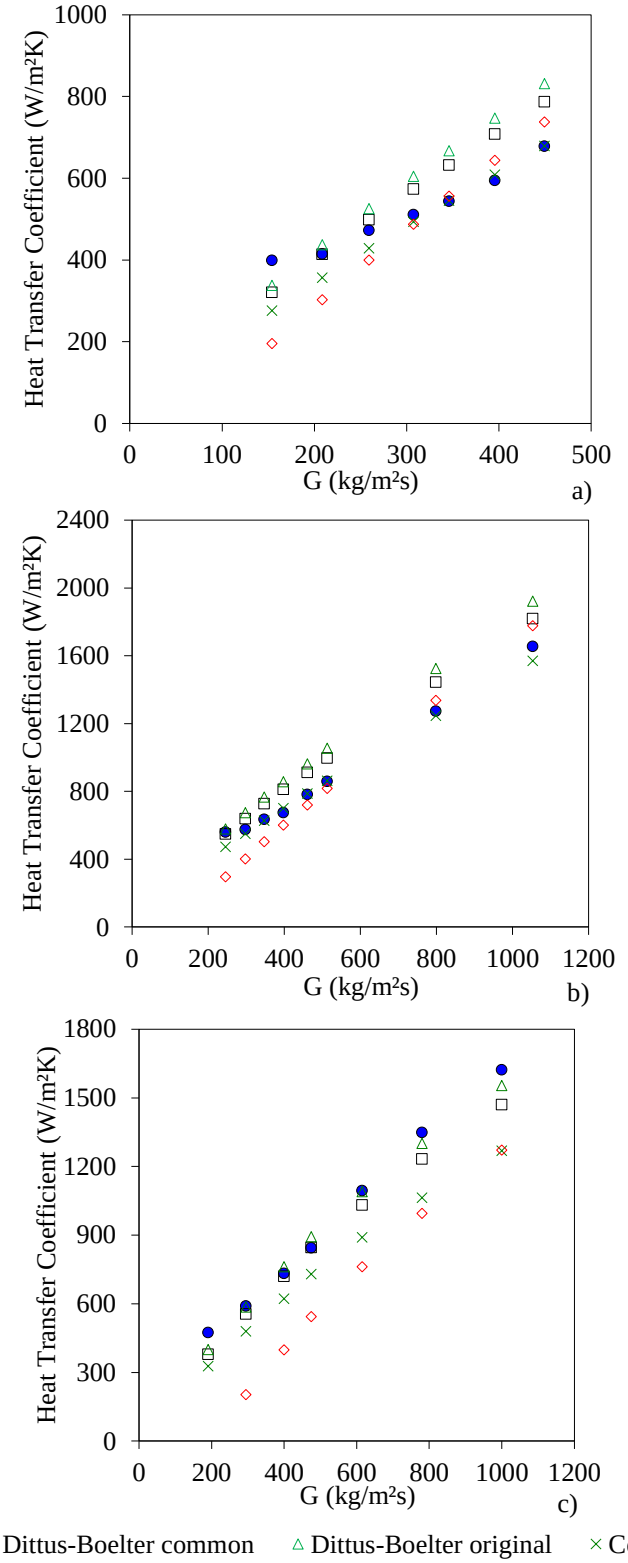

Figure 41: Experimental and predicted single-phase heat transfer coefficient vs mass flux for a) 8.84 mm internally-grooved tube, b) 4.54 mm internally-grooved tube, and c) 2.62 mm internally-grooved tube

The above single-phase energy balance and single-phase heat transfer statistical analysis indicates that the test setup is functioning properly and the experimental method is robust and can provide reliable measurements. This analysis also justifies the use of the Ravigururajan and Bergles [28] enhancement factor, E_{rb}, for predicting turbulence effects resulting from the groove structures in the two-phase internally-grooved tube correlation developed in Chapter 4.

Chapter 8: Two-Phase Data and Discussion

This chapter outlines the experimental validation of the physics-based heat transfer coefficient model described Chapter 4 that recognizes the role played by two-phase flow structures in enhancing thermal transport within internally-grooved tubes. Flow regime data, obtained with dynamic total-internal-reflection measurements described in Chapter 6, and heat transfer coefficient data, obtained with infrared thermography and the test setup described in Chapter 5, are presented and analyzed for two-phase HFE-7100 flow in horizontal, 2.62-8.84 mm diameter, smooth and internally-grooved tubes, with mass fluxes from 25-300 kg/m²s, heat fluxes from 4-56 kW/m², and exit vapor qualities approaching 1.

First, the flow regime results are compared to the Wojtan et al. [30] smooth tube map and the Sharar et al. [29] internally-grooved tube map. Next, the smooth tube and internally-grooved tubes heat transfer results will be compared at varying mass fluxes and heat fluxes to illustrate the validity of the current regime-based approach to explaining enhancement in internally-grooved tubes. This data is then used to statistically validate the new flow regime based heat transfer coefficient correlation, as well as correlations from the literature. Finally, the new heat transfer model will be compared to independent data in the literature and the chapter results will be summarized.

An extensive heat transfer coefficient and flow regime database of over 6,500 combined data points for the adiabatic and diabatic smooth and internally-grooved tubes, respectively, was acquired. For the sake of brevity, only select data and figures will be used to explain the points above. Please refer to Appendix C - Appendix E for all of the heat transfer data collected and Appendix F for a more comprehensive statistical analysis

of the correlations for smooth and internally-grooved tubes – only summaries and selected results are given herein.

As reported in the error analysis in Chapter 5, the reported heat transfer coefficients in the internally-grooved tubes are average augmented values accounting for the increased area enhancement. Therefore, uncertainty stemming from ambiguity in the reported area enhancement is not propagated in the heat transfer error measurement. However, when normalizing the results to account for area enhancement in summary charts, it should be expected that small ~1-5% error (based on a conversation with Wieland and the understanding that this is a carefully controlled industrial process) is introduced due to slight manufacturing deviations.

8.1 8.84mm Smooth and Internally-Grooved Tubes

8.1.1 Influence of Mass Flux and Flow Regime

Figure 42 shows the adiabatic results of the flow visualization/quantification, plotted in coordinates of mass flux and vapor quality and superimposed on the smooth tube and internally-grooved tube flow regime maps; Figure 42a is the smooth tube experimental results on the Wojtan et al. [30] map, Figure 42b is the internally-grooved tube results plotted on the Wojtan et al. map [30], and Figure 42c is the internally-grooved tube data plotted on the current Sharar et al. [29] map. Stratified data points are represented by red circles, Intermittent data points are blue triangles, and Annular data points are shown by green squares. Please note, for figure clarity, the diabatic flow visualization results are not shown but the adiabatic data points shown on Figure 42 are representative of the flow trends observed.

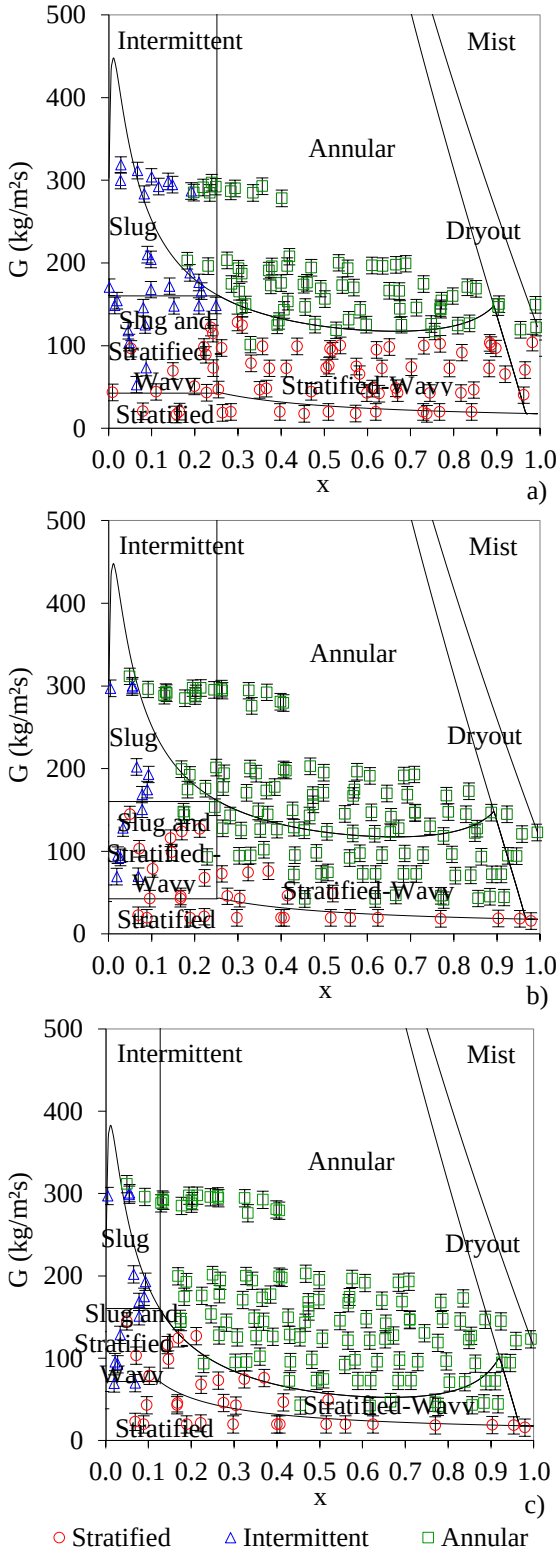

Figure 42: 8.84mm smooth tube data plotted on a) the Wojtan et al. [30] map and 8.84mm internally-grooved tube data plotted on b) the Wojtan et al. [30] map and c) the Sharar et al. [29] map with HFE-7100 at 61°C, G=50 kg/m²s, and q"=9 kW/m²

The transitions of flow pattern observed were Stratified, Intermittent, and Annular in the direction of increasing G and x. It's apparent from Figure 42 that the transition to Annular flow in the internally-grooved tube is seen to occur at lower mass flux and vapor quality compared to the smooth tube. For example, at a mass flux of G=75 kg/m²s and vapor quality greater than x=0.4, Annular flow was encountered in the internally-grooved tube while the smooth tube was operating in Stratified flow. In fact, Annular flow did not occur in the smooth tube for mass fluxes below G=125 kg/m²s while the internally-grooved tube was found to sustain Annular flow at mass fluxes as low as G=50 kg/m²s.

In addition to early Stratified-to-Annular transition, the internally-grooved tube provided early transition from Intermittent to Annular flow at higher mass fluxes. As an example, at a mass flux of G=200 kg/m²s and vapor quality greater than x=0.1 the internally-grooved tube is operating in Annular flow. This transition does not occur in the smooth tube until a vapor quality of approximately 0.3.

It's also interesting to note that at sufficiently low mass fluxes, $G \leq 25$ kg/m²s, both the smooth and internally-grooved tubes are operating in Stratified flow. Similarly, at high mass fluxes, $G \geq 125$ kg/m²s, and high vapor qualities, x=0.3, both the smooth tube and the internally-grooved tube are operating in Annular flow. As shown in Figure 42a, the Wojtan et al. [30] flow regime map captures these smooth tube trends well, correctly predicting 178/197 flow regime data points (90.3%). However, as shown in Figure 42b the Wojtan et al. [30] map does a poor job predicting flow regime in the internally-grooved tube, correctly predicting only 122/186 data points (65.6%). The Sharar et al. [29] modified flow regime map shown in Figure 42c correctly predicted 164/186 (87.7%) of the flow regime data in the internally-grooved tube, representing a 22% improvement in

predictive accuracy of the traditional Wojtan et al. [30] model. It's worth mentioning that the new model does mis-predict a number of Annular data points at low mass flux and high vapor quality; this is clear in Figure 42c at vapor qualities greater than 0.4 and a mass flux of 50 kg/m²s.

Figure 43 shows a comparison of experimental heat transfer coefficients for the smooth and internally-grooved tubes with HFE-7100 at a heat flux of 9 kW/m² for three mass fluxes; Figure 43a is a mass flux of 25 kg/m²s, Figure 43b is a mass flux of 75 kg/m²s, and Figure 43c is a mass flux of 200 kg/m²s. The experimental smooth tube data points are shown as red squares and the internally-grooved tube data points are green circles. 'IG 1' and 'smooth 1' were the first tests run and 'IG 2' and 'smooth 2' were the second tests run; these do not represent different tubes, just a second set of experiments for validation. The smooth tube heat transfer coefficient correlation as described by Wojtan et al. [31] and the internally-grooved tube heat transfer coefficient correlation, described in the current study, are plotted as solid red and dashed green lines, respectively.

As can be seen in Figure 43a, the smooth and internally-grooved tube heat transfer coefficients remain low over the full range of vapor qualities tested for a mass flux of 25 kg/m²s. This is a result of the prevalence of Stratified flow in both the smooth and internally-groove tube, as shown in Figure 43 and discussed above. At a mass flux of 25 kg/m²s the smooth and internally-grooved tubes have θ_{dry} values between 0 to 2π. Since early flow regime transition has not occurred in the internally-grooved tube, the full enhancement effect, combining area enhancement with favorable regime transition, has not been observed. In this case, the internally-grooved tube enhancement ratio, defined as the

grooved tube heat transfer coefficient divided by the smooth tube coefficient, is close to the area enhancement, 1.5.

As shown in Figure 43b, the smooth tube heat transfer coefficient for a mass flux 75 kg/m²s is similar to Figure 43a and remains low over the full range of vapor qualities tested. Again, this is due to the prevalence of Stratified flow and a large dry perimeter ($\theta_{dry} \neq 0$). This is evident from Figure 42a at a mass flux of 75 kg/m²s where the smooth tube is consistently operating in Stratified flow. However, the trend for the internally-grooved tube is much different from Figure 42a as a result of early transition to Annular flow and a fully wetted perimeter ($\theta_{dry}=0$). As can be seen in Figure 42b/c, at 75 kg/m²s and vapor qualities greater than x=0.4, Annular flow was encountered in the internally-grooved. The result is a progressively higher heat transfer coefficient as vapor quality increases, Annular flow develops in the tube, and the Annular film thins. Eventually, dryout occurs at vapor qualities close to 1 and the heat transfer coefficient significantly reduces to a value close to the smooth tube values. In this case, the internally-grooved tube enhancement ratio reaches a maximum value of close to 6.5 at high vapor quality, where thin film Annular flow prevails in the internally-grooved tube and Stratified flow persists in the smooth tube. The practical benefit of operating at this low mass flux where the enhancement is shown to be 6.5x is the reduction in pumping power associated with this operating condition.

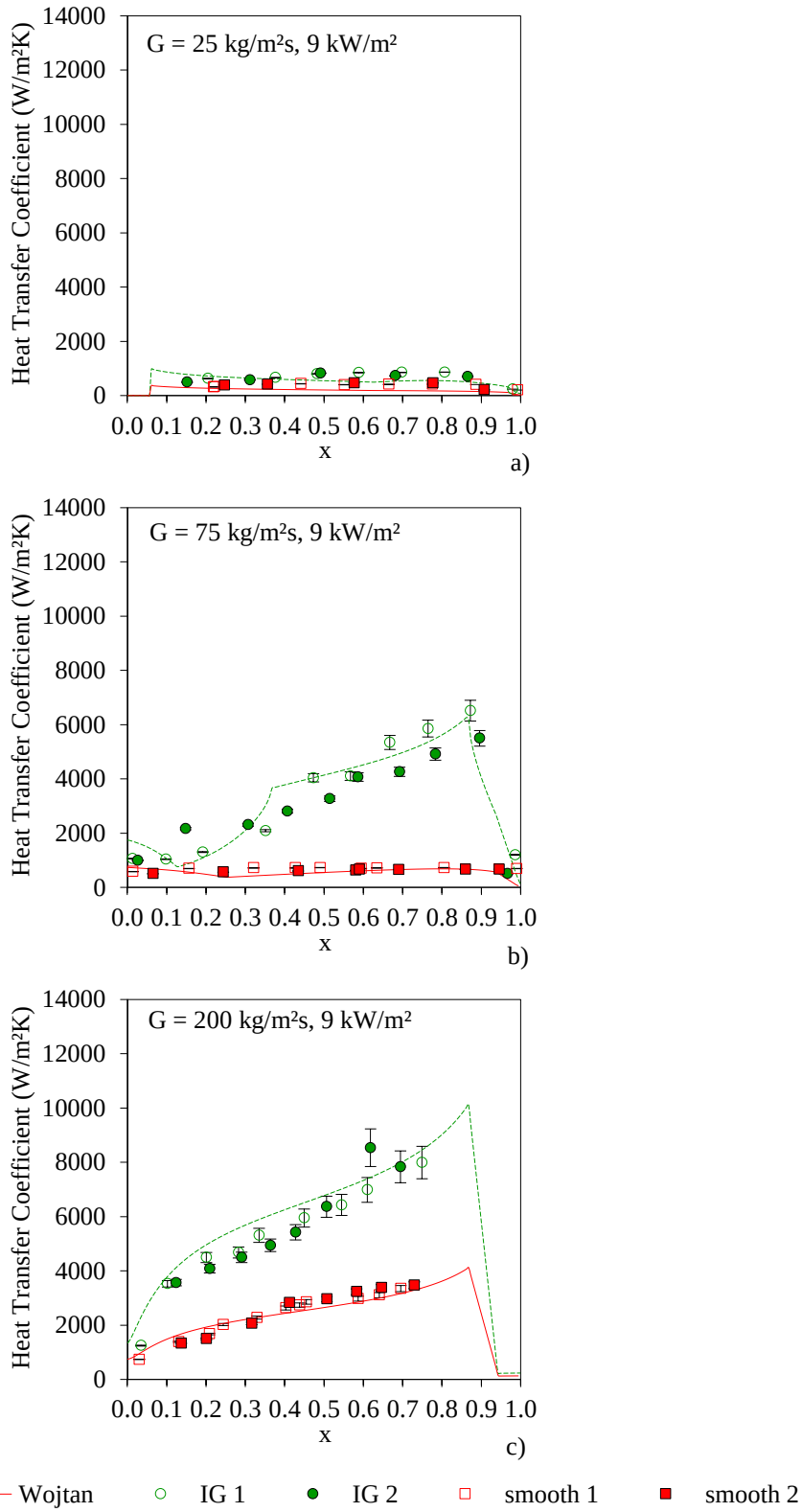

Figure 43: Comparison of heat transfer coefficient vs vapor quality for a mass flux of a) 25 kg/m²s, b) 75 kg/m²s, and c) 200 kg/m²s with HFE-7100 at 61°C and q"=9 kW/m² in the 8.84mm tubes

The trends shown in Figure 43c for a mass flux of 200 kg/m²s are, again, different from those observed at 25 and 75 kg/m²s. For both the smooth tube and the internally-grooved tube, the heat transfer coefficients increase monotonically as vapor quality increases. As shown in Figure 42, this is due to the predominance of Annular flow (θ_{dry}=0) in both the smooth and internally-grooved tube and a thinning Annular film as vapor quality increases. Similar to the case for 25 kg/m²s, the enhancement factor approaches the area enhancement at a mass flux of 200 kg/m²s because both tubes are operating in the same flow regime.

It's interesting to note that the measured heat transfer coefficient for different runs of the smooth tube agreed very well for all conditions shown in Figure 43, where it was operating deep in Stratified or Intermittent/Annular flow. The same is true for 25 kg/m²s and 200 kg/m²s in the internally-grooved tube where the tube is operating in Stratified or Intermittent/Annular flow. However, there is more variability between 'IG 1' and 'IG 2' at a mass flux of 75 kg/m²s near the Stratified-Wavy to Annular transition boundary. More detail on this point is given in 8.6.2 below.

8.1.2 Influence of Heat Flux

Heat flux has an impact on the contribution of nucleate boiling to thermal transport from the wetted wall and on dry-out inception and completion. A higher heat flux results in a higher wall temperature, thus causing faster and more aggressive bubble nucleation, growth, and departure. Therefore, higher heat flux generally enhances two-phase heat transfer coefficients. Alternatively, higher heat flux is also observed to yield earlier dryout at lower vapor quality compared to lower heat fluxes and, consequently, a degraded heat transfer coefficient. Figure 44 shows heat transfer coefficient vs vapor quality for the

8.84mm smooth and internally-grooved tubes for a mass flux of 200kg/m²s and six different heat fluxes; Figure 44a is a heat flux of 4 kW/m², Figure 44b is a heat flux of 9 kW/m², Figure 44c is a heat flux of 18 kW/m², Figure 44d is a heat flux of 28 kW/m², Figure 44e is a heat flux of 40 kW/m², and Figure 44f is a heat flux of 56 kW/m². Please refer to Appendix C for additional data.

The smooth tube and internally-grooved tube correlations both predict higher heat transfer coefficients at low vapor quality as the heat flux increases. For example, at a vapor quality of 0.1 the smooth tube correlation predicts an improvement from 1467 W/m²K to 2386 W/m²K when moving from a heat flux of 4 kW/m² to 56 kW/m² due to nucleate boiling enhancement. The internally-grooved tube correlation predicts a similar trend and increases from approximately 3820 W/m²K to 5068 W/m²K with heat fluxes of 4 kW/m² to 56 kW/m², respectively. However, this enhancement diminishes at higher vapor quality where nucleate boiling is suppressed and convective vaporization dominates. This is clear from Figure 44a and Figure 44f where the heat transfer coefficient is approximately 7500 W/m²K for both 4 kW/m² and 56 kW/m² in the internally-grooved tube. Another interesting effect is a reduction in the vapor quality at which dryout occurs with increasing heat flux. The vapor quality where dryout occurs changes from 0.91 to 0.63 for the smooth and internally-grooved tube correlations when moving from 4 kW/m² to 56 kW/m².

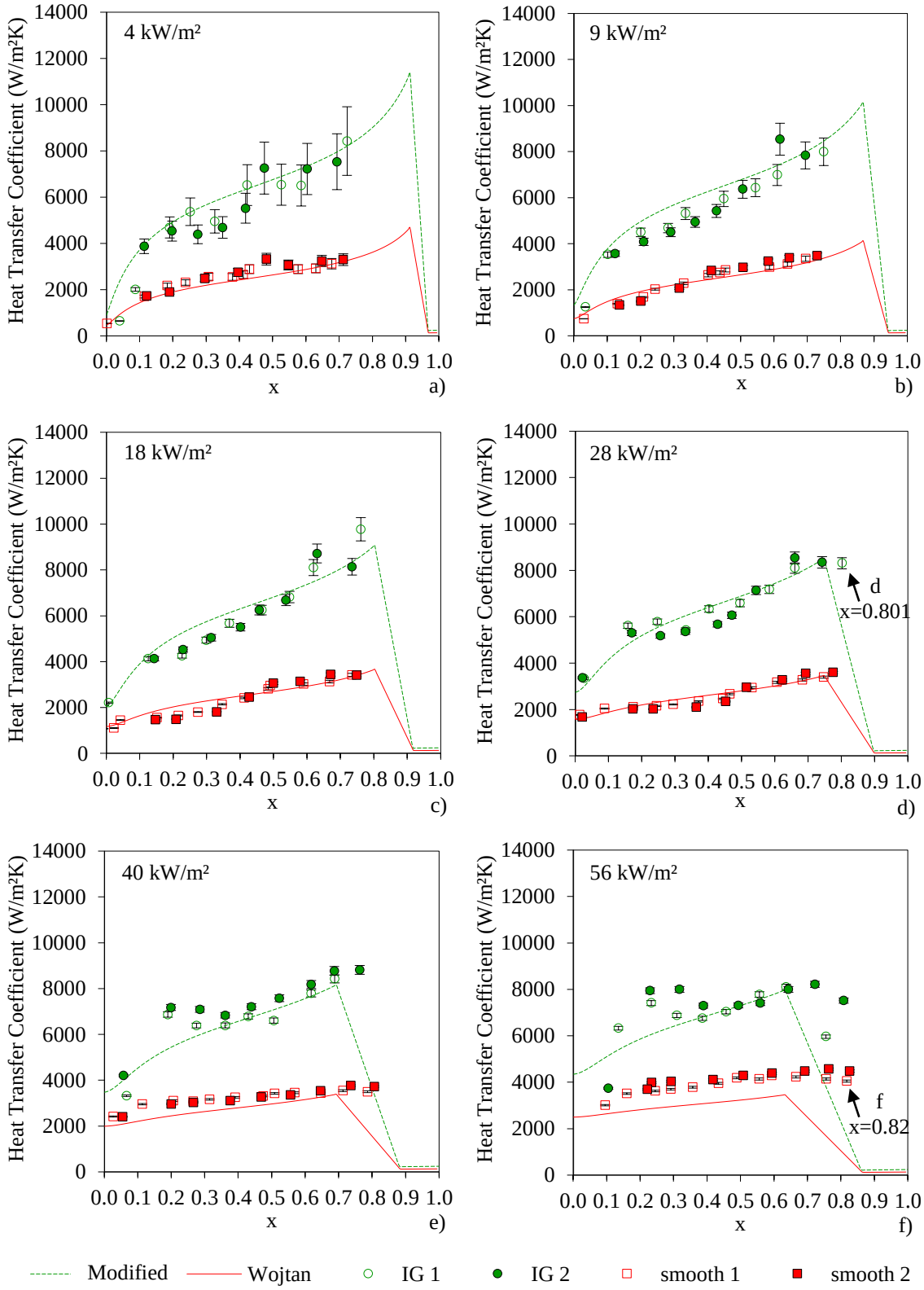

Figure 44: Comparison of heat transfer coefficient vs vapor quality for the 8.84mm tubes with HFE-7100 at 61°C and a mass flux of 200 kg/m²s for heat fluxes of a) 4 kW/m², b) 9 kW/m², c) 18 kW/m², d) 28 kW/m², e) 40 kW/m², and f) 56 kW/m²

The correlations were found to accurately predict data with heat fluxes at and below 28 kW/m² but were less accurate for the heat transfer data for higher heat flux values of 40 kW/m² and 56 kW/m². The mean deviation, $\overline{\varepsilon}$, and mean of absolute value of deviations, $|\overline{\varepsilon}|$, for a mass flux of 200 kg/m²s and heat flux ranging from 4-28 kW/m² was -4.01% and 11.01%, respectively, for the smooth tube data and original Wojtan et al. correlation. For the same conditions, but a heat flux between 40 and 56 kW/m², the mean and absolute deviation rose to -26.50% and 26.61%, respectively. This was less dramatic for the internally-grooved tube data with mean and absolute deviations of 13.92% and 12.54% for heat fluxes between 4 and 28 kW/m² and deviations of 12.91% and -11.87% for heat fluxes of 40 and 56 kW/m². This may be a result of enhanced convective cooling in the internally-grooved tube that acts to suppress boiling.

This effect is clear at the highest mass flux tested, 56 kW/m², and low to moderate vapor qualities where the measured dependence on heat flux was larger than the values predicted by the Wojtan et al. [31] correlation and the new correlation, defined in Chapter 4. The effect is, as expected, more dramatic in the nucleate boiling region (at low vapor qualities). These trends were also mentioned by in the PhD Thesis by Canerie [152] for R-134a in 7.91mm smooth tube and heat fluxes up to 25 kW/m² and for the data by da Silva Lima et al. [160].

As shown in Figure 44, the models have difficulty predicting the vapor quality at which dryout occurs. However, the models seem to predict the majority of the data at low to moderate heat flux well. Future studies and model development should focus on a more comprehensive understanding of nucleate boiling and dryout mechanisms in smooth and internally-grooved tubes.

8.2 4.54mm Smooth and Internally-Grooved Tubes

8.2.1 Influence of Mass Flux and Flow Regime

Figure 45 shows the adiabatic results of the flow visualization/quantification, plotted in coordinates of mass flux and vapor quality and superimposed on the smooth tube and internally-grooved tube flow regime maps; Figure 45a is the 4.54mm smooth tube experimental results on the Wojtan et al. [30] map, Figure 45b is the internally-grooved tube results plotted on the Wojtan et al. [30] map, and Figure 45c is the internally-grooved tube data plotted on the current Sharar et al. [29] map. Stratified data points are represented by red circles, Intermittent data points are blue triangles, and Annular data points are shown by green squares. The diabatic flow visualization results are not shown for figure clarity but the adiabatic data points shown are representative of the flow trends observed.

The transitions of flow pattern observed were Stratified, Intermittent, and Annular in the direction of increasing G and x. Similar to the 8.84mm results in Figure 42, the transition to Annular flow in the 4.54mm internally-grooved tube occurred at lower mass flux and vapor quality compared to the smooth tube. For example, at a mass flux of G=75 kg/m²s and vapor quality greater than x=0.45, the smooth tube was operating in Stratified flow and the internally-grooved tube had transitioned to Annular flow. Annular flow did not occur in the smooth tube for mass fluxes below G=100 kg/m²s while the internally-grooved sustained Annular flow at mass fluxes as low as G=50 kg/m²s.

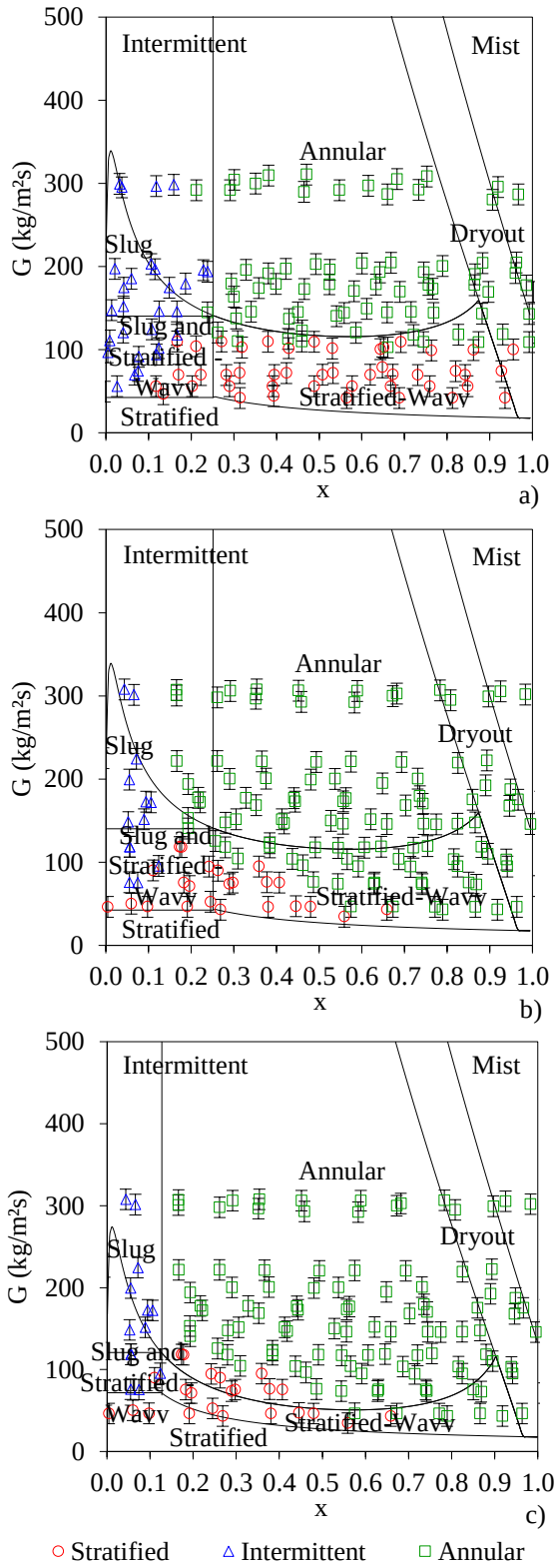

Figure 45: 4.54mm smooth tube data plotted on a) the Wojtan et al. [30] map and 4.54mm internally-grooved tube data plotted on b) the Wojtan et al. [30] map and c) the Sharar et al. [29] map with HFE-7100 at 61°C, G=50 kg/m²s, and q"=9 kW/m²

In addition to early Stratified to Annular transition, the internally-grooved tube provided early transition from Intermittent to Annular flow at higher mass fluxes. As an example, at a mass flux of G=200 kg/m²s and vapor quality greater than x=0.1 the internally-grooved tube was operating in Annular flow. This transition does not occur in the smooth tube until a vapor quality of approximately 0.25. It's also interesting to note that at sufficiently low mass fluxes and vapor qualities, $G \leq 100$ kg/m²s and $x \leq 0.4$, both the smooth and internally-grooved tubes were operating in Stratified flow. Similarly, at high mass fluxes, $G \geq 125$ kg/m²s, and high vapor qualities, $x \geq 0.25$, both the smooth tube and the internally-grooved tube are operating in Annular flow.

As shown in Figure 45a, Wojtan et al. [30] flow regime map captures these smooth tube trends well, predicting 145/165 data points (87.9% accurate). However, as shown in Figure 45b the Wojtan et al. [30] flow regime map does a poor job predicting flow regime in the internally-grooved tube because Annular flow is shifted to lower mass flux and vapor quality; only 119/166 data points are correctly predicted (71.7%). The Sharar et al. [29] modified flow regime map shown in Figure 45c does a good job predicting flow regime in the internally-grooved tube, correctly predicting 146/166 data points (87.9%); this represents an improvement of 16% over the traditional model. Again, the new model mis-predicts a small number of Annular data points at low mass flux and high vapor quality; one clear example is at a mass flux of 50 kg/m²s where the model is predicting Stratified-Wavy flow and the tube was found to operate in Annular flow.

Figure 46 shows a comparison of experimental heat transfer coefficients for the smooth and internally-grooved tubes with HFE-7100 at a heat flux of 9 kW/m² for three mass fluxes; Figure 46a for a mass flux of 50 kg/m²s, Figure 46b at a mass flux of 75

kg/m²s, and Figure 46c for a mass flux of 200 kg/m²s. The experimental smooth tube data points are shown as red squares and the internally-grooved tube data points are green circles. Additionally, the smooth tube heat transfer coefficient correlation as described by Wojtan et al. [31] and the internally-grooved tube heat transfer coefficient correlation described in the current study are plotted as solid red and dashed green lines, respectively.

As can be seen in Figure 46a, the smooth tube heat transfer coefficient remains low over the full range of vapor qualities tested for a mass flux of 50 kg/m²s. This is a result of the prevalence of Stratified flow in the smooth tube and a large dry perimeter ($\theta_{dry} \neq 0$), as shown in Figure 45; at a mass flux of 50 kg/m²s the smooth tube has θ_{dry} values between 0 to 2π. Under the same conditions, flow regime transition to Annular flow in the internally-grooved tube has occurred and the enhancement effect is observed. In this case, the internally-grooved tube enhancement ratio, defined as the grooved tube heat transfer coefficient divided by the smooth tube coefficient, is close to 6.5. It's interesting to note that the heat transfer coefficient significantly under predicts the heat transfer coefficient at high vapor quality, x=0.6-0.8, because the flow regime map and model predict that the flow regime should transition back to Stratified flow but the observed flow regime was Annular flow prior to dryout. This trend can also be seen in Figure 42c for the 8.84mm internally-grooved tube.

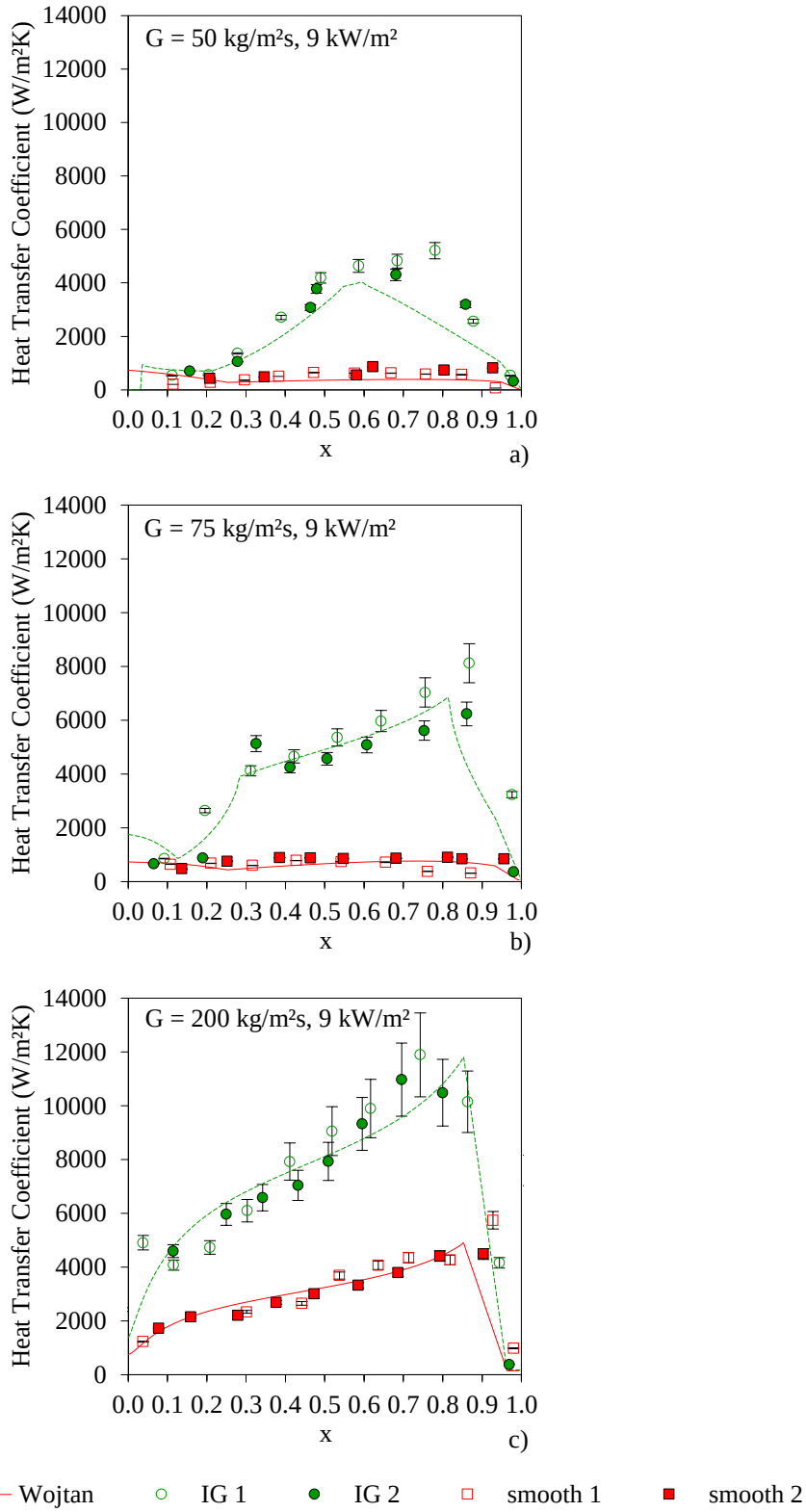

Figure 46: Comparison of heat transfer coefficient vs vapor quality for a mass flux of a) 50 kg/m²s, b) 75 kg/m²s, and c) 200 kg/m²s with HFE-7100 at 61°C and q"=9 kW/m² in the 4.54mm tubes

As shown in Figure 46b, the smooth tube heat transfer coefficients for a mass flux 75 kg/m²s are similar to Figure 46a and remain low over the full range of vapor qualities tested. Again, this is due to the prevalence of Stratified flow. This is clear from Figure 45a where it may be seen that, at a mass flux of 75 kg/m²s, the smooth tube is consistently operating in Stratified flow. However, as can be seen in Figure 45b, at 75 kg/m²s and vapor qualities greater than x=0.4, Annular flow was observed in the internally-grooved tube. The result is a progressively higher heat transfer coefficient as vapor quality increases, Annular flow is developed, and the Annular film thins. Eventually, dryout occurs at vapor qualities close to 1 and the heat transfer coefficient significantly reduces to a value close to the smooth tube values. In this case, the internally-grooved tube enhancement ratio reaches a maximum value of close to 6 at high vapor quality, where thin Annular flow prevails in the internally-grooved tube and Stratified flow persists in the smooth tube. Again this low-flowrate operating point represents the ability for maximum enhancement while simultaneously reducing pumping power.

The trends shown in Figure 46c for a mass flux of 200 kg/m²s are similar to those for the larger diameter tube, Figure 43c. For both the smooth tube and the internally-grooved tube, the heat transfer coefficients increase monotonically as vapor quality increases due to the predominance of Annular flow (θ_{dry}=0) and a thinning film as vapor quality increases. The enhancement factor approaches the area enhancement at a mass flux of 200 kg/m²s because both tubes are occupying the same flow regime. Similar to the 8.84mm tube results, the variability in 'IG 1' and 'IG 2' appears to be larger for conditions near flow regime transition (as is the case for the internally-grooved tube at 50 kg/m²s and 75 kg/m²s).

It's interesting to note that the observed and predicted heat transfer coefficients were larger for the 4.54mm tubes than the 8.84mm tubes for similar operating conditions. As shown in Figure 43c, at a mass flux of 200 kg/m²s, heat flux of 9 kW/m², and vapor quality of 0.7, the smooth tube coefficient was 3172 W/m²K and the internally-grooved tube coefficient was 7998 W/m²K. For the same conditions (Figure 46c) the 4.54mm smooth tube had a heat transfer coefficient of 3876 W/m²K and the internally-grooved tube had a coefficient of 9549 W/m²K. This represents a 16% to 18% improvement by transitioning from an 8.84mm to 4.54mm smooth or internally-grooved tube. This trend can be explained by analyzing the predicted film thickness (Equation (27)) and two-phase convective vaporization term (Equation (22)) described in Chapter 4. For a fixed mass flux, vapor quality, void fraction, and heat flux, the smaller diameter tube has a thinner film thickness. At the conditions above, the 8.84mm tube has a predicted film thickness of 89μm and the 4.54mm tube has a predicted film thickness of only 45μm. The two-phase convective vaporization term in Equation (22) is proportional to the fluid thermal conductivity divided by the liquid film thickness, i.e. $h_{cb} \sim \frac{k_L}{\delta}$. Therefore, a smaller diameter tube results in a thinner liquid film and a larger heat transfer coefficient.

8.2.2 Influence of Heat Flux

Figure 47 shows heat transfer coefficient vs vapor quality for the 4.54mm smooth and internally-grooved tubes for a mass flux of 200 kg/m²s and six different heat fluxes; Figure 47a is a heat flux of 4 kW/m², Figure 47b is a heat flux of 9 kW/m², Figure 47c is a heat flux of 18 kW/m², Figure 47d is a heat flux of 28 kW/m², Figure 47e is a heat flux of 40 kW/m², and Figure 47f is a heat flux of 56 kW/m². Refer to Appendix D for all data.

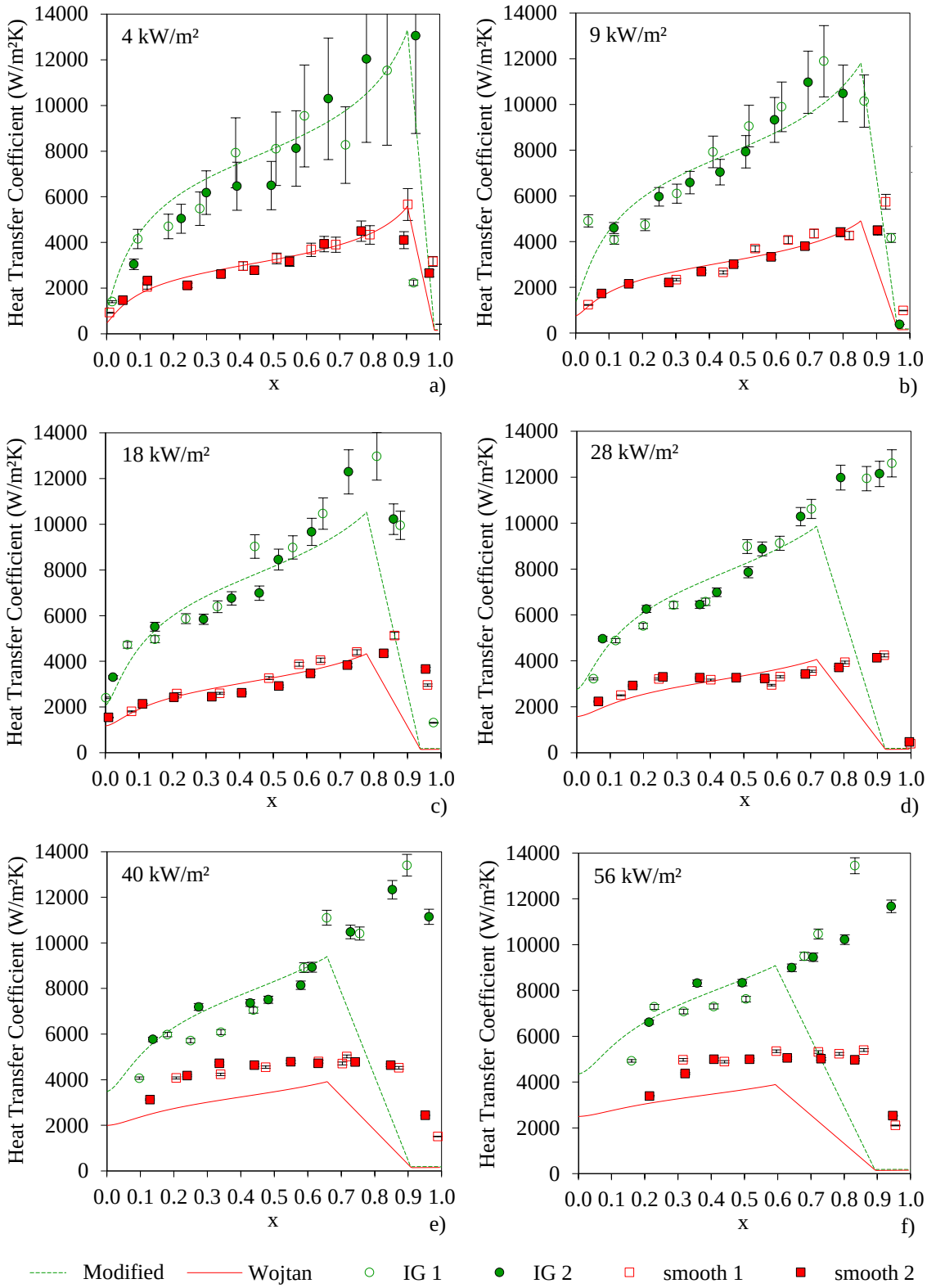

Figure 47: Comparison of heat transfer coefficient vs vapor quality for the 4.54mm tubes with HFE-7100 at 61°C and a mass flux of 200 kg/m²s for heat fluxes of a) 4 kW/m², b) 9 kW/m², c) 18 kW/m², d) 28 kW/m², e) 40 kW/m², and f) 56 kW/m²

The smooth tube and internally-grooved tube correlations both predict higher heat transfer coefficients at low vapor quality as the heat flux increases. For example, at a vapor quality of 0.1 the smooth tube correlation predicts an improvement from 1760 W/m²K to 2771 W/m²K when moving from a heat flux of 4 kW/m² to 56 kW/m² due to nucleate boiling enhancement. The internally-grooved tube correlation predicts a similar trend and increases from approximately 4148 W/m²K to 5618 W/m²K with heat fluxes of 4 kW/m² to 56 kW/m², respectively. However, this enhancement diminishes at higher vapor quality where nucleate boiling is suppressed and convective vaporization dominates. This can be seen from Figure 47a and Figure 47f where the heat transfer coefficient is approximately 8500 W/m²K for both 4 kW/m² and 56 kW/m² in the internally-grooved tube. Another interesting effect is a reduction in the vapor quality at which local dryout occurs with increasing heat flux. The predicted vapor quality where dryout occurs changes from 0.9 to 0.59 for the smooth and internally-grooved tube correlations when moving from 4 kW/m² to 56 kW/m².

The Wojtan et al. [31] smooth tube correlation was found to accurately predict the experimental results for heat fluxes at and below 28 kW/m², with mean and absolute deviations of 20.38% and -9.69%, but was less accurate for higher heat flux values of 40 kW/m² and 56 kW/m², yielding mean and absolute deviations of 46.22% and -46.22%. This trend is similar to what was observed for the 8.84mm smooth tube in Figure 44 and is a result of the combined effect of under-prediction at low vapor quality, as well as at high vapor quality where dryout was predicted, but the tube sustained Annular flow. This effect is clear at the highest heat flux tested, 56 kW/m², and the full range of vapor qualities where the measured dependence on heat flux was much larger than the values predicted by the

Wojtan et al. [31] correlation. Similarly, the 4.54mm internally-grooved tube experimental data matched the model reasonably well for heat fluxes from 4 to 28 kW/m², with mean and absolute deviations of 25.96% and 4.98%. However, the modified model described herein was less accurate at heat fluxes of 40 and 56 kW/m², with mean and absolute deviations of 31.83% and -21.21%. This appears to be largely due to mis-prediction of the vapor quality at which dryout occurs, resulting in under-prediction of the heat transfer coefficient at high vapor quality.

As described above, the models are not able to accurately predict the vapor quality at which dryout occurs for high heat fluxes. The result is an under-prediction of the dryout quality and under-prediction of the heat transfer coefficient at high vapor qualities (x>0.7). Therefore, future studies should focus on a more comprehensive understanding of dryout conditions in smooth and internally-grooved tubes. Inspiration should be drawn from recent experimental and numerical results from Bar-Cohen, Holloway, Riaz, and Kaffel [161] that provides a much more detailed description of interfacial wave patterns, instabilities, and local film rupture, compared to the current model that (incorrectly) assumes a thin uniform film at high vapor quality before dryout.

8.3 2.8mm Smooth and 2.62mm Internally-Grooved Tubes

8.3.1 Influence of Mass Flux and Flow Regime

Figure 48 shows the adiabatic results of the flow visualization/quantification, plotted in coordinates of mass flux and vapor quality and superimposed on the smooth tube and internally-grooved tube flow regime maps; Figure 48a is the 2.8mm smooth tube experimental results on the Wojtan et al. [30] map, Figure 48b is the internally-grooved tube results plotted on the Wojtan et al. [30] map, and Figure 48c is the internally-grooved

tube data plotted on the current Sharar et al. [29] map. Stratified data points are represented by red circles, Intermittent data points are blue triangles, and Annular data points are shown by green squares. The diabatic flow visualization results are not shown for figure clarity but the adiabatic data points shown are representative of the flow trends observed. Please refer to Appendix E for all of the data.

The transitions of flow pattern observed were Stratified, Intermittent, and Annular in the direction of increasing G and x. Similar to the 4.54mm and 8.84mm results in Figure 42 and Figure 45, the transition to Annular flow in the 2.62mm internally-grooved tube occurred at lower mass flux and vapor quality compared to the smooth tube. For example, at a mass flux of G=75 kg/m²s and vapor quality greater than x=0.35, the smooth tube was operating in Stratified flow and the internally-grooved tube had transitioned to Annular flow. Annular flow did not occur in the smooth tube for mass fluxes below G=100 kg/m²s while the internally-grooved sustained Annular flow at the lowest mass flux tested, G=75 kg/m²s.

In addition to early Stratified to Annular transition, the internally-grooved tube provided early transition from Intermittent to Annular flow at higher mass fluxes. As an example, at a mass flux of G=200 kg/m²s and vapor quality greater than x=0.15 the internally-grooved tube was operating in Annular flow. This transition does not occur in the smooth tube until a vapor quality of approximately 0.25.

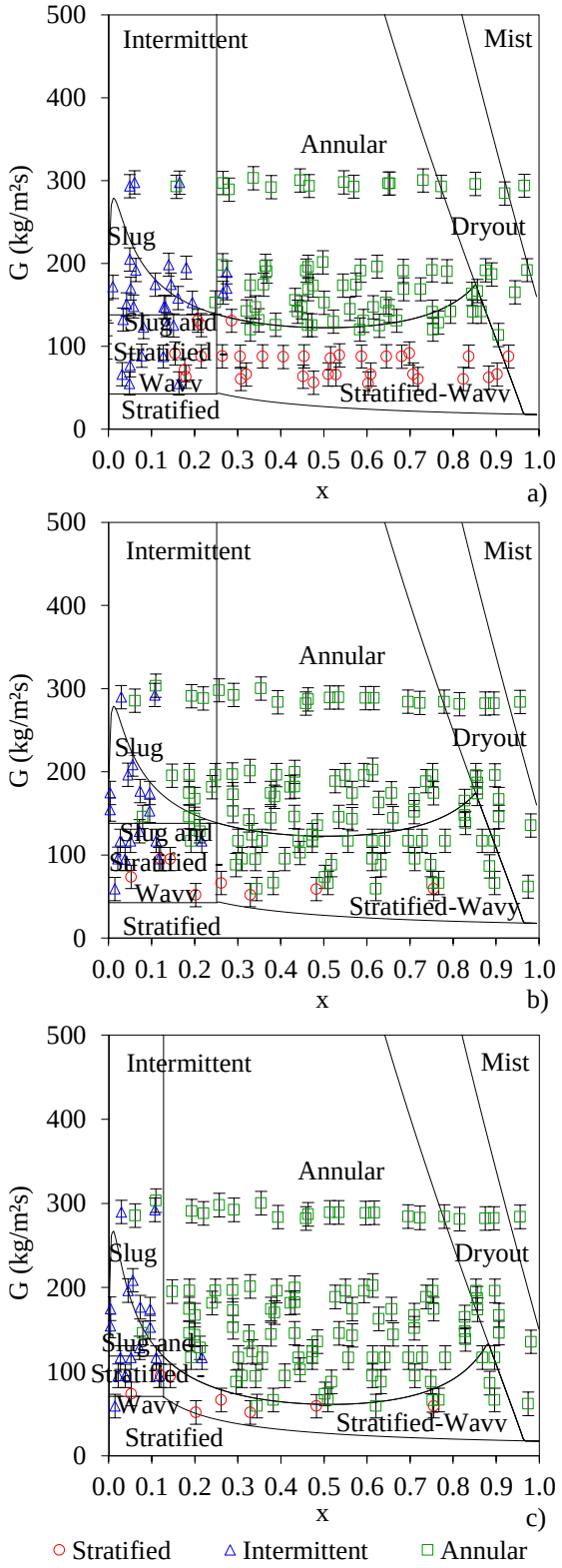

Figure 48: 2.8mm smooth tube data plotted on a) the Wojtan et al. [30] map and 2.62mm internally-grooved tube data plotted on b) the Wojtan et al. [30] map and c) the Sharar et al. [29] map with HFE-7100 at 61°C, G=50 kg/m²s, and q"=9 kW/m²

It's also interesting to note that at sufficiently low mass fluxes and vapor qualities, $G \leq 100$ kg/m²s and $x \leq 0.35$, both the smooth and internally-grooved tubes were operating in Stratified flow. Similarly, at high mass fluxes, $G \geq 125$ kg/m²s, and high vapor qualities, $x \geq 0.25$, both the smooth tube and the internally-grooved tube are operating in Annular flow. As shown in Figure 48a, the Wojtan et al. [30] flow regime map captures these smooth tube trends well, however, as shown in Figure 48b it does a poor job predicting flow regime in the internally-grooved tube; the Wojtan et al. [30] map correctly predicted 131/153 experimental data points for the smooth tube (85.6%) but only 96/153 data points for the internally-grooved tube (62.7%). The Sharar et al. [29] modified flow regime map shown in Figure 48c does a good job predicting flow regime in the internally-grooved tube, correctly predicting 136/153 experimental data points (88.9%). This represents an improvement of 26.2% by adopting the new Sharar, Bar-Cohen, and Jankowski [29] modified flow regime map. Again, the model does not predict Annular data points at low mass flux and high vapor quality, as is the case for 75 kg/m²s and vapor qualities greater than 0.6.

Figure 49 shows a comparison of experimental heat transfer coefficients for the smooth and internally-grooved tubes with HFE-7100 at a heat flux of 9 kW/m² for two mass fluxes; Figure 49a is the lowest mass flux tested for the 2.62-2.8mm tubes (75 kg/m²s) and Figure 49b is a mass flux of 200 kg/m²s. Mass fluxes below 75 kg/m²s could not be accurately tested due to the measurement range of the flow meters being used; please refer to Chapter 5 for more details. The experimental smooth tube data points are shown as red squares and the internally-grooved tube data points are green circles. The smooth tube heat transfer coefficient correlation, as described by Wojtan et al. [31], and the internally-

grooved tube heat transfer coefficient correlation, described in the current study, are plotted as solid red and dashed green lines, respectively.

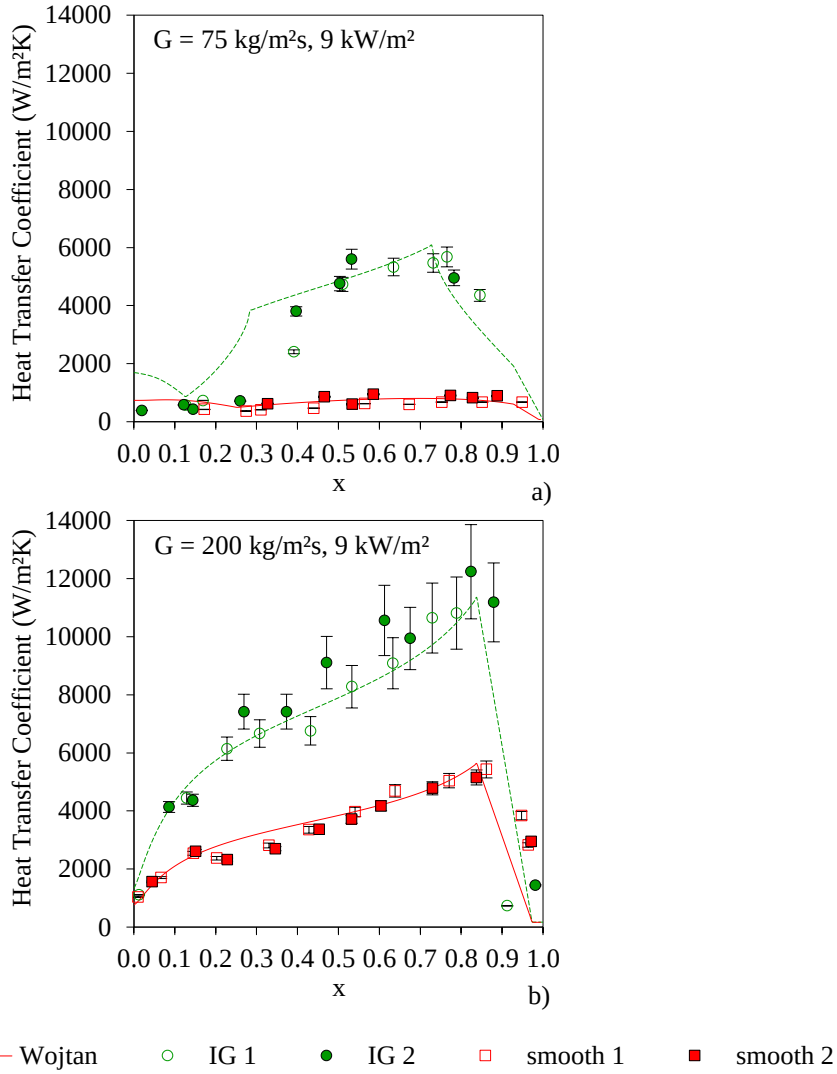

Figure 49: Comparison of heat transfer coefficient vs vapor quality for a mass flux of a) 75 kg/m²s and b) 200 kg/m²s with HFE-7100 at 61°C and q"=9 kW/m² in 2.62-2.8mm tubes

As can be seen in Figure 49a, the smooth tube heat transfer coefficient remains low over the full range of vapor qualities tested, for a mass flux of 75 kg/m²s. This is a result of the prevalence of Stratified flow, as shown in Figure 48a, in the smooth tube and a large dry perimeter ($\theta_{dry} \neq 0$). Under the same conditions, flow regime transition in the

internally-grooved tube has occurred and the enhancement effect is observed. In this case, the internally-grooved tube enhancement ratio, defined as the grooved tube heat transfer coefficient divided by the smooth tube coefficient, is close to 5.5; this condition represents maximum enhancement with the potential for pumping power reduction. It's interesting to note that the heat transfer coefficient model over-predicts the heat transfer coefficient at low vapor quality, x=0.1-0.4. The flow regime map and model predict that the heat transfer coefficient should increase sharply as the Stratified angle reduces and Annular flow is approached. Experimentally, however, Stratified flow was maintained and the heat transfer coefficient remained low until Annular flow was reached at a vapor quality of 0.4.

The trends shown in Figure 49b for a mass flux of 200 kg/m²s are similar to those for the larger diameter tubes, Figure 43c and Figure 46c. For both the smooth tube and the internally-grooved tube, the heat transfer coefficients increase monotonically as vapor quality increases due to the predominance of Annular flow (θ_{dry}=0) and a thinning film. The enhancement factor approaches the area enhancement at a mass flux of 200 kg/m²s because both tubes are occupying the same flow regime.

The observed and predicted heat transfer coefficients were larger for the 2.62mm internally-grooved tube and 2.8mm smooth tube than the 8.84mm tubes for similar operating conditions. As shown in Figure 43c, at a mass flux of 200 kg/m²s, heat flux of 9 kW/m², and vapor quality of 0.7, the smooth tube coefficient was 3172 W/m²K and the internally-grooved tube coefficient was 7998 W/m²K. For the same conditions (Figure 49b) the 2.8mm smooth tube had a heat transfer coefficient of 4642 W/m²K and the internally-grooved tube had a coefficient of 9494 W/m²K. This represents a 16% to 32% improvement by transitioning from an 8.84mm to 2.8mm smooth or 2.62mm internally-

grooved tube, respectively. It's interesting to note that this represents a significant 13% improvement over the 4.54mm smooth tube but a minor reduction for the internally-grooved tube performance. Intuitively this makes sense for the smooth tubes whereby a reduction in tube diameter leads to a thinner film and an increasing heat transfer coefficient. The seemingly contradictory results in the internally-grooved tube can be explained by closer inspection of the Ravigururajan and Bergles turbulent enhancement factor E_{rb} (Equation (36)); the 2.62mm internally-grooved tube has a smaller groove height, smaller number of fins, and smaller helix angle which reduces the component contributed in Equation (36) and (37).

8.3.2 Influence of Heat Flux

Figure 50 shows heat transfer coefficient vs vapor quality for the 2.8mm smooth and 2.62mm internally-grooved tubes for a mass flux of 200kg/ m²s and six different heat fluxes; Figure 50a is a heat flux of 4 kW/m², Figure 50b is a heat flux of 9 kW/m², Figure 50c is a heat flux of 18 kW/m², Figure 50d is a heat flux of 28 kW/m², Figure 50e is a heat flux of 40 kW/m², and Figure 50f is a heat flux of 56 kW/m². Please refer to Appendix E for additional data.

The smooth tube and internally-grooved tube correlations both predict higher heat transfer coefficients at low vapor quality as the heat flux increases. For example, at a vapor quality of 0.1 the smooth tube correlation predicts an improvement from 2083 W/m²K to 2928 W/m²K when moving from a heat flux of 4 kW/m² to 56 kW/m² due to nucleate boiling enhancement. The internally-grooved tube correlation predicts a similar trend and increases from approximately 4421 W/m²K to 5365 W/m²K with heat fluxes of 4 kW/m² to 56 kW/m², respectively. This enhancement diminishes at higher vapor quality where

nucleate boiling is suppressed and convective vaporization dominates. This can be seen at a vapor quality of 0.5 on Figure 50a and Figure 50f where the heat transfer coefficient is approximately 8000 W/m²K for both 4 kW/m² and 56 kW/m² in the internally-grooved tube. The vapor quality at which dryout occurs decreases with increasing heat flux. The vapor quality where dryout occurs changes from 0.9 to 0.56 for the smooth and internally-grooved tube correlations when moving from 4 kW/m² to 56 kW/m².

The Wojtan et al. [31] smooth tube correlation was found to accurately predict the data for heat fluxes at and below 28 kW/m², with a mean and absolute deviation of 30.74% and -0.50%, but was less accurate for higher heat flux values of 40 kW/m² and 56 kW/m², with a mean and absolute deviation of 43.20% and -43.13%. This trend is similar to what was observed for the 8.84mm and 4.54mm smooth tubes in Figure 44 and Figure 47, respectively. This effect is clear at the highest mass flux tested, 56 kW/m², and the full range of vapor qualities where the measured dependence on heat flux was larger than the values predicted by the Wojtan et al. [31] correlation, especially at high vapor quality where the model predicts dryout, but experimentally Annular flow was maintained and the heat transfer coefficient stayed high. The modified heat transfer correlation developed herein showed similar results, with a mean and absolute deviation of just 19.45% and -8.68% for heat fluxes ranging from 4 to 28 kW/m², and deviations of 23.14% and -16.31% for heat fluxes of 40 and 56 kW/m².

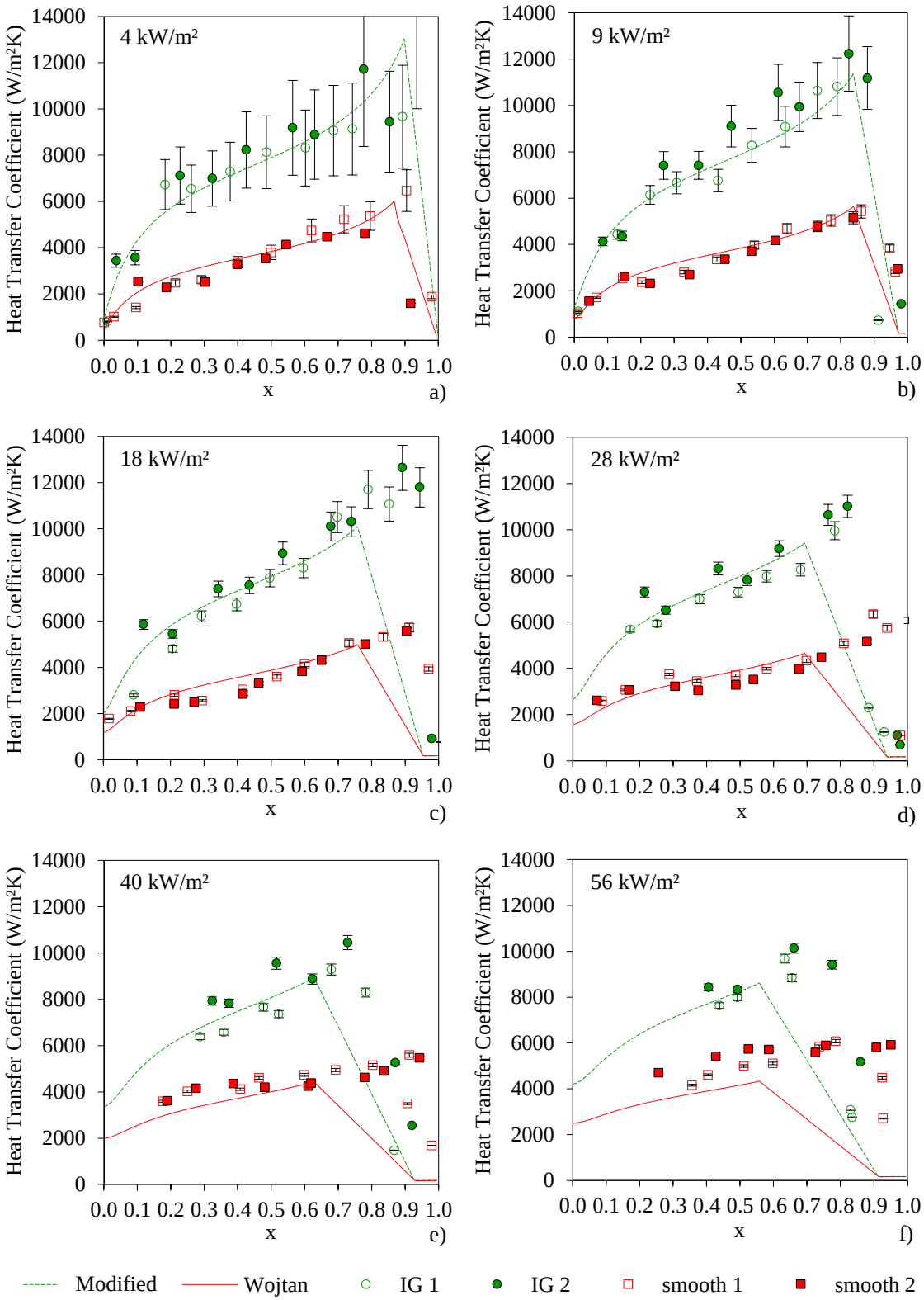

Figure 50: Comparison of heat transfer coefficient vs vapor quality for the 2.62-2.8mm tubes with HFE-7100 at 61°C and a mass flux of 200 kg/m²s for heat fluxes of a) 4 kW/m², b) 9 kW/m², c) 18 kW/m², d) 28 kW/m², e) 40 kW/m², and f) 56 kW/m²

Similar to the 2.0mm smooth tube results and, generally-speaking, the majority of the results in this chapter, a major source of deviation between the predicted and measured heat transfer coefficient appears to derive from a mis-prediction of the vapor quality at which dryout occurs. As shown in Figure 50, the models appear to predict the majority of the dryout data at heat fluxes at and below 9 kW/m² but generally under predicts the vapor quality at which dryout occurs for heat fluxes exceeding 18 kW/m². Future studies should focus on a more comprehensive understanding of dryout conditions in smooth and internally-grooved tubes.

8.4 Tabulation of Flow Regime Modeling Results

Table 15 shows a full tabulation of the predictive accuracy of the original Wojtan et al. [30] flow regime map for the 2.80mm, 4.54mm, and 8.84mm smooth tube data shown in Figure 42a, Figure 45a, and Figure 48a. The left column represents the experimentally observed flow regime or testing parameter and the next three columns represent the number of successful predictions and total data points (successful/total) for the three tube diameters when superimposed on the original Wojtan et al. [30] flow regime map.

As shown in Table 15, and in the previous sections, the Wojtan et al. [30] model did a very good job predicting Stratified and Intermittent flow in the smooth tubes; in fact, the traditional flow regime map correctly predicted 296/301 (98.3%) Stratified and Intermittent data points for the full range tested. However, the Wojtan et al. [30] map was not able to predict a number of Annular data points near the Stratified-Wavy to Annular transition. Despite this minor misgiving, the traditional Wojtan et al. [30] flow regime map correctly predicted 178/197 (90.3%), 145/165 (87.9%), and 131/153 (85.6%) data points

for the 8.84mm, 4.54mm, and 2.80mm smooth tubes, respectively. This represents a total weighted average success rate of 86.2% for all smooth tube data points.

Table 15: Predictive accuracy of Traditional Wojtan et al. [30] flow regime map for the smooth tube data

Fluid **Sat. Temp.** **Diameter**	HFE-7100 61°C 8.84mm	HFE-7100 61°C 4.54mm	HFE-7100 61°C 2.80mm
Model	**Wojtan**	**Wojtan**	**Wojtan**
Stratified **Intermittent** **Annular**	81/83 43/43 54/71	47/47 44/44 54/74	34/34 47/50 50/69
Total **%**	178/197 **90.3%**	145/165 **87.9%**	131/153 **85.6%**

Table 16 shows a full tabulation of the predictive accuracy of the original Wojtan et al. [30] flow regime map and the modified Sharar et al. [29] flow regime map developed in the current study for the 2.62mm, 4.54mm, and 8.84mm internally-grooved tube data, as shown in Figure 42b and c, Figure 45b and c, and Figure 48b and c. The left column represents the experimentally observed flow regime or testing parameter and the next six columns represent the number of successful predictions and total data points (successful/total) for the three tube diameters when superimposed on the original Wojtan et al. [30] flow regime map and the modified Sharar et al. [29] map. As shown in Table 16 and in the previous sections, the Wojtan et al. [30] model generally did a poor job predicting the flow regime in the internally-grooved tubes. The predictive accuracy for Stratified and Intermittent flow was generally good, but the Wojtan et al. [30] map predicted only 58/122, 65/112, and 52/109 Annular data points for the 8.84mm, 4.54mm, and 2.62mm internally-grooved tubes, respectively. This represents a 51.0% predictive accuracy of Annular flow in internally-grooved tubes using the traditional Wojtan et al. [30] flow regime map and a total weighted average success rate 66.7% for all data points.

Table 16: Predictive accuracy of Traditional Wojtan et al. [30] and Modified Sharar et al. [29] flow regime maps for the internally-grooved tube data

Fluid **Sat. Temp.** **Diameter**	HFE-7100 61°C 8.84mm		HFE-7100 61°C 4.54mm		HFE-7100 61°C 2.62mm	
Model	**Wojtan**	**Modified**	**Wojtan**	**Modified**	**Wojtan**	**Modified**
Stratified	34/34	31/34	25/25	19/25	8/8	8/8
Intermittent	30/30	28/30	29/29	29/29	36/36	35/36
Annular	58/122	105/122	65/112	95/112	52/109	93/109
Total	122/186	164/186	119/166	143/166	96/153	136/153
%	**65.6%**	**87.7%**	**71.7%**	**86.1%**	**62.7%**	**88.9%**

The new model, applied to the internally-grooved tubes, did not always improve the success of predicting Stratified and Intermittent flow compared to the Wojtan et al. [30] flow regime map. A minor reduction from 34/34 to 31/34 Stratified data points for the 8.84mm tube and 25/25 to 19/25 Stratified data points for 4.54mm tube was observed. Similarly, a minor reduction from 30/30 to 28/30 Intermittent data points for the 8.84mm tube, and 36/36 to 35/36 Intermittent data points for the 2.62mm tube was shown. However, the new model significantly improves the predictability for Annular flow in all of the studies. The new model improved Annular flow predictive accuracy from 58/122 to 105/122 for the 8.84mm tube, 65/112 to 95/112 for the 4.54mm tube, and 52/109 to 93/109 for the 2.62mm tube; this represents and improvement of 34.4% in predicting Annular flow, from 51.0% accuracy to 85.4%, by adopting the new model. Overall, the new model represents an improvement from 66.7% accuracy for the Wojtan et al. [30] model to 88.3% using the updated transition criteria. Based on these results, the new model appears to far more accurately predict early transition to Annular flow for the current data set.

8.5 Enhancement Ratio

Figure 51 shows a graphical summary of the enhancement ratio vs mass flux based on Figure 43, Figure 46, Figure 49, and additional 9 kW/m² data from Appendix C -

Appendix E. This is similar to the figure shown in the Chapter 4 summary of the simulated modeling results and is revisited here with superimposed experimental data.

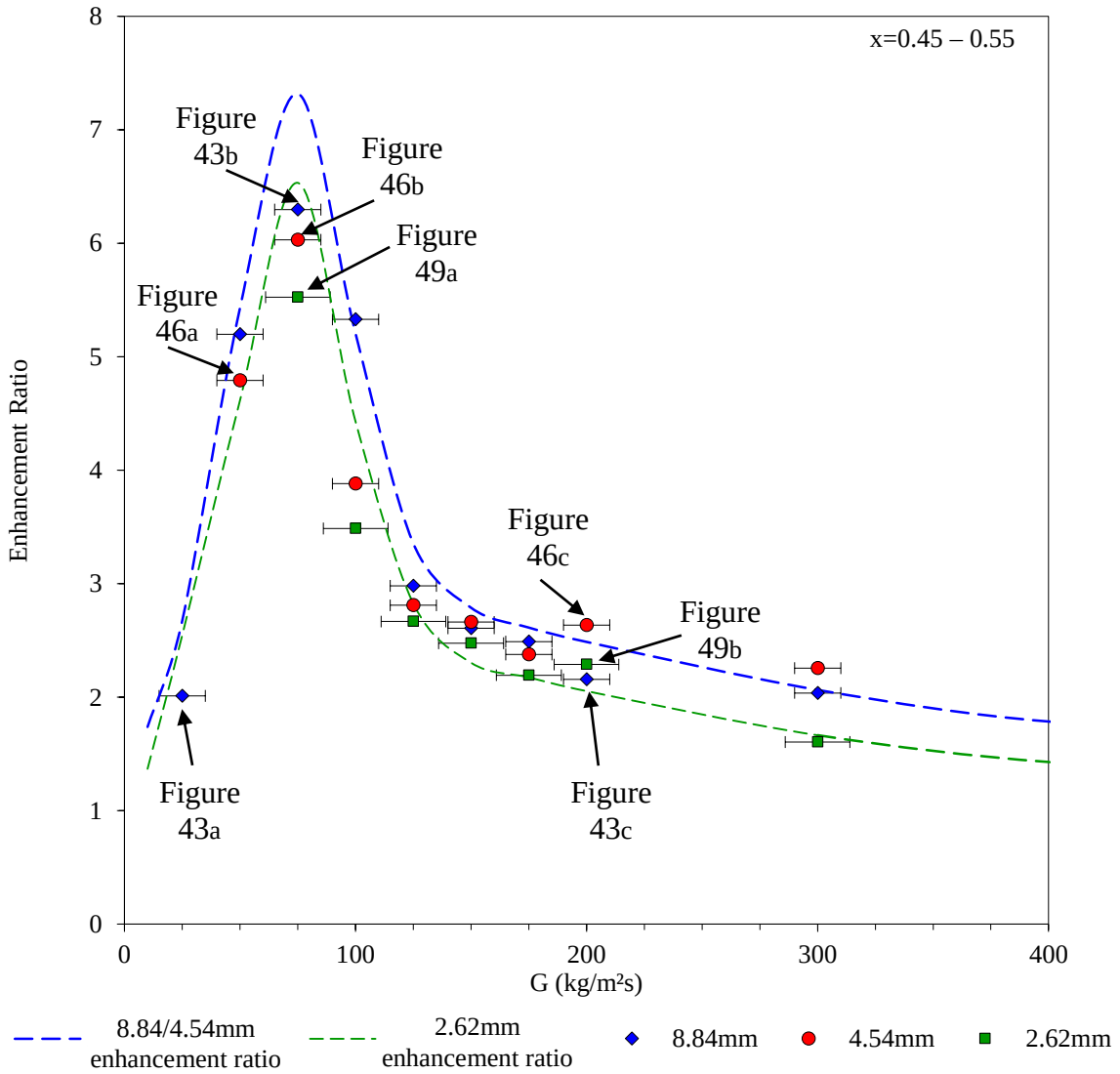

Figure 51: Enhancement ratio vs mass flux with current data for the 8.84mm, 4.54mm, and 2.62mm internally-grooved tubes

The blue dashed line represents the predicted enhancement ratios for a vapor quality of 0.45 to 0.55 for the specific geometric parameters of the 8.84mm tube and plotted as a function of mass flux; again, the enhancement ratio is defined as the internally-grooved tube heat transfer coefficient divided by the smooth tube heat transfer coefficient.

Specifically, this was calculated with HFE-7100 at a saturation temperature of 61°C in an 8.84mm tube with an area enhancement of 1.52, fin height of 0.2mm, and a helix angle of 18°; a similar enhancement ratio was predicted for the 4.54mm tubes and was not included here for figure clarity. The dashed green line is the predicted enhancement ratio for the 2.62mm internally-grooved tube; this was calculated for HFE-7100 at a saturation temperature of 61°C in an 2.62mm tube with an area enhancement of 1.6, fin height of 0.12mm, and a helix angle of 10° Horizontal error bars for the uncertainty in mass flux are shown. Additionally, labels for several data points direct the reader back to corresponding figures earlier in this chapter.

The figure shows heat transfer improvement approximately equal to the area ratio of 1.52 at sufficiently low mass flux where both the smooth and internally-grooved tubes were operating in Stratified or Stratified-Wavy flow; this was the case for the 8.84mm smooth and internally-grooved tube at 9 kW/m² and a mass flux of 25 kg/m²s, as shown in Figure 43a. The enhancement ratio also approached the area enhancement at high mass flux where both tubes were operating in the Slug, Intermittent, or Annular flow regime and the dry angle was zero (θ_{dry}=0); this can be clearly seen in Figure 43c, Figure 44b, Figure 46c, Figure 47b, Figure 49b, and Figure 50b. Large enhancement (5 to 7x) was predicted at low-to-intermediate mass fluxes where the smooth tube was operating in Stratified flow and the internally-grooved tube is operating in Annular flow; this was shown for the 8.84mm, 4.54mm, and 2.62mm internally-grooved tubes in Figure 43b, Figure 46a, Figure 46c, and Figure 49a. These trends are consistent with those described earlier and indicate that the new flow regime map and associated heat transfer coefficient can capture the physical mechanisms responsible for enhancement in internally-grooved tubes.

As shown in Figure 51, different tube geometric parameters (and fluids) result in different predicted enhancement ratios. Therefore, applying these exact predictions to different working fluids, saturation temperatures, and geometric parameters has limitations. Clearly, these parameters can affect the mass flux at which flow regime transition occurs and the relative effect of turbulence, Equation (36), and wet angle heat transfer coefficient, Equation (37). For example, the 2.62mm internally-grooved tube has a smaller helix angle (10° vs 18º), less fins (36 vs 60), and a smaller fin height (0.12mm vs 0.20mm) compared to the 8.84mm and 4.54mm internally-grooved tubes. This results in a reduction from 1.38 to 1.14 in the turbulence factor proposed by Ravagururajan and Bergles [28], and a corresponding reduction on Figure 51.

8.6 Statistical Assessment of the Heat Transfer Coefficient Correlations

In this section, several smooth tube and internally-grooved tube heat transfer coefficient models will be evaluated using the experimental database gathered in the current study for 2.8/2.62mm, 4.54mm, and 8.84mm tubes with heat fluxes from 4 kW/m² to 56 kW/m², mass fluxes ranging from 25 to 300 kg/m²s, and HFE-7100 at 61ºC as the working fluid. Graphs for the largest diameter, 8.84mm, will be shown below and a tabular summary of all results will be provided. Please refer to Appendix F for similar figures for the 4.54mm and 2.62/2.8mm smooth and internally-grooved tubes, and a more detailed table of results. Please note, the figures created only consider 'IG 1' and 'smooth 1' data points which are fully representative of the trends observed for 'IG 2' and 'smooth 2'; this allowed figure clarity. The summary tables, however, considered all of the experimental data. The statistical parameters of mean deviation, $\bar{\varepsilon}$, and mean of absolute value of deviations, $|\bar{\varepsilon}|$, were calculated based on the equations below:

$$\bar{\varepsilon} = \sum\left[\left(h_{predicted} - h_{experimental}\right)100/h_{experimental}\right] \tag{70}$$

$$|\bar{\varepsilon}| = \sum \mathrm{ABS}\left[\left(h_{predicted} - h_{experimental}\right)100/h_{experimental}\right] \tag{71}$$

where $h_{predicted}$ is the heat transfer coefficient predicted by the respective heat transfer coefficient correlation and $h_{experimental}$ is the measured heat transfer coefficient. These parameters are used to assess the success of the models in context of mass flux and flow regime.

8.6.1 Smooth Tubes

Measured smooth tube heat transfer coefficients were compared to the smooth tube two-phase correlations of Wojtan et al. [31], Chen [56], Shah [57], Kandlikar [93], Gungor and Winterton [59], and a simplified two-phase flow boiling correlation by Gungor and Winterton [60] (referred to hereafter as Gungor-Winterton 'new'). Figure 52 shows the predicted heat transfer coefficient values vs the experimental two-phase heat transfer coefficient values for different mass fluxes. The solid black line has a slope of 1, indicating perfect agreement between the model and experimental results. The dashed lines represent ±20% for reference. The properties used while evaluating these correlations were the average values between the inlet and outlet of the test section (at the location of the wall temperature measurements). Table 17 lists a summary of the statistical parameters for the six correlations used.

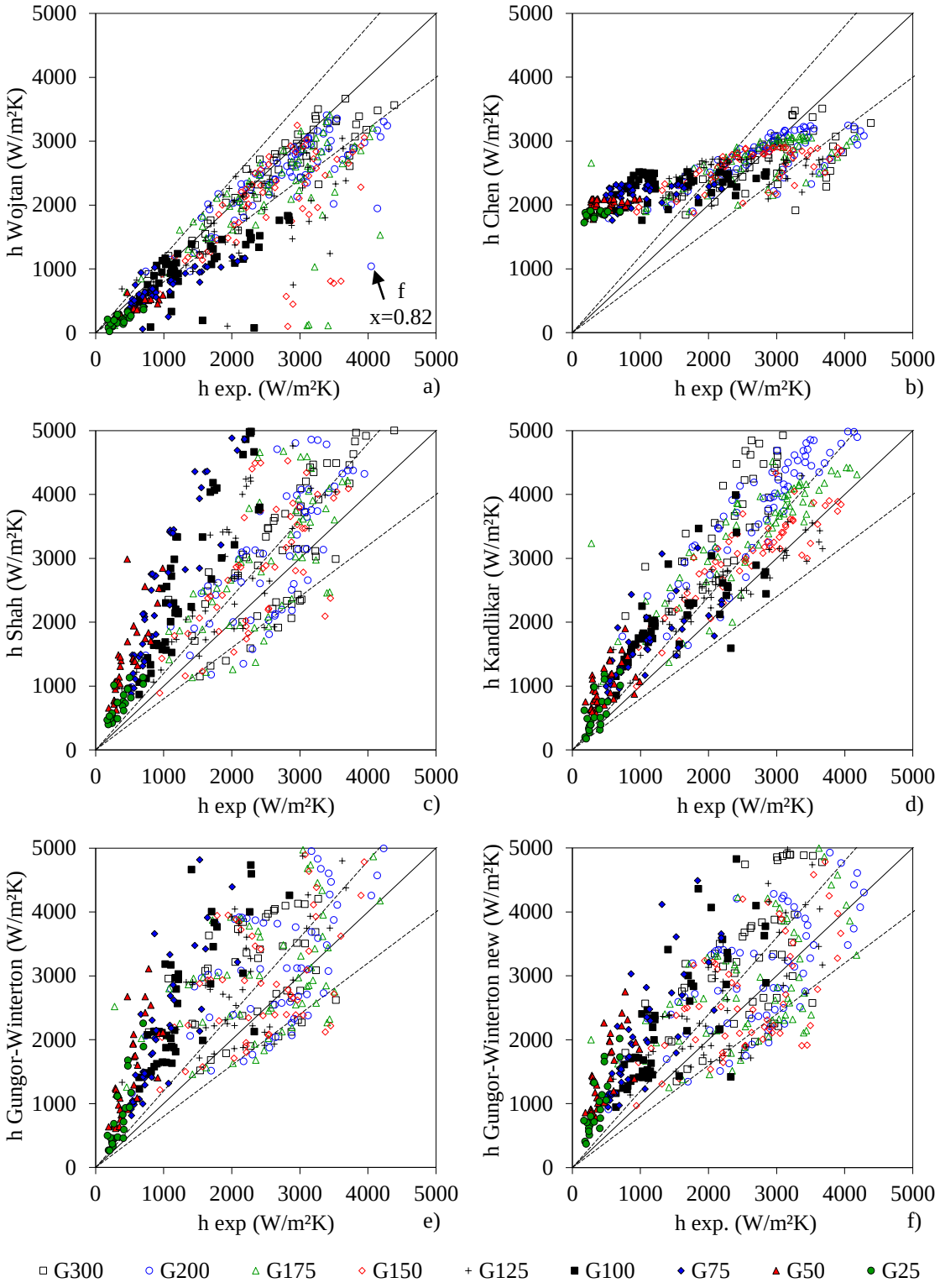

Figure 52: Comparison of the 8.84mm smooth tube experimental data for HFE-7100 at 61°C with correlations from a) Wojtan et al. [31], b) Chen [56], c) Shah [57], d) Kandlikar [93], e) Gungor-Winterton 'original' [59], and f) Gungor-Winterton 'new' [60]

As shown, and also apparent from Figure 52, the flow pattern based model of Wojtan et al. [31] was generally the most accurate for predicting two-phase flow of HFE-7100 in the 8.84 mm smooth tube. The mean and absolute deviations were the best among those evaluated, with values of -14.0% and 26.9%. These results were reasonably consistent across the full range of mass fluxes, indicating the ability of the correlation to predict heat transfer coefficients in different flow regimes.

As shown on Figure 52a, the data was reasonably well centered but the Wojtan et al. [31] model under-predicted a fair amount of data points. Many of these under-predicted data points were at high vapor quality where Annular flow was sustained in the smooth tubes and the model incorrectly predicted dryout. This is clear on Figure 44f at a mass flux of 200 kg/m²s, heat flux of 56 kW/m², and vapor quality of 0.82 where the experimental heat transfer coefficient was ~4200 W/m²K and the predicted value was ~1000 W/m²K; this data point is also indicated on Figure 52a and is clearly seen as falling well outside the ±20% lines. Again, this reinforces the assertion that modeling dryout conditions in smooth tubes needs to be revisited.

The Chen [56], Shah [57], Kandlikar [93], Gungor and Winterton [59], and 'new' Gungor and Winterton [60] correlations over-predicted much of the data and generally performed poorly over the full range of mass fluxes tested. This can be explained by the inability of these correlations to accurately predict heat transfer for Stratified-Wavy and Stratified flow in smooth tubes. For example, below 150 kg/m²s where Stratified-Wavy and Stratified flow was observed in the smooth tubes, the mean and absolute deviations rose to beyond 200% in many cases on Table 17. However, considering only mass fluxes above 150 kg/m²s where Intermittent and Annular flow were observed in the smooth tubes,

the models performed reasonably well. For example, the Chen [56] correlation showed a mean and absolute deviation of only 4.5% and 25.2% for the mass flux of 300 kg/m²s where Annular flow was the dominant flow regime and 679% mean and absolute error for a mass flux of 25 kg/m²s where Stratified flow dominated. It's worth noting that, as repeatedly observed by Rahim, Bar-Cohen, et al. [35] [55], the Chen [56] correlation performs remarkably well in the Annular flow regime and actually outperformed the Wojtan et al. [31] correlation at 300 kg/m²s. Similar trends can be seen for the Shah [57], Kandlikar [93], Gungor-Winterton [59], and 'new' Gungor-Winterton [60] correlations.

Table 17: Predictive accuracy of two-phase smooth tube heat transfer coefficient correlations from Wojtan et al. [31], Chen [56], Shah [57], Kandlikar [93], and Gungor-Winterton [59] [60] compared to the 2.8mm to 8.84mm experimental results

G kg/m²s	Wojtan %		Chen %		Shah %		Kandlikar %		Gungor-Winterton %		Gungor-Winterton new %	
	$\bar{\varepsilon}$	$\lvert\bar{\varepsilon}\rvert$	$\bar{\varepsilon}$	$\lvert\bar{\varepsilon}\rvert$	$\bar{\varepsilon}$	$\lvert\bar{\varepsilon}\rvert$	$\bar{\varepsilon}$	$\lvert\bar{\varepsilon}\rvert$	$\bar{\varepsilon}$	$\lvert\bar{\varepsilon}\rvert$	$\bar{\varepsilon}$	$\lvert\bar{\varepsilon}\rvert$
300	-13.1	25.0	4.5	25.2	9.67	31.6	96.2	97.5	15.3	40.3	3.3	34.4
200	-12.9	25.0	15.2	30.3	26.4	42.7	68.5	69.7	25.8	45.5	5.7	34.0
175	-13.7	25.6	24.6	37.4	34.8	52.5	60.9	63.5	34.1	54.1	9.6	38.9
150	-12.9	22.6	28.6	42.7	34.2	53.3	47.9	56.2	36.1	57.3	8.9	39.2
125	-13.5	24.4	54.4	59.8	56.4	64.8	56.5	59.1	61.8	71.7	26.1	42.2
100	-18.7	32.8	110.3	153.0	106.5	116.5	86.8	97.6	118.8	132.5	65.2	78.8
75	-10.2	28.3	274.1	274.1	200.7	200.8	130.8	131.9	204.2	204.3	134.3	134.6
50	-8.6	33.6	487.2	488.4	277.1	277.1	156.8	157.3	214.4	214.4	216.7	216.7
25	-47.3	47.9	679.1	679.1	98.8	98.8	59.0	63.6	88.7	90.7	157.0	157.0
total	-14.0	26.9	100.7	115.6	72.8	85.9	80.6	84.4	72.1	87.5	44.3	65.3

8.6.2 Internally-Grooved Tubes

Measured internally-grooved tube heat transfer coefficients were compared to the current two-phase correlation described in Chapter 4, and the correlations of Thome, Kattan, and Favrat [91], Cavallini et al. [117], Chamra and Mago [162], Wu et al. [103], and Yun et al. [90]. Figure 53 shows the predicted heat transfer coefficient values vs the experimental two-phase heat transfer coefficient values for different mass fluxes. Again, the solid black line has a slope of 1 indicating perfect agreement between the model and experimental results and the dashed lines represent ±20% deviation.

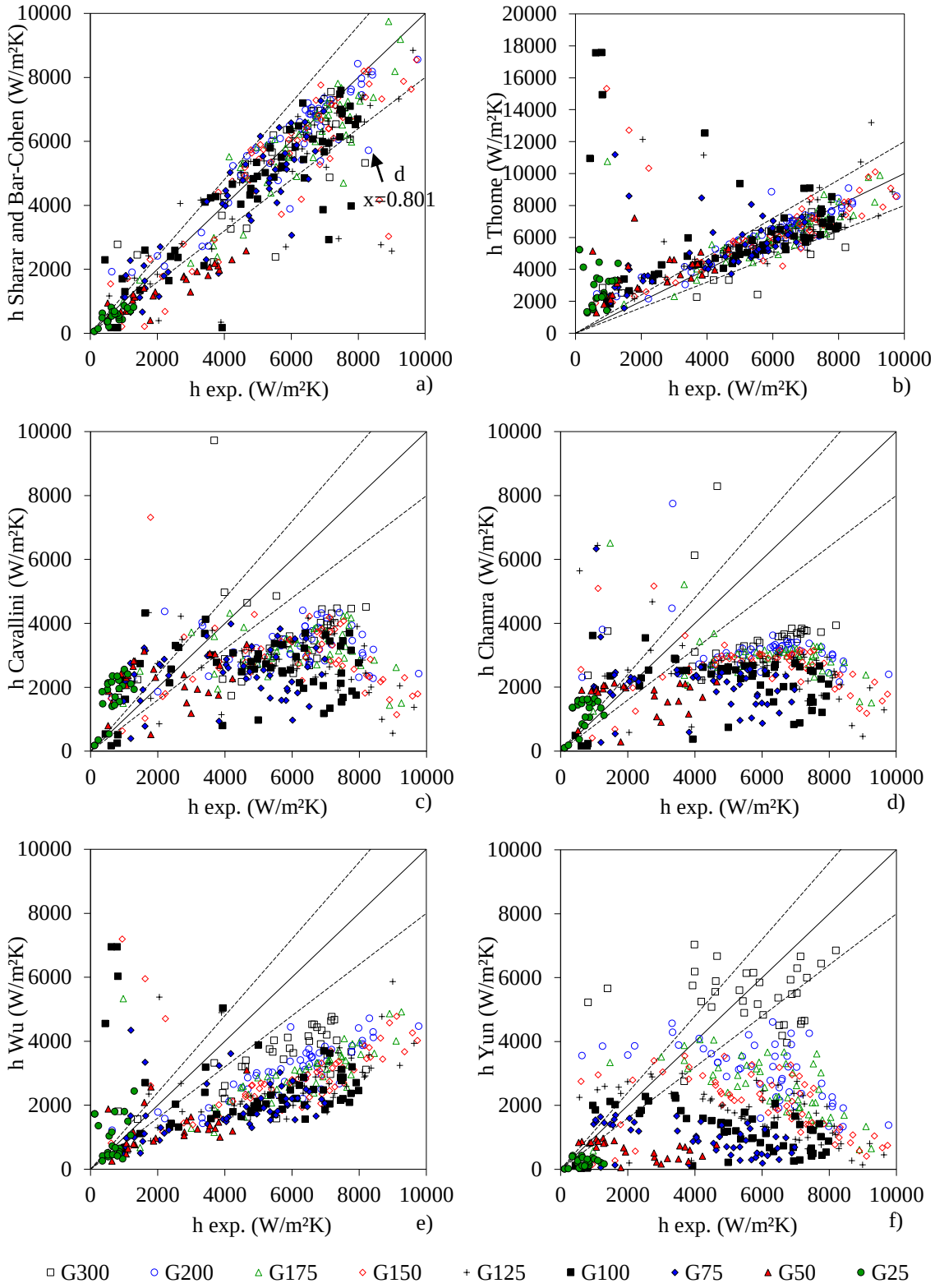

Figure 53: Comparison of the 8.84mm internally-grooved tube experimental data for HFE-7100 at 61°C with a) the Modified Sharar and Bar-Cohen correlation and correlations from b) Thome et al. [91], c) Cavallini et al. [117], d) Chamra and Mago [162], e) Wu et al. [103], and f) Yun et al. [90]

Table 18 lists a summary of the statistical parameters for the six internally-grooved correlations used. The mean deviation was best for the Wu et al. [103] correlation with a value of -2.4%, indicating that the data was 'well centered'. However, the absolute error was quite high with a value of 80.7%. The large absolute deviation is clear from Figure 53e. The small mean deviation, therefore, is a result of the large errors at high predicted values and low experimental values that offset the general trend of under-predicting heat transfer coefficient. The same assessment can be made for the Cavallini et al. [117], Chamra and Mago [162] correlations.

Table 18: Predictive accuracy of Modified Sharar and Bar-Cohen two-phase internally-grooved tube heat transfer coefficient correlation and correlations from Thome et al. [91], Cavallini et al. [117], Chamra and Mago [162], Wu et al. [103], and Yun et al. [90]

G	Modified %		Thome %		Cavallini %		Chamra %		Wu %		Yun %	
kg/m²s	$\bar{\varepsilon}$	$\lvert\bar{\varepsilon}\rvert$	$\bar{\varepsilon}$	$\lvert\bar{\varepsilon}\rvert$	$\bar{\varepsilon}$	$\lvert\bar{\varepsilon}\rvert$	$\bar{\varepsilon}$	$\lvert\bar{\varepsilon}\rvert$	$\bar{\varepsilon}$	$\lvert\bar{\varepsilon}\rvert$	$\bar{\varepsilon}$	$\lvert\bar{\varepsilon}\rvert$
300	-5.1	28.7	52.8	61.5	-23.4	44.0	30.0	91.3	-1.0	58.5	-35.7	55.3
200	1.1	25.1	67.3	74.7	-19.3	47.9	-10.9	55.9	-11.1	73.2	-55.9	68.3
175	11.2	31.3	82.0	87.3	-10.4	54.3	-5.6	61.4	-11.5	76.2	-63.7	70.1
150	21.7	40.9	99.5	105.0	-3.7	59.5	36.9	104.6	-8.9	84.0	-63.9	74.4
125	10.8	29.1	93.6	98.7	-0.7	60.9	-1.1	66.3	-17.7	77.1	-64.7	77.9
100	3.6	31.0	196.3	202.8	18.8	77.4	30.8	97.2	18.9	111.8	-70.7	76.4
75	-2.8	31.7	130.3	135.0	82.3	129.6	65.1	123.1	-16.1	73.8	-60.6	80.6
50	-12.9	41.1	250.7	252.3	76.6	119.2	75.8	132.5	22.6	95.5	-55.1	79.9
25	-21.3	48.9	530.3	530.3	210.7	223.9	129.7	152.9	112.4	133.7	-48.3	73.0
total	4.0	32.0	118.7	124.6	12.6	72.3	25.4	88.9	-2.4	80.7	-58.2	71.85

The Thome et al. [91], Cavallini et al. [117], Chamra and Mago [162], Wu et al. [103], and Yun et al. [90] correlations generally performed poorly over the full range of mass fluxes tested but worked markedly better for higher mass fluxes. Similar to the smooth tube correlations, this is explained by the inability of these correlations to accurately predict heat transfer for Stratified-Wavy (Slug and Stratified-Wavy) and Stratified flow. For example, below 150 kg/m²s on Figure 42c, where Stratified flow was observed in the internally-grooved tubes, the mean and absolute deviations rose to values in excess of 100% in many cases on Table 18. At and below mass fluxes of 75 kg/m²s,

where Stratified flow occupied 40% or 100% of the parametric space, deviations further increased. However, considering only mass fluxes above 150 kg/m²s where Intermittent and Annular flow were the dominant flow regimes in the internally-grooved tubes, some of the models performed reasonably well. For example, the Cavallini et al. [117] correlation showed a mean and absolute deviation of -23.4% and 44.0% for the mass flux of 300 kg/m²s where Annular flow was the dominant flow regime and 210.7% to 223.9% mean and absolute error for a mass flux of 25 kg/m²s where Stratified flow dominated.

From a practical standpoint, the model developed in this Dissertation was the best among those evaluated with a mean deviation of 4% and a relatively low absolute deviation of 32%. These results were reasonably consistent across the full range of mass fluxes, indicating the ability of the correlation to predict heat transfer coefficients in different flow regimes. As shown on Figure 53a, the data was reasonably well centered but under-predicted a substantial number of data points. Many of these under-predicted data points were at high vapor quality where Annular flow was sustained in the internally-grooved tubes and the model incorrectly predicted dryout; this effect was also noted for the smooth tube data and indicates the need to re-examine dryout conditions in smooth and internally-grooved tubes in the future. This is clear on Figure 44d at a mass flux of 200 kg/m²s, heat flux of 28 kW/m², and vapor quality of 0.801 where the experimental heat transfer coefficient was ~8300 W/m²K and the predicted value was ~5500 W/m²K; this data point is also indicated on Figure 53a and is clearly seen as falling well outside the ±20% lines.

It was also found that data around 50 kg/m²s (more so for the 8.84mm tube than the 4.54mm tube) deviated from the new model value more than other mass fluxes, as shown on Figure 53a. It is speculated that this is a result of experimental uncertainty in mass flux.

The mass flux experimental uncertainty was a fixed value of ±10.5 kg/m²s for the 8.84mm tubes. Therefore, at a mass flux of 50 kg/m²s, the actual mass flux could, in fact, be operating anywhere from 40 kg/m²s to 60 kg/m²s. Figure 54 shows an example of how much the heat transfer coefficient can be expected to change for mass fluxes ranging from 40 kg/m²s to 60 kg/m²s based on the heat transfer model described herein. Figure 54a is the Modified Sharar et al. [29] flow regime map for HFE-7100 in an 8.84mm internally-grooved tube superimposed with the loci of 40 kg/m²s, 50 kg/m²s, and 60 kg/m²s; they are shown as a blue dashed line, green dashed line, and red dashed line, respectively. Figure 54b is the simulated heat transfer coefficient, for the same mass fluxes, along with the smooth tube data and internally-grooved tube data at a mass flux of 50 kg/m²s and equivalent heat flux.

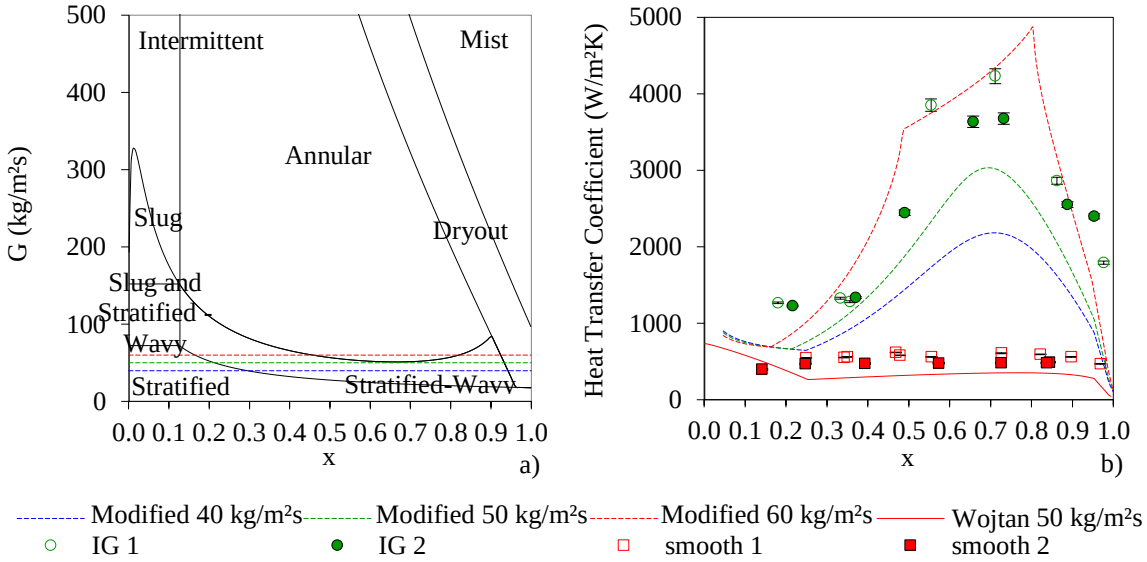

Figure 54: Example of heat transfer coefficient uncertainty and deviation near the transition boundary between Stratified-Wavy and Annular flow for HFE-7100 at 61°C in the 8.84mm tubes; a) locus of different flowrates on the Modified flow regime map and b) resulting heat transfer coefficients

As can be seen from Figure 54a, at a mass flux of 50 kg/m²s the tube is expected to be operating in Stratified flow at low vapor quality, then transition to Stratified-Wavy flow

at a vapor quality of 0.2, and approach Annular flow around a vapor quality of 0.7. The result, as seen on Figure 54b, is a relatively low heat transfer coefficient until Stratified-Wavy flow is reached, and a maximum heat transfer coefficient of 3032 W/m²K at x=0.7, where Annular flow is approached and the dry angle is small; the model at this mass flux under-predicts the experimental data. At a lower mass flux of 40 kg/m²s, where the model predicts Stratified and Stratified-Wavy flow, the heat transfer coefficient is worse-still due to a larger dry angle. In this case, the maximum heat transfer coefficient is only 2182 W/m²K, representing a 28% reduction in predicted performance from 50 kg/m²s; the model under-predicts the experimental data at 40 kg/m²s. At a higher mass flux of 60 kg/m²s, the flow regime starts as Stratified and Stratified-Wavy flow but transitions to Annular flow at a vapor quality of 0.49. This results in a much larger predicted heat transfer coefficient (maximum value of 4869 W/m²K), representing a 37% and 55% improvement over the predicted values for 40 kg/m²s and 50 kg/m²s, respectively. As shown, the predicted values at 40 and 50 kg/m²s tend to under-predict the measured values at 50 kg/m²s, but the 60 kg/m²s model simulation generally over-predicts the experimental results. This validates the argument that uncertainty in the experimental mass flux and proximity to the Stratified-Wavy to Annular transition line is the likely explanation of the large deviation at a mass flux of 50 kg/m²s. Future work should focus on improving the test facilities to reduce mass flux uncertainty and allow a more robust understanding and discussion of heat transfer around the Stratified-Wavy to Annular transition line.

It's interesting to note that the mass flux uncertainty may also explain variation between the predicted and measured enhancement ratio shown in Figure 51. As shown, a seemingly modest uncertainty of ±10.5 kg/m²s can result in large deviations in the

enhancement ratio because the slope of enhancement vs mass flux is very steep in the Stratified-Wavy to Annular transition region. Again, efforts should be made to reduce the uncertainty in the experimental mass flux to better map out the enhancement vs mass flux chart shown in Figure 51.

8.7 Comparison to Data from the Literature

The studies from Yu et al. [66], Colombo et al. [79], and Spindler and Müller-Steinhagen [74], discussed in Chapter 3, demonstrated the shift of the dominant Annular flow regimes in internally-grooved tubes to lower mass flux and vapor quality and an expansion of the parametric space occupied by Annular flow. The traditional Wojtan et al. [30] map did a poor job predicting flow regimes in these studies due to the observed flow regime transition; this conclusion from the literature review was a driving factor in undertaking the current research effort. The goal of this section is to revisit those studies and compare their flow regime and heat transfer coefficient data to the new flow regime map and regime based heat transfer coefficient correlation. This serves several purposes; a) further substantiate early flow regime transition to Annular flow as an enhancement mechanism in internally-grooved tubes; b) provide an independent validation of the flow regime map and heat transfer coefficient developed Chapter 4.

8.7.1 Flow Regime Data

Yu, Lin, and Tseng [66] performed a flow visualization and heat transfer study with R134a at 6ºC in a 10.7 mm ID smooth and an 11.1 mm ID internally-grooved tube with an 18° helix angle. Mass fluxes from 163 to 408 kg/m²s, heat flux between 2.2 and 56 kW/m², and a fixed heated length of 1.5 m were tested. Figure 55a shows the results of the internally-grooved tube flow visualization, plotted in the coordinates of mass flux and

vapor quality and superimposed on the Wojtan et al. [30] flow regime map and modified Sharar et al. [29] map; Figure 55a is the data plotted on the Wojtan et al. [30] map and Figure 55b is the internally-grooved tube results plotted on the Sharar et al. [29] map. As shown in Figure 55a, the Wojtan et al. [30] flow regime map predicted 45/47 Intermittent data points but only 6/30 Annular flow data points for the Yu et al. [66] internally-grooved tube. In total, the Wojtan et al. [30] flow regime map predicted 51/77 experimental data points, equaling 66% of the internally-grooved tube data. As shown in Figure 55b, the current flow regime modifications, which shift Annular flow to lower vapor quality and mass flux, greatly improved the predictive accuracy for the Yu et al. [66] internally-grooved tube data. The new model predicted 43/47 Intermittent data points and 21/30 Annular data points; this is a weighted average total of 83% of the data from Yu et al. [66].

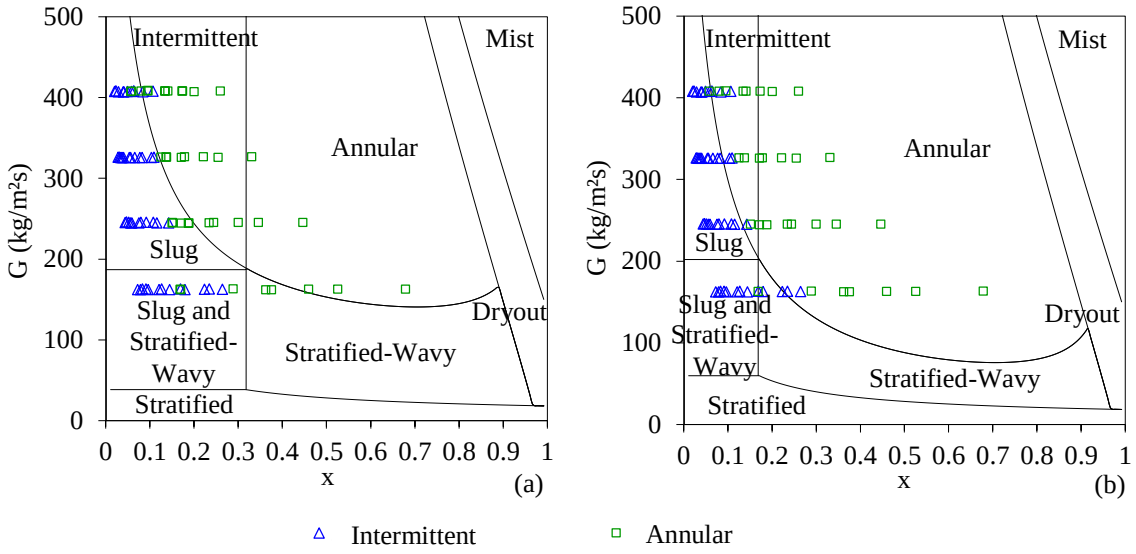

Figure 55: 11.1 mm ID internally-grooved tube experimental flow visualization results from Yu et al. [66] for R134a at 6°C with a heat flux of 20 kW/m² plotted on the a) original Wojtan et al. [30] map and b) Modified Sharar et al. [29] map

Colombo et al. [79] performed a flow visualization and evaporative heat transfer study with R134a at a saturation temperature of 5°C in a horizontal 8.92 mm ID smooth

tube and two internally-grooved tubes with inside diameters of 8.62 and 8.92 mm. Both internally-grooved tubes had helix angles of 18° and apex angles of 40º but had alternating fin heights ranging from 0.16 to 0.23 mm and the number of grooves ranging from 54 to 82. The resulting internally-grooved tube area ratio ranged from 1.55 to 1.82. Mass fluxes from 100 to 340 kg/m²s, heat flux between 2.2 and 56 kW/m², vapor qualities from 0.1 to 0.9, and a fixed heated length of 1.3 m were tested.

Figure 56 shows the results of the flow visualization, plotted in the coordinates of mass flux and vapor quality and superimposed on the Wojtan et al. [30] flow regime map and Sharar et al. [29] map; Figure 56a is the internally-grooved tube experimental results on the traditional map [30] and Figure 56b is the same results on the new model [29] described herein. As shown, the modified map markedly improves predictability of flow regime in the internally-grooved tube, particularly for Annular flow. Compared to the smooth tube model, Figure 56a, which predicted 31/31 Stratified data points, 2/4 Intermittent data points, and only 25/42 Annular data points, the new model, Figure 56b, predicted 28/31 Stratified data points, 0/4 Intermittent data points, and 42/42 Annular data points. This represents an improvement from 75% to 91% predictive accuracy when switching from the Wojtan et al. [30] model to the new Sharar et al. [29] model.

Spindler and Müller-Steinhagen [74] performed an experimental investigation of heat transfer and flow regime during evaporative cooling in an 8.92 mm ID internally-grooved tube with a 15° helix angle using two different refrigerants, R134a and R404A. Experiments were conducted in a 1 m long, heated test section with mass fluxes ranging from 25 to 150 kg/m², heat flux from 1 to 15 kW/m², inlet vapor qualities ranging from 0.1 to 0.7, and a saturation temperature of -20ºC. Stratified, Intermittent, and Annular flow

were observed, however, Annular flow was the dominant regime for mass fluxes at or above 65 kg/m²s.

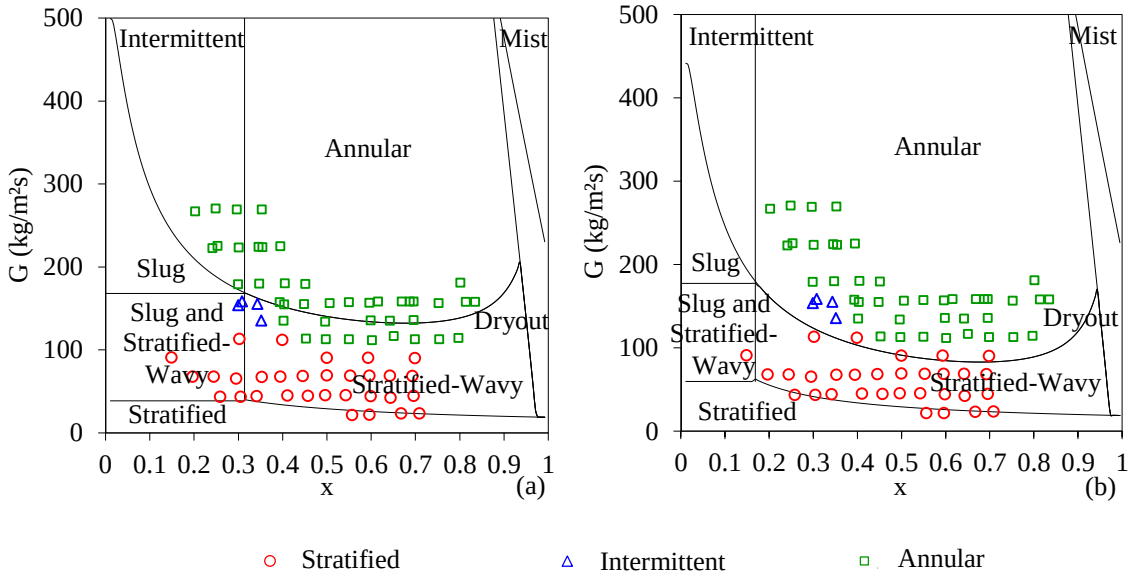

Figure 56: 8.92 mm ID internally-grooved tube experimental flow visualization results from Colombo et al. [79] with R134a at 5ºC and a heat flux of 4.2 kW/m² plotted on the a) original Wojtan et al. [30] map and b) Modified Sharar et al. [29] map

Figure 57a and Figure 57b show the R134a internally-grooved tube data of Spindler and Müller-Steinhagen [74] plotted on the traditional flow regime map [30] and the modified map [29], respectively. Similar to Figure 55 and Figure 56 above, the modified map improves predictability of flow regime in the internally-grooved tube. The smooth tube Wojtan et al. [30] model, Figure 57a, predicted 2/3 Stratified data points and 3/11 Annular data points while the new model [29], Figure 57b, predicted 2/3 Stratified data points and 9/11 Annular data points. This represents an improvement from 36% predictive accuracy to 79% accuracy.

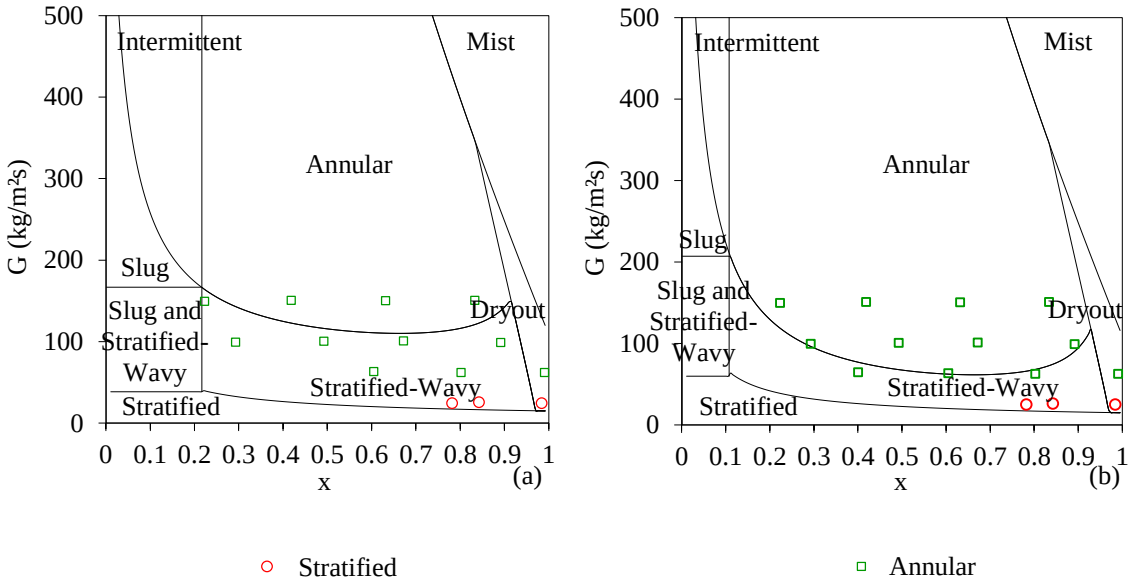

Figure 57: 8.92 mm ID internally-grooved tube experimental flow visualization results from Spindler and Müller-Steinhagen [74] for R134a at -20ºC with a heat flux of 7.5 kW/m² plotted on the a) original Wojtan et al. [30] map and b) Modified Sharar et al. [29] map

Figure 58 shows the R404a internally-grooved tube data of Spindler and Müller-Steinhagen [74] plotted on the traditional [30] and modified Sharar et al. [29] flow regime maps. As is consistent with the above results, the modified model greatly improved predictive accuracy for the data set. The original model correctly predicted 2/3 Stratified data points but only 3/11 Annular data points while the modified model predicted 2/3 Stratified data points and a much improved 10/11 Annular data points. The represents an overall accuracy improvement of 49%, from 36% for the Wojtan et al. [30] model (only 5/14 correct) to 85% for the Sharar et al. [29] model (12/14 correct).

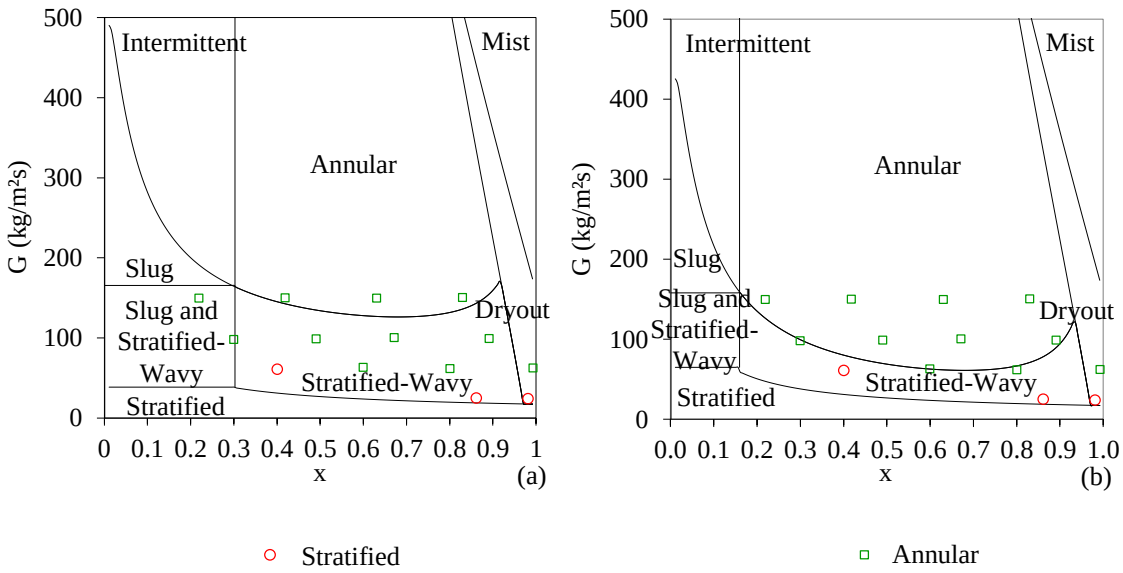

Figure 58: 8.92 mm ID internally-grooved tube experimental flow visualization results from Spindler and Müller-Steinhagen [74] for R404a at -20ºC with a heat flux of 7.5 kW/m² plotted on the a) original Wojtan et al. [30] map and b) Modified Sharar et al. [29] map

A full tabulation of the success of the original Wojtan et al. [30] and modified Sharar et al. [29] flow regime maps are shown in Table 19. The left column represents the experimentally observed flow regime or testing parameters and the next 8 columns represent the number of successful predictions and total data points (successful/total) for the Yu et al. [66], Colombo et al. [79], and Spindler and Müller-Steinhagen [74] studies when superimposed on the traditional Wojtan et al. [30] and modified Sharar et al. [29] models. As shown, the modified model outperforms the traditional model for predicting flow regime in internally-grooved tubes. The net result is a weighted average success rate improvement of 21%, from 65% for the original model to 86% for the modified model.

The new model, applied to the internally-grooved tubes, did not always improve the success of predicting Stratified and Intermittent flow. A minor reduction from 45/47 to 43/47 Intermittent data points for the Yu et al. [66] study and from 2/4 to 0/4 Intermittent data points for the Colombo et al. [79] study was observed. Similarly, a minor reduction

from 31/31 Stratified data points to 28/31for the Colombo et al. [79] study was observed. However, the new model vastly improved the predictability for Annular flow in all of the studies. The new model improved Annular flow predictive accuracy from 6/30 to 21/30 for the Yu et al. [66] study, 25/42 to 42/42 for the Colombo et al. [79] study, and 6/22 to 19/22 for the two Spindler and Müller-Steinhagen [74] tests; this represents an improvement of 48% in predicting Annular flow, from 39% accuracy to 87%, by adopting the new model. These trends are consistent with those described in Section 8.4, and summarized in Table 16, for the current data set.

Table 19: Predictive accuracy of Traditional Wojtan et al. [30] and Modified Sharar et al. [29] flow regime maps

	Yu et al.		**Colombo et al.**		**Spindler and Müller-Steinhagen**			
Fluid **Sat. Temp.** **Diameter**	R134a 6°C 11.1mm		R134a 5°C 8.92mm		R134a -20°C 8.92mm		R404a -20°C 8.92mm	
Model	**Wojtan**	**Modified**	**Wojtan**	**Modified**	**Wojtan**	**Modified**	**Wojtan**	**Modified**
Stratified	N/A	N/A	31/31	28/31	2/3	2/3	2/3	2/3
Intermittent	45/47	43/47	2/4	0/4	N/A	N/A	N/A	N/A
Annular	6/30	21/30	25/42	42/42	3/11	9/11	3/11	10/11
Total	51/77	64/77	58/77	70/77	5/14	11/14	5/14	12/14
%	**66%**	**83%**	**75%**	**91%**	**36%**	**79%**	**36%**	**85%**

8.7.2 Heat Transfer Coefficient

Figure 59 shows heat transfer coefficient vs vapor quality for the smooth (solid red circles) and internally-grooved tubes (hollow red circles) tested at 163 kg/m²s in the Yu et al. [66] study. The original smooth tube Wojtan et al. [31] heat transfer model and the current internally-grooved tube model are also plotted on Figure 59; The Wojtan et al. [31] model is represented by a solid red line and the new model is a dashed green line. As shown in the figure, the heat transfer coefficient remains relatively low but slightly increases over the range of vapor qualities tested for the smooth tube. Again, this is due to the prevalence of Stratified flow and a large dry perimeter ($\theta_{dry} \neq 0$) up until a vapor quality of 0.32 when it approaches Annular flow; refer back to Figure 8. As shown, this trend is

reasonably well predicted by the original Wojtan et al. [31] smooth tube heat transfer coefficient correlation.

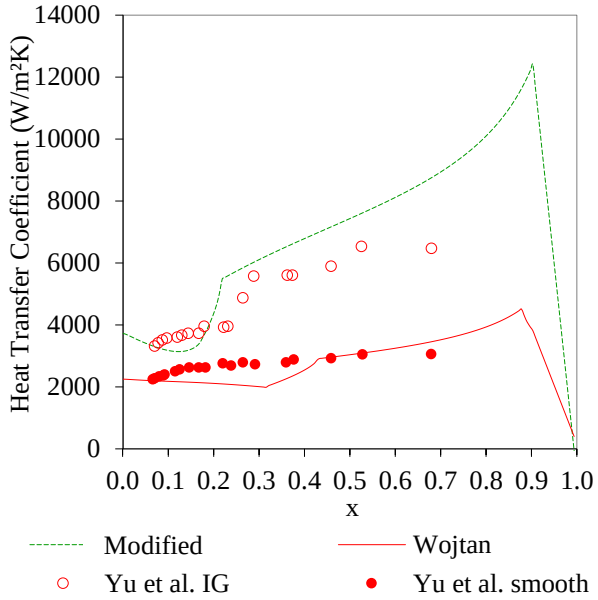

Figure 59: Heat transfer coefficient vs vapor quality for the original Wojtan et al. [31] model, Modified heat transfer coefficient described in this Dissertation, and data from Yu et al. [66] for an 11.1 mm smooth and internally-grooved tube with R134a at 6ºC and a heat flux of 20 kW/m²

The trend for the internally-grooved tube is much different as a result of early transition to Annular flow and a fully wetted perimeter (θ_{dry}=0). As can be seen in Figure 55b at 163 kg/m²s and vapor qualities greater than x=0.3, transition from Slug and Stratified-Wavy to Annular flow occurred in the internally-grooved tube. The result, as shown on Figure 59, is a relatively poor heat transfer coefficient for vapor qualities below 0.2-0.3, after which a sharp increase is seen; this sharp increase corresponds directly with the transition to Annular flow. For vapor qualities below 0.2 where both the smooth and internally-grooved tube are operating in Slug and Stratified-Wavy flow, the tube heat transfer enhancement ratio approaches the area ratio; at a vapor quality of 0.15, the smooth tube has a heat transfer coefficient of 2631 W/m²K and the internally-grooved tube has a

value of 3738 W/m²K (3738/2631=1.42). However, the enhancement ratio reaches a maximum value of close to 2.25 at vapor quality of 0.52 where thin film Annular flow prevails in the internally-grooved tube and Stratified-Wavy flow persists in the smooth tube. The results further demonstrate that the large heat transfer enhancement at low-to-intermediate mass fluxes commonly observed in internally-grooved tubes is strongly related to early transition to Annular flow. As shown in Figure 59, the model described herein captures these trends and provides a tool for analytically and physically defining this enhancement mode.

Figure 60 shows the normalized enhancement ratio vs mass flux for a vapor quality of 0.45-0.55 for the data from Yu et al. [66] (hollow red circles), Filho et al. [75] [38] (hollow blue triangles), Colombo et al. [79] (hollow black diamonds), and the current data from Figure 51; error bars were not included to maintain figure clarity, however, please refer to Sections 8.5 and 8.6.2 for a discussion. The independent data was extracted from the two enhancement ratio vs vapor quality figures (Figure 9 and Figure 10) shown in Chapter 3. The enhancement ratios shown in Figure 60 have been normalized by dividing the tube heat transfer enhancement by the tube area enhancement; this provided a 'smooth tube equivalent' and allows easier comparison among tubes with different geometric parameters. The blue and green dashed lines represent the 8.84mm and 2.62mm predicted normalized enhancement ratios averaged over a vapor quality of 0.45 to 0.55 and plotted as a function of mass flux. The predicted values are obtained by comparing the predicted results from the current internally-grooved tube model, described in Chapter 4, to the Wojtan et al. [31] smooth tube model. The model comparison predicts heat transfer improvement approaching 1 (recall these results are normalized to eliminate the effect of

area enhancement) at sufficiently low mass flux where both tubes are operating in Stratified flow and high mass flux where both tubes are in the Annular flow regime. Large enhancement is predicted at low-to-intermediate mass fluxes where the smooth tube is operating in Stratified flow and the internally-grooved tube is operating in Annular flow.

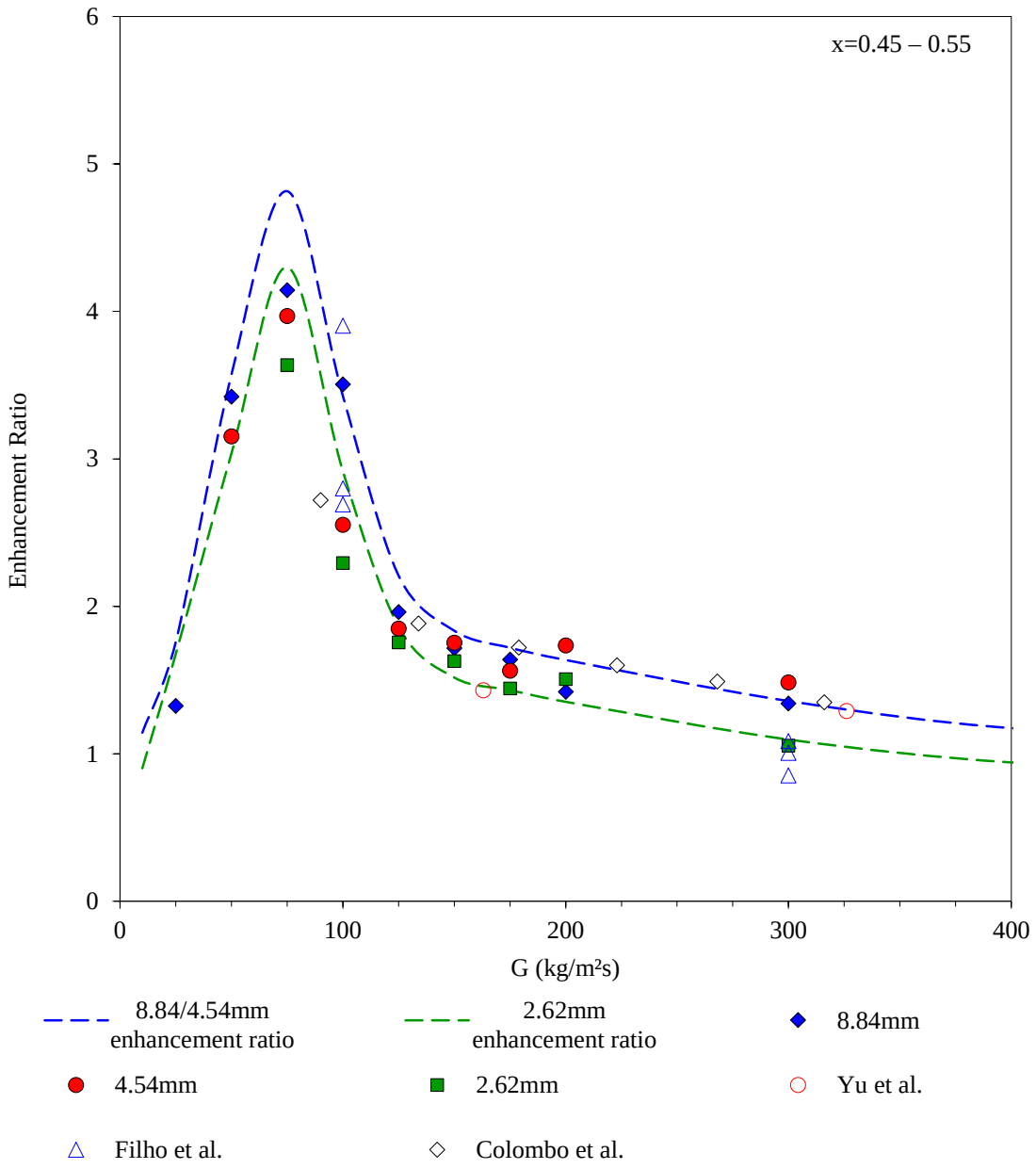

Figure 60: Normalized enhancement ratio vs mass flux with data from the current study and data from three independent researchers

It should be noted that the predicted enhancement shown in Figure 60 is for HFE-7100 and the unique geometric parameters of the internally-grooved tubes used in the current study. Again, applying these exact predictions to different working fluids, saturation temperatures, and geometric parameters has limitations because these parameters can affect the mass flux at which flow regime transition occurs, the relative effect of turbulence, and the grooved tube enhancement. However, the model appears to adequately predict the trends shown by Yu et al. [66], Filho et al. [75] [38], and Colombo et al. [79].

8.8 Applicability of the Sharar et al. Model

The current flow map and heat transfer coefficient correlation were validated herein with data from Yu et al. [66], Colombo et al. [79], Spindler Müller-Steinhagen [74], Filho et al. [75] [38], and the current data set, which in-total covered internally-grooved tubes with internal diameters of 2.62mm, 4.54mm, 8.84mm, 8.92mm, and 11.1mm with R-134a, R404a, and HFE-7100 as the working fluids, and heat fluxes up to 56 kW/m². The Liebenberg et al. [114] Intermittent to Annular transition used in the current study covered internally-grooved tubes with internal diameters from 8 to 9 mm and refrigerants R-134a, R-22, and R-407C. Furthermore, the database used to create the original Wojtan et al. [30] map covers tubes with internal diameters from 12 to 14 mm and common refrigerants, namely R-134a, R-22, and R-410a. A detailed discussion on the range of conditions used to validate the original Wojtan et al. flow regime map [30] and heat transfer correlation [31], as well as the Ravigururajan and Bergles [28] internally-grooved tube enhancement factor, E_{rb}, and the empirically derived enhancement factor introduced by Thome et al. [91], E_{mf}, can be found in Chapter 4.

It is reasonable to expect that the modified Sharar et al. [29] map, validated with multiple tube sizes and fluids, is valid for a wider range of tube diameters and fluids. The basis for the modified model, the Wojtan et al. [30] model, originated from the Taitel-Dukler [46] physics-based transition criteria which contains little empirical fitting and should theoretically apply to most fluids and channel sizes. Additionally, a comparison of fluid properties at atmospheric pressure, as shown in Table 20 [163], reveals that the fluids used to validate the modified Stratified-Wavy to Annular transition, R-134a, R404a, and HFE-7100, have similar properties to fluids used in the original Wojtan et al. [30] model and other common heat transfer fluids. Referring to Chapter 4, consistency in the fluid properties in Table 20 would imply similar fluidic performance and applicability of the modified model to R113, R134a, R22, R245fa, R410a, FC-72, and HFE-7100. It's worth noting that due to the similarity in the fluid properties, the boundaries and extent of the predicted flow regimes and heat transfer coefficients are similar for the range of fluids considered in this Dissertation.

However, predicting flow regimes with water as the working fluid will likely not work due to the disparate fluid properties. This point is emphasized by Figure 38c and the analysis in Chapter 6 that showed that the Wojtan et al. [30] flow regime map did not accurately predict flow regimes for water/vapor as the working fluids in an 8.84mm smooth channel. Again, the likely explanation for this deviation is that the Wojtan et al. [30] flow regime map was (at least partially) empirically fit to match the common refrigerants, shown in Table 20, which have fluid properties vastly different than water. In effect, the empirical constants allow for better predictive accuracy for operating conditions close to the data set used to develop the correlations, but may not extrapolate well to different conditions. The

current model would benefit from future experimental validation to reinforce these assertions.

Table 20: Saturated Properties of Various Fluids

Fluid	Properties at 0.1 MPa					
	Boiling pt. (°C)	ρ_L (kg/m³)	ρ_V (kg/m³)	σ (mN/m)	μ_L (μPa-s)	μ_V (μPa-s)
R113	47	1509	7.29	14.8	493	10.3
R134a	-26	1377	5.19	15.5	380	9.76
R22	-41	1410	4.64	18.1	347	9.68
R245fa	14.5	1367	5.83	15.4	466	9.97
R410a	-52	1361	4.12	17.8	387	9.89
FC-72	56	1680	13.4	10	262	12.1
HFE-7100	61	1370	9.87	14	275	11.3
Water	100	958	0.59	58.9	283	12.3

8.9 Refitting the Sharar et al. Flow Regime Map

The Sharar et al. [29] flow regime map, developed based on trends observed in the literature and described in detail in Chapter 4 was not refitted based on the current set of data using HFE-7100 in 2.62-8.84mm internally-grooved tubes. While it was shown to be accurate for 86-88% of the flow regime data for the current data set, it is likely that alterations based on the collection of new data, in conjunction with data from the literature, will improve flow regime predictability and subsequently, heat transfer predictability. This section aims to carefully and precisely address this theory, indicating the merits of a more-comprehensive future effort.

One trend that was observed for the 2.62mm, 4.54mm, and 8.84mm internally-grooved tubes was mis-prediction of Annular flow near the transition boundary between Stratified-Wavy and Annular flow. Specifically, at low mass fluxes of 50 and 75 kg/m²s and vapor qualities greater than 0.60, the Sharar et al. [29] flow regime map predicted that the grooved tubes should transition from Annular flow to Stratified-Wavy flow. However, as shown for the 8.84mm (Figure 42c), 4.54mm (Figure 45c), and 2.62mm (Figure 48c) internally-grooved tubes, the experimental flow regime was found to be Annular flow for

this range of operating conditions. Figure 45c for the 4.54mm grooved tube is reproduced on Figure 61a below for convenience.

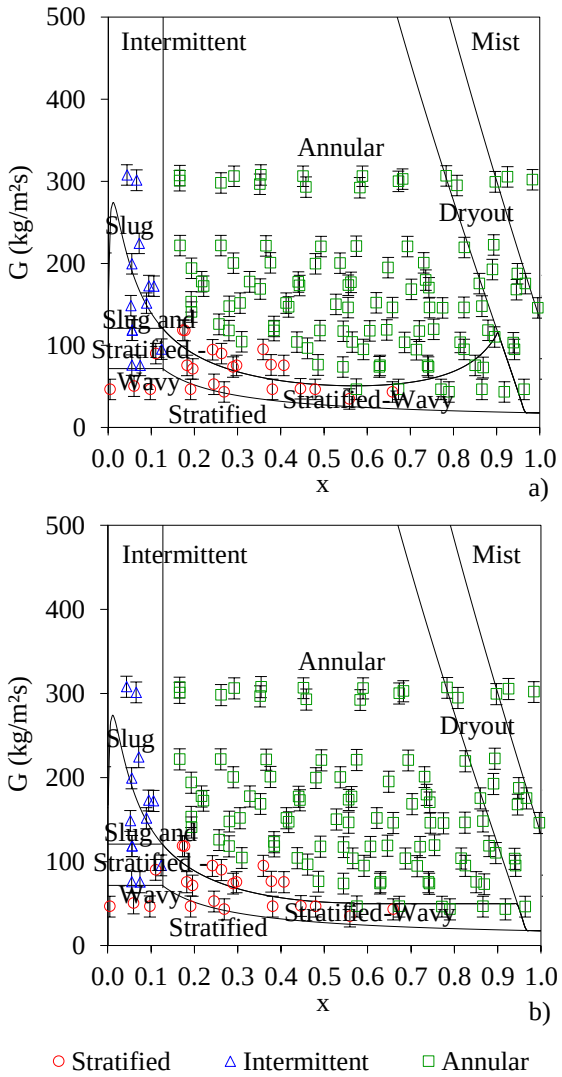

Figure 61: 4.54mm internally-grooved tube data plotted on a) the Sharar et al. map [29] described in Chapter 4 and b) the adjusted map based on the current data set with HFE-7100 at 61°C, G=50 kg/m²s, and q"=9 kW/m²

It's interesting to note that the heat transfer coefficient generally under-predicts the heat transfer coefficient for the same conditions because the flow regime map and heat transfer model incorrectly predict Stratified flow and a large dry angle. This is clearly shown on Figure 46a for the 4.54mm grooved tube with a mass flux of 50 kg/m²s and vapor

qualities greater than 0.6; this data is reproduced on Figure 62a below, again for convenience. Therefore, this region of low mass flux, ranging from 50 to 75 kg/m²s, and high vapor qualities, greater than 0.60, represents a parametric space that could benefit from adjustment to the flow regime map.

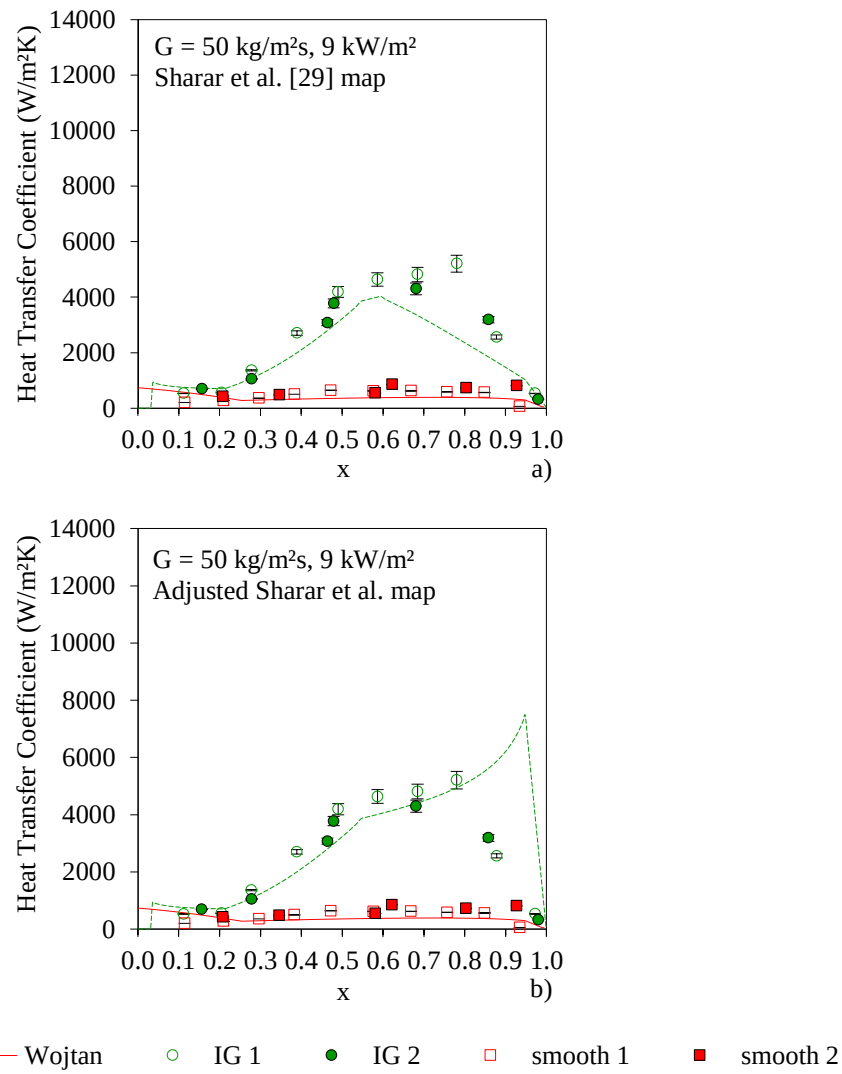

Figure 62: Comparison of heat transfer coefficient vs vapor quality for a mass flux of 50 kg/m²s with HFE-7100 at 61°C and q"=9 kW/m² in the 4.54mm tubes superimposed with a) heat transfer coefficient based on Sharar et al. [29] map and b) adjusted Sharar et al. map

To better capture this trend, an adjustment to the Stratified-Wavy to Annular transition boundary can be made; if $x > x_{G_{wavy\,min}}$, $G_{wavy} = G_{wavy\,min}$. This revision

prevents the Stratified-Wavy to Annular transition boundary from increasing past the minimum predicted value at high vapor quality. Figure 61 shows the 4.54mm internally-grooved tube flow visualization results plotted in coordinates of mass flux and vapor quality and superimposed on the Sharar et al. [29] map, described in Chapter 4, and revised Sharar et al. [29] flow regime map based on the above adjustment; Figure 61a is the 4.54mm internally-grooved tube experimental results on the Sharar et al. [29] map and Figure 61b is the internally-grooved tube results plotted on the adjusted Sharar et al. [29] flow regime map. Stratified data points are represented by red circles, Intermittent data points are blue triangles, and Annular data points are shown by green squares.

As shown by the figure, the proposed modification increases the predictability of Annular flow at low mass flux (50-75 kg/m²s) and high vapor quality (x>0.6). Specifically, the prediction of Annular flow increases from 95/112 data points to 102/112 data points. This represents an improvement from 84.8% to 91.1% for predicting Annular flow in the 4.54mm internally-grooved tube and a weighted average improvement from 86.1% to 90.4%. This modification does not result in any change to the predictability of Stratified and Intermittent flow. This analysis would be expected to provide improved predictability for the 8.84mm and 2.62mm internally-grooved tube data; future work should focus on justifying this assertion.

Figure 62 shows a comparison of experimental heat transfer coefficients for the smooth and internally-grooved tubes with HFE-7100 at a heat flux of 9 kW/m², mass flux of 50 kg/m²s, and a tube diameter of 4.54mm; Figure 62a is the experimental results plotted with the heat transfer correlation predicted based on the Sharar et al. [29] map and Figure 62b is the predicted heat transfer coefficient based on the above alteration. The

experimental smooth tube data points are shown as red squares and the internally-grooved tube data points are green circles.

As previously mentioned, the heat transfer coefficient correlation based on the Sharar et al. [29] map (Figure 62a) significantly under predicts the heat transfer coefficient at high vapor quality, x=0.6-0.8. This is a result of the flow regime map mis-predicting transition to Stratified-Wavy flow where the observed experimental flow regime was Annular flow, prior to dryout. The predicted heat transfer coefficient based on the adjusted flow regime map, shown in Figure 62b, predicts Annular flow and a reduced dry angle at this operating condition. As a result, the predicted heat transfer coefficient more closely resembles the experimental heat transfer results at vapor qualities from 0.6-0.8.

As shown at a vapor quality of approximately 0.85 on Figure 62b, there is still uncertainty in predicting performance at these conditions, despite the favorable outcome of this adjustment. Therefore, a more comprehensive feedback study needs to be conducted to firmly establish the flow regime transition boundaries and what constitutes 'optimum' boundaries for minimizing error between the model and combined data from the literature and current study. Future studies should focus not only on the Stratified-Wavy to Annular transition, but also the Intermittent to Annular transition, and the effect of heat flux on the Dryout boundaries.

8.10 Summary

The preceding chapter has presented an experimental and analytical study of flow boiling of HFE-7100 in horizontal 2.62mm - 8.84 mm diameter smooth and internally-grooved tubes, with mass fluxes from 25-300 kg/m²s, heat fluxes from 4-56 kW/m², and exit vapor qualities approaching 1. The new physics-based flow regime map and heat

transfer model described in Chapter 4 were quantitatively and statistically validated using the current data and data from the literature. Models from the literature were also compared to the current data set.

It was shown that the Wojtan et al. [31] regime-based heat transfer coefficient correlation, with a mean and absolute deviation of -14.0% and 26.9%, outperformed the smooth tube models of Chen [56], Shah [57], Kandlikar [93], Gungor and Winterton [59], and simplified two-phase flow boiling correlation by Gungor and Winterton [60]. This was especially true at mass fluxes below 150 kg/m²s where Stratified-Wavy and Stratified flow occupied a large portion of the parametric space. Deficiencies in the Wojtan et al. [31] model for predicting heat transfer coefficient at high heat flux and near dryout conditions represent a future research opportunity.

Similarly, the new Sharar et al. [29] flow regime map and associated regime-based heat transfer coefficient correlation outperformed the internally-grooved tube correlations from Thome et al. [91], Cavallini et al. [117], Chamra and Mago [162], Wu et al. [103], and Yun et al. [90], particularly at mass fluxes below 75 kg/m²s where Stratified-Wavy and Stratified flow occupied a large portion of the parametric space; the mean and absolute deviation for the new model was 4.0% and 32%, respectively. The largest source of deviation was at high vapor quality where the model predicted dryout and Annular flow was sustained in the internally-grooved tubes. Additionally, larger-than-normal errors arose near the transition boundary between Stratified-Wavy and Annular flow, presumably due to uncertainty in the reported mass flux. Suggestions for future flow regime and heat transfer model improvements (as well as improvements to the experimental test setup) were made, focusing primarily on the need for future research on high heat flux, dry-out

conditions, and operation close to flow regime transition boundaries. Along these lines, a section of this chapter was devoted to identifying the merits of altering the newly developed flow regime map and heat transfer coefficient correlation. This analysis indicated that a more comprehensive feedback study needs to be conducted to firmly establish the flow regime transition boundaries and what constitutes 'optimum' boundaries for minimizing error between the model and combined data from the literature and current study.

Based on results from the current study and those from independent researchers, it was shown that heat transfer enhancement at low-to-intermediate mass flux is primarily due to early flow regime transition in internally-grooved tubes. Additionally, it was shown that heat transfer enhancement approaches the area enhancement when the smooth and internally-grooved tubes are operating in the same flow regime. This applied at sufficiently low mass flux, where Stratified flow is expected, as well as high mass flux, where Annular flow is expected. This result fulfills the goal of developing and validating a physics-based heat transfer model that represents the impact of two-phase flow structures and is coupled to a reliable flow regime map [105].

Chapter 9: Conclusions and Future Work

9.1 Conclusions

The predictive accuracy for two-phase flow boiling in smooth channels has benefitted from the adoption and proliferation of regime-based heat transfer coefficients. Unfortunately, the same level of phenomenological insight and physical modeling for internally-grooved tubes has not yet been developed. Therefore, a stronger experimental and theoretical knowledge base needs to be established for enhancement in internally-grooved tubes, focusing on a more comprehensive understanding of the physical mechanisms responsible for improved performance in these tubes. Pursuant to this goal, this work focused on the analytical development and experimental validation of a physics-based flow regime map and heat transfer coefficient model that recognize the role played by two-phase flow structures in enhancing thermal transport within internally-grooved tubes.

A detailed analysis of smooth and internally-grooved tube data for two-phase flow of refrigerants, obtained from the literature and superimposed on the Wojtan et al. [30] flow regime map, revealed that performance improvement (3-7 times that of a plain tube) in internally-grooved tubes at low-to-intermediate mass flux is a result of early transition to Annular flow. At high mass flux where the smooth tube and internally-grooved tube are operating in Annular flow, the enhancement reduces to the internal area ratio (1.5 to 1.8 times that of a plain tube). The current state of two-phase flow regime maps and heat transfer correlations for internally-grooved tubes was summarized and motivation for the current research effort was established.

Based on the trends revealed in the literature review, the existing Wojtan et al. [30] flow regime map was modified using the Liebenberg et al. [114] Intermittent to Annular transition and the Sharar et al. [29] Stratified-Wavy to Annular transition criteria. Additionally, the Ravigururajan and Bergles [28] turbulence factor and an empirically derived enhancement factor introduced by Thome et al. [11] were adopted to modify the associated heat transfer coefficient correlation. These modifications represent changes in the physical mechanisms responsible for enhancement in internally-grooved tubes and resulted in varying the calculation of the dry perimeter angle, θ_{dry}. Through analytical modeling simulations, it was shown that heat transfer enhancement of 3-7 times a smooth tube at low-to-intermediate mass flux can be modeled by early flow regime transition to Annular flow in internally-grooved tubes. Additionally, it was shown that using the same model, it is possible to predict heat transfer enhancements that approach the area ratio when the smooth and internally-grooved tubes are operating in the same flow regime. These trends were consistent with those distilled from the literature review.

A single- and two-phase test facility was designed and fabricated to experimentally validate the newly-developed flow regime map and regime-based heat transfer coefficient correlation; focus was given to collecting and processing thermofluidic data, namely flow regime and heat transfer coefficient, to substantiate flow regime transition as a key enhancement mechanism in internally-grooved tubes. Before two-phase experiments were considered, a single-phase energy balance and heat transfer statistical analysis was conducted. Theoretical predictions from Dittus-Boelter (both 'common' and 'original' form), Colburn, and Gnielinski were compared to the single-phase smooth tube experimental data [25]. The 'common' form of the Dittus-Boelter correlation was the most

accurate for predicting single-phase flow of HFE-7100 in 2.8mm, 4.54mm, and 8.84mm smooth tubes with a mean and absolute deviation of 7.07% and 9.02%, respectively. The Dittus-Boelter (both 'common' and 'original' form), Colburn, and Gnielinski correlations were modified using the Ravigururajan and Bergles [28] turbulence factor to predict single-phase flow in the internally-grooved tubes. The 'common' form of the Dittus-Boelter correlation (modified with the turbulence factor) was the most accurate for predicting single-phase flow of HFE-7100 in 2.62mm, 4.54mm, and 8.84mm internally-grooved tubes with a mean and absolute deviation of 4.46% and 11.08%, respectively. This illustrated that the test setup was functioning properly and the experimental method was robust and capable of providing reliable measurements. This also validated the use of the Ravigururajan and Bergles [28] turbulence factor in the heat transfer coefficient correlation described in this dissertation.

A non-intrusive optical sensor, based on Total Internal Reflection (TIR) and capable of determining the liquid film thickness, was developed to study the dynamic nature of two-phase flows. The new method represents a more reliable method for experimentally determining flow regime compared to the common visual and verbal flow regime definitions. The method consisted of shining a red fiber-optic light source through the top of an optically transparent glass tube, using a CMOS camera to capture light rings resulting from total internal reflection at the liquid-vapor interface, and extracting a film thickness profile from the resulting images. It was found that different flow regimes resulted in unique temporally varying film thickness profiles, which were confirmed using high speed visualization. Using these profiles, quantitative flow regime identification measures were developed, including the ability to explain and quantify the more subtle

transitions that occur between dominant flow regimes. The flow regime maps of Taitel-Dukler [46], Ullmann-Brauner [141], and Wojtan et al. [30] were found to correlate the smooth-tube experimental data accurately, to varying degrees, thus validating the use of the TIR technique in predicting flow regime.

Flow regime data, based on the newly-developed Total Internal Reflection method, and heat transfer coefficient data, using infrared thermography, was collected for two-phase HFE-7100 flow in horizontal 2.62mm - 8.84mm diameter smooth and internally-grooved tubes with mass fluxes from 25-300 kg/m²s, heat fluxes from 4-56 kW/m², and vapor qualities approaching 1. In total, over 6,500 combined data points for the adiabatic and diabatic smooth and internally-grooved tubes were acquired.

For the current smooth tube data, it was shown that the Wojtan et al. [31] regime-based heat transfer coefficient correlation, with a mean and absolute deviation of -14.0% and 26.9%, outperformed the smooth tube models of Chen [56], Shah [57], Kandlikar [93], Gungor and Winterton [59], and the simplified two-phase flow boiling correlation by Gungor and Winterton [60]. This was especially true at mass fluxes below 150 kg/m²s, where Stratified-Wavy and Stratified flow occupied a large portion of the parametric space. Similarly, the modified Sharar et al. [29] flow regime map and associated regime-based heat transfer coefficient correlation, described herein, outperformed the internally-grooved tube correlations from Thome et al. [91], Cavallini et al. [117], Chamra and Mago [162], Wu et al. [103], and Yun et al. [90], particularly at mass fluxes below 75 kg/m²s where Stratified-Wavy and Stratified flow occupied a large portion of the parametric space; the mean and absolute deviations for the new model were 4.0% and 32%, respectively. Adoption of the new flow regime map [29] improved flow regime predictive accuracy from

66.7% to 88.3% for the current data set and from 65% to 86% when compared to data from Yu et al. [66], Colombo et al. [79], and Spindler and Müller-Steinhagen [74].

Based on results from the current study and those from independent researchers, it was shown that heat transfer enhancement at low-to-intermediate mass flux is primarily due to early flow regime transition in internally-grooved tubes. Additionally, it was shown that heat transfer enhancement approaches the area enhancement when the smooth and internally-grooved tubes are operating in the same flow regime. This applied at sufficiently low mass flux, where Stratified flow is expected, as well as high mass flux, where Annular flow is expected. These results fulfill the goal of developing a physics-based heat transfer model that represents the impact of two-phase flow structures in internally-grooved tubes.

9.2 Future Work

Several recommendations for future internally-grooved tube research have been identified based on the preceding literature review and experimental work:

a. The largest deviation between the current model and experimental results was at high vapor quality where the model predicted dryout and Annular flow was sustained in the internally-grooved tubes. Additionally, larger-than-normal errors arose near the transition boundary between Stratified-Wavy and Annular flow, presumably due to uncertainty in the reported mass flux. Future research on high heat flux, dry-out conditions, and operation close to flow regime transition boundaries should be undertaken.

b. Even though the new flow regime map and heat transfer model improves predictive accuracy, there is still uncertainty in predicting performance under certain conditions. It was shown that alterations to the map, based on the

collection of new data and data from the literature, can improve flow regime predictability and subsequently, heat transfer predictability. Therefore, a comprehensive feedback study needs to be conducted to firmly establish the flow regime transition boundaries and what constitutes optimum boundaries for minimizing error between the model and available data. Future studies should focus not only on the Stratified-Wavy to Annular transition, but also the Intermittent to Annular transition, and the effect of heat flux on the Dryout boundaries.

c. Similarly, deficiencies in the Wojtan et al. [31] model for predicting heat transfer coefficient at high heat flux and near dryout conditions represents future research opportunities.

d. Researchers have observed performance differences for identical test conditions but variable tube groove parameters. Therefore, a more systematic study of the effect of fin shape, fin height, number of fins, helix and apex angle, and ratio of relevant parameters needs to be undertaken to determine the relationship between these parameters, flow regime, and thermofluid performance, and what constitutes a geometrically-optimum tube for given operating conditions.

e. It is not entirely clear what impact operation of refrigerants and CO_2 at high reduced pressure has on flow regimes and heat transfer in internally-grooved tubes. Future studies are needed. Please refer to Chapter 3 for more details.

f. All of the small diameter internally-grooved tube studies in the literature for refrigerant/oil mixtures used CO_2 at 10ºC and polyalkylene glycol (PAG).

Thus, there is a need to extend the experimental database to other refrigerant and oil combinations.

When undertaking the above tasks, effort should be made to adhere to the following research guidelines:

a. Concurrent heat transfer and quantitative flow regime data should be collected over a wide range of operating conditions, particularly low mass flux, to establish the intrinsic relationship between the dominant flow structure and thermofluid performance in internally-grooved tubes. Additionally, comparison to existing correlations, flow regime maps, and smooth tube data as a means to normalize the results should accompany all experiments to determine the current state of internally-grooved tube predictive methods.

b. The majority of the studies in the literature relied solely on subjective flow regime data collection, which calls into question the accuracy of the results. Future studies should focus on objective flow regime determination methods to obtain more accurate and repeatable results.

Appendix A Atomic Layer Deposition Tube Coating Method

As described in Chapter 5, the smooth and internally-grooved tubes were coated with 8 μm Parylene-C in a Specialty Coating Systems PDS2010 coating tool followed by 12,000 Å of Titanium and 2,000 Å of Platinum in a CHA E-beam evaporator using a rotating stepper motor assembly. This supplied a robust, conformal, thin film resistor necessary to experimentally heat the tubes. However, there were alternative heating methods that were being explored. This Appendix gives a brief description of candidate heating methods and focuses on an attempt to create thin film heaters with Atomic Layer Deposition (ALD).

A.1 Candidate Heating Methods

When choosing a heating method it is important that appropriate heat flux levels can be met for all of the tubes. For a maximum heat flux of 56 kW/m², the 8.84mm, 4.54mm, and 2.62/2.8mm smooth and internally-grooved tubes need to have 210W, 100W, and 60W of heat applied, respectively. For the 35V, 10A TENMA DC power supply used, this suggests resistances of 5.83Ω for the 8.84mm tubes, 12.25Ω for the 4.54mm tubes, and ~20.5Ω for the 2.62 and 2.8mm tubes. In addition to staying within these resistance levels, the chosen method should provide a uniform heat flux and should allow for IR imaging.

One option was to electrically heat the tubes themselves. In the case of the smooth and internally-grooved copper tubes, the resistance varied from 91μΩ to 500μΩ. With the 35V 10A TENMA DC power supply, these resistances would only provide 0.05W and 0.009W of thermal energy to the smooth and internally-grooved tubes; this is clearly inadequate given the goal of 210W to 60W. Thinning of the tube walls through chemical

etching or machining would likely double the resistance, and power dissipation, but would not be adequate to reach high heat fluxes. Wieland does not manufacture stainless steel or other low electrical conductivity material tubes, therefore, direct heating of the tube wall was not possible. Another option considered was wrapping the tube with a wire or electrical heater. However, due to the potential variable contact resistance, and associated non-uniform heat flux, the wire wrapping method is not an appropriate solution. Additionally, cross flow of hot water in an annulus was considered prohibitively complex, would likely not provide a uniform heat flux condition, and would not allow IR imaging.

A.2 Atomic Layer Deposition Heating

One alternative to the above methods was to deposit a thin layer of dielectric material on the outer surface of the tube followed by a thin layer of metal. This method would provide electrical isolation between the tube and resistor, allow for IR imaging, virtually eliminate contact resistance, and provide repeatability if ALD (atomic layer deposition) or other cleanroom tools are employed. Based on these perceived benefits, an ALD coated thin film heater was considered a preferred method for heating the smooth and internally-grooved tubes.

ALD is a chemical vapor deposition (CVD) method that (as-advertised) allows building nanometer thick, pinhole-free, conformal thin films on any 3D shape and geometry. Proponents of this technology cite further benefits such as excellent adhesion, self-terminating reactions, precision, and repeatability. Based on these claims, the use of ALD appeared to be an attractive solution to coating the tubes.

To provide the primary insulating layer, Alumina was chosen because it has a very high electrical resistivity, good voltage hold-off (10V/nm) [164]), good thermal

conductivity (40W/mK), and is relatively inexpensive. Furthermore, Alumina is widely used in ALD processes and is, therefore, well characterized. Based on the properties of Alumina, the insulating layer needed to be at least 3.5nm thick to provide the 35V hold-off necessary for the power supply; for a large safety factor and a more robust film, a final thickness of 200nm was deposited. To provide the secondary resistor layer, Ruthenium was chosen based on lab capabilities. The Ruthenium layer should be 100-250 nm to provide appropriate resistances and allow the appropriate heat fluxes to be applied. Shown in Table 21 are the physical properties and thicknesses needed for the copper tube, Alumina layer, and Ruthenium layer.

Table 21: Material properties of interest for ALD coated copper tubes

Material	Thermal Conductivity (W/mK)	Electrical Resistivity (nΩ-m)	Voltage Hold-off (V/nm)	Thickness (nm)
Copper	400	16.8	-	-
Alumina	40	-	10 [164]	200
Ruthenium	117	71	-	100-250

A .2.1 ALD Uniformity

One concern is that the Alumina and, more importantly, the Ruthenium layers are uniform circumferentially and axially along the tube. If the Alumina is not uniform, it may not provide the required electrical isolation. Furthermore, if the Ruthenium is not uniform, then the resistance will vary along the tube and a uniform heat flux condition will not be obtained. It is difficult to measure film thickness on a curved surface such as a tube. In order to simulate the sides of the tube (top, bottom, left, and right) several 1” silicon wafers were attached to a custom cantilever fixture and placed in the ALD tool; a schematic of the setup is shown in Figure 63. The silicon wafers were plated with several microns of titanium and copper in an evaporator before the ALD process. The purpose of this step

was to better simulate adhesion to the copper tubes and also provide a conducting undercoat so that probes could be used to determine if the Alumina was insulating.

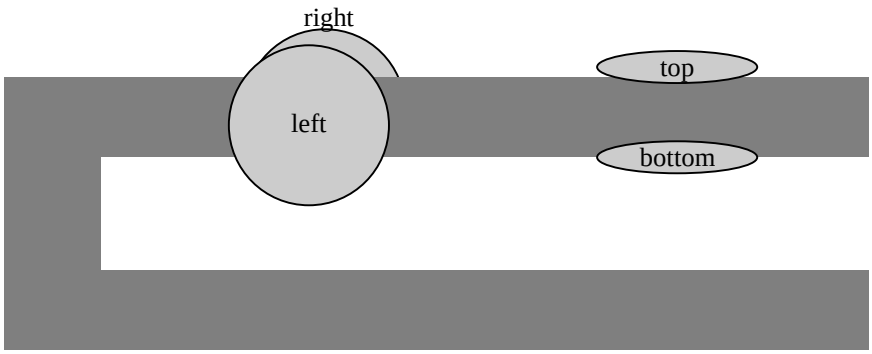

Figure 63: Schematic (side view) of the cantilever test setup made to test material thickness in the ALD tool

Using a Cambridge NonoTech Fiji ALD tool, the process consisted of a repeating cycle of trimethylaluminum (TMA) precursor pulse, purge, H_2O pulse, and a final purge for a total of 2000 cycles. The TMA and H_2O yield ALD Al_2O_3. The process had a deposition rate of approximately 1 angstrom per cycle, resulting in approximately 200nm of Alumina. Two different Alumina processes were explored: 'plasma' Alumina and 'thermal' Alumina. Using an ellipsometer to measure film thickness, results showed that the Plasma process did not vary axially but varied by as much as 14% circumferentially. The Thermal process did not vary axially and varied by only 4% circumferentially. For both processes, the Alumina film was insulating. Therefore, the 'thermal' Alumina process was better suited to coat the copper tubes due to the increased uniformity.

A .2.2 Pinhole Defects in ALD

As discussed above, ALD is advertised as a pinhole-free conformal coating, however, various researchers including Zhang et al. [165] have shown that Alumina ALD coatings can suffer from pinholes and defects that can degrade film integrity. Pinholes

would represent a void in the insulating layer and a potential avenue for an electrical short from the resistive layer to the copper tube. Therefore, before coating with Ruthenium, experiments were conducted to ensure that the Alumina thin films were pinhole free.

In addition to being uniform and transparent, voids in the ALD thin films can be on the same order as the films themselves, nanometers, which can make detection a formidable task. Using conventional microscopy techniques can be difficult for void detection. Instead, the pinhole defect density can be characterized by using a copper electroplating visualization technique developed by Zhang et al. [165]. Figure 64 is a schematic showing the formation of a copper metallic bump on a conductive substrate. In the current case, the initial copper layer used to better simulate adhesion on the copper tubes serves as the conductive material. When the sample is placed in an electroplating bath and a potential is applied between the conductive substrate and the solution, copper will deposit in the pinhole and a copper bump will form. Not surprisingly, electroplating is commonly used to make metal nanowires and interconnects in nanoporous templates [166]. As shown in the schematic, the copper bump is larger in size than the pinhole and also opaque which makes imaging possible with conventional methods.

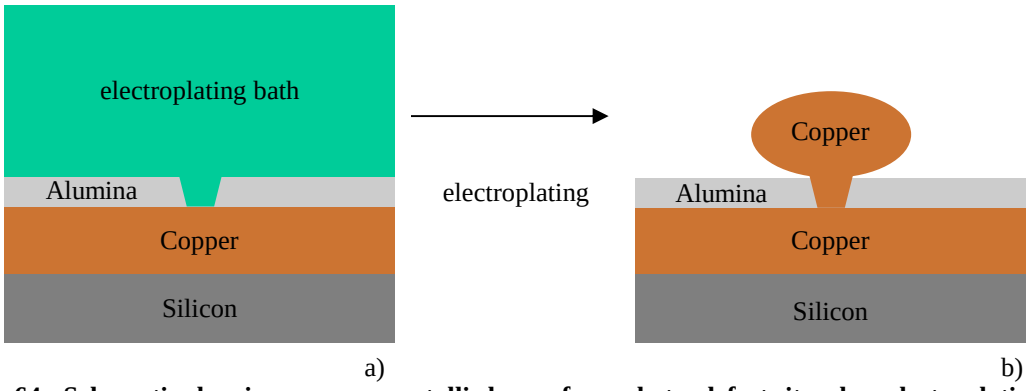

Figure 64: Schematic showing a copper metallic bump formed at a defect site when electroplating a conductive substrate in an electrolytic solution of H_2SO_4 and $CuSO_4$ (adapted from [165])

Figure 65 shows SEM images of an Alumina-coated Silicon substrate that was pre-treated with a titanium-copper coating. The figure on the left is the substrate before the electroplating process and the figure on the right is after the plating process. In the current study, the copper electrolyte bath was composed of 15 g/L of Cu and 210 g/L sulfuric acid [167]. Samples were plated for 20 minutes each. It is clear from the figure that defects are not readily apparent before electroplating but copper nodules are clearly visible after electroplating. For several samples tested, the defect density exceeded 50/cm². Defect densities on this order would provide paths for potential short circuiting of the thin film resistor to the underlying conductive substrate/tube. It is reasonable to assume that the electroplating bath had little to no deleterious effect on the Al_2O_3 film [168].

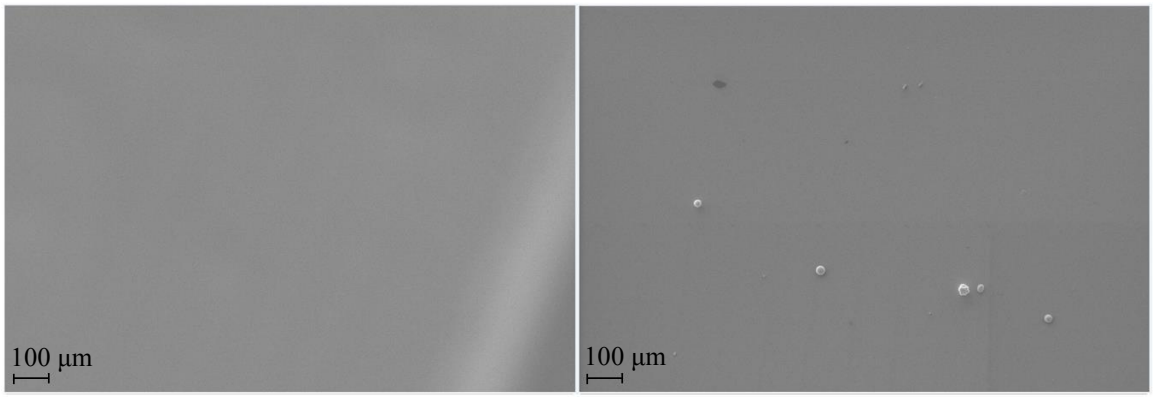

a) b)

Figure 65: Comparison between SEM images of 200nm thick Alumina deposited on Cu-coated Si substrates a) before and b) after electroplating process

To confirm that the defects would eliminate the necessary electrical isolation, several copper tubes were coated with 200nm Al_2O_3 and sent to Impreglon [169] to be coated with Titanium Nitride (TiN). TiN is an extremely hard ceramic material commonly used to coat machine tools such as drill bits and milling cutters. In addition to the robust mechanical properties, TiN is also electrically conductive so it is suitable as a resistive

material. After the tubes were coated by Impreglon, they were tested for electrical isolation between the copper tube and TiN film. Unfortunately, the two layers were not effectively isolated by the 200nm Al_2O_3 layer. Presumably, this was a result of the pinhole defects previously discussed.

A .2.3 Ruthenium ALD

Despite the known concerns with the primary Al_2O_3 insulating layer, experiments were also conducted using the Cambridge NonoTech Fiji ALD tool to observe the properties of the secondary conducting Ru layer. Unfortunately, the Ru layer suffered from nucleation effects, which are temperature and substrate dependent [170]; Figure 66 shows a SEM image of Ru nucleation sites taken during the current study. Cambridge customer support indicated that a chamber conditioning step of 3000-5000 cycles of Ru would promote the stable growth of Ru films. Unfortunately, the Ru precursor material was prohibitively expensive and a more detailed experimental study involving extensive chamber conditioning steps was not feasible. We were sufficiently satisfied with being able to explain 'why' this proposed methodology was not working, and relied on the Parylene and Ti-Pt process for creating thin film heaters for the current study.

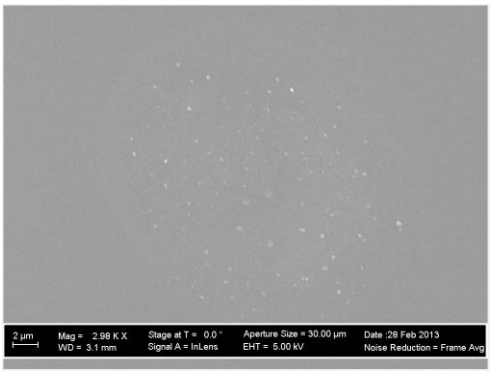

Figure 66: SEM image of Ruthenium nucleation sites

Appendix B Matlab Code for Total Internal Reflection

This appendix describes the Matlab code used for systematically calculating film thickness and flow regime for Chapter 6. The process involves pulling the individual '.png' picture files from a specified file location, then undertaking the image processing steps outlined in Chapter 6 and included below for the reader's convenience. The basis of the Matlab algorithm was determining the distance between the light source and the reflected rays and calculated the liquid film thickness using the following relationship:

$$t_l = \frac{x - 2t_w \tan\theta_{cwa}}{2\tan\theta_{clv}} \tag{72}$$

Several image processing steps were required to extract a film thickness value from an unrefined image. First, the image was captured with an appropriate camera. Shown in Figure 67a is a captured image with no film (dry channel). The black shaft on the bottom-center of the figure is the painted fiber optic LED connecting to the diffuse coating. The reflected light ring is visible, but not distinct enough to extract accurate film thickness values. Next, the image was converted to red-only to eliminate background light noise. Then, adaptive contrast enhancement was performed to normalize the image and remove complications stemming from intensity variations in the reflected light ring as a result of LED mounting imperfections. Figure 67b shows the original image after eliminating green and blue light, and adaptive contrast enhancement. Next, a 2-D median filter was applied to eliminate salt and pepper noise and a simple contrast enhancement code was applied, resulting in a binary image, as shown in Figure 67c. The reflected light ring is now clearly visible.

The center of the LED was manually identified. In Figure 67c, the center of the LED is indicated with a red point. Next, a Sobel filter was used to locate the edges where the binary image changes from black to white and vice versa; the Sobel filter function outputs a matrix of these locations. As shown on Figure 67c, the third 'edge' identified by the Sobel filter will represent the first fully reflected ray. Then, a custom Matlab code was used to count left and right (pixel-by-pixel) out from the LED center point while searching for the third location where the contrast changes. The diameter of the light ring, in pixels, is the sum of the distance measured to the left and right. Next, the pixel distance was translated to a physical distance using the width of the LED (1.27 mm) as a reference scale. Finally, Equation (49) was used to relate the light ring to a liquid film thickness.

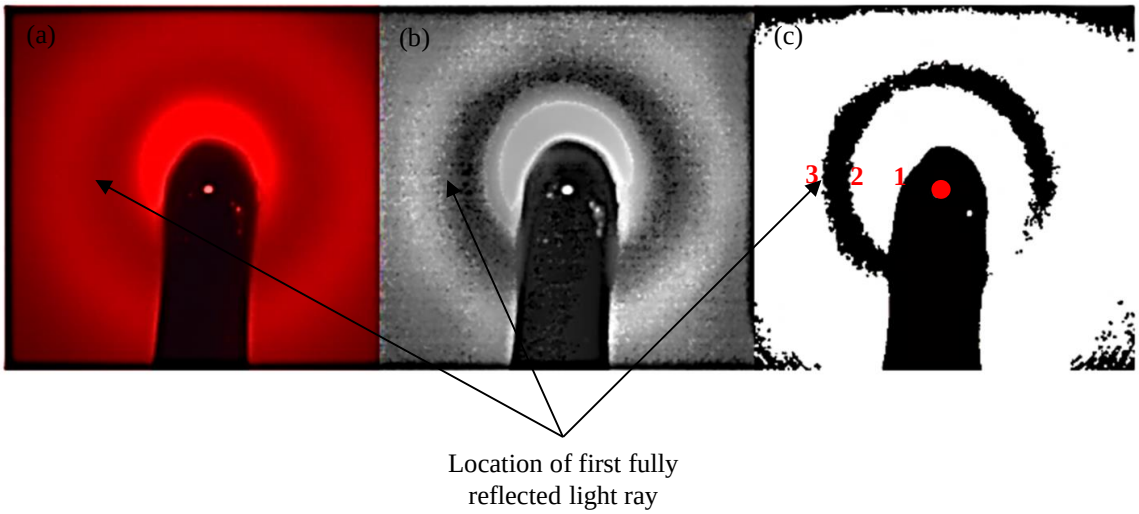

Figure 67: a) Raw image of reflected light ring on a glass tube with no film thickness, b) Image after converting to black and white and contrast enhancement, and c) Image after converting to binary

The Matlab code used to accomplish this is shown below, along with comments to assist the reader:

```
clc

clear all

close all
```

B.1 Preprocessing

```
fiber_dia=0.00127;                    % diameter of the fiber optic LED

fiber_pix=176;                        % diameter (in pixels) of the fiber optic

pix=fiber_dia/fiber_pix;      % defines m/pixel (pixel ‘length’)

center=[603,360];             % manually determined by inspection
```

B.2 Importing the Picture and Finding the Location of the First Fully Reflected Ray

```
I = imread('183 micrometer calibration.png');  % read the file

figure('Name','I');  % name the figure

imshow(I)  % show the figure - Figure 67a

I_2=I(:,:,1);  % change the image to red

Max=max(max(I_2));  % find the maximum

Min=min(min(I_2)); % find the minimum

figure('Name','I_2');  % name the figure

imshow(I_2)  % show the figure

[N,M]=size(I_2);  % size of the 'contrast' matrix
```

```
filtered=medfilt2(medfilt2(medfilt2(medfilt2(medfilt2(medfilt2((medfilt2(I_2))))))));  % median filter used to eliminate salt and pepper noise

figure ('Name','filtered');  % name the figure

imshow(filtered) % show the figure

adapthisteq=adapthisteq(filtered,'NumTiles',[8 8],'ClipLimit',0.1,'NBins',1000,'Distribution','uniform');  % adaptive contrast enhancement based on local maximum and minimum

figure ('Name','adapthisteq');  % name the figure

imshow(adapthisteq) % show the figure

contrast=255*((adapthisteq-Min)/(Max-Min));  % increase the contrast as described by Shedd and Newell [81]

figure('Name','contrast')  % name the figure

imshow(contrast)  % show the figure Figure 67b

hold on;

filtered2=medfilt2(medfilt2(medfilt2(medfilt2(medfilt2(medfilt2((medfilt2(contrast,[11 11])))))))); % median filter used to eliminate salt and pepper noise

figure ('Name','filtered2'); % name the figure

imshow(filtered2) % show the figure

hold on

plot(603,360,'r.','MarkerSize',20) % plot the LED center point on the figure
```

```
sobel=edge(filtered2,'sobel');  % Sobel filter finds the 'edges' of the high contrast region
(highest slope)

figure('Name','sobel');  % name the figure

imshow(sobel)  % show the figure

hold on

plot(603,360,'r.','MarkerSize',20) % plot the LED center point on the figure Figure 67c


hold off
```

B.3 Determining the Number of Pixels Between Lines

```
iii=0;

jjj=0;

kkk=0;

ring=zeros(N,M);

band=60; % region above and below the center point that will be ‘searched’

% search for first fully reflected ray to the right

for i =center(2)-band/2:center(2)+band/2

   iii=0;

   jjj=0;

   kkk=0;
```

```
    for j =center(1):M
        if sobel(i,j) == 1
            iii=iii+1 % transition counter
        end
        if iii == 2
            if contrast(i,j) == 0
                jjj=jjj+1;  % counts number of consecutive black pixels
            elseif contrast(i,j) == 255
                jjj=0;
            end
        end
        if iii == 3
            dist_r(i)=abs(j-center(1));
            break
        end
    end
end
dist_r;
```

```
% search for first fully reflected ray to the left

i=0;

j=0;

iii=0;

jjj=0;

kkk=0;

for i =center(2)-band/2:center(2)+band/2

    iii=0;

    jjj=0;

    kkk=0;

    for jj =center(1):M

        kkk=kkk+1;

        j=jj-2*kkk;     % creating a negatively moving index

        if sobel(i,j) == 1

            iii=iii+1; % transition counter

        end

        if iii == 2

            if contrast(i,j) == 0
```

```
            jjj=jjj+1;  % counts number of consecutive black pixels
        elseif contrast(i,j) == 255
            jjj=0;
        end
    end
    if iii == 3
        dist_l(i)=abs(j-center(1));
        break
    end
  end
end
avg_dist=(dist_r+dist_l)/2; % the light ring radius is half of the diameter
total_dist=dist_r+dist_l;
actual_radius=avg_dist*pix;
non_zero=actual_radius(actual_radius~=0); % eliminates any discontinuities
avg=mean(non_zero);
avg_mm=avg*1000;
max=max(non_zero);
```

```
max_mm=max*1000;

plot(1:length(avg_dist),avg_dist) % plot the average distance (in pixels)
```

B.4 Defining Properties and Dimensions

```
n_tube=1.52;     % index of refraction of tube wall (microscope slide)

n_vapor=1;         % index of refraction of air/vapor

n_film=1.524;          % index of refraction of UV curing adhesive (in actual applications
it will be the index of the fluid at the appropriate temperature)

t_tube=0.00101;        % thickness of the tube wall in meters (microscope slide)

avg_dist=avg;        % average radius of the light ring in meters
```

B.5 TIR Film Thickness Calculation

```
theta_crit_cl=asin(n_vapor/n_film);

theta_crit_cw=asin(n_vapor/n_tube);

theta_crit_wl=asin(n_film/n_tube);

x_dry=2000*t_tube*tan(theta_crit_cw)

thickness_avg=(avg-2*t_tube*tan(theta_crit_cw))/(2*tan(theta_crit_cl))

thickness_mm_avg=thickness_avg*1000

max_thickness=(t_tube*(tan(theta_crit_wl)-tan(theta_crit_cw)))/(tan(theta_crit_cl));
```

```
x_dry =

    1.7646

Thickness_avg =

   1.8031e-04

thickness_mm_avg =

    0.1803
```

Published with MATLAB® 7.14

Appendix C 8.84mm Smooth and Internally-Grooved Tube Data

This Appendix is a compilation of all of the diabatic 8.84mm smooth and internally-grooved tube data collected during the course of this study; in total, 2098 diabatic data points are shown below. The Wojtan et al. [31] heat transfer coefficient correlation as well as the correlation developed in this dissertation are included for reference. Select figures from this data set were used for the analysis in Chapter 8. Please refer to Chapter 8 for a description of the more salient trends observed; this Appendix mainly serves as a means to document the entirety of the experimental results.

Each figure represents a different flowrate (25-300 kg/m²s) and six different heat fluxes (4-56 kW/m²s). In some scenarios, high heat fluxes could not be accurately measured because the heat transfer coefficient was too low or dryout occurred and the tube overheated. However, the heat transfer coefficient correlations were still included for reference. One example of this is Figure 75 with a heat flux of 56 kW/m²s.

The experimental smooth tube data points are shown as red squares and the internally-grooved tube data points are green circles. 'IG 1' and 'smooth 1' were the first tests run and 'IG 2' and 'smooth 2' were the second tests run; as indicated in Chapter 8, these do not represent different tubes, just a second run of experiments for validation. The smooth tube heat transfer coefficient correlation [31] and the current internally-grooved tube heat transfer coefficient correlation are plotted as solid red and dashed green lines, respectively.

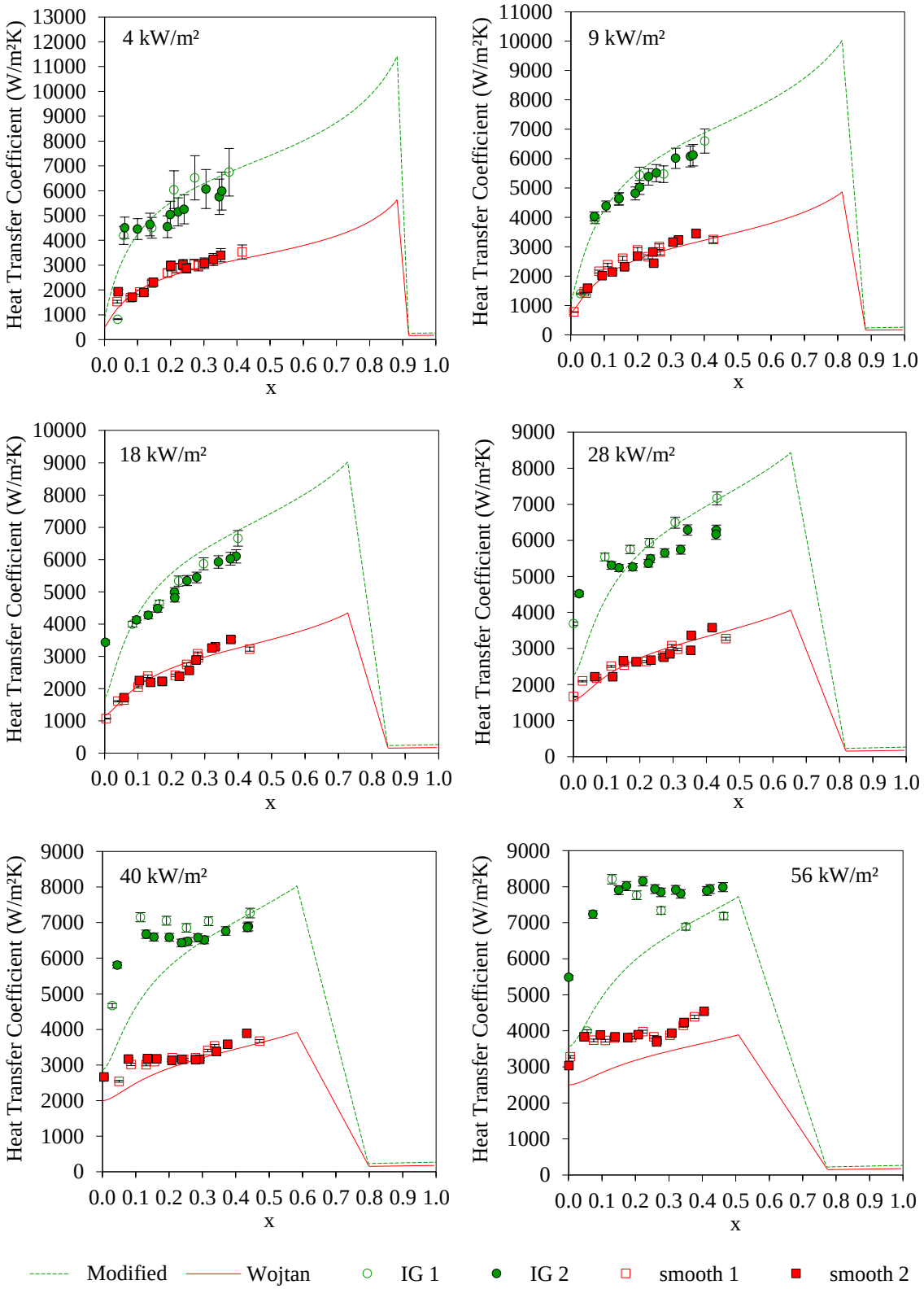

Figure 68: Heat transfer coefficient vs vapor quality for 8.84 mm ID smooth and internally-grooved tubes at a mass flux of 300 kg/m²s and different heat fluxes

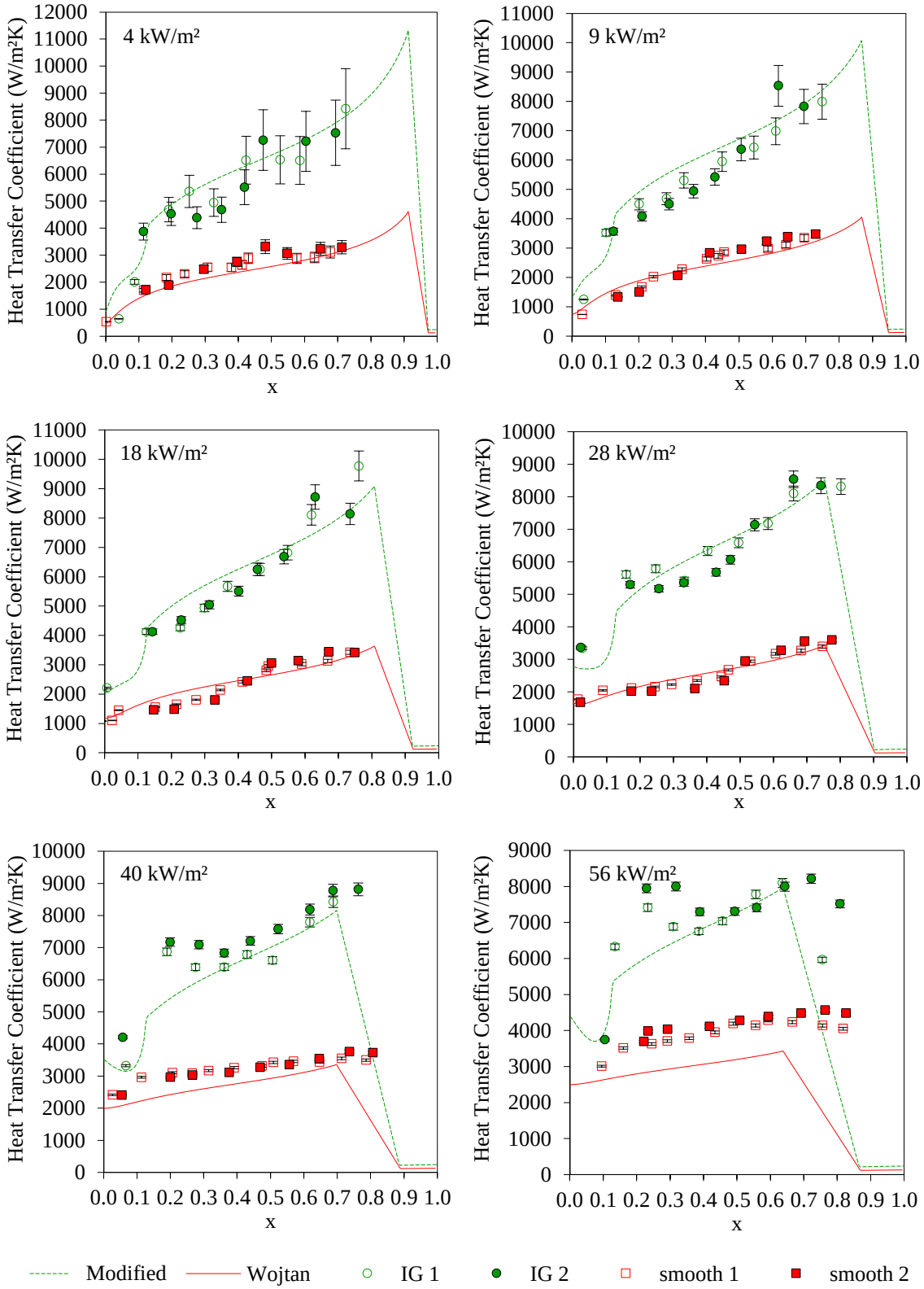

Figure 69: Heat transfer coefficient vs vapor quality for 8.84 mm ID smooth and internally-grooved tubes at a mass flux of 200 kg/m²s and different heat fluxes

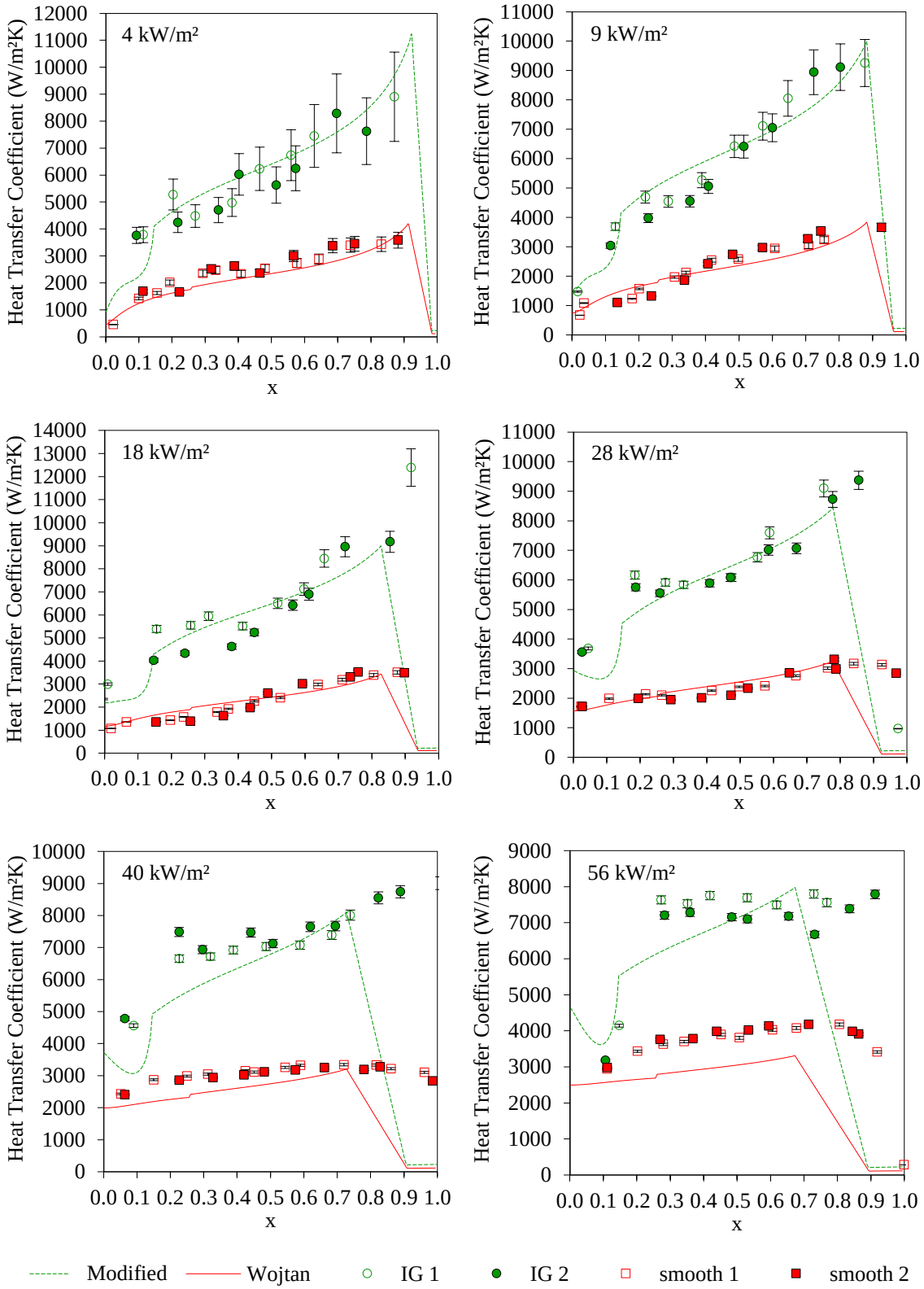

Figure 70: Heat transfer coefficient vs vapor quality for 8.84 mm ID smooth and internally-grooved tubes at a mass flux of 175 kg/m²s and different heat fluxes

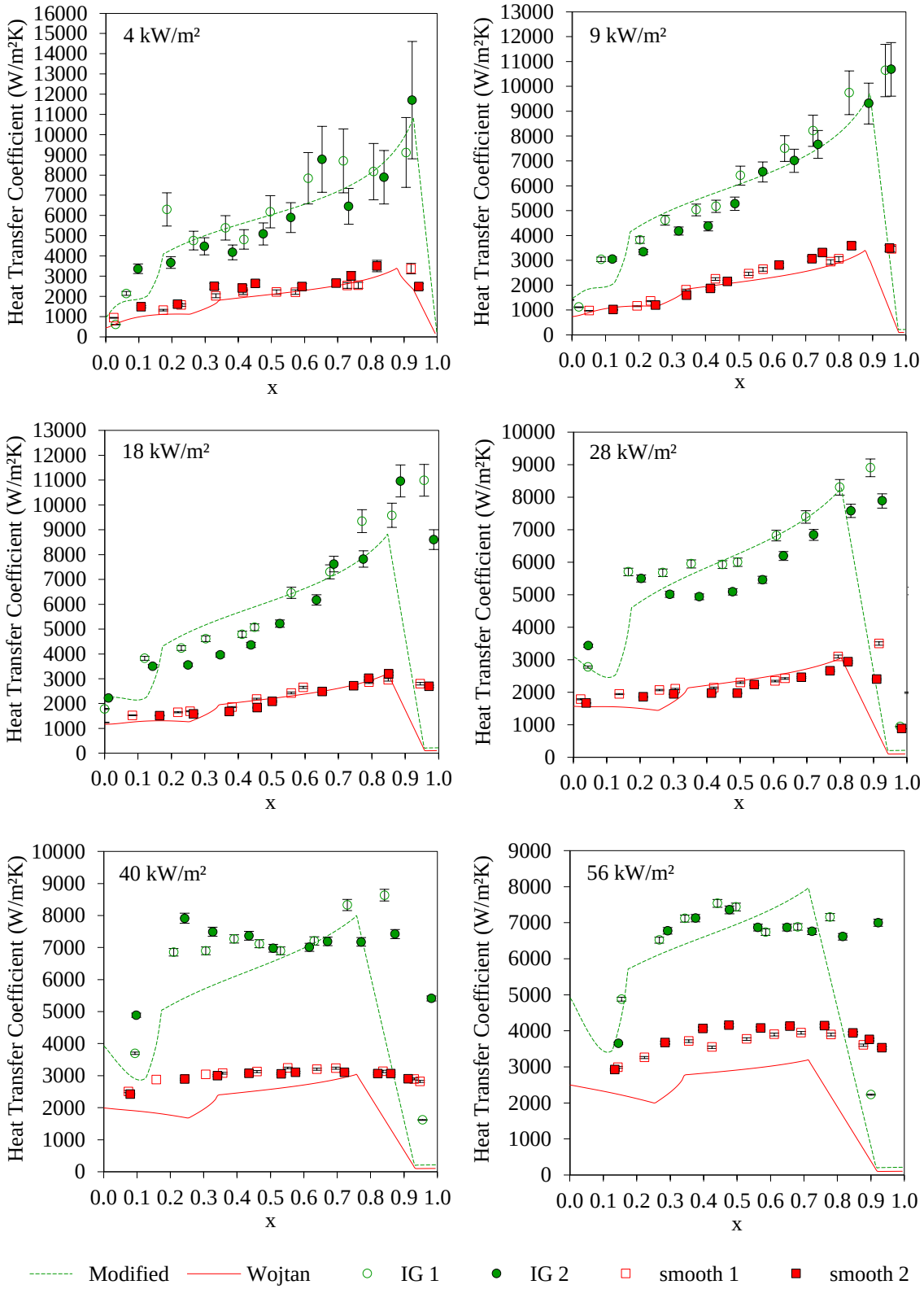

Figure 71: Heat transfer coefficient vs vapor quality for 8.84 mm ID smooth and internally-grooved tubes at a mass flux of 150 kg/m²s and different heat fluxes

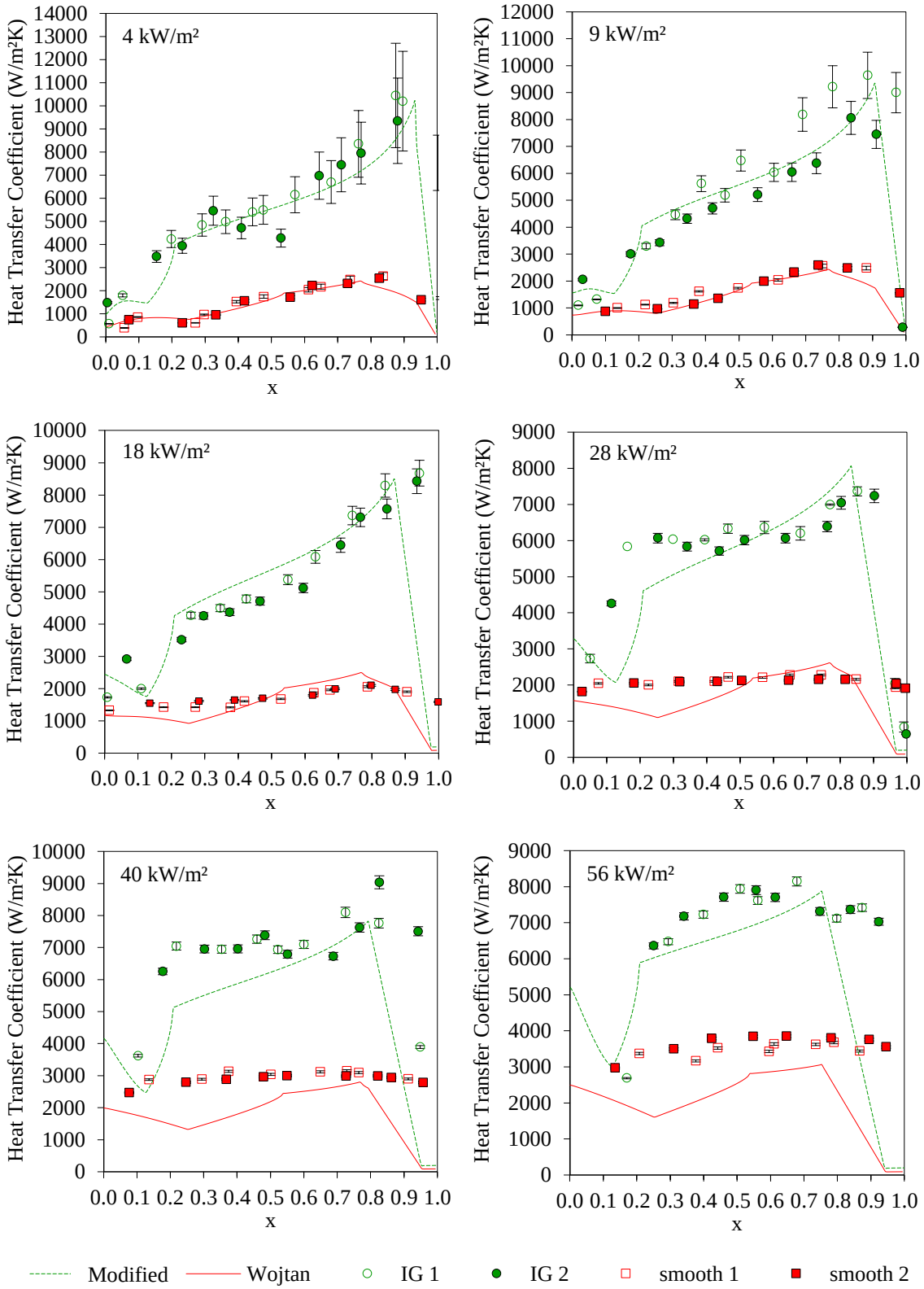

Figure 72: Heat transfer coefficient vs vapor quality for 8.84 mm ID smooth and internally-grooved tubes at a mass flux of 125 kg/m²s and different heat fluxes

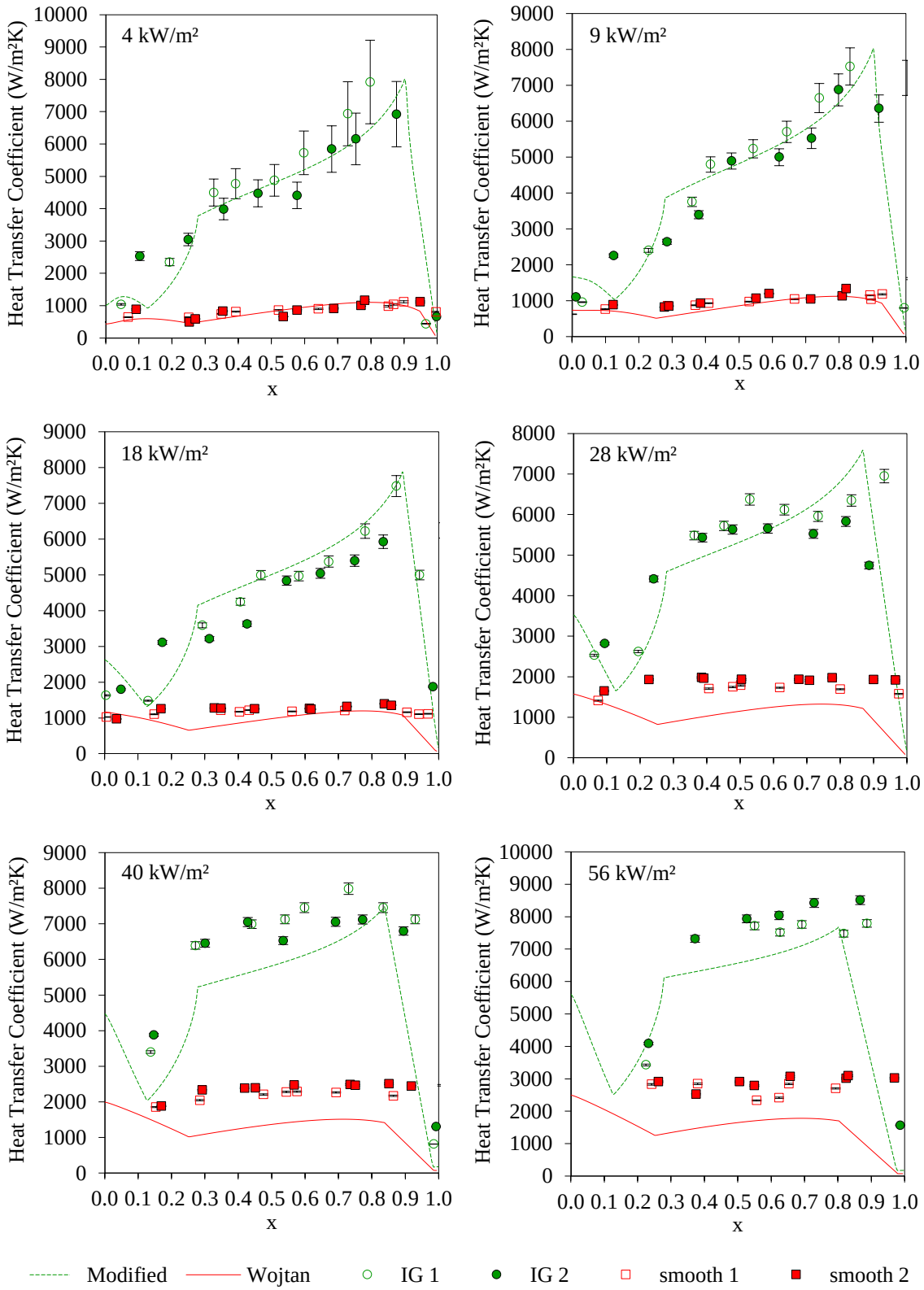

Figure 73: Heat transfer coefficient vs vapor quality for 8.84 mm ID smooth and internally-grooved tubes at a mass flux of 100 kg/m²s and different heat fluxes

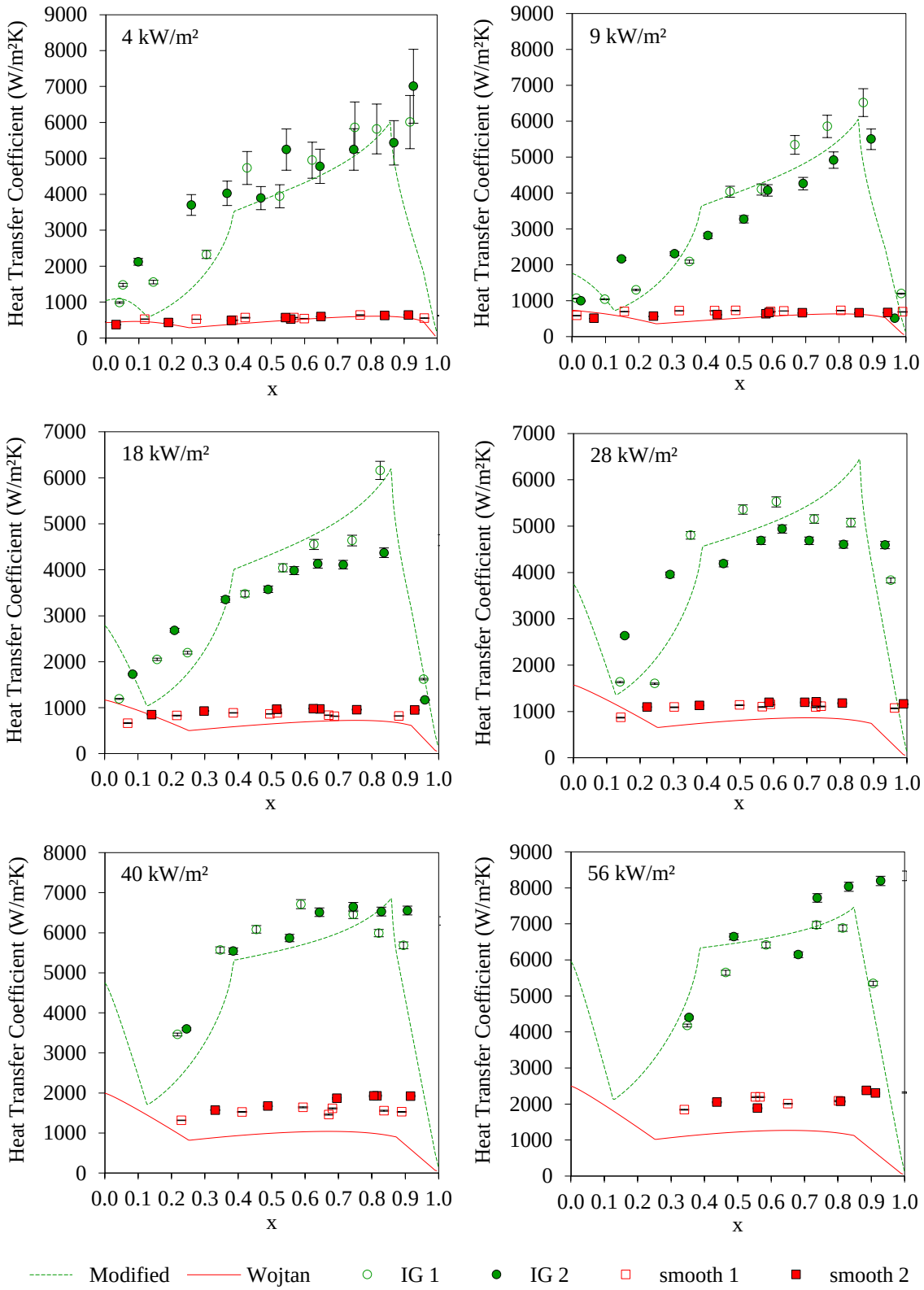

Figure 74: Heat transfer coefficient vs vapor quality for 8.84 mm ID smooth and internally-grooved tubes at a mass flux of 75 kg/m²s and different heat fluxes

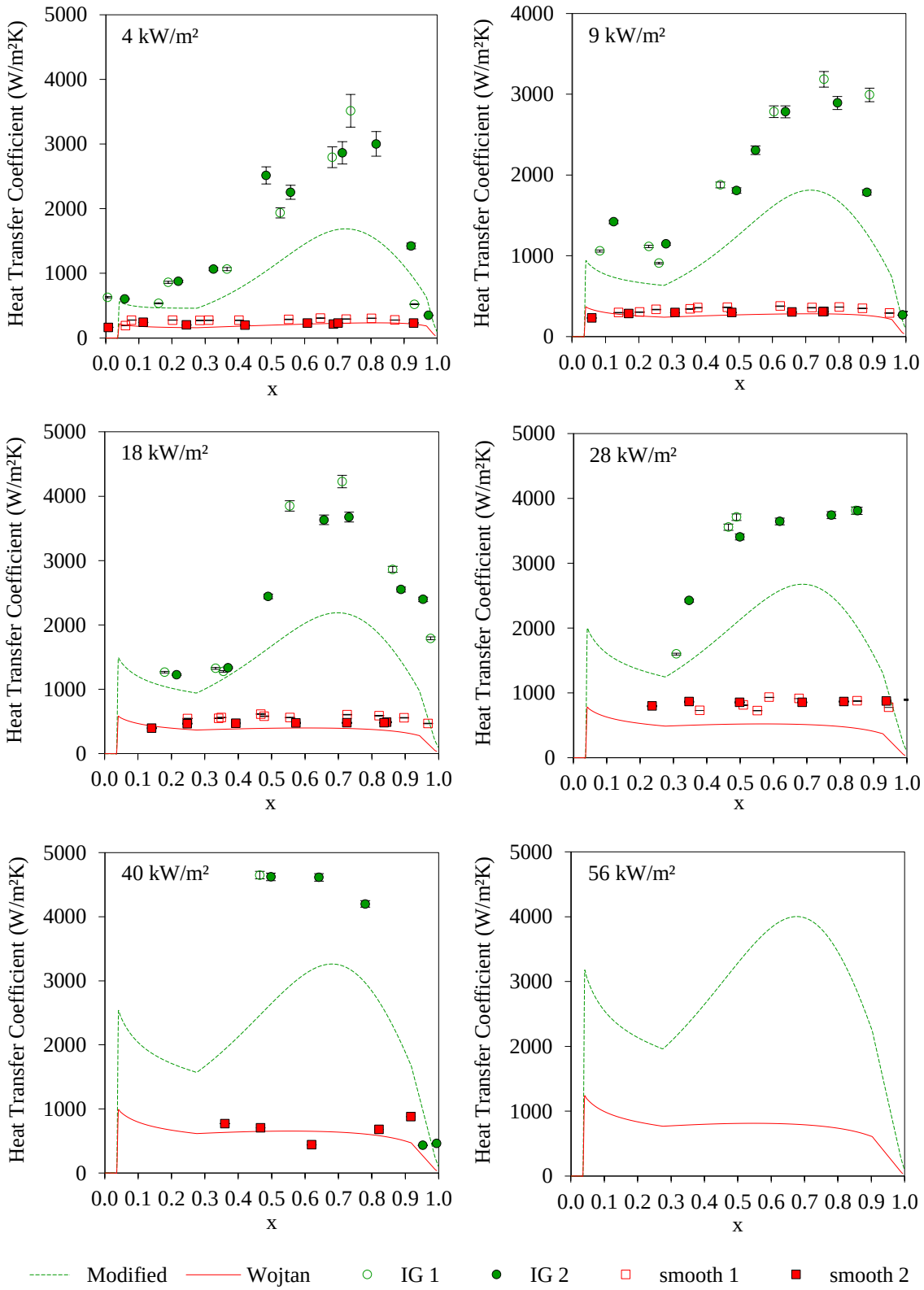

Figure 75: Heat transfer coefficient vs vapor quality for 8.84 mm ID smooth and internally-grooved tubes at a mass flux of 50 kg/m²s and different heat fluxes

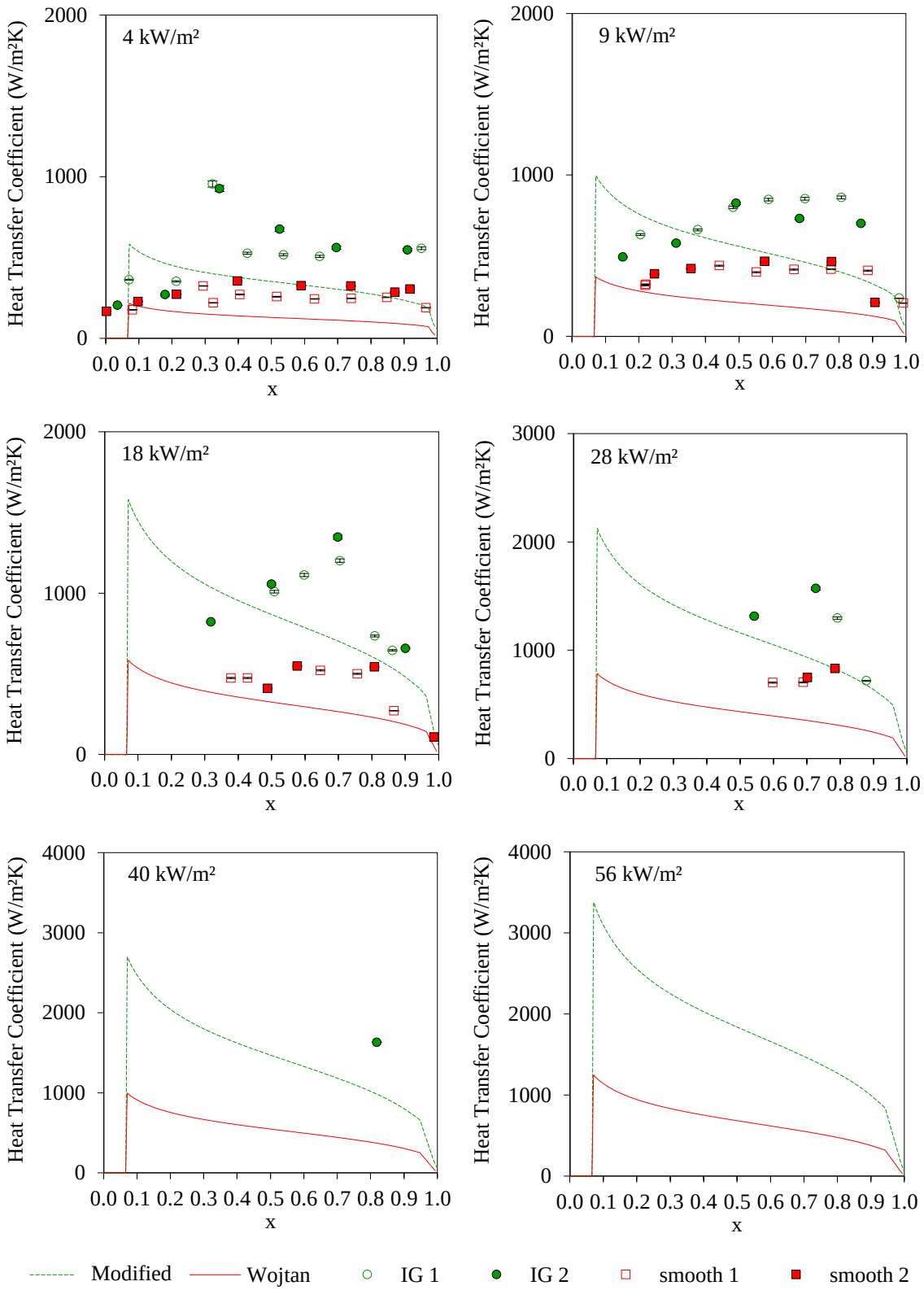

Figure 76: Heat transfer coefficient vs vapor quality for 8.84 mm ID smooth and internally-grooved tubes at a mass flux of 25 kg/m²s and different heat fluxes

Appendix D 4.54mm Smooth and Internally-Grooved Tube Data

This Appendix is a compilation of all of the diabatic 4.54mm smooth and internally-grooved tube data collected during the course of this study; in total, 1722 diabatic data points are shown below. The Wojtan et al. [31] heat transfer coefficient correlation as well as the correlation developed in this dissertation are included for reference. Select figures from this data set were used for the analysis in Chapter 8. Please refer to Chapter 8 for a description of the more salient trends observed; this Appendix mainly serves as a means to document the entirety of the experimental results.

Each figure represents a different flowrate (50-300 kg/m²s) and six different heat fluxes (4-56 kW/m²s). In some scenarios, high heat fluxes could not be accurately measured because the heat transfer coefficient was too low or dryout occurred and the tube overheated. However, the heat transfer coefficient correlations were still included for reference. One example of this is Figure 84 with a heat flux of 56 kW/m²s.

The experimental smooth tube data points are shown as red squares and the internally-grooved tube data points are green circles. 'IG 1' and 'smooth 1' were the first tests run and 'IG 2' and 'smooth 2' were the second tests run; as indicated in Chapter 8, these do not represent different tubes, just a second run of experiments for validation. The smooth tube heat transfer coefficient correlation [31] and the current internally-grooved tube heat transfer coefficient correlation are plotted as solid red and dashed green lines, respectively.

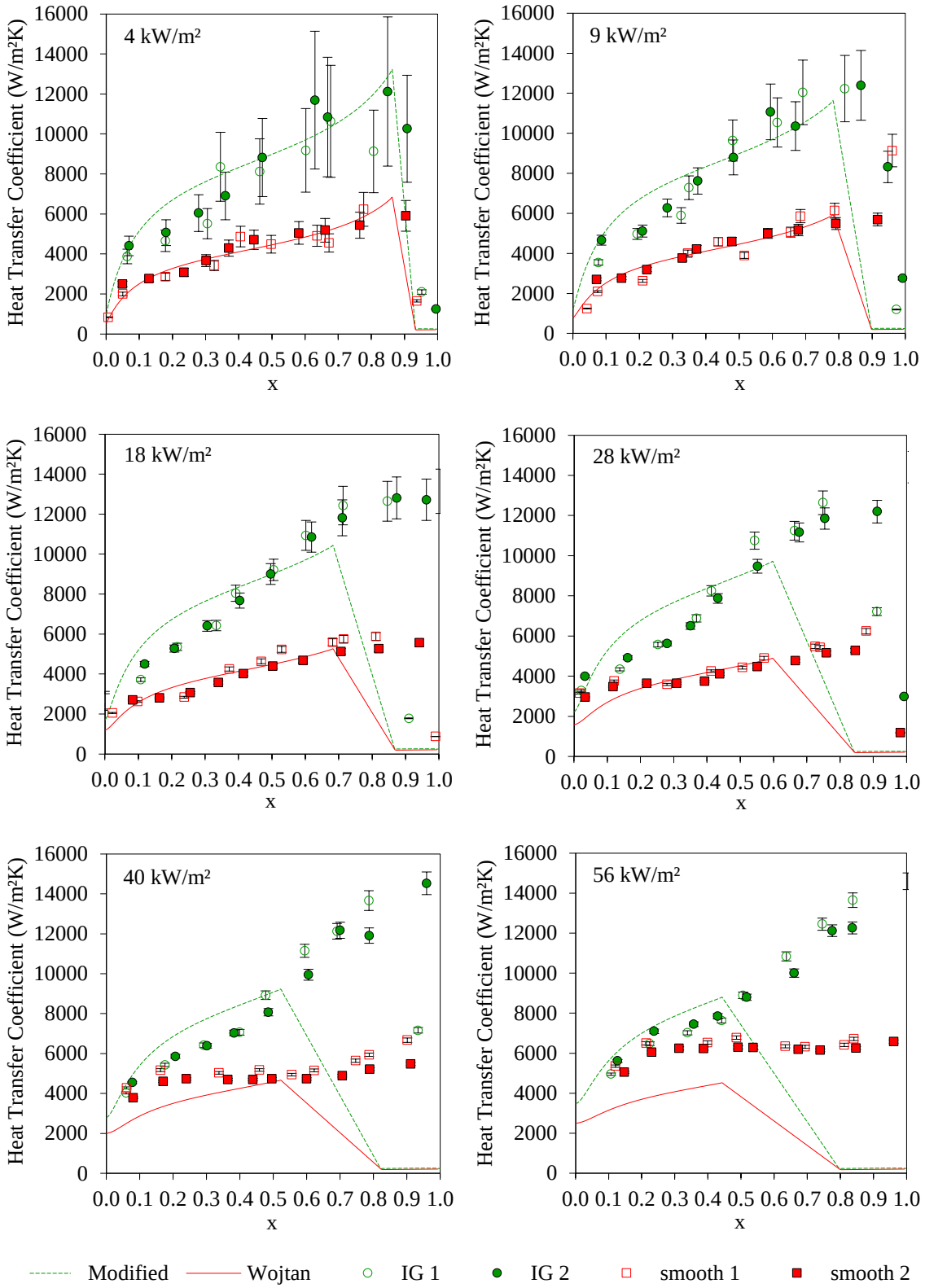

Figure 77: Heat transfer coefficient vs vapor quality for 4.54 mm ID smooth and internally-grooved tubes at a mass flux of 300 kg/m²s and different heat fluxes

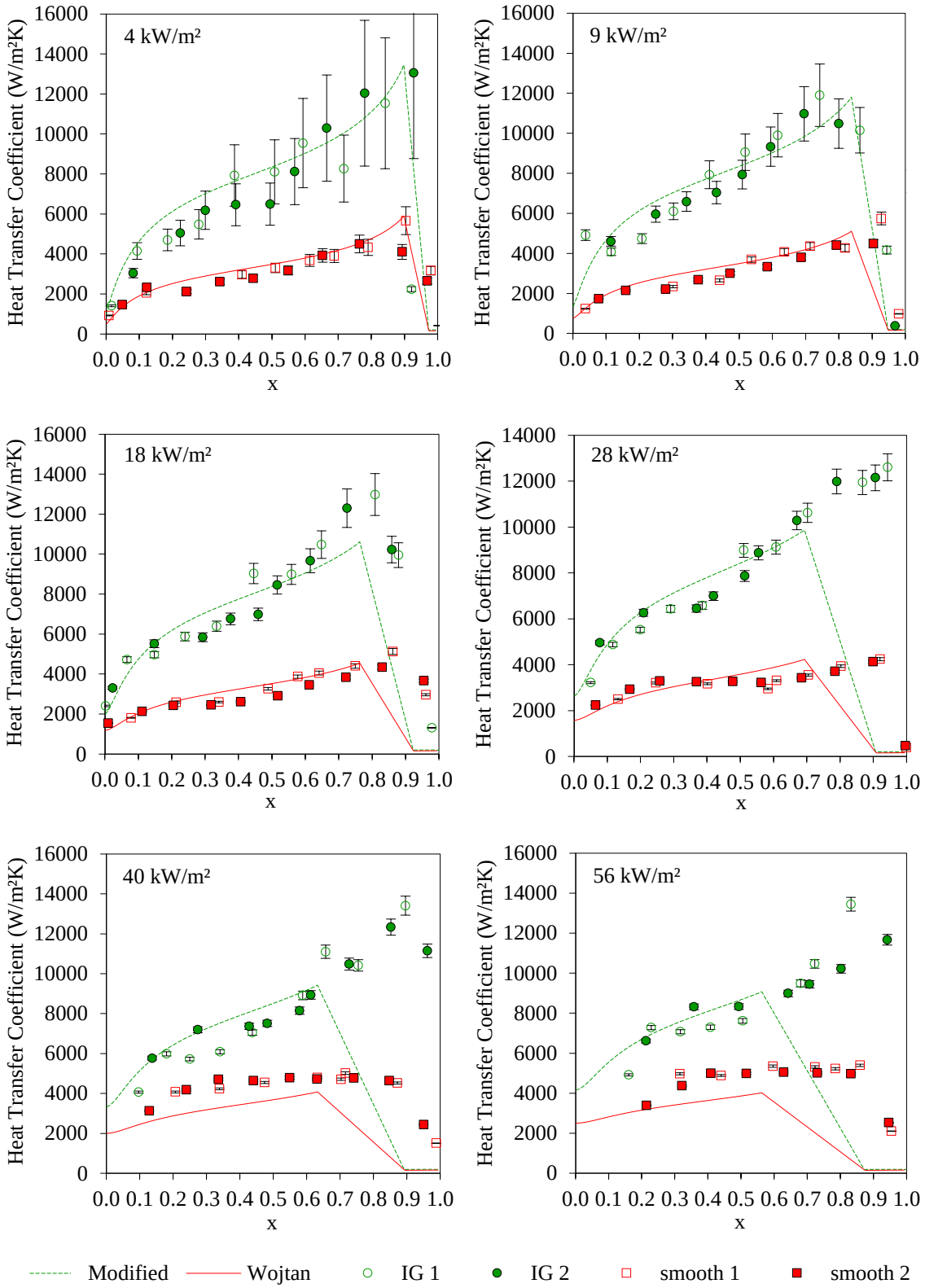

Figure 78: Heat transfer coefficient vs vapor quality for 4.54 mm ID smooth and internally-grooved tubes at a mass flux of 200 kg/m²s and different heat fluxes

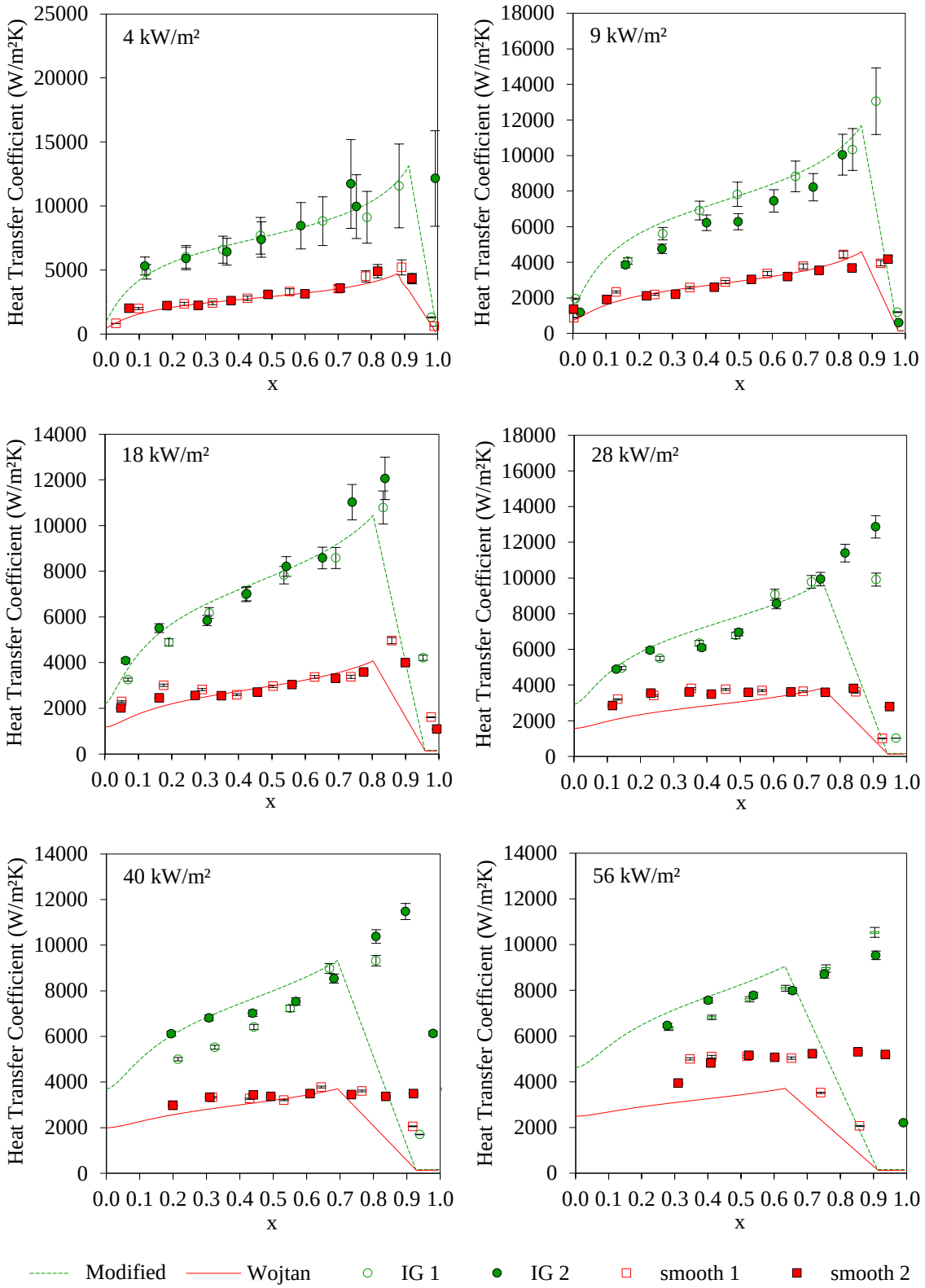

Figure 79: Heat transfer coefficient vs vapor quality for 4.54 mm ID smooth and internally-grooved tubes at a mass flux of 175 kg/m²s and different heat fluxes

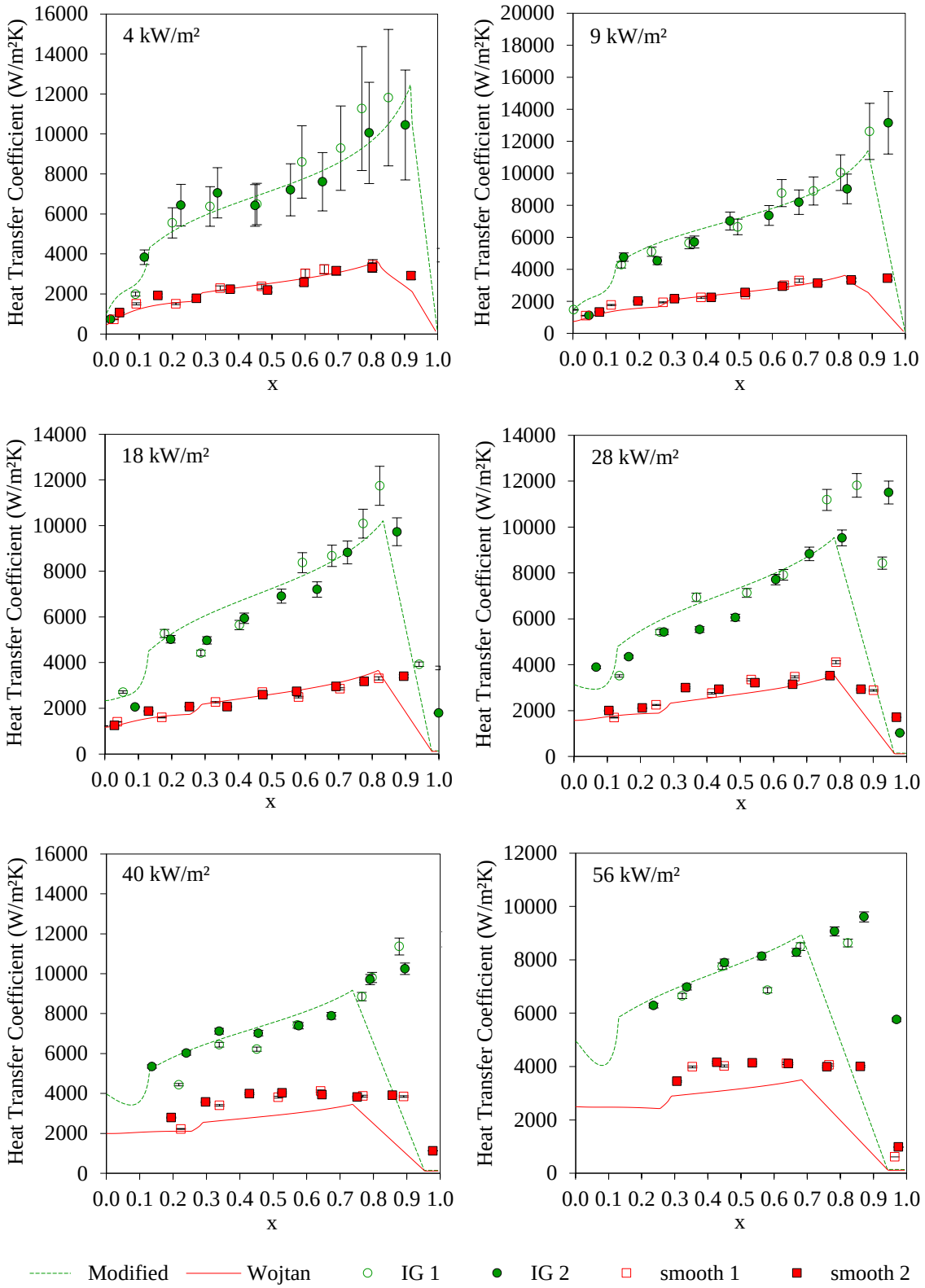

Figure 80: Heat transfer coefficient vs vapor quality for 4.54 mm ID smooth and internally-grooved tubes at a mass flux of 150 kg/m²s and different heat fluxes

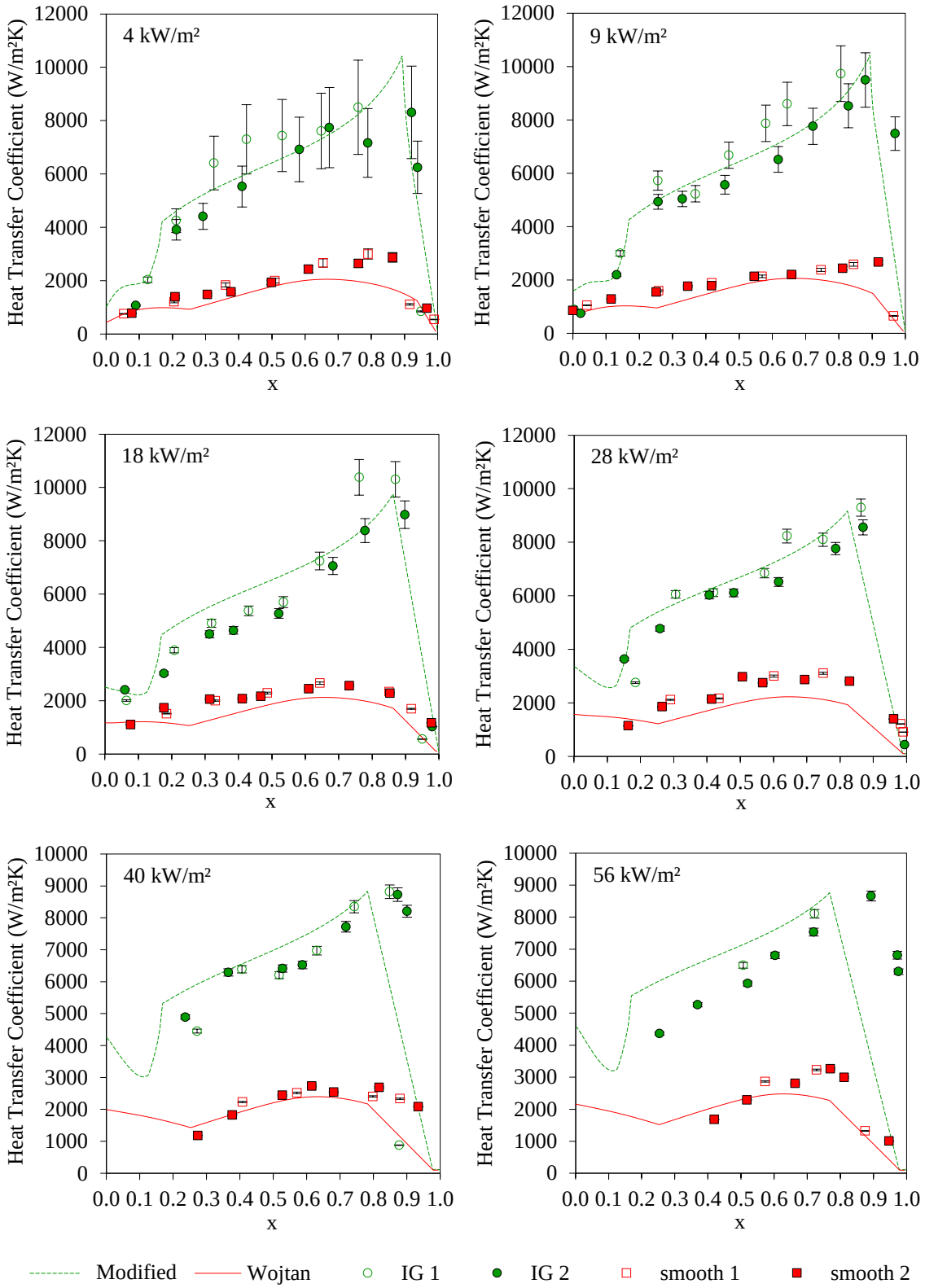

Figure 81: Heat transfer coefficient vs vapor quality for 4.54 mm ID smooth and internally-grooved tubes at a mass flux of 125 kg/m²s and different heat fluxes

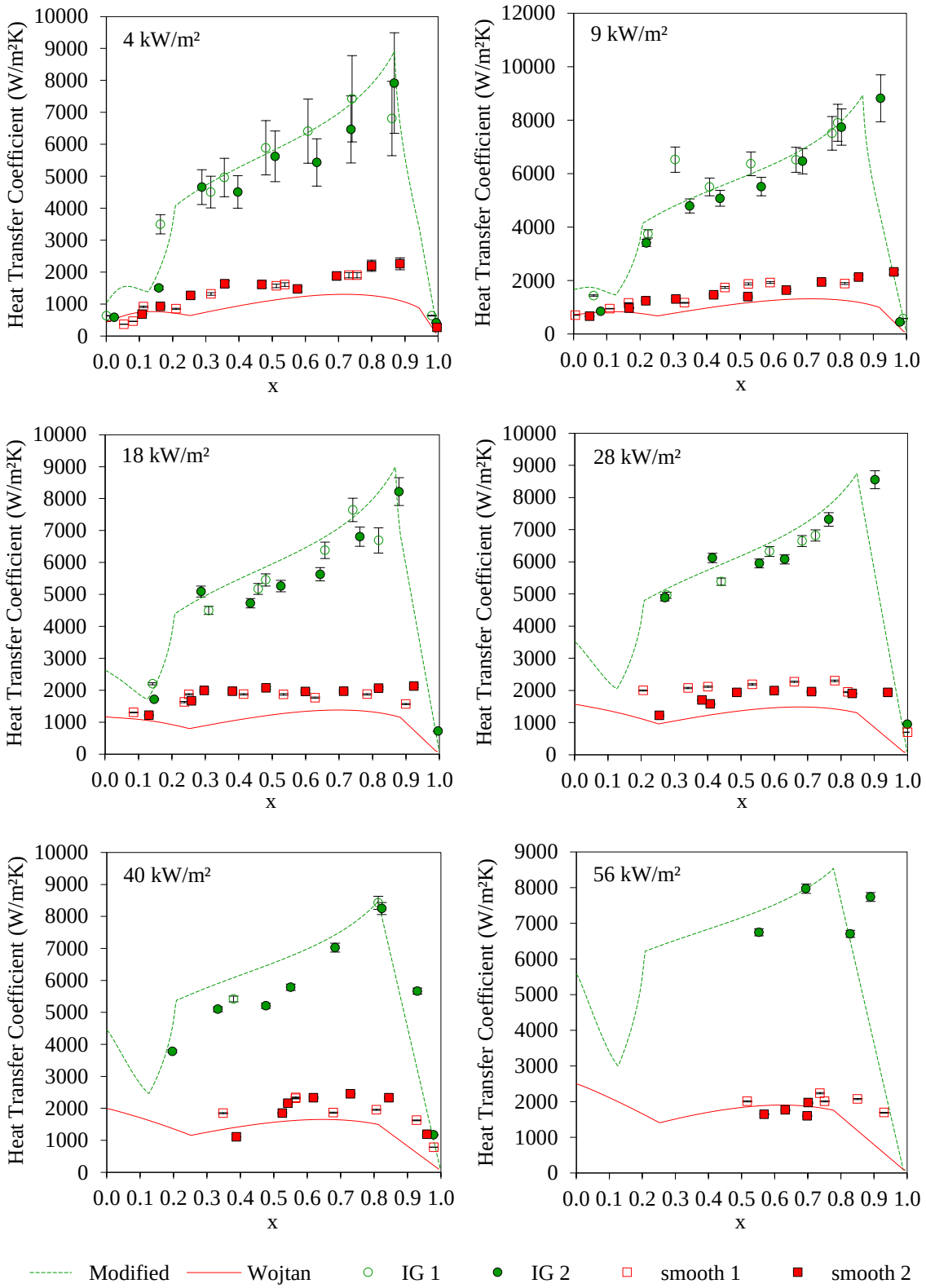

Figure 82: Heat transfer coefficient vs vapor quality for 4.54 mm ID smooth and internally-grooved tubes at a mass flux of 100 kg/m²s and different heat fluxes

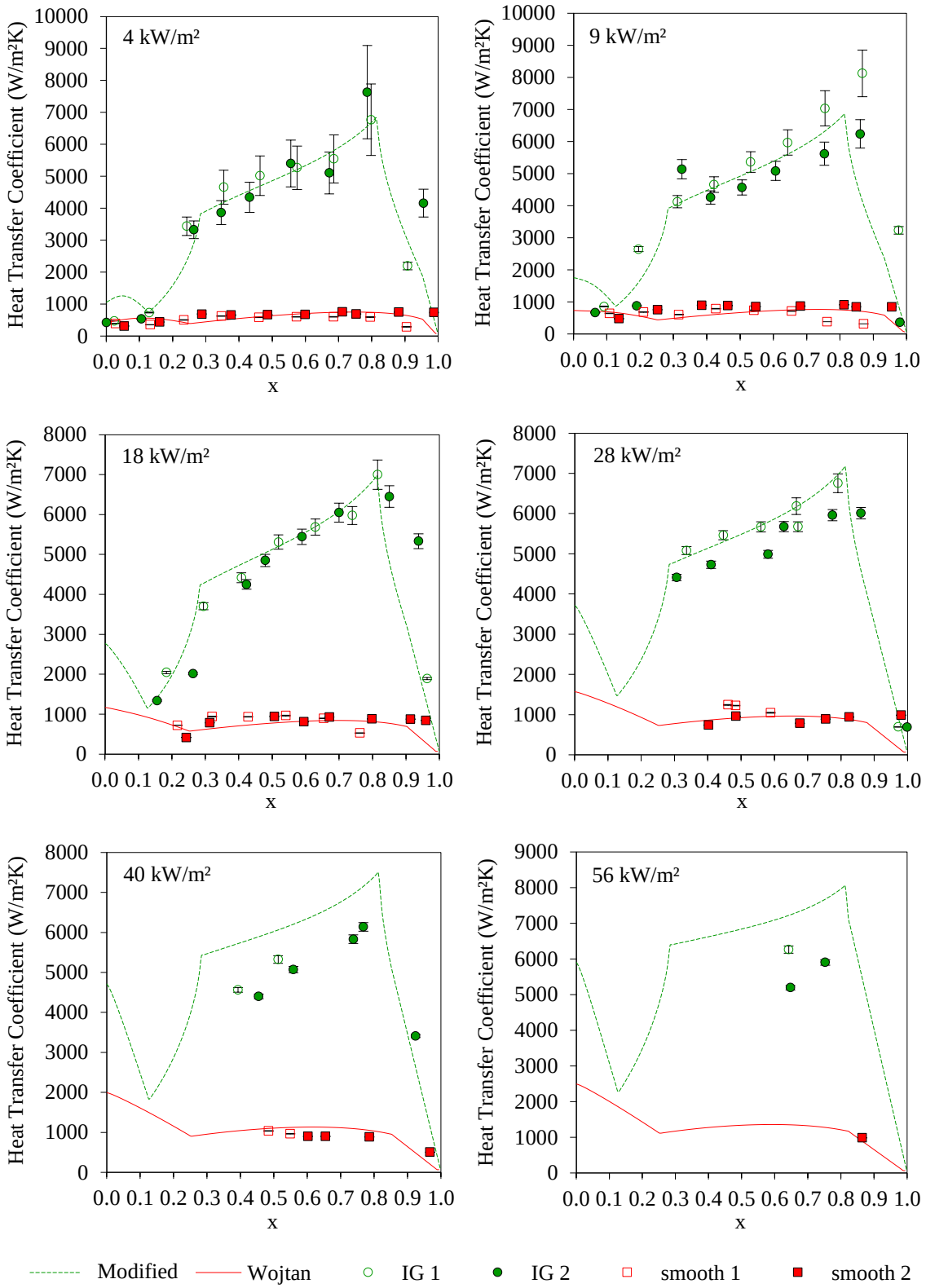

Figure 83: Heat transfer coefficient vs vapor quality for 4.54 mm ID smooth and internally-grooved tubes at a mass flux of 75 kg/m²s and different heat fluxes

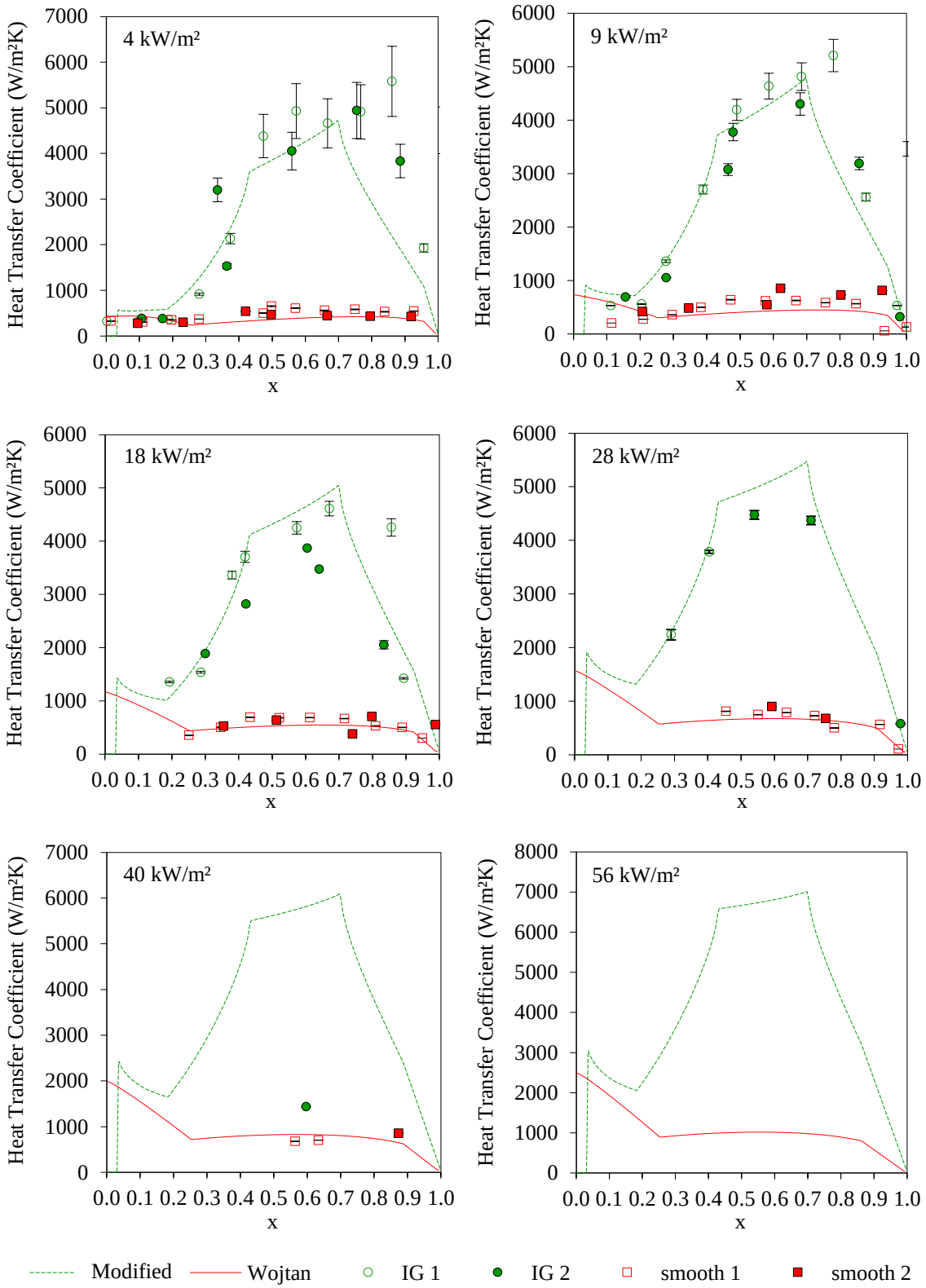

Figure 84: Heat transfer coefficient vs vapor quality for 4.54 mm ID smooth and internally-grooved tubes at a mass flux of 50 kg/m²s and different heat fluxes

Appendix E 2.8mm Smooth and 2.62mm Internally-Grooved Tube Data

This Appendix is a compilation of all of the diabatic 2.8mm smooth and 2.62mm internally-grooved tube data collected during the course of this study; in total, 1573 diabatic data points are shown below. The Wojtan et al. [31] heat transfer coefficient correlation, as well as the internally-grooved tube correlation developed in this dissertation are included for reference. Select figures from this data set were used for the analysis in Chapter 8. Please refer to Chapter 8 for a description of the more salient trends observed; this Appendix mainly serves as a means to document the entirety of the experimental results.

Each figure represents a different flowrate (75-300 kg/m²s) and six different heat fluxes (4-56 kW/m²s). In some scenarios, high heat fluxes could not be accurately measured because the heat transfer coefficient was too low or dryout occurred and the tube overheated. However, the heat transfer coefficient correlations were still included for reference. One example of this is Figure 91 with a heat flux of 56 kW/m²s.

The experimental smooth tube data points are shown as red squares and the internally-grooved tube data points are green circles. 'IG 1' and 'smooth 1' were the first tests run and 'IG 2' and 'smooth 2' were the second tests run; as indicated in Chapter 8, these do not represent different tubes, just a second run of experiments for validation. The smooth tube heat transfer coefficient correlation and the current internally-grooved tube heat transfer coefficient correlation are plotted as solid red and dashed green lines, respectively.

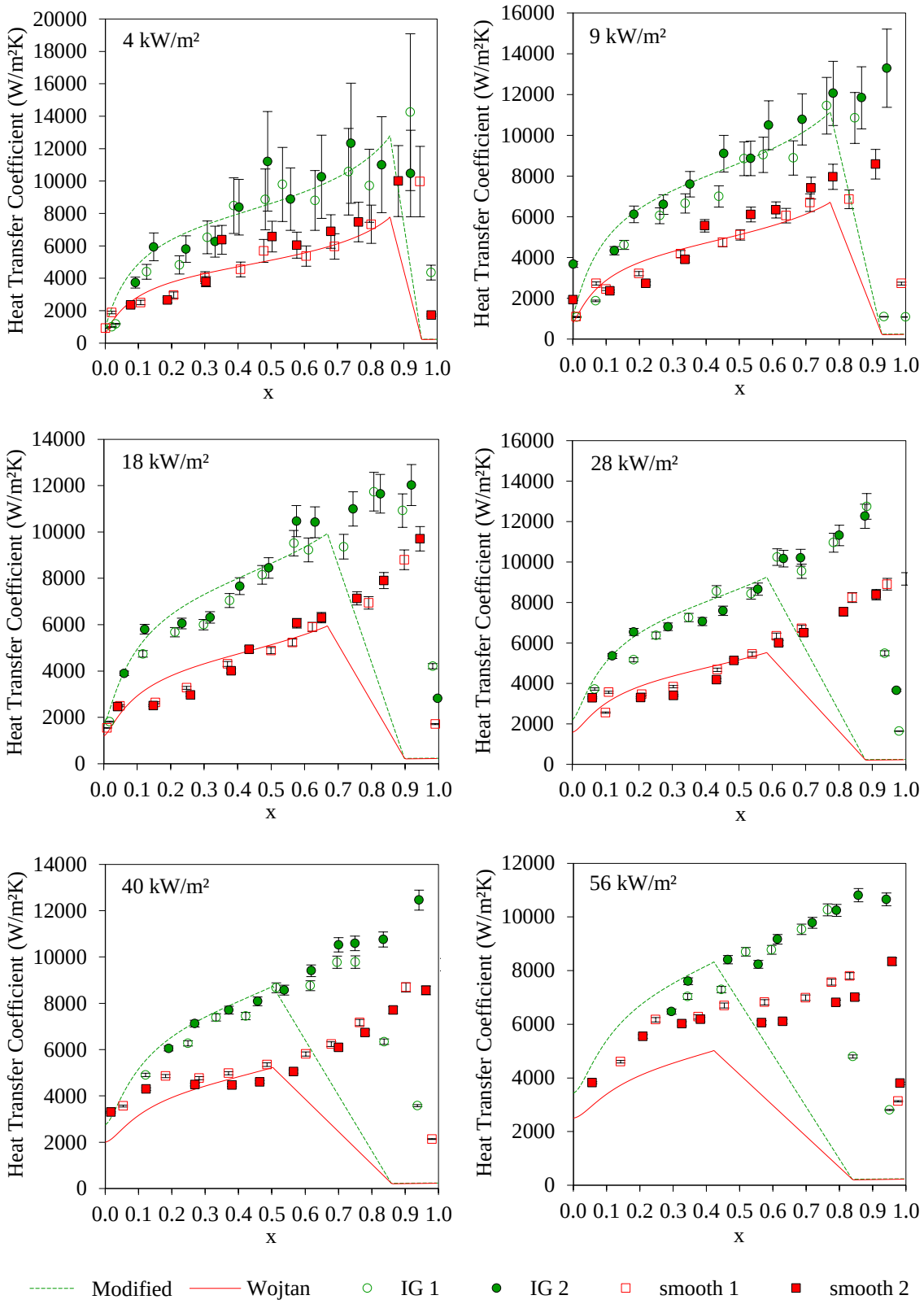

Figure 85: Heat transfer coefficient vs vapor quality for 2.8 mm ID smooth and 2.62 mm ID internally-grooved tubes at a mass flux of 300 kg/m²s and different heat fluxes

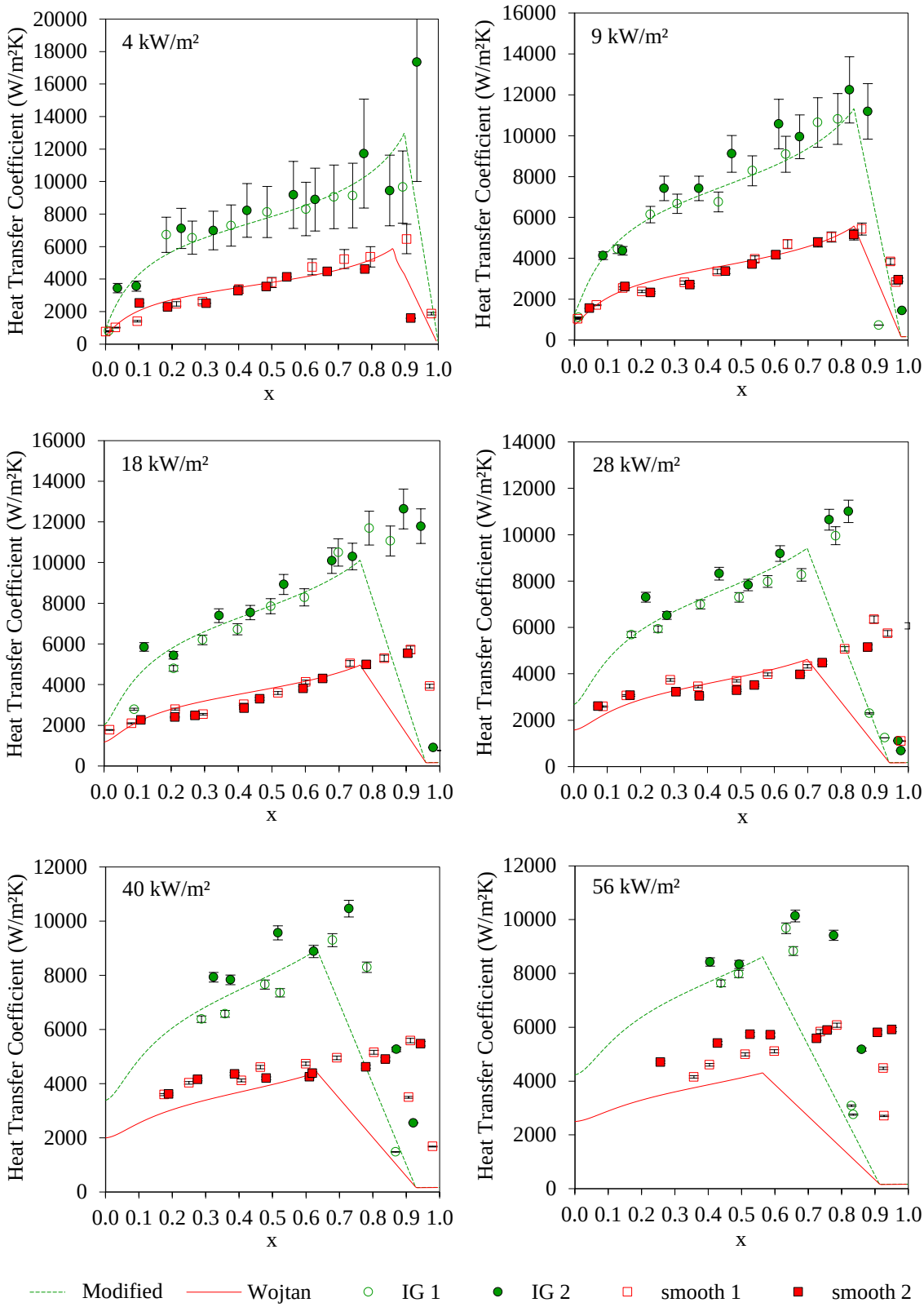

Figure 86: Heat transfer coefficient vs vapor quality for 2.8 mm ID smooth and 2.62 mm ID internally-grooved tubes at a mass flux of 200 kg/m²s and different heat fluxes

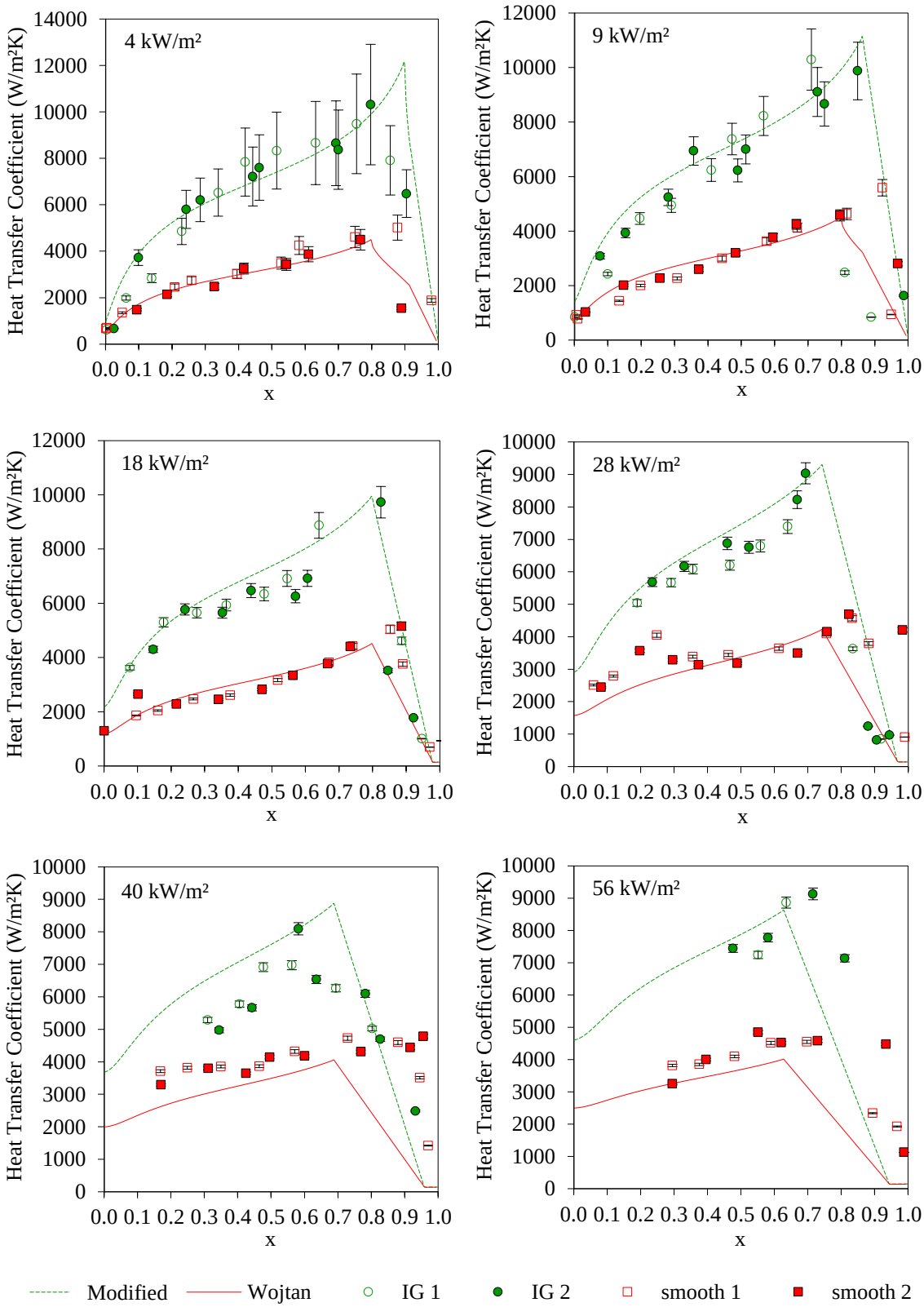

Figure 87: Heat transfer coefficient vs vapor quality for 2.8 mm ID smooth and 2.62 mm ID internally-grooved tubes at a mass flux of 175 kg/m²s and different heat fluxes

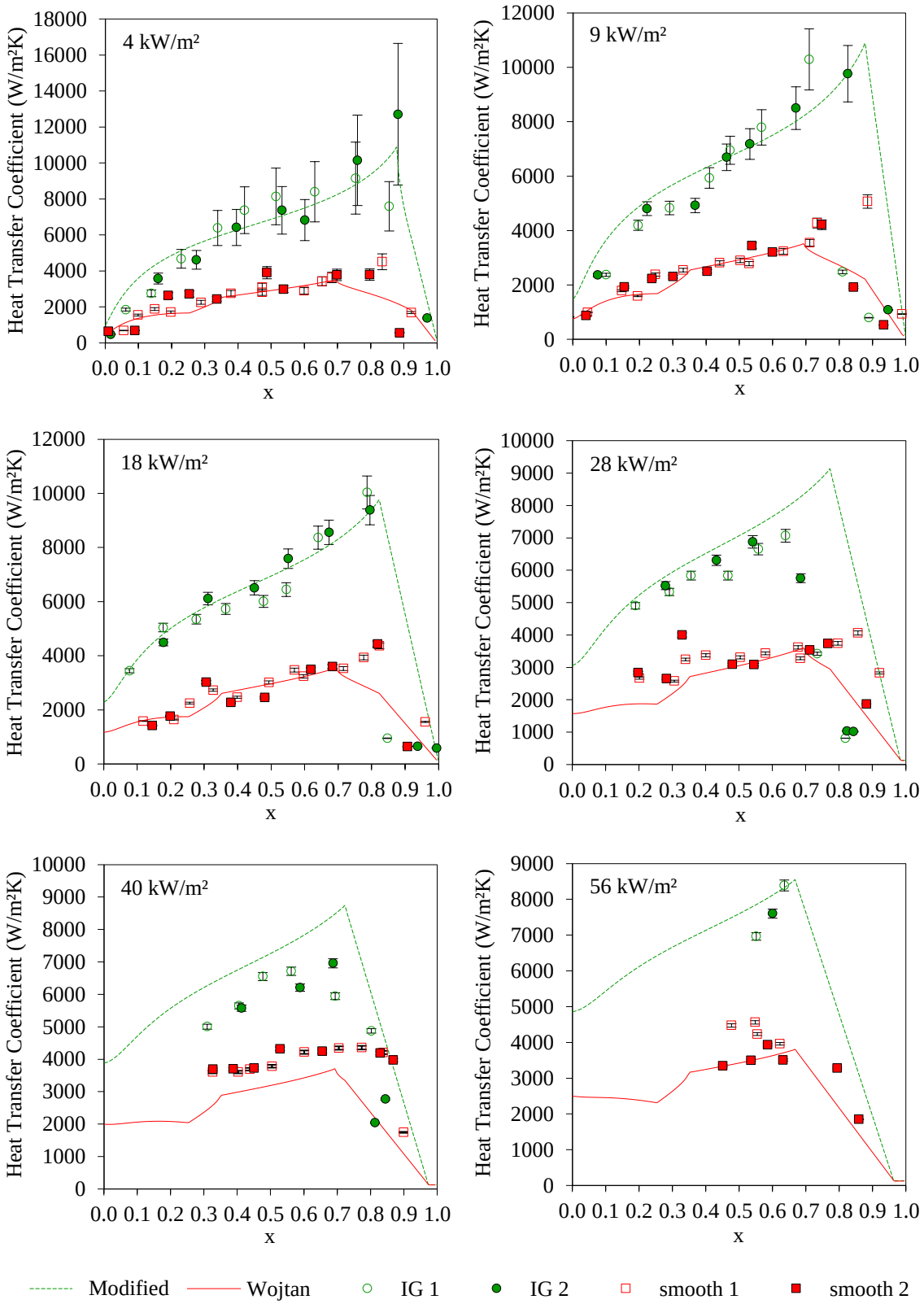

Figure 88: Heat transfer coefficient vs vapor quality for 2.8 mm ID smooth and 2.62 mm ID internally-grooved tubes at a mass flux of 150 kg/m²s and different heat fluxes

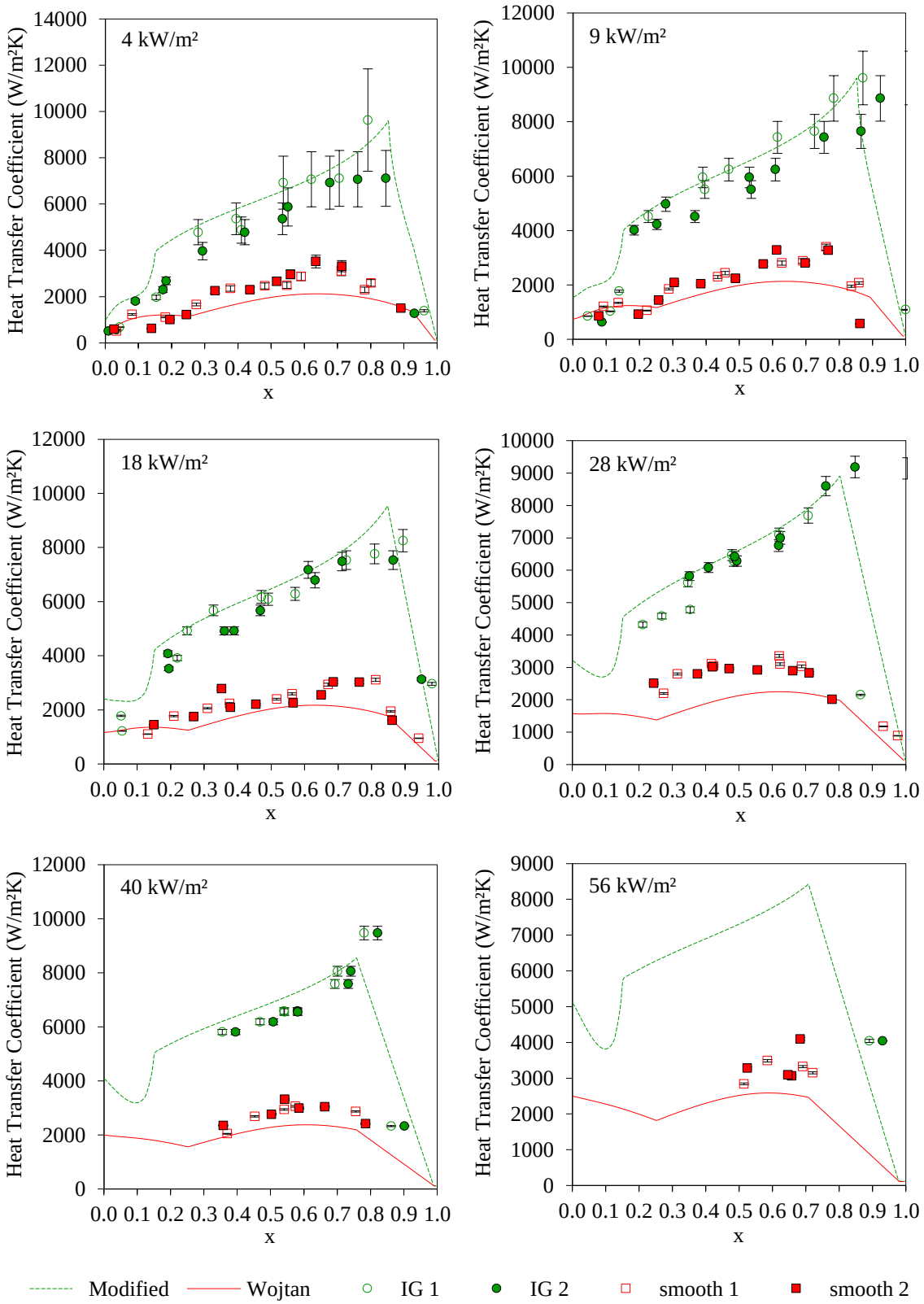

Figure 89: Heat transfer coefficient vs vapor quality for 2.8 mm ID smooth and 2.62 mm ID internally-grooved tubes at a mass flux of 125 kg/m²s and different heat fluxes

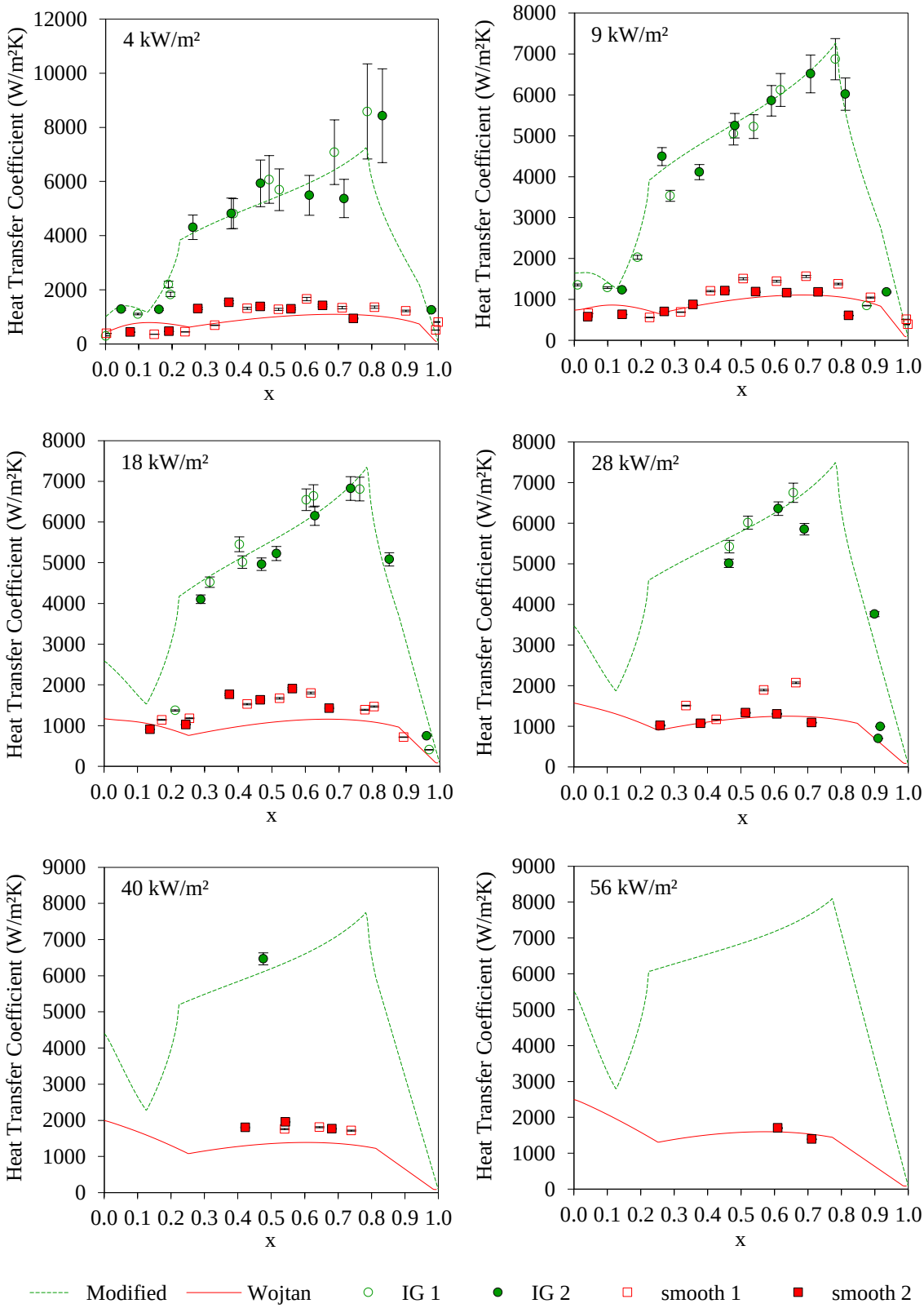

Figure 90: Heat transfer coefficient vs vapor quality for 2.8 mm ID smooth and 2.62 mm ID internally-grooved tubes at a mass flux of 100 kg/m²s and different heat fluxes

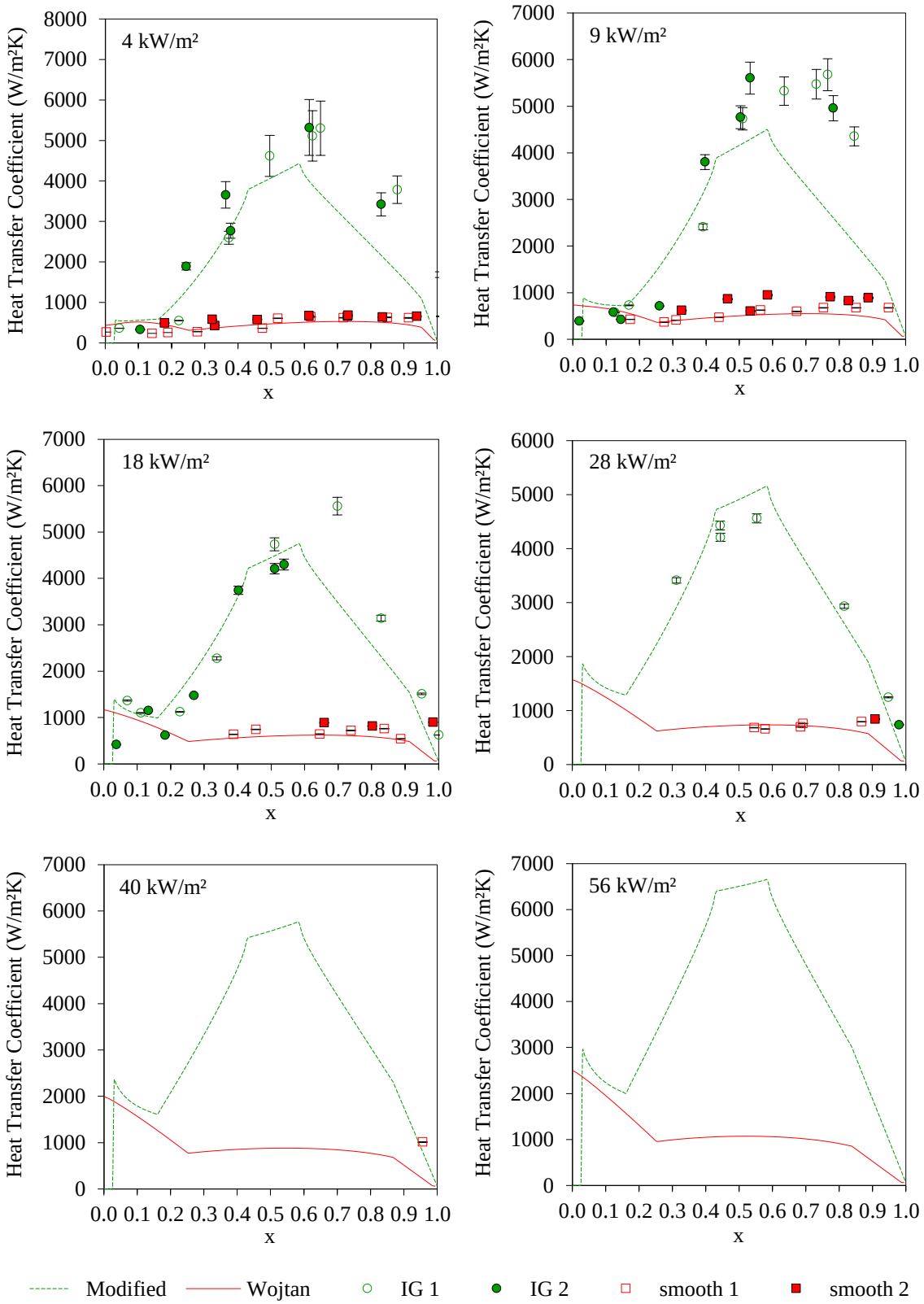

Figure 91: Heat transfer coefficient vs vapor quality for 2.8 mm ID smooth and 2.62 mm ID internally-grooved tubes at a mass flux of 75 kg/m²s and different heat fluxes

Appendix F Statistical Analysis of Heat Transfer Results

This Appendix provides more detail of the statistical analysis results of the 8.84mm, 4.54mm, and 2.62/2.8mm smooth and internally-grooved tubes. The more salient features are discussed in Chapter 8. The figures created only consider 'IG 1' and 'smooth 1' data points, which are fully representative of the trends observed for 'IG 2' and 'smooth 2'. This allowed figure clarity. The summary tables, however, considered all of the experimental data. Please refer to Appendix C - Appendix E for a full catalog of the diabatic experimental results. The statistical parameters of mean deviation, $\bar{\varepsilon}$, and mean of absolute value of deviations, $|\bar{\varepsilon}|$, were calculated based on the equations below:

$$\bar{\varepsilon} = \sum\left[\left(h_{predicted} - h_{experimental}\right)100/h_{experimental}\right] \tag{73}$$

$$|\bar{\varepsilon}| = \sum \mathrm{ABS}\left[\left(h_{predicted} - h_{experimental}\right)100/h_{experimental}\right] \tag{74}$$

where $h_{predicted}$ is the heat transfer coefficient predicted by the respective heat transfer coefficient correlation and $h_{experimental}$ is the measured heat transfer coefficient. These parameters are used to assess the accuracy of the models in context of mass flux and flow regime.

Measured smooth tube heat transfer coefficients were compared to the smooth tube two-phase correlations of Wojtan et al. [31], Chen [56], Shah [57], Kandlikar [93], Gungor and Winterton [59], and a simplified two-phase flow boiling correlation by Gungor and Winterton [60] (referred to hereafter as Gungor-Winterton 'new'). Measured internally-grooved tube heat transfer coefficients were compared to the current two-phase correlation described in Chapter 4, and the correlations of Thome, Kattan, and Favrat [91], Cavallini et al. [117], Chamra and Mago [162], Wu et al. [103], and Yun et al. [90]. Figure 92-Figure

94 show the smooth tube results and Figure 95 - Figure 97 show the internally-grooved tube results. The solid black line on the figures has a slope of 1 indicating perfect agreement between the model and experimental results. The dashed lines represent ±20%, for reference. The properties used while evaluating these correlations were the average values between the inlet and outlet of the test section (at the location of the wall temperature measurements). Table 22 - Table 25 provide a summary of the smooth tube modeling results for individual tube diameters and flowrates, and Table 26 - Table 29 provide the same information for the internally-grooved tubes. Please note, Figure 92, Figure 95, Table 25, and Table 29 are the same as those shown in Chapter 8.

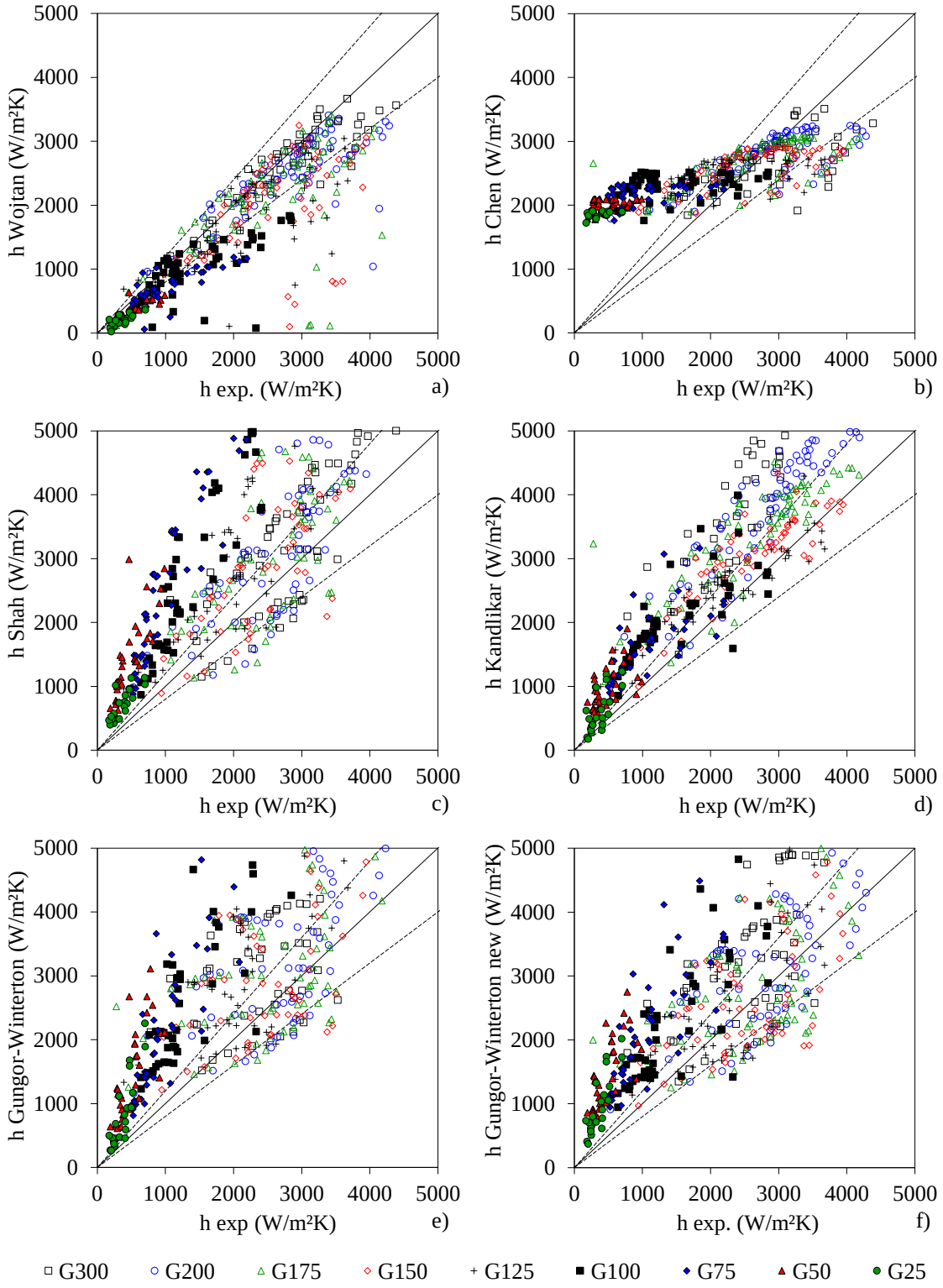

Figure 92: Comparison of the 8.84mm smooth tube experimental data for HFE-7100 at 61°C with a) Wojtan et al. [31], b) Chen [56], c) Shah [57], d) Kandlikar [93], e) Gungor-Winterton 'original' [59], and f) Gungor-Winterton 'new' [60]

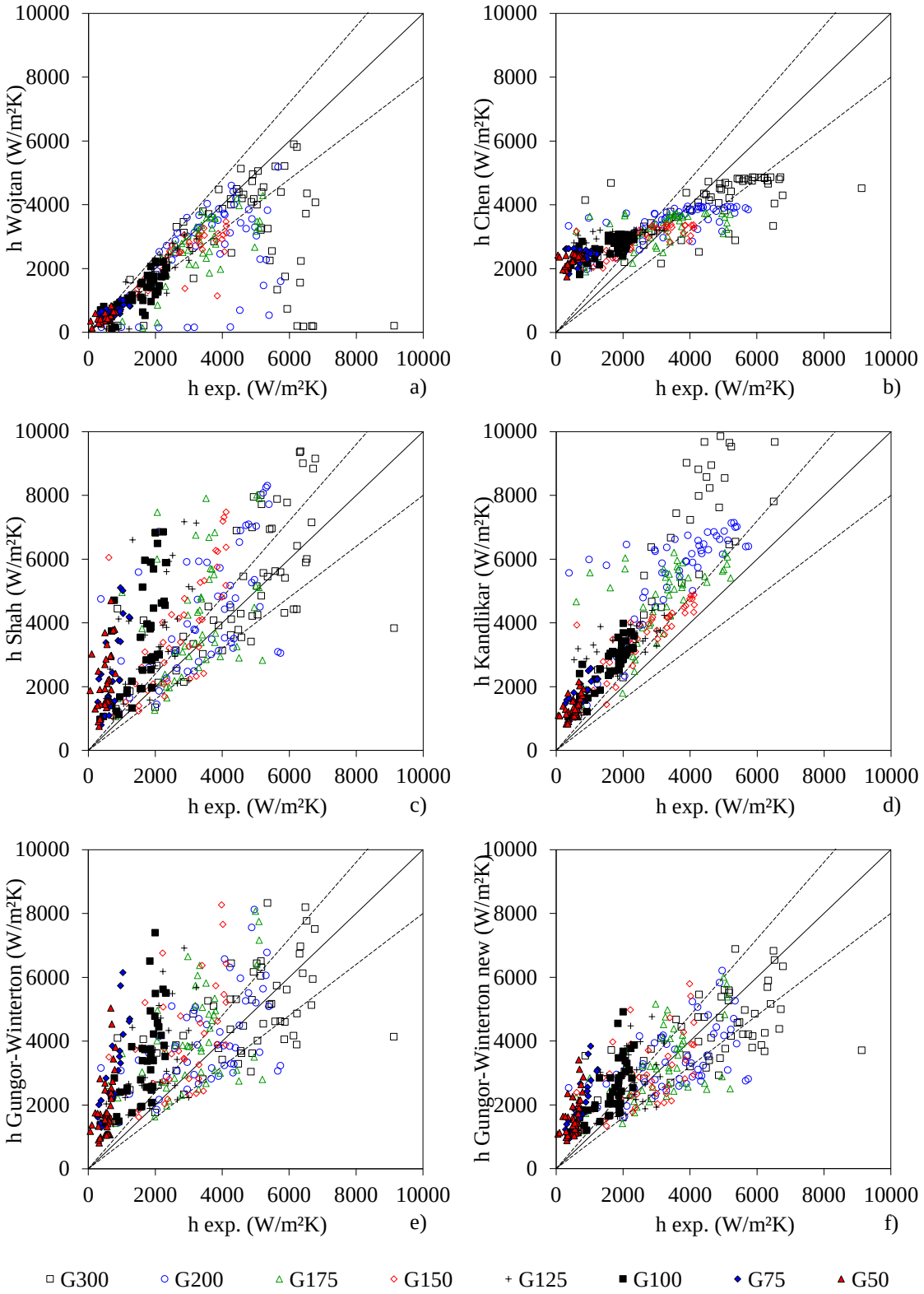

Figure 93: Comparison of the 4.54mm smooth tube experimental data for HFE-7100 at 61°C with a) Wojtan et al. [31], b) Chen [56], c) Shah [57], d) Kandlikar [93], e) Gungor-Winterton 'original' [59], and f) Gungor-Winterton 'new' [60]

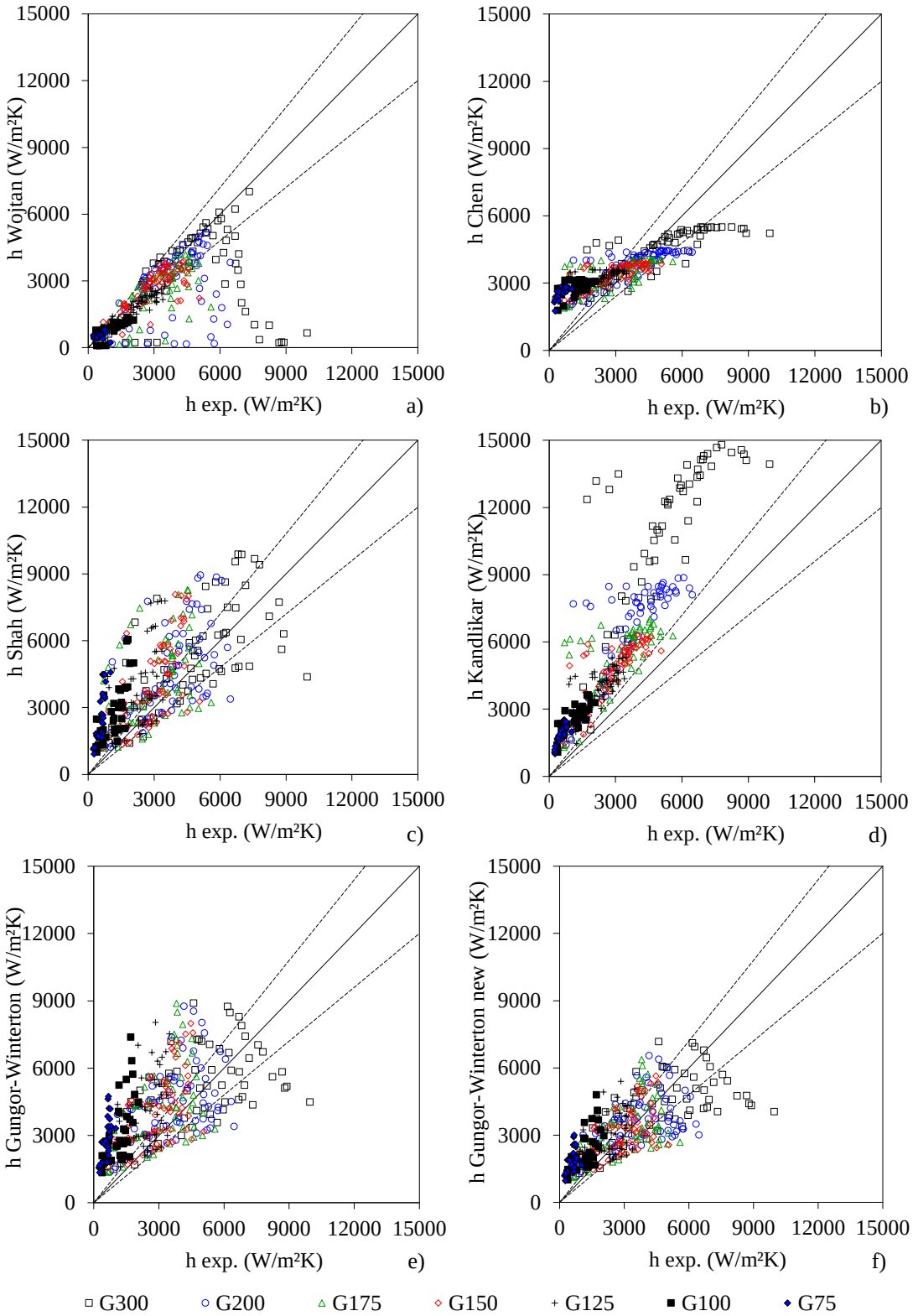

Figure 94: Comparison of the 2.8mm smooth tube experimental data for HFE-7100 at 61°C with a) Wojtan et al. [31], b) Chen [56], c) Shah [57], d) Kandlikar [93], e) Gungor-Winterton 'original' [59], and f) Gungor-Winterton 'new' [60]

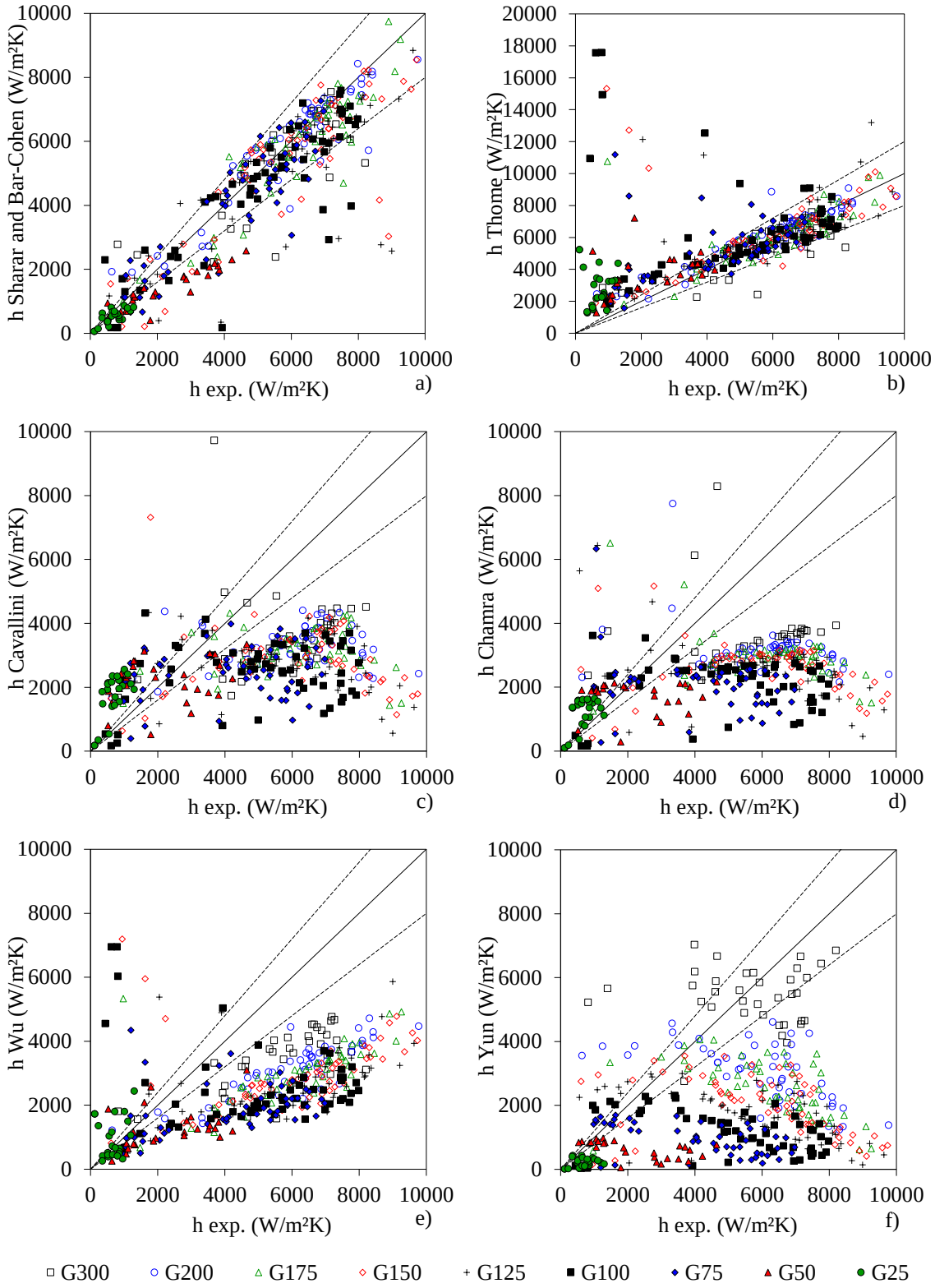

Figure 95: Comparison of the 8.84mm internally-grooved tube experimental data for HFE-7100 at 61°C with a) the Modified Sharar and Bar-Cohen correlation, and correlations from b) Thome et al. [91], c) Cavallini et al. [117], d) Chamra and Mago [162], e) Wu et al. [103], and f) Yun et al. [90]

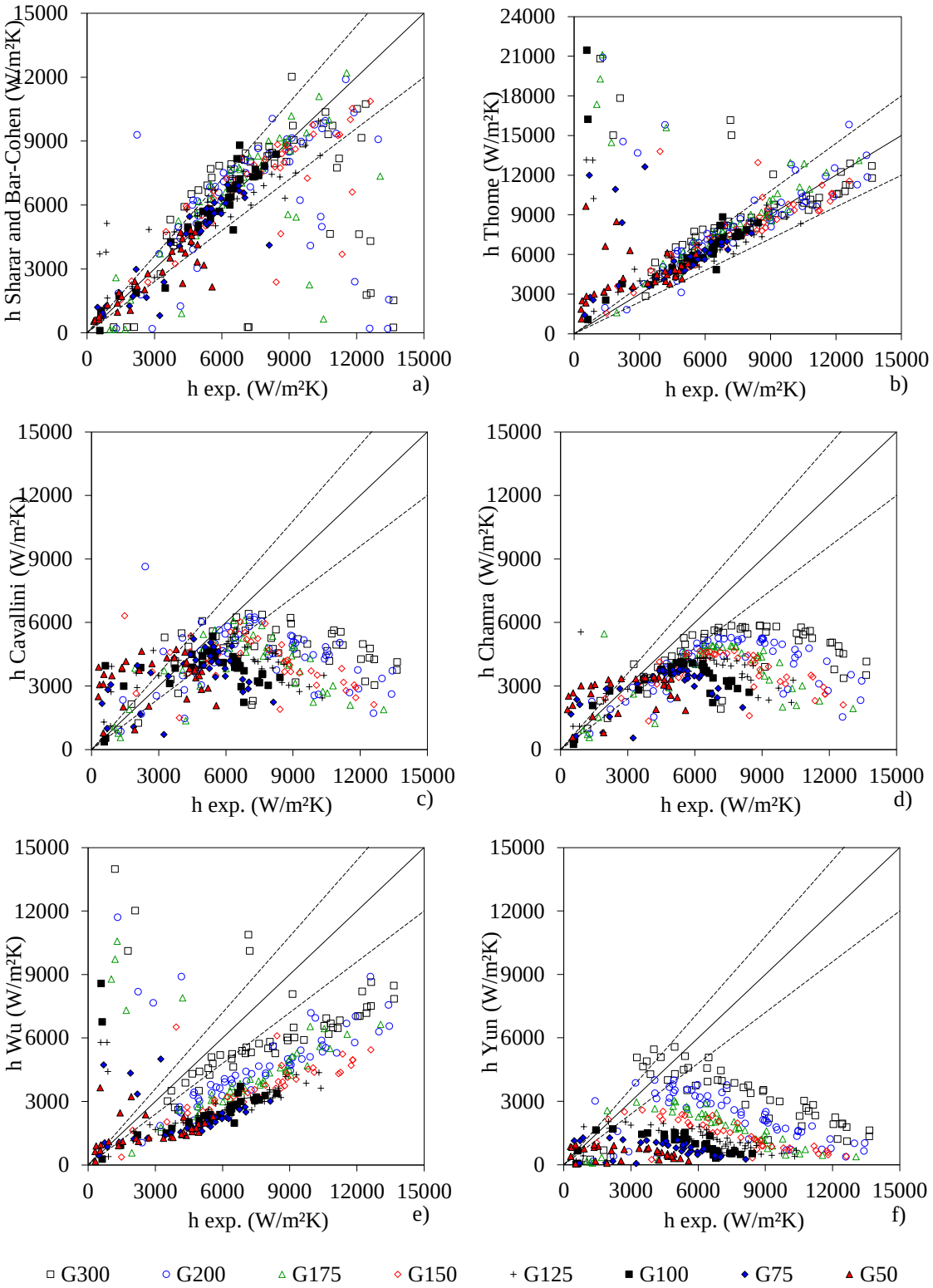

Figure 96: Comparison of the 4.54mm internally-grooved tube experimental data for HFE-7100 at 61°C with a) the Modified Sharar and Bar-Cohen correlation, and correlations from b) Thome et al. [91], c) Cavallini et al. [117], d) Chamra and Mago [162], e) Wu et al. [103], and f) Yun et al. [90]

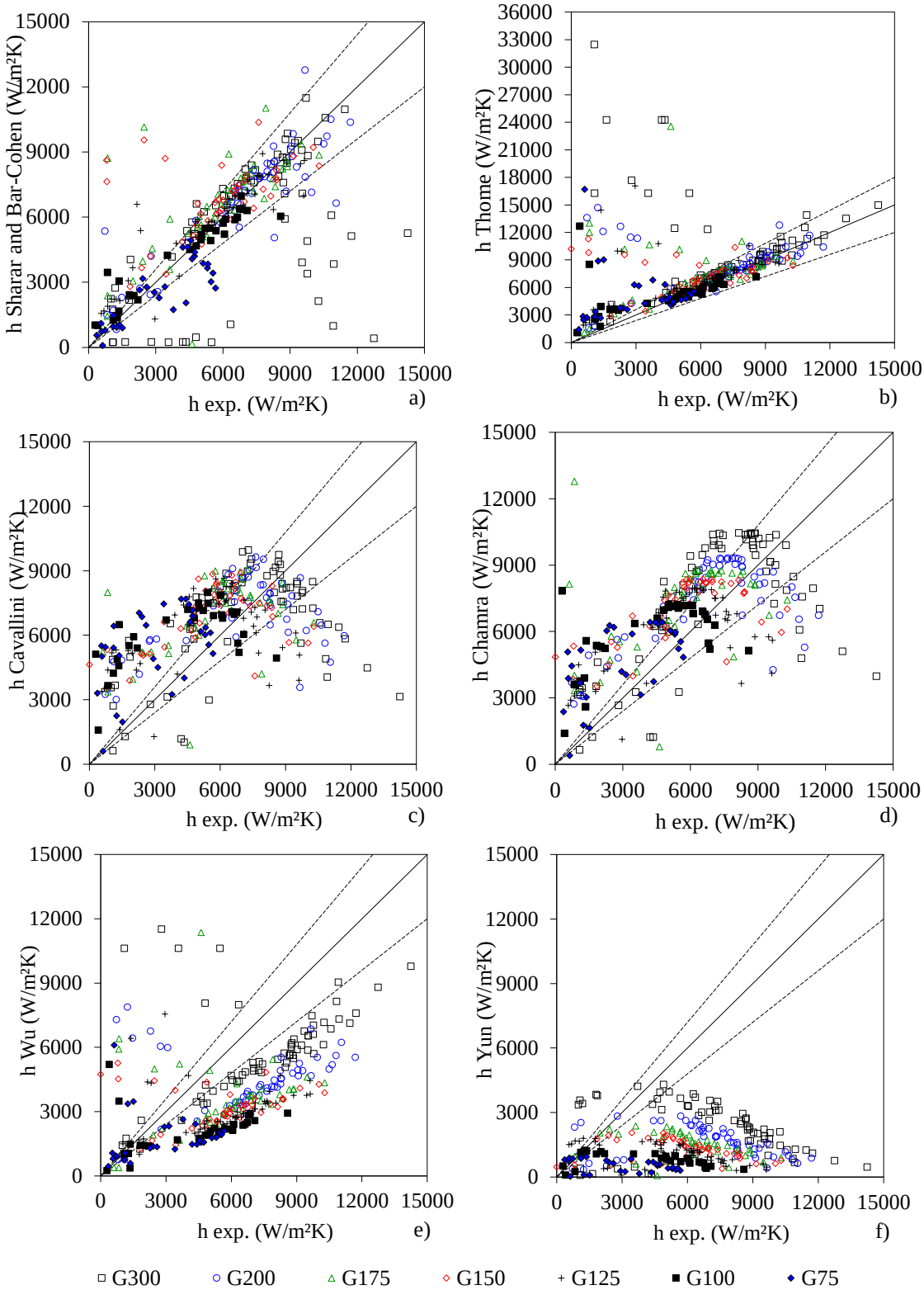

Figure 97: Comparison of the 2.62mm internally-grooved tube experimental data for HFE-7100 at 61°C with a) the Modified Sharar and Bar-Cohen correlation, and correlations from b) Thome et al. [91], c) Cavallini et al. [117], d) Chamra and Mago [162], e) Wu et al. [103], and f) Yun et al. [90]

Table 22: Predictive accuracy of two-phase smooth tube heat transfer coefficient correlations from Wojtan et al. [31], Chen [56], Shah [57], Kandlikar [93], and Gungor-Winterton [59] [60] compared to the 8.84mm experimental results

G kg/m²s	Wojtan %		Chen %		Shah %		Kandlikar %		Gungor-Winterton %		Gungor-Winterton new %	
	$\bar{\varepsilon}$	$\lvert\bar{\varepsilon}\rvert$	$\bar{\varepsilon}$	$\lvert\bar{\varepsilon}\rvert$	$\bar{\varepsilon}$	$\lvert\bar{\varepsilon}\rvert$	$\bar{\varepsilon}$	$\lvert\bar{\varepsilon}\rvert$	$\bar{\varepsilon}$	$\lvert\bar{\varepsilon}\rvert$	$\bar{\varepsilon}$	$\lvert\bar{\varepsilon}\rvert$
300	-4.6	11.1	3.5	17.0	8.5	28.6	55.0	58.8	26.9	44.6	16.2	36.2
200	-10.7	15.7	7.1	22.1	19.8	33.9	33.8	35.6	23.6	41.7	7.1	31.4
175	-11.0	25.8	20.9	35.0	36.1	54.1	37.5	42.9	30.4	52.1	10.9	41.2
150	-20.6	23.8	8.8	34.9	17.7	44.5	13.2	34.7	15.8	48.9	-2.8	38.5
125	-17.8	26.0	38.0	49.1	39.3	45.1	23.6	27.8	43.8	52.4	16.0	32.3
100	-36.3	43.6	51.2	166.5	74.0	101.7	36.0	68.4	76.9	116.8	37.1	73.8
75	-24.2	30.8	189.2	189.2	139.8	139.8	67.3	70.6	106.4	106.5	96.4	97.5
50	-16.5	34.1	486.9	489.1	223.8	223.8	134.6	135.6	187.5	187.7	217.9	217.9
25	-47.3	47.9	679.1	679.1	98.8	98.8	59.0	63.6	88.8	90.7	157.0	157.0
total	-18.8	26.8	115.0	138.6	62.9	77.0	47.1	56.1	58.7	76.1	47.8	69.1

Table 23: Predictive accuracy of two-phase smooth tube heat transfer coefficient correlations from Wojtan et al. [31], Chen [56], Shah [57], Kandlikar [93], and Gungor-Winterton [59] [60] compared to the 4.54mm experimental results

G kg/m²s	Wojtan %		Chen %		Shah %		Kandlikar %		Gungor-Winterton %		Gungor-Winterton new %	
	$\bar{\varepsilon}$	$\lvert\bar{\varepsilon}\rvert$	$\bar{\varepsilon}$	$\lvert\bar{\varepsilon}\rvert$	$\bar{\varepsilon}$	$\lvert\bar{\varepsilon}\rvert$	$\bar{\varepsilon}$	$\lvert\bar{\varepsilon}\rvert$	$\bar{\varepsilon}$	$\lvert\bar{\varepsilon}\rvert$	$\bar{\varepsilon}$	$\lvert\bar{\varepsilon}\rvert$
300	-18.6	28.8	3.7	24.6	10.6	29.6	102.4	102.5	6.9	30.7	-4.0	27.3
200	-18.8	26.8	22.6	37.9	35.7	51.6	79.8	80.3	27.6	46.1	6.8	35.0
175	-17.4	22.6	19.6	31.7	27.0	44.6	60.3	61.6	26.5	46.1	4.2	32.1
150	-18.0	20.4	31.2	41.2	39.7	54.6	45.1	48.3	43.3	58.1	12.3	37.4
125	-11.6	22.1	67.9	70.0	71.7	79.6	69.0	71.1	74.3	82.8	34.5	47.8
100	-11.6	24.3	106.3	106.3	101.5	103.5	81.5	81.7	106.3	107.4	56.5	60.9
75	-1.5	31.5	322.7	322.7	229.9	229.9	144.1	144.1	253.0	253.0	153.7	153.7
50	-0.8	33.2	487.6	487.6	330.3	330.3	179.0	179.0	241.2	241.2	215.5	215.5
25												
total	-13.4	25.9	107.5	116.2	89.1	99.9	90.6	91.5	82.7	94.9	48.1	66.3

Table 24: Predictive accuracy of two-phase smooth tube heat transfer coefficient correlations from Wojtan et al. [31], Chen [56], Shah [57], Kandlikar [93], and Gungor-Winterton [59] [60] compared to the 2.8mm experimental results

G kg/m²s	Wojtan %		Chen %		Shah %		Kandlikar %		Gungor-Winterton %		Gungor-Winterton new %	
	$\bar{\varepsilon}$	$\lvert\bar{\varepsilon}\rvert$	$\bar{\varepsilon}$	$\lvert\bar{\varepsilon}\rvert$	$\bar{\varepsilon}$	$\lvert\bar{\varepsilon}\rvert$	$\bar{\varepsilon}$	$\lvert\bar{\varepsilon}\rvert$	$\bar{\varepsilon}$	$\lvert\bar{\varepsilon}\rvert$	$\bar{\varepsilon}$	$\lvert\bar{\varepsilon}\rvert$
300	-16.0	35.1	6.2	33.6	9.9	36.9	131.2	131.2	12.1	45.7	-2.3	39.8
200	-9.4	32.6	16.3	31.6	23.8	42.8	92.0	93.3	26.3	48.7	3.3	35.8
175	-12.8	28.5	33.5	45.5	41.4	58.8	85.1	86.2	45.1	64.1	13.8	43.5
150	-0.2	23.8	45.7	51.6	45.2	60.9	85.5	85.8	49.1	64.9	17.3	41.8
125	-11.1	25.0	60.9	63.0	58.3	69.8	76.8	78.2	67.4	80.1	27.6	46.5
100	-8.2	30.6	194.0	194.0	144.1	144.3	143.0	143.0	173.3	173.3	102.0	102.0
75	-4.8	22.6	339.6	339.6	232.4	232.7	181.1	181.1	253.3	253.3	152.8	152.8
50												
25												
total	-9.3	28.8	85.9	85.9	63.5	78.4	107.6	108.2	71.8	88.8	33.3	57.4

Table 25: Summary of the predictive accuracy of two-phase smooth tube heat transfer coefficient correlations from Wojtan et al. [31], Chen [56], Shah [57], Kandlikar [93], and Gungor-Winterton [59] [60] to the 2.8mm to 8.84mm experimental results

G kg/m²s	Wojtan %		Chen %		Shah %		Kandlikar %		Gungor-Winterton %		Gungor-Winterton new %	
	$\bar{\varepsilon}$	$\lvert\bar{\varepsilon}\rvert$	$\bar{\varepsilon}$	$\lvert\bar{\varepsilon}\rvert$	$\bar{\varepsilon}$	$\lvert\bar{\varepsilon}\rvert$	$\bar{\varepsilon}$	$\lvert\bar{\varepsilon}\rvert$	$\bar{\varepsilon}$	$\lvert\bar{\varepsilon}\rvert$	$\bar{\varepsilon}$	$\lvert\bar{\varepsilon}\rvert$
300	-13.1	25.0	4.5	25.2	9.67	31.6	96.2	97.5	15.3	40.3	3.3	34.4
200	-12.9	25.0	15.2	30.3	26.4	42.7	68.5	69.7	25.8	45.5	5.7	34.0
175	-13.7	25.6	24.6	37.4	34.8	52.5	60.9	63.5	34.1	54.1	9.6	38.9
150	-12.9	22.6	28.6	42.7	34.2	53.3	47.9	56.2	36.1	57.3	8.9	39.2
125	-13.5	24.4	54.4	59.8	56.4	64.8	56.5	59.1	61.8	71.7	26.1	42.2
100	-18.7	32.8	110.3	153.0	106.5	116.5	86.8	97.6	118.8	132.5	65.2	78.8
75	-10.2	28.3	274.1	274.1	200.7	200.8	130.8	131.9	204.2	204.3	134.3	134.6
50	-8.6	33.6	487.2	488.4	277.1	277.1	156.8	157.3	214.4	214.4	216.7	216.7
25	-47.3	47.9	679.1	679.1	98.8	98.8	59.0	63.6	88.7	90.7	157.0	157.0
total	-14.0	26.9	100.7	115.6	72.8	85.9	80.6	84.4	72.1	87.5	44.3	65.3

Table 26: Predictive accuracy of the Modified Sharar and Bar-Cohen internally-grooved tube correlation, and correlations from Thome et al. [91], Cavallini et al. [117], Chamra and Mago [162], Wu et al. [103], and Yun et al. [90] compared to the 8.84mm experimental results

G kg/m²s	Modified %		Thome %		Cavallini %		Chamra %		Wu %		Yun %	
	$\bar{\varepsilon}$	$\lvert\bar{\varepsilon}\rvert$	$\bar{\varepsilon}$	$\lvert\bar{\varepsilon}\rvert$	$\bar{\varepsilon}$	$\lvert\bar{\varepsilon}\rvert$	$\bar{\varepsilon}$	$\lvert\bar{\varepsilon}\rvert$	$\bar{\varepsilon}$	$\lvert\bar{\varepsilon}\rvert$	$\bar{\varepsilon}$	$\lvert\bar{\varepsilon}\rvert$
300	0.1	16.7	1.0	17.0	-35.8	48.4	111.9	192.5	-34.9	38.0	4.6	34.1
200	0.5	15.5	6.8	15.5	-43.0	50.1	-32.2	63.4	-46.3	47.8	-40.3	56.4
175	-5.2	17.8	12.5	21.8	-47.9	51.3	-43.9	59.1	-46.4	54.3	-55.5	58.9
150	-4.9	23.7	30.2	37.1	-42.3	57.6	70.8	177.0	-40.6	57.2	-55.7	68.0
125	-7.2	22.4	85.8	96.0	-44.9	55.8	-28.7	80.0	-21.2	83.7	-61.3	72.5
100	-17.6	35.0	137.6	147.0	-46.5	57.7	-38.3	77.5	-5.1	87.7	-71.0	76.2
75	-14.4	34.2	67.2	73.8	-34.8	56.2	-38.7	67.1	-37.8	60.8	-68.6	77.3
50	-38.4	47.4	224.3	225.1	11.7	70.9	-10.0	68.0	9.4	83.2	-66.5	72.7
25	-21.3	49.0	530.3	530.3	210.7	224.0	129.7	153.0	112.4	133.7	-48.3	73.0
total	-10.8	27.5	93.7	101.9	-23.2	65.2	5.8	102.1	-20.7	68.3	-52.2	65.5

Table 27: Predictive accuracy of the Modified Sharar and Bar-Cohen internally-grooved tube correlation, and correlations from Thome et al. [91], Cavallini et al. [117], Chamra and Mago [162], Wu et al. [103], and Yun et al. [90] compared to the 4.54mm experimental results

G kg/m²s	Modified %		Thome %		Cavallini %		Chamra %		Wu %		Yun %	
	$\bar{\varepsilon}$	$\lvert\bar{\varepsilon}\rvert$	$\bar{\varepsilon}$	$\lvert\bar{\varepsilon}\rvert$	$\bar{\varepsilon}$	$\lvert\bar{\varepsilon}\rvert$	$\bar{\varepsilon}$	$\lvert\bar{\varepsilon}\rvert$	$\bar{\varepsilon}$	$\lvert\bar{\varepsilon}\rvert$	$\bar{\varepsilon}$	$\lvert\bar{\varepsilon}\rvert$
300	-7.0	36.5	77.6	82.1	-38.9	42.3	-38.3	39.3	16.7	67.1	-54.9	58.8
200	-1.9	27.5	72.3	77.6	-34.5	44.4	-25.7	56.6	-4.8	73.9	-64.1	66.5
175	-6.1	23.2	104.6	108.0	-36.7	42.2	-40.2	45.5	1.3	86.7	-71.3	74.2
150	-3.5	18.3	39.8	44.0	-29.7	46.4	-22.0	63.8	-36.5	60.9	-70.5	75.9
125	15.3	33.6	129.7	134.2	-16.9	49.8	-26.2	51.0	-2.8	91.6	-70.5	78.1
100	6.2	24.1	256.0	260.0	-6.3	56.4	20.1	94.4	43.9	139.9	-71.9	80.5
75	8.3	27.3	139.3	142.4	24.1	70.9	41.4	104.0	-9.7	85.8	-66.0	84.4
50	12.5	34.9	277.2	279.6	141.5	167.5	161.6	197.0	35.9	107.9	-43.8	87.3
25												
Total	2.0	28.1	125.9	130.0	-7.6	59.8	-0.2	74.5	3.7	86.7	-64.6	74.4

Table 28: Predictive accuracy of the Modified Sharar and Bar-Cohen internally-grooved tube correlation, and correlations from Thome et al. [91], Cavallini et al. [117], Chamra and Mago [162], Wu et al. [103], and Yun et al. [90] compared to the 2.62mm experimental results

G	Modified %		Thome %		Cavallini %		Chamra %		Wu %		Yun %	
kg/m²s	$\bar{\varepsilon}$	$\lvert\bar{\varepsilon}\rvert$	$\bar{\varepsilon}$	$\lvert\bar{\varepsilon}\rvert$	$\bar{\varepsilon}$	$\lvert\bar{\varepsilon}\rvert$	$\bar{\varepsilon}$	$\lvert\bar{\varepsilon}\rvert$	$\bar{\varepsilon}$	$\lvert\bar{\varepsilon}\rvert$	$\bar{\varepsilon}$	$\lvert\bar{\varepsilon}\rvert$
300	-8.4	32.9	80.0	85.6	4.3	41.4	16.6	42.1	15.1	70.6	-57.0	73.1
200	4.7	32.3	123.1	131.2	19.5	49.5	25.2	47.9	17.6	97.9	-63.6	81.9
175	44.8	52.9	129.0	132.3	53.2	69.3	67.2	79.7	10.6	87.7	-64.5	77.2
150	73.5	80.8	228.7	233.9	61.0	74.7	62.1	73.1	50.2	133.9	-65.8	79.4
125	24.3	31.1	65.1	66.1	59.6	77.1	51.5	68.1	-29.2	56.0	-62.5	83.2
100	22.3	34.0	195.5	201.4	109.3	118.1	110.9	119.7	18.1	108.0	-69.3	72.4
75	-2.4	33.7	184.5	188.9	257.8	261.7	192.8	198.4	-0.9	74.9	-47.1	80.1
50												
25												
total	21.4	42.0	132.0	136.8	63.1	83.9	62.0	78.4	11.1	87.6	-61.6	78.1

Table 29: Summary of the predictive accuracy of the Modified Sharar and Bar-Cohen internally-grooved tube correlation, and correlations from Thome et al. [91], Cavallini et al. [117], Chamra and Mago [162], Wu et al. [103], and Yun et al. [90] for the 2.62mm to 8.84mm experimental results

G	Modified %		Thome %		Cavallini %		Chamra %		Wu %		Yun %	
kg/m²s	$\bar{\varepsilon}$	$\lvert\bar{\varepsilon}\rvert$	$\bar{\varepsilon}$	$\lvert\bar{\varepsilon}\rvert$	$\bar{\varepsilon}$	$\lvert\bar{\varepsilon}\rvert$	$\bar{\varepsilon}$	$\lvert\bar{\varepsilon}\rvert$	$\bar{\varepsilon}$	$\lvert\bar{\varepsilon}\rvert$	$\bar{\varepsilon}$	$\lvert\bar{\varepsilon}\rvert$
300	-5.1	28.7	52.8	61.5	-23.4	44.0	30.0	91.3	-1.0	58.5	-35.7	55.3
200	1.1	25.1	67.3	74.7	-19.3	47.9	-10.9	55.9	-11.1	73.2	-55.9	68.3
175	11.2	31.3	82.0	87.3	-10.4	54.3	-5.6	61.4	-11.5	76.2	-63.7	70.1
150	21.7	40.9	99.5	105.0	-3.7	59.5	36.9	104.6	-8.9	84.0	-63.9	74.4
125	10.8	29.1	93.6	98.7	-0.7	60.9	-1.1	66.3	-17.7	77.1	-64.7	77.9
100	3.6	31.0	196.3	202.8	18.8	77.4	30.8	97.2	18.9	111.8	-70.7	76.4
75	-2.8	31.7	130.3	135.0	82.3	129.6	65.1	123.1	-16.1	73.8	-60.6	80.6
50	-12.9	41.1	250.7	252.3	76.6	119.2	75.8	132.5	22.6	95.5	-55.1	79.9
25	-21.3	48.9	530.3	530.3	210.7	223.9	129.7	152.9	112.4	133.7	-48.3	73.0
total	4.0	32.0	118.7	124.6	12.6	72.3	25.4	88.9	-2.4	80.7	-58.2	71.85

Chapter 10: Works Cited

[1] C. Mi, M. A. Masrur and D. Gao, Hybrid Electric Vehicles: Principles and applications with practical perspectives, West Sussex: John Wiley and Sons Ltd., 2011.

[2] B. Robinson, "defensesystems.com," 26 February 2010. [Online]. Available: http://www.defensesystems.com/Articles/2010/03/11/Defense-IT-3-Greens.aspx. [Accessed 2 August 2012].

[3] "U.S. Department of Energy: Energy Efficiency and Renewable Energy," 7 December 2010. [Online]. Available: http://www1.eere.energy.gov/vehiclesandfuels/resources/fcvt_plans_roadmaps.html. [Accessed 3 August 2012].

[4] S. Garimella and V. Singhal, "Single-phase flow and heat transport in microchannel heat sinks," *1st International Conference on Microchannels and Minichannels*, April 2003.

[5] C. Coutteau, "Advanced planning briefing to industry (APBI), TARDEC ground vehicle power and mobility (GVPM)," US Army RDECOM-TARDEC, Warren, Michigan, October 2008.

[6] I. Mudawar, "Assessment of high-heat-flux thermal management schemes," *IEEE Transactions on Components and Packaging Technologies*, vol. 24, no. 2, pp. 122-141, June 2001.

[7] D. Saums, "Vaporizable dielectric fluid cooling of IGBT power semiconductors for vehicle powertrains," *6th International Conference on Integrated Power Electronics Systems*, pp. pp. 437-444, 2010.

[8] D. Sharar, N. Jankowski, B. Morgan and A. Bar-Cohen, "Two-phase minichannel cold plate for Army vehicle power electronics," *ASME InterPACK*, vol. 2, pp. 133-142, 2011.

[9] A. Bergles, "Heat transfer enhancement - the encouragement and accommodation of high heat fluxes," *Journal of Heat Transfer*, vol. 119, pp. 8-19, 1997.

[10] A. Bergles, "Techniques to enhance heat transfer," in *Handbook of Heat Transfer*, New York, NY, McGraw-Hill, 1998.

[11] J. Thome, Enhanced Boiling Heat Transfer, CRC Press, 1990.

[12] R. Webb, Principles of Enhanced Heat Transfer, New York, NY: John Wiley and Sons, Inc., 1994.

[13] S. Kandlikar and P. Spiesman, "Augmentation of saturated flow boiling heat transfer," in *Chapter 18, Handbook of Phase Change*, Philadelphia, PA, Taylor and Francis, 1999.

[14] G. Moreno, S. Naramanchi, S. Thiagarajan, K. Bennion and T. Venson, "Enhanced surfaces to improve power electronics cooling," in *MEPTEC*, San Jose, 2011.

[15] S. Yilmaz, J. Hwalck and J. Westwater, "Pool boiling heat transfer performance for commercial enhanced tube surfaces," ASME Paper 90-HT-41, 1980.

[16] H. Kim, J. Kim and M. Kim, "Effect of nanoparticles on CHF enhancement in pool boiling of nano-fluids," *International Journal of Heat and Mass Transfer,* vol. 49, pp. 5070-5074, 2006.

[17] J. Thome, "Chapter 11: Boiling heat transfer inside enhanced tubes," in *Wolverine Engineering Data Book III*, 2004.

[18] M. Jensen and H. Bensler, "Saturated forced-convection boiling heat transfer with twisted-tape inserts," *Journal of Heat Transfer,* vol. 108, pp. 93-99, 1986.

[19] S. Laohalertdecha and S. Wongwises, "An experimental study into the evaporation heat transfer and flow characteristics of R-134a refrigerant flowing through corrugated tubes," *International Journal of Refrigeration,* vol. 34, pp. 280-291.

[20] D. Sharar, J. Nicholas, B. Morgan and A. Bar-Cohen, "Enhanced Two-Phase Cooling," in *IMAPS 2012 Chesapeake Chapter*, College Park, MD, 2012.

[21] M. Houfuku, "Development trends in inner-grooved tubes in Japan," *Hitachi Cable Review,* vol. 26, pp. 1-3, 2007.

[22] "Inner-grooved tubes," Wieland, [Online]. Available: http://www.wieland-thermalsolutions.com/internet/en/branchenprodukte/kltetechnik/kaltwasserstze/innenberippterohre/Innenberippte_Rohre.jsp. [Accessed 18 January 2013].

[23] C. Dang, N. Haraguchi and E. Hihara, "Flow boiling heat transfer of carbon dioxide inside a small-sized microfin tube," *International Journal of Refrigeration,* vol. 33, pp. 655-663, 2012.

[24] L. Gao, Y. Watanabe and T. Honda, "CO2 flow boiling in small diameter smooth and microfin tubes," *Journal of JSEM,* vol. 11, pp. 66-72, 2011.

[25] F. P. Incropera, D. P. Dewitt, T. L. Bergman and A. S. Lavine, Fundamentals of Heat and mass Transfer, 6th ed., Hoboken: John Wiley & Sons,, 2007.

[26] M. Kim and J. Shin, "Evaporating heat transfer of R22 and R410A in horizontal smooth and microfin tubes," *International Journal of Refrigeration,* vol. 28, pp. 940-948, 2005.

[27] T. Shedd and T. Newell, "Visualization of two-phase flow through microgrooved tubes for understanding enhanced heat transfer," *International Journal of Heat and Mass Transfer,* vol. 46, pp. 4169-4177, 2003.

[28] T. Ravigururajan and A. Bergles, "General correlations for pressure drop and heat transfer for single-phase turbulent flow in internally ribber tubes," *Augmentation of Heat Transfer in Energy Systems,* vol. 52, pp. 9-20, 1985.

[29] D. Sharar, N. Jankowski and A. Bar-Cohen, "Modified model for improved flow regime prediction in internally-grooved tubes," in *InterPACK*, Burlingame, CA, 2013.

[30] L. Wojtan, T. Ursenbacher and J. Thome, "Investigation of flow boiling in horizontal tubes: Part I - A new diabatic two-phase flow pattern map," *International Journal of Heat and Mass Transfer,* vol. 48, pp. 2955-2969, 2005.

[31] L. Wojtan, T. Ursenbacher and J. Thome, "Investigation of flow boiling in horizontal tubes: Part II - Development of a new hea ttransfer model for stratified-wavy, dryout, and mist flow regimes," *International Journal of Heat and Mass Transfer,* vol. 48, pp. 2970-2985, 2005.

[32] L. Cheng, G. Ribatski and J. Thome, "Two-phase flow patterns and flow-pattern maps: Fundamentals and applications," *Applied Mechanics Reviews,* vol. 61, no. 5, p. 28, 2008.

[33] J. Thome, A. Bar-Cohen, R. Revellin and I. Zun, "Unified mechanistic multiscale mapping of two-phase flow patterns in microchannels," *Experimental Thermal and Fluid Science,* vol. 44, pp. 1-22, 2013.

[34] V. Carey, Liquid vapor phase change phenomena, Washington D.C.: Hemisphere, 1992.

[35] A. Bar-Cohen and E. Rahim, "Modeling and prediction of two-phase microgap channel heat transfer characteristics," *Heat Transfer Engineering,* vol. 30, no. 8, pp. 601-625, 2009.

[36] M. Cortina-Diaz and J. Schmidt, "Flow boiling heat transfer of n-Hexane and n-Octane in a minichannel," in *13th International Heat Transfer Conference,* Sydney, Australia, 2006.

[37] Y. Yang and Y. Fujita, "Flow boiling heat transfer and flow pattern in rectangular channel of mini-gap," in *Proc. 2nd International Conference on Microchannels and Minichannels,* New York, USA, 2004.

[38] E. Bandarra Filho and J. Saiz Jabardo, "Convectiev boiling performance of refrigerant R-134a in herringbone and microfin copper tubes," *International Journal of Refrigeration,* vol. 29, pp. 81-91, 2006.

[39] J. Thome and G. Ribatski, "State-of-the-art of two-phase flow and flow boiling heat transfer and pressure drop of CO2 in macro- and micro-channels," *International Journal of Refrigeration,* vol. 28, pp. 1149-1168, 2005.

[40] L. Cheng, G. Ribatski, J. Quiben and J. Thome, "New prediction methods for CO2 evaporation inside tubes: Part I - A two-phase flow pattern map and a flow pattern based phenomenological model for two-phase flow frictional pressure drops," *International Journal of Heat and Mass Transfer,* vol. 51, pp. 111-124, 2008.

[41] L. Cheng, G. Ribatski, L. Wojtan and J. Thome, "New flow boiling heat transfer model and flow pattern map for carbond dioxide evaporating inside horizontal tubes," *International Journal of Heat and Mass Transfer,* vol. 49, pp. 4082-4094, 2006.

[42] O. Baker, "Simultaneous Flow of Oil and Gas," *Oil and Gas Journal,* vol. 53, no. 12, pp. 185-195, 1954.

[43] J. Mandhane, G. Gregory and K. Aziz, "A flow pattern map for gas liquid flow in horizontal pipes," *International Journal of Multiphase Flow,* vol. 1, no. 4, pp. 537-553, 1974.

[44] Y. Taitel and A. Dukler, "A model for predicting flow regime transitions in horizontal and near horizontal gas-liquid flow," *AiChE Journal,* vol. 22, no. 1, pp. 47-55, 1976.

[45] J. Weisman, D. Duncan, J. Gibson and T. Crawford, "Effect of fluid properties and pipe diameter on two-phase flow pattern in horizontal lines," *Internation Journal of Multiphase Flow,* vol. 5, no. 6, pp. 437-462, 1979.

[46] Y. Taitel, "Flow pattern transition in two phase flow," *Proc. in 9th International Heat Transfer Conference,* pp. 237-254, 1990.

[47] N. Kattan, J. Thome and D. Favrat, "Flow boiling in horizontal tubes. Part I: Development of a diabatic two-phase flow pattern map," *Journal of Heat Transfer,* vol. 120, no. 1, pp. 140-147, 1998.

[48] O. Zurcher, J. Thome and D. Favrat, "Evaporation of ammonia in a smooth horizontal tube: Heat transfer measurements and predictions," *Journal of Heat Transfer,* vol. 121, pp. 89-101, 1999.

[49] O. Zurcher, D. Favrat and J. Thome, "Development of a diabatic two-phase flow pattern map for horizontal flow boiling," *International Journal of Heat and Mass Transfer,* vol. 45, pp. 291-301, 2002.

[50] J. Thome and J. El Hajal, "Two-phase flow pattern map for evaporation in horizontal tubes: Latest version," *Heat Transfer Engineering,* vol. 24, no. 6, pp. 3-10, 2003.

[51] F. Mancini, S. Minetto and E. Fornasieri, "Thermodynamic analysis and experimental investigation of CO2 household heat pump dryer," *International Journal of Refrigeration,* vol. 34, pp. 851-858, 2011.

[52] H. Abou-Ziyan, M. Ahmed, M. Metwally and H. Abd El-Hameed, "Solar assisted R22 and R134a heat pump systems for low-temperature applications," *Applied Thermal Engineering,* vol. 17, pp. 455-469, 1997.

[53] A. Diani, S. Mancin and L. Rossetto, "R1234ze(E) flow boiling inside a 3.4 mm ID microfin tube," *International Journal of Refrigeration,* 2014.

[54] R. Mastrullo, A. Mauro, J. Thome, D. Toto and G. Vanoli, "Flow pattern maps for convective boiling of CO2 and R410A in a horizontal smooth tube: Experiments and new correlations analyzing the effect of reduced pressure," *International Journal of Heat and Mass Transfer,* vol. 55, no. 5-6, pp. 1519-1528, 2012.

[55] E. Rahim, R. Revellin, J. Thome and A. Bar-Cohen, "Characterization and prediction of two-phase flow regimes in miniature tubes," *International Journal of Multiphase Flow,* vol. 37, pp. 12-23, 2011.

[56] J. Chen, "Correlation for boiling heat transfer to saturated fluids in convective flow," *Industrial and Engineering Chemistry - Process Design and Development,* vol. 5, pp. 322-329, 1966.

[57] M. Shah, "A new correlation for heat transfer during boiling flow through pipes," *ASHRAE Transactions,* vol. 82, pp. 66-86, 1976.

[58] S. Kandlikar and P. Balasubramanian, "An extension of the flow boiling correlation to transition, laminar, and deep laminar flows in minichannels and microchannels," *Heat Transfer Engineering,* vol. 25, pp. 86-93, 2004.

[59] K. Gungor and R. Winterton, "A general correlation for flow boiling in tubes and annuli," *International Journal of Heat and Mass Transfer,* vol. 29, pp. 351-358, 1986.

[60] K. Gungor and R. Winterton, "Simplified general correlation for saturated flow boiling and comparisons of correlations with data," *Chemical Engineering Research and Design,* vol. 65, pp. 148-156, 1987.

[61] N. Kattan, J. Thome and D. Favrat, "Flow boiling in horizontal tubes - Part II: New heat transfer for five refrigerants," *ASME Journal of Heat Transfer,* vol. 120, pp. 148-155, 1998.

[62] N. Kattan, J. Thome and D. Favrat, "Flow boiling in horizontal tubes - Part III: Development of a new heat transfer model based on flow patterns," *ASME Journal of Heat Transfer,* vol. 120, pp. 156-165, 1998.

[63] A. Bergles and R. Manglik, "Current progress and new developments in enhanced heat and mass transfer," *Journal of Enhanced Heat Transfer,* vol. 20, no. 1, pp. 1-15, 2013.

[64] D. Sharar and A. Bar-Cohen, "Two-phase flow regimes and evaporative heat transfer in internally-grooved tubes," *Journal of Enhanced Heat Transfer* , vol. 21, no. 2-3, pp. 195-230, 2014.

[65] L. Liebenberg and J. Meyer, "Objective classification of two-phase flow regimes," *Heat Transfer Engineering,* vol. 29, no. 1, pp. 1-2, 2008.

[66] M. Yu, T. Lin and C. Tseng, "Heat transfer and flow pattern during two-phase flow boiling of R-134a in horizontal smooth and microfin tubes," *International Journal of Refrigeration,* vol. 25, pp. 789-798, 2002.

[67] S. Oh and A. Bergles, "Visualization of the effects of spiral angle on the enhancement of in-tube flow boiling in microfin tubes," *ASHRAE Trans.,* vol. 108, no. 2, pp. 509-515, 2002.

[68] T. Shedd, T. Newell and P. K. Lee, "The effects of the number and angle of microgrooves on the liquid film in horizontal annular two-phase flow," *International Journal of Heat and Mass Transfer,* vol. 46, pp. 4179-4189, 2003.

[69] B. Shen and E. Groll, "A critical review of the influence of lubricants on the heat transfer and pressure drop of refrigerants, Part I: Lubricant influence on pool and flow boiling," *Internation Journal of HVAC&R Research,* vol. 11, no. 3, pp. 341-359, 2005.

[70] A.-E. Schael and M. Kind, "Flow pattern and heat transfer characteristics during flow boiling of CO2 in a horizontal micro fin tube and comparison with smooth tube data," *International Journal of Refrigeration,* vol. 28, pp. 1186-1195, 2005.

[71] J. Cho and M. Kim, "Experimental studies on the evaporative heat transfer and pressure drop of CO2 in smooth and micro-fin tubes of the diameters of 5 and 9.52 mm," *International Journal of Refrigeration,* vol. 30, pp. 986-994, 2007.

[72] W. Targanski and J. Cieslinski, "Evaporation of R407C/oil mixtures inside corrugated and micro-fin tubes," *Applied Thermal Engineering,* vol. 27, pp. 2226-2232, 2007.

[73] H. Hu, G. Ding and K. Wang, "Heat transfer characteristics of R41oA-oil mixture flow boiling inside a 7mm straight microfin tube," *International Journal of Refrigeration,* vol. 31, no. 6, pp. 1081-1093, 2008.

[74] K. Spindler and H. Muller-Steinhagen, "Flow boiling heat transfer of R134a and R404A in a microfin tube at low mass fluxes and low heat fluxes," *Heat Mass Transfer,* vol. 45, pp. 967-977, 2009.

[75] E. Filho and P. Barbieri, "Flow boiling performance in horizontal microfinned copper tubes with the same geometric characteristics," *Experimental Thermal and Fluid Sciences,* vol. 35, pp. 832-840, 2011.

[76] A. Padovan, D. Del Col and L. Rossetto, "Experimental study on flow boiling of R134a and R410A in a horizontal microfin tube at high saturation temperatures," *Applied Thermal Engineering,* vol. 31, pp. 3814-3826, 2011.

[77] V. Hatamipour and M. Akhavan-Behabadi, "Visual study on flow patterns and heat transfer during convective boiling inside horizontal smooth and microfin tubes," *World Academy of Science, Engineering, and Technology,* vol. 69, pp. 700-706, 2012.

[78] X. Zhao and P. Bansal, "Flow boiling heat transfer analysis of new experimental data of CO2 in a micro-fin tube at -30C," *International Journal of Thermal Sciences,* vol. 59, pp. 38-44, 2012.

[79] L. Colombo, A. Lucchini and A. Muzzio, "Flow patterns, heat transfer, and pressure drop for evaporation and condensation of R134A in microfin tubes," *International Journal of Refrigeration,* vol. 35, pp. 2150-2165, 2013.

[80] D. Sharar and A. Bar-Cohen, "Flow regimes and evaporative heat transfer coefficients for flow boiling in smooth and internally-grooved tubes," in *ITHERM2016,* Las Vegas, NV, USA, 2016.

[81] T. Shedd and T. Newell, "An automated optical liquid film thickness measurement method," *Masters Thesis, University of Illinois, Urbana, IL.*

[82] T. Shedd and T. Newell, "Observation of the influence of helical microgrooves on the behavior of Annular two-phase flow," in *Zero Leakage - Minimum Charge,* Stockholm, Sweden, 213-220.

[83] H. Kimura and M. Ito, "Evaporating heat transfer in horizontal internal spiral-grooved tubes in the region of low flow rates," *JSME,* vol. 24, no. 195, pp. 1602-1607, 1981.

[84] M. Ito and H. Kimura, "Boiling heat transfer and pressure drop in internal spiral-grooved rubes," *JSME,* vol. 22, pp. 1251-1257, 1979.

[85] S. Yoshida, T. Matsunaga, H. Hong and K. Nishikawa, "Heat trasnfer enhancement in horizontal, spirally grooved evaporator tubes," *JSME International Journal Ser II,* vol. 31, no. 3, pp. 505-512, 1988.

[86] S. Yoshida, T. Matsunaga, H. Hong and K. Nishikawa, "Heat transfer to refrigerants in horizontal evaporator tubes with internal, spiral grooves," in *ASME-JSME Thermal Engineering Joint Conference,* 1987.

[87] S. Cui, Y. Tan and Y. Lu, "Heat transfer and flow resistance of R-502 flow boiling inside horizontal ISF tubes," in *Multiphase flow and heat transfer: Second international symposium,* Hemisphere Publishing Corp., 1992, pp. 662-670.

[88] A. Liu and R. Winterton, "A general correlation for saturated and subcooled flow boiling in tubes and annuli based on a nucleate pool boiling equation," *International Journal of Heat and Mass Transfer,* vol. 34, no. 11, pp. 2759-2766, 1991.

[89] K. Murata, "A correlation for forced convective boiling heat transfer of binary refrigerant mixtures: 2nd report, a spirally grooved tube," *Trans. Jpn. Soc. Mech. Eng. Ser. B,* vol. 62, pp. 2732-2728, 1996.

[90] R. Yun, Y. Kim, K. Seo and H. Kim, "A generalized correlation for evaporation heat transfer of refrigerants in micro-fin tubes," *International Journal of Heat and Mass Transfer,* vol. 45, pp. 2003-2010, 2002.

[91] J. Thome, N. Kattan and T. Favrat, "Evaporation in micro-fin tubes: a generalized prediction model," in *Convective Flow and Pool Boiling Conference,* Kloster, Irsee, 1997.

[92] S. Koyama, J. Yu, S. Momoki, T. Fujii and H. Honda, "Forced convective flow boiling heat transfer of pure refrigerants inside a horizontal microfin tube," in *Engineering Foundation Conference on Convective Flow Boiling,* Banff, Canada, 1995.

[93] S. Kandlikar, "A model for correlating flow boiling heat transfer in augmented tubes and compact evaporators," *Journal of Heat Transfer,* vol. 113, pp. 966-972, 1991.

[94] C. Park and P. Hrnjak, "Flow boiling heat transfer of CO2 at low temperatures in a horizontal smooth tube," *Journal of Heat Transfer,* vol. 127, pp. 1305-1312, 2005.

[95] T. Cubaud and C. Ho, "Transport of bubbles in square microchannels," *Phys. Fluids,* vol. 16, pp. 4575-4585, 2004.

[96] A. Serizawa, Z. Feng and Z. Kawara, "Two-phase flow in microchannels," *Experimental Thermal Fluid Science,* vol. 26, pp. 703-714, 2002.

[97] L. Gao and T. Honda, "Experiments on flow boiling heat transfer of pure CO2 and CO2-oil mixtures in horizontal smooth and microfin tubes," in *International Refrigeration and Air Conditioning Conference,* 2006.

[98] L. Gao, T. Honda and S. Koyama, "Experiments on flow boiling heat transfer of almost pure CO2 and CO2-oil mixtures in horizontal smooth and microfin tubes," *HVAC&R Research,* vol. 13, pp. 415-425, 2007.

[99] L. Gao, T. Ono and T. Honda, "Pressure drops of CO2 and oil mixtures in horizontal smooth and micro-fin tube evaporators," in *International Congress of Refrigeration ICR07-B1-1262,* Beijing, 2007.

[100] Y. Kim, J. Cho and M. Kim, "Experimental study on the evaporative heat transfer and pressure drop of CO2 flowing upward in vertical smooth and micro-fin tubes

with the diameter of 5mm," *International Journal of Refrigeration,* vol. 31, pp. 771-779, 2008.

[101] T. Ono, L. Gao and T. Honda, "Heat transfer and flow characteristics of flow boiling of CO2-oil mixtures in horizontal smooth and micro-fin tubes," *Heat Transfer - Asian Research,* vol. 39, no. 3, pp. 195-207, 2010.

[102] L. Cheng, G. Ribatski and J. Thome, "New prediction methods for CO2 evaporation inside tubes: Part II - An updated general flow boiling heat transfer model based on flow patterns," *International Journal of Heat and Mass Transfer,* vol. 51, pp. 125-135, 2008.

[103] Z. Wu, Y. Wu and B. L. W. Sunden, "Convective vaporization in micro-fin tubes of different geometries," *Experimental Thermal Fluid Science,* vol. 44, pp. 298-308, 2013.

[104] S. Mancin, A. Diani and L. Rossetto, "R134a flow boiling heat transfer and pressure drop inside a 3.4 mm ID microfin tube," in *68th Conference of the Italian Thermal Machines Engineering Association, ATI2013*, 2014.

[105] J. Thome, "Two-phase heat transfer using no-phase flow models?," *Heat Transfer Engineering,* vol. 25, no. 6, pp. 1-2, 2014.

[106] S. Nozu and H. Honda, "Condensation of refrigerants in horizontal, spirally grooved microfin tubes: numerical analysis of heat transfer in annular flow regime," *Journal of Heat Transfer,* vol. 122, pp. 80-91, 2000.

[107] H. Honda, H. Wang and S. Nozu, "A theoretical model of film condensation in horizontal microfin tubes," *Journal of Heat Transfer,* vol. 124, pp. 94-101, 2002.

[108] H. Wang, H. Honda and S. Nozu, "Modified theoretical models of film condensation in horizontal microfin tubes," *International Journal of Heat and Mass Transfer,* vol. 45, pp. 1513-1523, 2002.

[109] H. Mori, S. Yoshida, S. Koyama, A. Miyara and S. Momoki, "Prediction of heat transfer coefficients for refrigerants flowing in horizontal spirally grooved evaporator tubes," in *2002 Japan Society of Refrigerating and Air Conditioning Engineers Annual Conference*, Okayama, Japan, 2002.

[110] H. Honda and Y. Wang, "Theoretical study of evaporation heat transfer in horizontal microfin tubes: stratified flow model," *International Journal of Heat and Mass Transfer,* vol. 47, pp. 3971-3983, 2004.

[111] O. Makishi, H. Honda and Y. Wang, "New theoretical models of evaporation heat transfer in horizontal microfin tubes," *International Journal of Heat and Mass Transfer,* vol. 49, pp. 2328-2336, 2006.

[112] Y. Wang, Y. Wang, G.-X. Wang and H. Honda, "Prediction of evaporation heat transfer coefficient based on gas-liquid two-phase annular flow regime in horizontal microfin tubes," *Applied Thermal Engineering,* vol. 29, pp. 2970-2976, 2009.

[113] S. Momoki, S. Higashiiue, T. Shigechi, H. Mori, Yamaguchi and T, "Prediction of evaporation heat transfer coefficient of refrigerants inside a horizontal spirally grooved tube based on flow regime information," in *Transactions of the Japan Society of Refrigerating and Air Conditioning Engineers*, 2006.

[114] L. Liebenberg and J. Meyer, "Refrigerant condensation flow regimes in enhanced tubes and their effect on heat transfer coefficients and pressure drops," *Heat Transfer Engineering,* vol. 29, pp. 506-520, 2008.

[115] L. Doretti, C. Zilio, S. Mancin and A. Cavallini, "Condensation flow patterns inside plain and microfin tubes: A review," *International Journal of Refrigeration,* vol. 36, pp. 567-587, 2013.

[116] P. Rollman and K. Spindler, "A new flow pattern map for flow boiling in microfin tubes," *International Journal of Multiphase Flow,* vol. 72, pp. 181-187, 2015.

[117] A. Cavallini, D. Del Col, L. Doretti, G. Longo and L. Rosetto, "Refrigerant vaporization inside enhanced tubes: a heat transfer model," in *Eurotherm Seminar,* Grenoble, France, 1998.

[118] L. Liebenberg, J. Thome and J. Meyer, "Flow visualization and flow pattern identification with power spectral density distributions of pressure traces during refrigerant condensation in smooth and microfin tubes," *Journal of Heat Transfer,* pp. 209-220, 2005.

[119] J. Thome, "Update on Kattan-Thome-Favrat flow boiling model and flow pattern map," in *5th International conference on boiling heat transfer*, 2003.

[120] J. Thome, J. El Hajal and A. Cavallini, "Condensation in horizontal tubes, part 2: new heat transfer model based on flow regimes," *International Journal of Heat and Mass Transfer,* vol. 46, pp. 3365-3387, 2003.

[121] D. Barnea, O. Shoham, Y. Taitel and A. Dukler, "Flow pattern transition for downward inclined two phase flow; horizontal to vertical," *Chem. Eng. Sci.,* vol. 37, pp. 735-740, 1982.

[122] D. Steiner, "Heat transfer to boiling saturated liquids," *VDI-Warmeatlas (VDI Heat Atlas.*

[123] L. Wojtan, T. Ursenbacher and J. Thome, "Dynamic void fractions in stratified types of flow, Part II: Measurements for R-22 and R-410A," *Int. J. Multiphase Flow,* vol. 30, pp. 125-137, 2004.

[124] D. Biberg, "An explicit approximation for the wetted angle in two-phase stratified pipe flow," *Canadian Journal of Chemical Engineering,* vol. 77, pp. 1221-1224, 1999.

[125] H. Mori, S. Yoshida, K. Ohishi and Y. Kokimoto, "Dryout quality and post dryout heat transfer coefficient in horizontal evaporator tubes," in *Proc. of 3rd European Thermal Sciences Conference*, 2000.

[126] S. Kutateladze, "On the transition to film boiling under natural convection," *Kotloturbostroenie,* vol. 3, no. 10, 1948.

[127] M. Cooper, "Saturated nucleate pool boiling: A simple correlation," in *First UK National Heat Transfer Conference*, 1984.

[128] J. El Hajal, J. Thome and A. Cavallini, "Condensation in horizontal tubes, Part 2: New heat transfer model based on flow regimes," *International Journal of Heat and Mass Transfer,* vol. 46, no. 18, pp. 3365-3387, 2003.

[129] D. Groeneveld, "Post dry-out heat transfer at reactor operating conditions," in *ANS Topical Meeting on Water Reactor Safety*, Salt Lake City, 1973.

[130] R. Dougall and W. Rohsenow, "Film boiling on the inside of vertical tubes with upward flow of the fluid at low vapor qualities," MIT Report no. 9079-26, 1963.

[131] L. Wojtan, Experimental and analytical investigation of void fraction and heat transfer during evaporation in horizontal tubes, Lausanne, Switzerland: PhD Thesis, Department of Mechanical Engineering, Swiss Federal Institute of Technology, 2004.

[132] M. Lallemand, C. Branescu and P. Haberschill, "Local heat transfer coefficients during boiling of R-22 and R-407C in horizontal smooth and microfin tubes," *International Journal of Refrigeration,* vol. 24, pp. 57-72, 2001.

[133] M. Steinke and S. Kandlikar, "Control and effect of dissolved air in water during flow boiling in microchannels," *International Journal of Heat and Mass Transfer,* vol. 47, pp. 1925-1935, 2003.

[134] A. Smith, N. Jankowski and L. Boteler, "Measurement of high performance thermal interfaces using a reduced scale steady-state tester and infrared microscopy," *Journal of Heat Transfer,* Accepted manuscript posted December 7, 2015.

[135] J. Bennett and E. Ashley, "Infrared reflectance and emittance of silver and gold evaporated in ultrahigh vacuum," *Applied Optics,* vol. 4, no. 2, pp. 221-224, 1965.

[136] O. Loebich, "The optical properties of gold," in *Gold Bull*, 1972, pp. 2-10.

[137] D. Sharar, A. Bergles, N. Jankowski and A. Bar-Cohen, "Non-intrusive optical validation of two-phase flow regimes in a small diameter tube," in *ASME FEDSM*, Chicago, 2014.

[138] T. Salem, D. Ibitayo and B. Geil, "Validation of infrared camera thermal measurements on high-voltage power electronic components," *IEEE Transactions on Instrumentation and Measurement,* vol. 56, no. 5, pp. 1973-1978, 2007.

[139] E. Rahim, "Limits of thin film cooling in microgap channels," *Doctor of Philosophy, UMD, Department of Mechanical Engineering,* 2011.

[140] P. Bevington and D. Robinson, Data reduction and error analysis for the physical sciences, McGraw-Hill Education; 3rd edition, 2002.

[141] A. Ullmann and B. Brauner, "The prediction of flow pattern maps in mini channels," *Multiphase Science Technology,* vol. 19, no. 1, pp. 49-73, 2007.

[142] D. Sharar, A. Bergles, N. Jankowski and A. Bar-Cohen, "Non-intrusive optical validation of two-phase flow regimes in a small diameter tube," *Jouurnal of Heat Transfer Engineering,* vol. 37, no. 11, 2016.

[143] J. Drahos and J. Cermak, "Diagnostics of gas-liquid flow patterns in chemical engineering systems," *Chemical Engineering and Processing,* vol. 26, no. 2, pp. 147-164, 1989.

[144] C. Owen, J. Jones and N. Zuber, "The interrelation between void fraction fluctuations and flow patterns in two-phase flow," *International Journal of Multiphase Flow,* pp. 273-306, 1975.

[145] M. Vince and R. Lahev, "On the development of an objective flow regime indicator," *International Journal of Multiphase Flow,* pp. 93-124, 1982.

[146] R. Rahim and M. Rahiman, "Non-invasive imaging of liquid/gas flow using ultrasonic transmission-mode tomography," *Sensors and Actuators,* pp. 337-345, 2007.

[147] J. Burns, C. Ramshaw and R. Jachuck, "Measurement of liquid film thickness and the determination of spin-up radius on a rotating disc using an electrical resistance technique," *Chemical Engineering Science,* pp. 2245-2253, 2003.

[148] H. Caniere, B. Bauwens, C. T'Joen and M. DePaepe, "Mapping of horizontal refrigerant two-phase flow patterns based on clustering of capacitive sensor signals," *International Journal of Heat and Mass Transfer,* pp. 5298-5307, 2010.

[149] R. Revellin, V. Dupont, T. Ursenbacher, J. Thome and I. Zun, "Characterization of two-phase flows in microchannels: Optical measurement technique and flow parameter results for R-134a in a 0.5mm channel," *International Journal of Multiphase Flow,* vol. 32, pp. 755-774, 2006.

[150] E. Jassim, T. Newell and J. Chato, "Probabilistic determination of two-phase flow regimes in horizontal tubes utilizing an automated image recognition technique," *Experiments in Fluids,* pp. 563-573, 2007.

[151] T. Ursenbacher and L. T. J. Wojtan, "Interfacial measurements in stratified types of flow - Part 1: New optical measurement technique and dry angle measurement," *Internationl Journal of Multiphase Flow,* pp. 107-124, 2004.

[152] H. Canière, "Flow pattern mapping of horizontal evaporating refrigerant flow based on capacitive void fraction measurements," *Ph.D. Thesis, Ghent University - UGent, Gent, Belgium,* 2009.

[153] A. Pautsch and T. Shedd, "Adiabatic and diabatic measurements of the liquid film thickness during spray cooling with FC-72," *International Journal of Heat and Mass Transfer,* vol. 49, pp. 2610-2618, 2006.

[154] T. Shedd and T. Newell, "Automated optical liquid film thickness measurement method," *Review of Scientific Instruments,* vol. 69, no. 12, pp. 4205-4213, 1998.

[155] S. Rouhani and M. Sohal, "Two-phase flow patterns: A review of research results," *Prog. Nucl. Energy,* vol. 11, no. 3, pp. 219-259, 1983.

[156] "OLS4000 Optical Metrology," Olympus, [Online]. Available: http://www.olympus-ims.com/en/metrology/ols4000/. [Accessed 20 August 2013].

[157] "Norland Optical Adhesive 65," Norland Products, [Online]. Available: https://www.norlandprod.com/adhesives/noa%2065.html. [Accessed 21 August 2013].

[158] K. Triplett, S. Ghiaasiaan, S. Abdel-Khalik and D. Sadowski, "Gas-Liquid two-phase flow in micro-channels, part 1: two-phase flow pattern," *Int. J. Multiphase Flow,* vol. 25, pp. 377-394, 1999.

[159] R. Revellin, "Experimental Two-phase Fluid Flow in Microchannels. PhD. Thesis (Prof. John R. Thome, Director), LTCM-EPFL, Swiss Federal Institute of Technology," 2005.

[160] R. da Silva Lima, J. Moreno Quiben and J. Thome, "Flow boiling in horizontal smooth tubes: New heat transfer results for R-134a at three saturation temperatures," *Applied Thermal Engineering,* vol. 29, no. 7, pp. 1289-1298, 2009.

[161] A. Bar-Cohen, C. Holloway, A. Riaz and A. Kaffel, "Waves and instabilities in high quality adiabatic flow in microgap channels," *International Journal of Multiphase Flow,* p. accepted for publication, 2016.

[162] L. Chamra and P. Mago, "Modelling of evaporation heat transfer of pure refrigerants and refrigerant mixtures in microfin tubes," *Journal of Mechanical Engineering Science,* vol. 221, no. Part C, pp. 443-454, 2007.

[163] E. Lemmon, M. Huber and M. McLinden, *NIST Standard Reference Database 23: Reference Fluid Thermodynamic and Transport Properties - REFPROP, Version 7.0,* Gaithersburg: National Institute of Standards and Technology, Standard Reference Data Program.

[164] H. Lin, P. Ye and G. Wilk, "Leakage current and breakdown electric-field studies on ultrathin atomic-layer-deposited Al2O3 on GaAs," *Applied Physics Letters,* vol. 87.

[165] Y. Zhang, J. Bertrand, R. Yang and S. L. Y. George, "Electroplating to visualize defects in Alumina thin films grown using atomic layer deposition," *Thin Solid Films,* vol. 517, pp. 3269-3272, 2009.

[166] M. Kroll, W. Blau, R. Grandjean, F. Benfield, P. Lusi, L. Paulus and J. de Jongh, "Magnetic properties of ferromagnetic nanowires embedded in nanoporous alumina membranes," *Journal of Magnetism and Magnetic Materials,* vol. 249, pp. 241-245, 2002.

[167] M. Schlesinger and M. Paunovic, Modern Electroplating, New York: John Wiley & Sons, 2000.

[168] Y. Zhang, D. Seghete, A. Abdulagatov, Z. Gibbs, A. Cavanagh, R. Yang, S. George and Y. Lee, "Investigation of the defect density in ultra-thin Al2O3 films grown using atomic layer deposition," *Surface & Coatings Technology,* vol. 205, pp. 3334-3339, 2011.

[169] "Impreglon Worldwide Quality Coatings," [Online]. Available: http://www.impreglon.us/front_content.php?changelang=3. [Accessed 2013].

[170] W.-S. Kwack, H.-J. Choi, W.-C. O. H.-R. Choi, S.-Y. M. K. K. J.-Y. Shin, Y.-K. Jeong and S.-H. Kwon, "Charging characteristics of Ru Nanocrystals embedded in Al2O3 matrix prepared by using the initial growth stage of Ru plasma-enhanced atomic layer deposition," *Journal of Ceramic Processing Research,* vol. 13, no. 3, pp. 338-342, 2012.